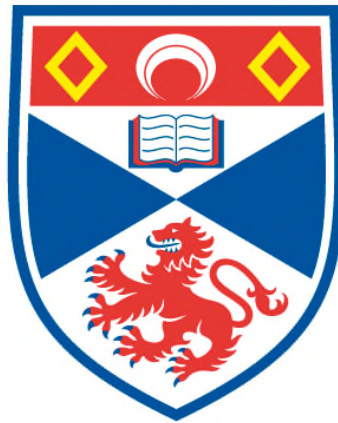


**NUMERICAL SIMULATIONS OF FOOTPOINT DRIVEN
CORONAL HEATING**

Jennifer Patricia O'Hara

**A Thesis Submitted for the Degree of PhD
at the
University of St Andrews**



2016

**Full metadata for this item is available in
St Andrews Research Repository
at:**

<http://research-repository.st-andrews.ac.uk/>

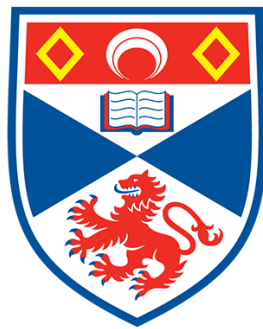
Please use this identifier to cite or link to this item:

<http://hdl.handle.net/10023/8871>

This item is protected by original copyright

Numerical Simulations of Footpoint Driven Coronal Heating

Jennifer Patricia O'Hara



University of
St Andrews

This thesis is submitted in partial fulfilment for the degree of PhD
at the
University of St Andrews

May 18, 2016

Abstract

Magnetic field permeates the solar atmosphere and plays a crucial role in the dynamics, energetics and structures observed. In particular, magnetic flux tubes provide the structure for coronal loops that extend from the solar surface into the corona. In this thesis, we present 3D numerical simulations examining the heating produced by reconnection between flux tubes driven by rotational footpoint motions. The basic model consists of two, initially aligned, flux tubes that are forced to interact by rotational driving velocities on the flux concentrations on the boundaries. A single, twisted current layer is created in the centre of the domain and strong, localised heating is produced. We extend this model by altering the number, distribution and strength of the sources, while maintaining the same total magnetic flux on the boundaries. The dynamical evolution and the resultant magnitude, distribution and timing of the heating events are examined for the different flux distributions. In all cases, the magnetic field is stressed by the boundary motions and a current grows within the domain. A comparison of cases with two and four sources shows that there are more locations of current concentrations, but with reduced maximum current density values, for the four source case. This produces weaker reconnection and less efficient heating. In addition, for the case with two sources, we also consider the effect of splitting up one of the sources into many smaller flux fragments. The evolution and heating are shown to be very similar to the two source case. The impact of increasing the strength of the background field between the flux tubes is also examined and we find that it delays and increases the strength of the heating, although by how much depends on the distribution of the flux sources.

Declarations

I, Jennifer O'Hara, hereby certify that this thesis, which is approximately 50,000 words in length, has been written by me, and that it is the record of work carried out by me, or principally by myself in collaboration with others as acknowledged, and that it has not been submitted in any previous application for a higher degree.

I was admitted as a research student in September 2012 and as a candidate for the degree of Ph.D in September 2013; the higher study for which this is a record was carried out in the University of St Andrews between 2012 and 2016.

Date: Signature of candidate:

I hereby certify that the candidate has fulfilled the conditions of the Resolution and Regulations appropriate for the degree of Ph.D in the University of St Andrews and that the candidate is qualified to submit this thesis in application for that degree.

Date: Signature of supervisor:

In submitting this thesis to the University of St Andrews I understand that I am giving permission for it to be made available for use in accordance with the regulations of the University Library for the time being in force, subject to any copyright vested in the work not being affected thereby. I also understand that the title and the abstract will be published, and that a copy of the work may be made and supplied to any bona fide library or research worker, that my thesis will be electronically accessible for personal or research use unless exempt by award of an embargo as requested below, and that the library has the right to migrate my thesis into new electronic forms as required to ensure continued access to the thesis. I have obtained any third-party copyright permissions that may be required in order to allow such access and migration, or have requested the appropriate embargo below.

The following is an agreed request by candidate and supervisor regarding the publication of this thesis:

PRINTED COPY

No embargo on print copy

ELECTRONIC COPY

No embargo on electronic copy

Date:

Signature of candidate: Signature of supervisor:

Acknowledgements

There are many people who I would like to thank, who have made the time I have spent during my Ph.D. both productive and enjoyable...

My supervisor, Ineke, whose guidance and encouragement inspired me to become more confident in my research and in myself. The entire maths department, both staff and fellow students, who make St Andrews such a wonderful place to study.

My family, who were always ready at the end of the phone, to share both the highs and the lows over the four years and to remind me to smile. Especially my parents, for everything they have done for me, both during my Ph.D. and for my whole life. My sister, Katie, for doing what sisters do best: driving me crazy and making me laugh at the same time. My Grannie, from whom, I am reliably informed, I inherited any ability I have in mathematics.

All my friends, both in St Andrews and across the world. Particularly, all my office mates over the past few years, who provided helpful suggestions and welcome distractions and whose commitment to supplying 'office breakfast' has helped fuel my studies. Likewise, Zoe and Crisi, whose enthusiasm and friendship has made the long work days, and importantly the long lunch breaks, so much more enjoyable. Rocio, who I am so glad also chose to do a Ph.D. in St Andrews so I was able to meet her and share all the long walks and beautiful dinners. Rachael, whose replies to the enquiries from someone who was (then) practically a stranger, helped to convince me to enter into a Ph.D. and who then proved to be the most amazing house-mate, baker and friend.

Finally, Casey, for your all your help and unlimited support. For listening to all my problems and then for helping me to forget about them. I am forever happy that you decided to take the trip across the ocean and share the past four years with me.

Thank you to all of you who were part of the whole experience.

Contents

1	Introduction	1
1.1	The Sun	1
1.1.1	The Structure of the Sun	2
1.1.2	Common Visible Solar Features	4
1.2	Magnetohydrodynamics	6
1.2.1	Summary of the MHD Equations	7
1.2.2	Derived Equations, Quantities and Features	8
1.3	The Coronal Heating Problem	11
1.3.1	AC and DC Heating	11
1.3.2	Creation of Small-scales	12
1.3.3	Nanoflares	14
1.4	Summary of 3D Simulations of Coronal Heating	14
1.5	Introduction to the Lare3D Code	18
1.5.1	Lare3D Normalisation	18
1.5.2	Shock Viscosity	19
1.5.3	The Grid	20
1.6	Outline	21
2	Creating an Initial Two Flux Tube Configuration	23
2.1	Comparison of Flux Tube Set-ups	23
2.1.1	Numerical Set-up	23
2.1.2	Initial Conditions and Normalisation	25
2.1.3	Magnetic Field	26
2.1.4	Current Density	28
2.1.5	Density, Pressure and Temperature	31
2.1.6	Velocity	33

2.1.7	Evolution of Energy	34
2.1.8	Plasma β and Lorentz Force	36
2.1.9	Summary	38
2.2	Discussion of Normalisation Values	40
2.3	A Comparison of Periodic Boundary Conditions and Neumann and Dirichlet Boundary Conditions	41
3	Driving Two Flux Tubes: Resistivity Test Cases	45
3.1	Description of Velocity Driver	45
3.2	Investigating Resistivity	46
3.2.1	Investigating the Effect of Varying Values of Uniform Resistivity	46
3.2.2	Investigating the Effect of Localised Resistivity Regions	59
4	Resolution Comparison: Two Flux Tubes	73
4.1	Comparing the Two Flux Tube Set-up at Higher Resolutions	73
4.2	Comparing Rotation of Two Flux Tubes at Higher Resolutions	78
5	Extended Loop Length Comparison	87
5.1	Comparing the Relaxation of Flux Tubes of Increased Length	87
5.2	Comparing the Rotation of Flux Tubes of Increased Length	88
6	Comparison of Two and Four Flux Tubes	99
6.1	Comparing Two and Four Flux Tubes Set-up	99
6.2	Comparing Two and Four Flux Tubes Under Rotation	107
6.2.1	Magnetic Flux Connectivity and Evolution	107
6.2.2	Current Formation and Forces	117
6.2.3	Energetics	123
6.2.4	Distribution and Magnitude of Heating	129
6.2.5	Summary	133
6.3	Impact of Resistivity	136
6.3.1	Unstable Behaviour at Later Time	136
6.3.2	Increasing $\eta_0 = 10^{-4}$ to $\eta_0 = 10^{-3}$	137
7	Comparison of Two and Four Flux Tubes with a Background Field	145
7.1	Comparing the Flux Tube Set-up with a Background Field	145
7.2	Comparing Flux Tubes with a Background Field Under Rotation	148
7.2.1	Dynamical Evolution	148

7.2.2	Connectivity Evolution	150
7.2.3	Efficiency of Heating and Energetics	155
7.2.4	Summary	160
8	Fragmented Sources	161
8.1	Creating a Fragmented Source Flux Tube Set-up	161
8.2	Comparing Fragmented Sources under Rotation	165
9	Conclusions and Future Work	171
A	Uniform Magnetic Field	177
	Bibliography	182

Chapter 1

Introduction

This thesis uses numerical simulations to investigate elementary heating events in the solar atmosphere. In this chapter, we begin by describing some of the important features of the Sun and open questions that pertain to this thesis, in particular the *coronal heating problem*. In Section 1.2, we describe the theory of Magnetohydrodynamics (MHD) and its use in modelling solar phenomena. In Section 1.3, a short summary of coronal heating theories is given, before we go on in Section 1.4 to discuss MHD simulations that investigate these theories. The numerical code we use is introduced in Section 1.5 and finally, in Section 1.6, a brief outline of this thesis is given.

1.1 The Sun

As our nearest star and the source of light and therefore life on our planet, the Sun has been a captivating object of study throughout history. The Sun has been a prominent feature in many civilisations' cultures and mythologies and solar observations began at least as early as 2000 BC, when the Chinese are known to have recorded solar eclipses. Later, in 1543 the importance of the Sun in the solar system was reaffirmed by Copernicus, who first suggested that the planets revolved around the Sun. Since this time, our understanding of the Sun has greatly improved and much of this progress is due to the increasing number and quality of observations. From the first telescope observations in the 17th century, to the exciting advancements in solar observations from the many satellite missions (such as Skylab, SoHO, TRACE and SDO to name but a few) occurring over the last quarter of a century, huge leaps of understanding have occurred. However, the developments in observations have also coincided with large advancements in the theory and computational modelling of physical processes on the Sun.

1.1.1 The Structure of the Sun

The Sun is essentially a giant ball of hot plasma and its structure is commonly divided into the *interior* and the *atmosphere*, which lie above and below the visible surface of the Sun called the *photosphere*, respectively. Within these categories, the structure of the Sun is further divided into different regions, shown in Figure 1.1, depending on the region's properties and dominant physical processes.

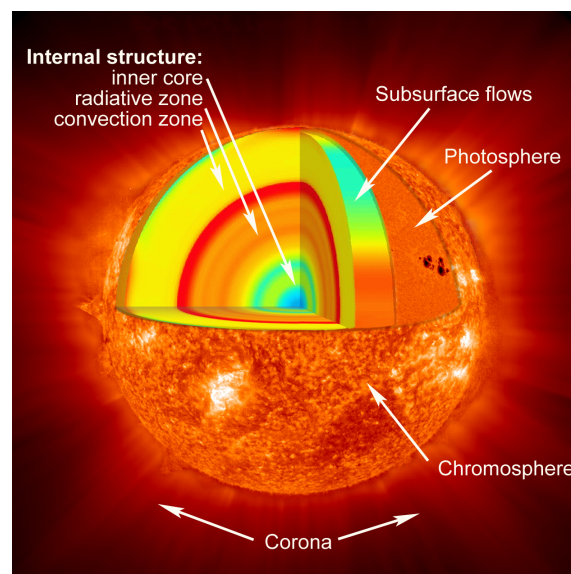


Figure 1.1: Artistic impression of the layers making up the solar interior and atmosphere (NASA).

The Solar Interior

The solar interior extends from the centre of the Sun to the solar radius (R_{\odot}) of 695.5 Mm. The innermost region of the Sun is called the *core*, which extends out to 150 Mm ($0.22R_{\odot}$) and defines where energy is generated by nuclear fusion. The energy then travels out towards the solar surface over the next ≈ 300 Mm, over a region called the *radiative zone*, before forming enormous columns of energy and particles which convect outwards from $0.7R_{\odot}$ in the *convection zone*. This creates turbulent convective motions on a variety of scales that rise up to the visible surface of the Sun.

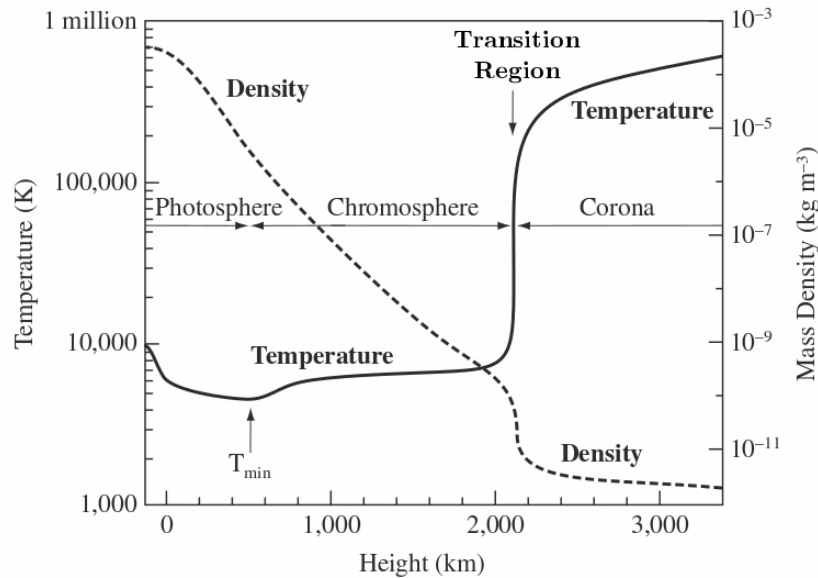


Figure 1.2: A schematic representation of the average variation in temperature and density with height in the solar atmosphere, based on (Priest, 2014).

The Solar Atmosphere

As mentioned above, the photosphere is the visible surface of the Sun, which emits most of the Sun's visible light. It is a thin layer of plasma (a few 100 km thick), which is relatively dense ($\approx 10^{-3} \text{ kg m}^{-3}$) and its temperature decreases with radius from approximately 10000 K to 4500 K. It consists of millions of *granules* of various sizes, from $\approx 1 \text{ Mm}$ to *supergranules* of the order 10's of Mm. These *granules* are the top of convective cells formed by the upper convective zone and have a mean lifetime of 5–10 minutes (Priest, 2014). The centre of the granules consist of hot plasma rising to the surface and the plasma then flows horizontally to the edge of these granules (the *intergranular lanes*) where the cooling plasma falls. The convection therefore produces a range of velocities on the solar surface.

The *chromosphere* is a region ($\approx 2500 \text{ km}$ thick) that lies directly above the photosphere. The temperature increases with height in the chromosphere to about 20,000 K. Above this lies a narrow region called the *transition region*, where the temperature increases rapidly to a value of around 1 MK. The *corona* is the outer layer of the Sun's atmosphere which extends out from the top of the transition region into interplanetary space. An interesting feature of the corona is that it has a very high temperature, in excess of 1 MK. In contrast to the temperature, the density decreases with height in the solar atmosphere (see Figure 1.2) and therefore in the corona the density is generally very low ($\approx 10^{-11} \text{ kg m}^{-3}$).

In the corona the plasma is predominantly Hydrogen, but there are also other elements, and

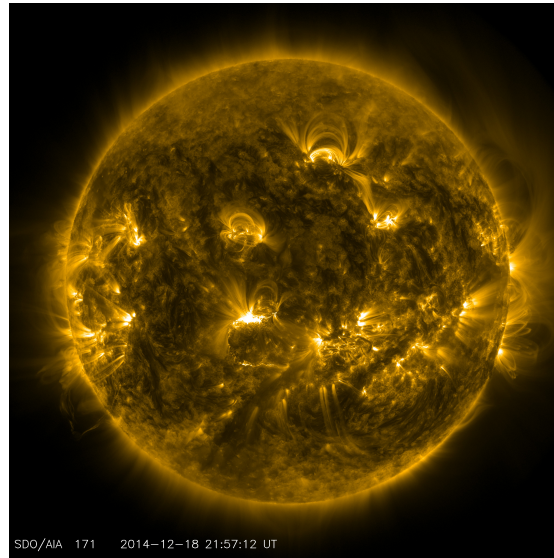


Figure 1.3: An image of the solar corona from the Atmospheric Imaging Assembly (AIA) on Solar Dynamics Observatory (SDO) at 171 \AA taken on 18th December 2014 (NASA).

at the extremely hot temperatures the plasma is highly ionised. Optically thin radiation, mass outflows and thermal conduction are the main ways energy is lost, but despite these energy losses, the atmosphere maintains its high temperatures. Not normally seen in visible light (except during an eclipse), the corona is often observed in EUV and soft X-rays, shown in Figure 1.3.

Intuitively one would think that the temperature would decrease with distance from the energy source at centre of the Sun. Therefore, accounting for the observed increase in temperature through the chromosphere and the corona has become one of the most vibrant research areas in the solar physics community. This open question is commonly termed the *coronal heating problem*.

1.1.2 Common Visible Solar Features

The atmosphere of the Sun is permeated by magnetic field, generated inside the Sun by the solar dynamo and extending through the photosphere into the chromosphere and corona. Many of the visible features of the Sun are governed by the magnetic field. We shall now list several key features of interest to our work:

Sunspots and Active Regions

As previously mentioned, the photosphere emits the majority of the visible light from the Sun. Dark features are also observed on the photosphere, which are known as *sunspots* (shown in Figure 1.4a). Over the last 30 years, ground based and satellite observations have enabled us to

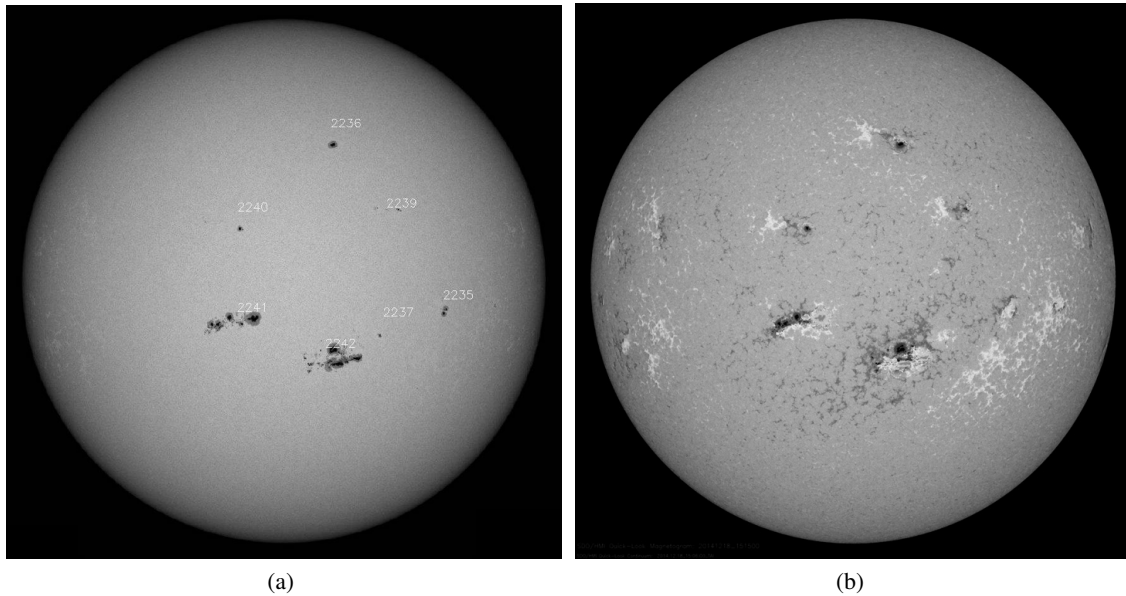


Figure 1.4: Comparison of the sunspots and the magnetic field configurations on the photosphere. (a) SDO/HMI image of sunspots where the numbers label active regions and (b) shows HMI magnetogram at the same time as Figure 1.3 (NASA).

measure the magnetic field strength on the photosphere, showing that the observed sunspots are regions of strong magnetic field, as seen by comparing Figures 1.4a and 1.4b.

Magnetic field maps of the solar surface show a very dynamic magnetic field that is continually evolving and encompassing a range of scales (e.g. Schrijver et al., 1998). Convection and granulation, and the subsequent complex velocities created, impact the evolution of the magnetic field on the solar surface. The magnetic flux is observed to *emerge* and can interact with surrounding flux regions, *coalescing* with flux of the same polarity or *cancelling* with oppositely signed magnetic flux, as well as *fragmenting* into smaller regions of flux (Schrijver et al., 1997). The term *magnetic carpet* is often used to describe the small-scale, evolving photospheric magnetic field incorporating all these processes (e.g. Title and Schrijver, 1998).

There are many different observed magnetic flux features, with a range of sizes. From large scale regions (ranging between 50 and 100000 Mm^2 with average field strength of 100 to 500 G), often called *active regions*, which are associated with sunspots, down to much smaller (100 km), stronger flux elements of strength of the order of 1 kG. The flux within larger features such as active regions is also considered to be concentrated into many of these smaller, stronger flux elements. The structure of the magnetic field is hugely varied and we do not mention all of the observed features here, but seek to emphasise its complexity. The present resolution achievable is near to 100 km (Priest, 2014) and so it remains to be seen whether even more intricate magnetic field distributions are yet unobserved.

Coronal Loops

Above the photosphere, measurements of the magnetic field become more difficult. However, the high temperature of the corona (> 1 MK) means the plasma becomes highly ionised and therefore can not easily flow across the magnetic field. The emissions of the hot plasma therefore give us some idea of the complex magnetic field structure extending from the photosphere into the corona.

Coronal loops are a common feature observed in the solar corona, shown in Figure 1.3. These are often seen as arched structures anchored in the photosphere between regions of strong magnetic field of opposite polarity. They can vary greatly in size and complexity, from large loops extending hundreds of megametres into the corona to small loops that remain very low (a few megametres long) in the atmosphere. Indeed, it is believed that much of the magnetic field emerging from the photosphere remains very low. The temperatures of coronal loops can vary from 10^5 to 10^7 K and similarly a range of densities are observed from 10^8 up to 10^{12} cm^{-3} , where the highest values are typically only seen in flaring loops (Reale, 2010).

The observed loops often appear to have a constant cross section in the corona, however, there is some evidence that they expand in the transition region (e.g. Gabriel, 1976). Coronal loops are also not able to be fully resolved with our current level of resolution. Studies (Reale, 2010, and references therein) suggest that the large features we see may in fact be made up of many smaller *strands*. This in turn can have an impact on the understanding of how these features are formed and heated. It has been suggested that if they are considered as a group of smaller, individually heated strands, then the levels and timing of modelled emissions compare favourably to observations (Peter, 2015, and see Section 1.3.1).

1.2 Magnetohydrodynamics

In this thesis, Magnetohydrodynamics (MHD) shall be used to model features of the solar atmosphere. The MHD approximation, which was developed by Alfvén in the 1940's, combines the laws of fluid dynamics with Maxwell's laws of electromagnetism to model the plasma as a single, electrically conducting fluid and its interaction with the magnetic field on a macroscopic level. There are many important assumptions that are made when deriving the MHD equations, which include:

- the plasma length scales are much greater than the microscopic length scales of the electron and ion dynamics (larger than the gyro-radius and mean free path length),
- the plasma time scales are much longer than the time scales of the electron and ion dynamics,

- the plasma is assumed to be quasi-neutral,
- the plasma is treated as a single fluid,
- the plasma speeds involved are much less than the speed of light, c (non-relativistic).

These are important to keep in mind when using MHD to model different physical processes. We have outlined these briefly but refer to Goedbloed and Poedts (2004) and Priest (2014) (and references therein) for a more detailed description of the assumptions and applicability of MHD.

1.2.1 Summary of the MHD Equations

$$\frac{\partial \rho}{\partial t} = -\nabla \cdot (\rho \mathbf{v}) \quad (\text{mass continuity equation}) \quad (1.1)$$

$$\rho \frac{D\mathbf{v}}{Dt} = -\nabla P + \mathbf{j} \times \mathbf{B} + \mathbf{F} \quad (\text{equation of motion}) \quad (1.2)$$

$$\rho \frac{D\epsilon}{Dt} = -P \nabla \cdot \mathbf{v} - \mathcal{L} \quad (\text{energy equation}) \quad (1.3)$$

$$\frac{\partial \mathbf{B}}{\partial t} = -\nabla \times \mathbf{E} \quad (\text{Faraday's law}) \quad (1.4)$$

$$P = \frac{k_B}{\mu_m} \rho T \quad (\text{equation of state}) \quad (1.5)$$

where the variables \mathbf{j} and \mathbf{E} are given by:

$$\nabla \times \mathbf{B} = \mu_0 \mathbf{j} \quad (\text{a form of Ampère's law}) \quad (1.6)$$

$$(\mathbf{E} + \mathbf{v} \times \mathbf{B}) = \eta \mathbf{j} \quad (\text{Ohm's law}) \quad (1.7)$$

and the initial condition for the magnetic field:

$$\nabla \cdot \mathbf{B} = 0 \quad (\text{solenoidal constraint}) \quad (1.8)$$

where μ_0 is the *magnetic permeability of a vacuum* ($\mu_0 = 4\pi \times 10^{-7} \text{ H m}^{-1}$), $k_B = 1.3807 \times 10^{-23} \text{ J K}^{-1}$ is the Boltzmann constant, P is the *pressure*, ρ is the *density*, \mathbf{B} is the *magnetic field*,

\mathbf{E} is the *electric field*, \mathbf{j} is the *electric current density*, \mathbf{v} is the *velocity*, η is the *resistivity*, t is *time* and ϵ is the *specific internal energy density*. This is related to temperature and density by:

$$\epsilon = \frac{P}{\rho(\gamma - 1)} = \frac{T k_B}{\mu_m(\gamma - 1)}, \quad (1.9)$$

where γ is the ratio of specific heats (taken to be $\frac{5}{3}$ as in a fully ionised hydrogen plasma), μ_m is the reduced mass (i.e. the average mass of all particles in the plasma and for a fully ionised plasma is taken to be $0.5m_p$, where $m_p = 1.6726 \times 10^{-27}$ kg is the proton mass).

These are the resistive MHD equations. The *ideal* equations can be recovered by setting $\eta = 0$. The term \mathbf{F} in the equation of motion (Equation 1.2) refers to any additional forces such as gravity or viscous forces. Similarly, the term \mathcal{L} in the energy equation (Equation 1.3) refers to any additional energy sources or sinks such as Ohmic heating (ηj^2), viscous heating, thermal conduction and radiative losses.

In this thesis we shall neglect gravity, conduction and radiation, but viscosity is included and this is discussed further in Section 1.5.2.

1.2.2 Derived Equations, Quantities and Features

The MHD equations (and the approximations needed to use them) typically lead to several characteristic quantities and equations, which we will readily encounter in our work. We therefore list several specific examples for use in later investigations.

Induction Equation

In MHD the electric field \mathbf{E} and electric current density \mathbf{j} are often eliminated in Equations 1.6, 1.4 and 1.7 for convenience to produce:

$$\frac{\partial \mathbf{B}}{\partial t} = \nabla \times (\mathbf{v} \times \mathbf{B}) - \nabla \times (\eta' \nabla \times \mathbf{B}). \quad (1.10)$$

This is known as the Induction Equation, where $\eta' = \frac{1}{\mu_0 \sigma}$ is the diffusivity ($\text{m}^2 \text{s}^{-1}$). If the diffusivity is considered constant this can be written as

$$\frac{\partial \mathbf{B}}{\partial t} = \nabla \times (\mathbf{v} \times \mathbf{B}) + \eta' \nabla^2 \mathbf{B}. \quad (1.11)$$

In this thesis we will often consider a spatially dependent diffusivity, but for now consider this form of the induction equation to infer the importance of the different terms in defining the plasma properties.

Magnetic Reynolds Number

The first and second terms in the induction equation are known as the *advection* and *diffusion* terms, respectively. The ratio of these terms is an important dimensionless parameter called the *magnetic Reynolds number* (R_m):

$$R_m = \frac{|\nabla \times (\mathbf{v} \times \mathbf{B})|}{|\eta' \nabla^2 \mathbf{B}|} \approx \frac{v_0 l_0}{\eta'}, \quad (1.12)$$

where l_0 is the typical length scale and v_0 the plasma velocity. This parameter gives an indication of how the magnetic field interacts with the plasma. If $R_m \gg 1$, the advection term dominates and the magnetic field moves with the plasma, whereas if $R_m \ll 1$ then diffusion is most important. On the Sun, typically $R_m \gg 1$ as the length scales (l_0) and velocities (v_0) are generally large, and the change in the magnetic field is governed by the plasma motions. However, there are exceptions to this, where small length scales are formed in the magnetic field (see Section 1.3.2) and diffusion becomes important.

Magnetic Tension and Magnetic Pressure

The $\mathbf{j} \times \mathbf{B}$ term in the equation of motion (Equation 1.2) is known as the *Lorentz force* and using Equation 1.6 and a vector identity this can be written as

$$\mathbf{j} \times \mathbf{B} = \frac{1}{\mu_0} (\nabla \times \mathbf{B}) \times \mathbf{B} = \frac{1}{\mu_0} (\mathbf{B} \cdot \nabla) \mathbf{B} - \nabla \left(\frac{B^2}{2\mu_0} \right). \quad (1.13)$$

The Lorentz force can therefore be considered to be separated into two parts, namely the *magnetic tension* force ($(\mathbf{B} \cdot \nabla) \mathbf{B} / \mu_0$) and the *magnetic pressure* force ($-\nabla (B^2 / 2\mu_0)$).

Plasma β

Another dimensionless parameter is the ratio of the plasma pressure P to the magnetic pressure ($B^2 / 2\mu_0$), which is called the plasma beta (β):

$$\beta = \frac{P}{B^2 / 2\mu_0} = \frac{2\mu_0 P}{B^2} \quad (1.14)$$

In the photosphere typically $\beta > 1$ and the plasma is considered to mostly dominate the magnetic field. The plasma beta reduces rapidly with distance above the photosphere so that in the corona (where $\beta < 1$) the reverse is true.

Flux Tubes

A *magnetic flux tube* is a collection of magnetic field lines that intersect a simple closed curve (Priest, 2014), where the net flux Φ (i.e. strength of the flux tube) is given by the integral:

$$\Phi = \int_S \mathbf{B} \cdot \mathbf{n} \, dS, \quad \text{where } S \text{ is the surface inside the closed curve.} \quad (1.15)$$

These are often modelled as isolated features but in reality would interact with their surrounding magnetic field. They are associated with many observable features such as sunspots on the solar surface and (most importantly for this thesis) they act as the confining magnetic field structure that produce the observed coronal loops.

Force Free and Potential Fields

A comparison of the magnitude of the terms in the equation of motion (Equation 1.2) can also be considered, where $\rho_0, l_0, v_0, P_0, B_0$ etc. are typical plasma values. The velocity variations on the left hand side can be neglected if the flow speed is much less than the Alfvén speed (v_A) ($v_0 \ll v_A = B_0 / \sqrt{\mu_0 \rho_0}$) and the sound speed ($v_0 \ll c_s = \sqrt{\gamma P_0 / \rho_0}$). Therefore the equation of motion reduces to the magnetohydrostatic equation in force balance:

$$\mathbf{0} = -\nabla P + \frac{1}{\mu_0} \mathbf{j} \times \mathbf{B}.$$

Similarly when $\beta \ll 1$ the pressure force can be neglected in favour of the $\mathbf{j} \times \mathbf{B}$ term, which is known as the *Lorentz force*. If included, gravity can also be neglected when the length scales are much less than the pressure scale height ($l_0 \ll H = P_0 / \rho_0 g$) and the equation reduces to:

$$\mathbf{0} = \mathbf{j} \times \mathbf{B}. \quad (1.16)$$

Magnetic fields satisfying this are called *force-free*. There are several solutions to this equation. One solution to this is the seemingly trivial solution

$$\mathbf{j} = \mathbf{0},$$

where the current density is identically zero everywhere. Solutions of this type produce fields that are called *potential*. The potential field constructed from the normal component of the magnetic field given on a closed surface is the minimal possible energy state of the magnetic field (Priest, 1982). An approximation to the coronal field is often given analytically by force free and potential field models.

1.3 The Coronal Heating Problem

The coronal heating problem is an ongoing area of research with a long history and many different theories have been put forward. It is generally agreed that there is sufficient energy entering the solar atmosphere through the photosphere from the convective zone beneath, to account for the observed high temperatures. However, there are many questions that remain, such as: How is the energy dissipated? Where is it dissipated in the atmosphere? On what time-scales and with what magnitudes do the energy depositions occur? How does energy deposited vary with the structure of the solar atmosphere? How does the structuring of the magnetic field (quiet sun, active regions, coronal loops) impact the energy release? In order to improve our understanding of coronal heating, many of these questions are often considered individually. However, it is likely that many of the answers will be inherently interlinked.

In the following section, we briefly describe some of the suggested theories to explain the temperatures of the solar atmosphere, focussing on those that are most relevant to the investigations in this thesis. For further details and broader discussions, we refer to the many reviews of the subject (e.g. Walsh and Ireland, 2003; Parnell and De Moortel, 2012; De Moortel and Browning, 2015).

1.3.1 AC and DC Heating

Despite the many open questions in coronal heating, it is generally agreed that the energy entering the atmosphere is due to the presence of the magnetic field that is rooted in the convection zone and extends through the photosphere into the solar atmosphere. The high β environment at the photospheric level means that the plasma motions will govern the evolution of the field. The dynamic processes within the photosphere, such as the convective motions and flux emergence will therefore impact the magnetic field. In the past, the convective motions acting on the magnetic field have been considered in two categories, namely *slow* and *fast*, relative to the Alfvén speed (v_A). The fast motions will excite waves in the magnetic field which can propagate through the atmosphere and dissipate in the corona. This is known as AC heating. Alternatively, the slow motions will gradually stress the magnetic field, allowing it to move through a series of (quasi-)equilibria, thereby increasing the energy stored in the magnetic field, which can then be dissipated in the corona. This is known as DC heating. In both of these scenarios it still remains to be explained what mechanisms can dissipate the energy (either stored in the magnetic field or transported in the form of waves into the atmosphere) at the required time-scales and values to explain the observations. These two categories of AC and DC heating mechanisms have historically been considered separately. However, recently it is more commonly argued that the processes involved in heating the solar atmosphere will involve a range of scales and processes (see Peter, 2015).

In this thesis, we shall focus on heating mechanisms associated with DC heating and refer the

reader to the many review articles by Parnell and De Moortel (2012); De Moortel and Nakariakov (2012); Arregui (2015) and references therein for summaries on waves and AC heating.

When slow ($\ll v_A$) footpoint motions are applied, the magnetic field becomes stressed and the energy injected is stored in the field as magnetic energy. The amount of energy which enters the atmosphere through the motions acting on the magnetic field is given by the *Poynting flux* through the photospheric boundary. In the corona, it is expected that there are generally very low levels of dissipation as the magnetic Reynolds number (R_m) is very large ($\approx 10^{13}$). The diffusion term in the induction Equation (1.11) only becomes important if small spatial length scales arise ($R_m < 1$). The creation of high currents (due to large gradients in the magnetic field) produce these large changes over small length scales and leads to heating by Ohmic dissipation and magnetic reconnection.

Magnetic Reconnection

Magnetic reconnection allows magnetic field lines to change connectivity and form a lower energy state, thereby releasing the stored magnetic energy into heat, bulk kinetic energy and fast particle energy. This process is prevalent in many astrophysical settings, including the Earth's magnetosphere and the solar corona (Priest and Forbes, 2000). Magnetic reconnection has been studied in detail, originally in two dimensions and more recently extended to three dimensions. However, the process of magnetic reconnection is still very much an open area of study and there are many questions that remain, particularly in understanding the details of magnetic reconnection in 3D. For a full discussion we refer to Priest and Forbes (2000); Birn and Priest (2007) (and references therein), who give an extensive overview of magnetic reconnection.

1.3.2 Creation of Small-scales

It was first suggested by Levine (1974) and Parker (1972) that the dissipation of many small current sheets could lead to coronal heating. How the formation of localised currents (often called *current layers* or *current sheets*) could occur in the solar atmosphere has been considered by many people and different scenarios have been put forward. A selection of these are described below:

Braiding

The first theory we shall consider, is the suggestion by Parker (1972) that complex photospheric velocity patterns acting on the base of a uniform magnetic field could create the small scales required. Parker suggested a *braiding* of the magnetic field in coronal loops, where complex driving

velocities acting on a uniform magnetic field could create current sheets (tangential discontinuities).

Coronal Tectonics and Topological Features

Priest et al. (2002) proposed that simple photospheric flows acting on the base of a complex magnetic field, with many topological features, could produce current formations. This is known as *coronal tectonics*. It has long been argued that topological features of the magnetic field such as separators, separatrix surfaces and null points are prime locations for current formation and reconnection (e.g. Lau and Finn, 1990; Priest and Titov, 1996). Priest et al. emphasise the importance of the intricate substructure and topology of features such as magnetic loops on the formation of current layers. Each strand within a loop will be rooted into the photosphere in individual flux fragments, which are moved independently. Priest et al. suggest that between each of these strands, topological features such as separatrix surfaces will separate regions of flux with different connectivity and, as the fragments are buffeted by the photospheric motions, currents will form along these features.

QSLs and Geometrical Features

The idea of topological features such as separatrices being important locations for heating was extended to more generalised geometrical features termed *quasi separatrix layers* (QSLs) by Démoulin et al. (1996). Separatrices are topological surfaces where the mapping of the magnetic field line connectivity is discontinuous, whereas Démoulin defined QSLs as regions of rapid (but continuous) change in the field line connectivity. This means that neighbouring field lines passing through a QSL will have footpoints that are very far apart. The extent of the change in field line connectivity can be quantified by the *squashing degree* Q (Titov et al., 2002). A high Q value suggests a steeper gradient in the mapping of the field line connectivity and, in the limit $Q \rightarrow \infty$, it has been suggested that QSLs tend to separatrices (Démoulin, 2006b). QSLs have since been extensively studied and found to be regions associated with reconnection and energy release, similar to separatrices (see Section 1.4).

There are many other suggested mechanisms for the creation of small-scale structures for DC heating, such as instabilities and turbulence. However, these are not the aim of our experiments and for brevity we shall not describe these in detail here, but refer the reader to more in depth discussions (e.g Klimchuk, 2006; Priest, 2014).

1.3.3 Nanoflares

The above scenarios suggest how current layers may be formed in the solar atmosphere to act as locations of heating and reconnection. Attention has now also turned towards looking for evidence of such heating and reconnection events in the solar atmosphere, particularly since the number and quality of observations have improved. It was the observation of many small localised X-ray brightenings by Lin et al. (1984) of relatively small energies between 10^{24} and 10^{27} ergs that inspired Parker (1988) to suggest that a large number of relatively small energy release reconnection events, which he termed *nanoflares*, could produce these observations.

What is meant by the term nanoflare has evolved since Parker introduced the concept. Parker originally referred to impulsive heating events of approximately 10^{24} ergs that could be accounted for due to the slow braiding of the field and the subsequent energy released by the localised magnetic reconnection at the formed current sheets. However, the term nanoflare is often used to refer to more general impulsive energy release events (Klimchuk, 2015), which may also have lower energies than Parker envisaged. There have been extensive theories, models and observations (summarised in recent reviews by De Moortel and Browning, 2015; Klimchuk, 2015; Peter, 2015) that try to suggest how the proposed nanoflares can occur, and with what frequency and magnitude, to effectively explain the required heating.

It is clear that even considering DC heating mechanisms alone, there are a variety of questions still under investigation. For example, within the frame work of DC heating, theories still need to account for the amount of energy dissipation that needs to occur in order to sustain the estimated temperatures observed in the corona. The large amount of energy required suggests that the magnetic field must be allowed to build up sufficient energy before dissipation occurs (Klimchuk, 2015). This suggests that energy release events (such as nanoflares) must be triggered (rather than happening continuously), raising many questions of what triggers them and also on what time-scales and at what locations.

1.4 Summary of 3D Simulations of Coronal Heating

In Section 1.2, the MHD equations and their applicability to the solar corona were described. Much analytical work has been carried out (see Priest, 2014, and references therein) by taking approximations to the full MHD equations. However, since the increase in numerical capability and resources, the area of MHD simulations has expanded. Simulations are currently being used to model many different features of the Sun, from the creation of its dynamo and the evolution of the global magnetic field, to the evolution of individual active regions and even smaller scale features.

There are a wide range of MHD simulations motivated by coronal heating and the focus of the simulations has evolved as the theories around coronal heating have developed (see Section 1.3). The numerical simulations can be used in conjunction with high resolution observations to find evidence that supports or contradicts the evolving theory. We shall limit our discussion to those simulations aimed at examining the validity of the theory of DC heating.

One subset of coronal heating simulations are those directly motivated by Parker's notion of braiding of the magnetic field (Parker, 1972). Many of these simulations focussed on providing numerical evidence for the creation of current sheets, which Parker predicted would form when a uniform field is acted upon by a complex photospheric driver. One of the first simulations of braiding by Ballegooijen (1988) subjected the magnetic field to a series of shears and found fine scales of current develop, where the length scales decrease exponentially with the number of shears applied. Shearing of the magnetic field was investigated further, as the resolution and numerical schemes improved, by many other numerical simulations (e.g Mikic et al., 1989; Galsgaard and Nordlund, 1996). More recently, Bowness et al. (2013) carried out a full 3D MHD resistive evolution of a multiply sheared field at high resolution with an emphasis on the current layer formations and accurately following the evolution of energy in the domain.

In addition to these shearing experiments, a range of other (often rotational) boundary velocity drivers have been applied to magnetic fields to investigate a braiding scenario (e.g Longcope and Sudan, 1994; Rappazzo et al., 2007, 2008; Ng et al., 2012). A detailed overview of flux braiding experiments is given by Wilmot-Smith (2015), who concludes that although thin current layers are found to form due to braiding of magnetic loops, current sheets are not necessarily formed; the slow braiding motions inevitably lead to dissipation and the heating of coronal loops, however details of how this heating depends on the velocity driver and numerical schemes, initial conditions and parameters (e.g. resistivity) still require further investigation.

Coronal tectonics (Priest et al., 2002) can be seen as an extension to Parker's field braiding idea, when the topological features of the field are included, as described in Section 1.3.2. One of the first numerical simulations directly influenced by coronal tectonics was carried out by Mellor et al. (2005), who examined a simple potential field configuration, constructed from four flux patches, which are subjected to a shearing motion. The simulation included a background field and therefore the flux patches were separated by quasi-separatrix layers (QSLs) as opposed to separatrices. Mellor et al. found that the application of this very simple driver to the field with an existing complex geometry created current concentrations. The current was also shown to scale with resolution, which is indicative of current sheet formation. They also examined the resultant energy release due to dissipation at these current concentrations and found that the form of heating appeared dependent on the form of resistivity used.

The proposed tectonics heating mechanism was then further investigated in a series of numer-

ical simulations by De Moortel and Galsgaard (2006a,b); Wilmot-Smith and De Moortel (2007). They numerically investigated flux tube configurations described by Priest et al. (2005), who had analytically investigated the energy storage and heating at separators and separatrix surfaces. Priest et al. (2005) proposed that the arbitrary motions of sources to produce current layers can be divided into rotation (large scale) and spinning (small scale) motions. De Moortel and Galsgaard (2006a) and De Moortel and Galsgaard (2006b) carried out 3D resistive numerical simulations to investigate the energy build up and release for these two drivers, applied to two aligned, straight flux tubes. De Moortel and Galsgaard found that current formed along the separatrices (QSLs - for cases with background field) and that the nature of the footpoint motions had an impact on the current formation. They examined the resulting reconnection and energy release for cases with and without an additional background field between the flux tubes, and found that when no background field was present, the heating for the two applied motions was very similar. However when a background field was included, the heating was greater for the spinning case by an order of magnitude. Wilmot-Smith and De Moortel (2007), who subjected two initially intertwined flux tubes to the same spinning motions, also found that current was built up and reconnection occurred at the separator current sheet, but at an earlier time compared to the initially straight flux tubes in De Moortel and Galsgaard (2006b).

Similarly to many of the braiding experiments, the tectonics simulations by Mellor et al. (2005); De Moortel and Galsgaard (2006a) and De Moortel and Galsgaard (2006b) modelled straight coronal loop magnetic fields, which extended between magnetic flux sources defined on two parallel surfaces and are carried out in a Cartesian geometry. In comparison, another series of simulations by Galsgaard et al. (2000); Parnell and Galsgaard (2004); Galsgaard and Parnell (2005a) included the curvature of the field. The flux sources all lay on one surface modelled as a 'photospheric' plane. The authors investigated the behaviour of two independent flux systems with an overlying field when they are forced to interact by an imposed velocity driver. Current is shown to form along the topological features of the field and the two flux sources are shown to reconnect thereby also releasing energy. Galsgaard and Parnell (2005a) found that the total energy released through Joule dissipation was independent of the speed of the driving velocity but instead related to the distance travelled by the sources.

Another series of simulations that can be seen as coronal tectonics are carried out by Gudiksen and Nordlund (2002); Peter et al. (2004); Gudiksen and Nordlund (2005). These model a complex magnetic field that is extrapolated from a smoothed magnetogram of an active region and apply a more realistic photospheric driver that is designed to emulate observed convection processes. These large-scale realistic simulations of active regions, although not resolving the individual locations of dissipation, found that the amount of energy dissipation was in line with the values suggested by observations of loops. These simulations can be related to tectonics, as the complex field implicitly includes topological and geometrical features as locations of current formation and

therefore heating, although they do not examine these individual processes specifically.

The importance of topological features as locations of current formation has also been examined directly in smaller scale numerical MHD simulations. Many simulations have examined the nature of current formation and reconnection at individual topological features such as separators (e.g Stevenson et al., 2015; Parnell et al., 2010) and null points in both 2D and 3D (see Priest and Forbes, 2000, and references within). A review of the importance of topology in heating the corona is given by Parnell et al. (2015), who discuss the possible impact of both the global and local topology on heating in the solar atmosphere. Parnell et al. suggest that although topological features are not necessary for reconnection and heating to occur, knowledge of the magnetic topology is important in determining what heating mechanisms may be important at different locations.

In addition to the extensive studies on the importance of topological features, many simulations are now also trying to evaluate the importance of geometrical features, such as QSLs, as locations for reconnection and subsequent heating. Since Démoulin et al. (1996) first gave analytical arguments for QSLs to be a natural location for current sheets to form, many simulations have sought to corroborate or disprove the hypothesis. MHD simulations have been used to model the coronal field from observations of the photospheric magnetic field and it has been argued that the calculated locations of QSLs coincide with observed heating and reconnection signatures (such as observed flare ribbons) (see review by Janvier et al., 2015, and references within). MHD analytical work and simulations examining the reconnection at QSLs have also led to the development of ideas of *flipping* (Priest and Forbes, 2000) and *slip running* (Aulanier et al., 2006) reconnection. Here, the terms *slipping* or *flipping* describe the apparent motion of the field lines when undergoing reconnection in QSLs. As with topological features, reconnection does not necessarily occur at QSLs but they are a likely location for it to occur. Aulanier (2011) argues that observational and numerical evidence suggest that QSLs are a ubiquitous feature in the solar atmosphere, occurring naturally in complex magnetic field distributions, and therefore may play an important role in heating the corona.

Despite the many assumptions used in deriving the MHD equations, numerical simulations have shown them to be robust and effective in modelling many features, which have been successfully compared to observations (Peter, 2015). However, the initial conditions and parameters of numerical models have also been shown to impact the results. In non-ideal heating simulations, the evolution of the magnetic field and Ohmic heating is strongly dependent on the value of the resistivity (or the Magnetic Reynold's number) (e.g Bowness et al., 2013; Ng et al., 2012; Rappazzo et al., 2008; Longcope and Sudan, 1994). In the solar corona, the resistivity is expected to be very small ($\approx 10^{-6} \Omega \text{ m}$, Goedbloed and Poedts, 2004). However, in numerical simulations, it needs to be much greater in order to accurately follow the energy evolution. The value of resistivity in numerical simulations can have a large impact on the timing and therefore strength of energy release events, as a smaller resistivity would mean that smaller scales are able to be created before

the diffusion becomes important.

Many approaches have been considered to create a model with a more ‘realistic’ resistivity. These include having *anomalous resistivity* to create enhanced dissipation in localised regions of high current. This creates a ‘switch’ effect where the diffusive term of the induction equation only becomes important after a threshold of electric current density is reached (e.g. Stevenson et al., 2015). Another method is using a *localised non-ideal diffusion region* (e.g. Pontin et al., 2005), where resistivity is only defined for a subsection of the domain. Despite the large difference between our numerical capabilities in modelling resistivity and the realistic values in the corona, many simulations are able to contribute to the understanding of reconnection and heating.

It is important to bear in mind that all of the simulations are a simplification of the reality. Whether it is a simplified geometry, such as modelling straight field lines, or a reduced MHD model, which does not consider the full energy equation, or a simplified model of the solar atmosphere, all of the simulations make simplifications. However, this diversity of numerical simulations can also be seen as a benefit. The focussed simulations remove extra details to allow us to further our understanding of individual processes. These in turn can be seen as important building blocks towards self-consistent fully 3D MHD simulations.

1.5 Introduction to the Lare3D Code

In this thesis, numerical simulations are carried out using the 3D LAgrangian-eulerian REmap code: *Lare3D*, as described in Arber et al. (2001). *Lare3D* solves the MHD equations and allows the user to control the settings for various parameters, such as viscosity and resistivity. Further details of the code are fully explained in Arber et al. (2001) and the *LareXd* manual (available at <http://ccpforge.cse.rl.ac.uk/gf/project/lare3d/docman/>).

1.5.1 Lare3D Normalisation

In the *Lare3D* code, the MHD equations are normalised through choosing normalising values for the magnetic field B_0 , density ρ_0 and length L_0 . These can then be used to define the normalisations for the remaining variables from the MHD equations:

$$\begin{aligned} v_0 &= \frac{B_0}{\sqrt{\mu_0 \rho_0}}, & P_0 &= \frac{B_0^2}{\mu_0}, & j_0 &= \frac{B_0}{\mu_0 L_0}, & t_0 &= \frac{L_0}{v_0}, \\ E_0 &= v_0 B_0, & T_0 &= \frac{\bar{m} v_0^2}{k_B}, & \epsilon_0 &= v_0^2, \end{aligned} \quad (1.17)$$

where \bar{m} is the average mass of ions in the plasma and we shall use $\bar{m} = m_p$ to represent pure Hydrogen. Thus, the dimensionless quantities are defined as; $x = L_0 \hat{x}$, $\mathbf{B} = B_0 \hat{\mathbf{B}}$, $\rho = \rho_0 \hat{\rho}$, $\mathbf{v} = v_0 \hat{\mathbf{v}}$, $\mathbf{j} = j_0 \hat{\mathbf{j}}$, $t = t_0 \hat{t}$, $P = P_0 \hat{P}$ and $\epsilon = \epsilon_0 \hat{\epsilon}$.

In Lare3D the variable η is the resistivity defined as $\frac{1}{\sigma}$, not the magnetic diffusivity ($\eta' = \frac{1}{\sigma \mu_0}$) and this notation is used in this thesis. From Equation 1.11 the normalisation value η_0 for the resistivity can also be derived, giving

$$\eta_0 = \mu_0 L_0 v_0, \quad (1.18)$$

and hence $\eta = \eta_0 \hat{\eta}$, where $\hat{\eta}$ is the resistivity in the normalised equations. In summary, the normalised resistive MHD equations we solve in Lare3D (dropping the hats on the normalised variables) are:

$$\frac{D\rho}{Dt} = -\rho \nabla \cdot \mathbf{v}, \quad (1.19)$$

$$\frac{D\mathbf{B}}{Dt} = (\mathbf{B} \cdot \nabla) \mathbf{v} - \mathbf{B}(\nabla \cdot \mathbf{v}) - \nabla \times (\eta \nabla \times \mathbf{B}), \quad (1.20)$$

$$\frac{D\mathbf{v}}{Dt} = -\frac{1}{\rho} \nabla P + \frac{1}{\rho} (\nabla \times \mathbf{B}) \times \mathbf{B}, \quad (1.21)$$

$$\frac{D\epsilon}{Dt} = -\frac{P}{\rho} \nabla \cdot \mathbf{v} + \frac{\eta}{\rho} j^2. \quad (1.22)$$

In these equations and in our simulations we have neglected gravity, thermal conduction and optically thin radiation.

1.5.2 Shock Viscosity

Viscosity has also been neglected in the equations above but, if desired, it can be included in the equation of motion in Lare3D:

$$\frac{D\mathbf{v}}{Dt} = -\frac{1}{\rho} \nabla P + \frac{1}{\rho} (\nabla \times \mathbf{B}) \times \mathbf{B} + \frac{1}{\rho} \frac{\partial}{\partial x_i} S_{ij}. \quad (1.23)$$

Viscous heating would also need to be included in the energy equation (Equation 1.22):

$$\frac{D\epsilon}{Dt} = -\frac{P}{\rho} \nabla \cdot \mathbf{v} + \frac{\eta}{\rho} j^2 + \frac{1}{\rho} \epsilon_{ij} S_{ij}, \quad (1.24)$$

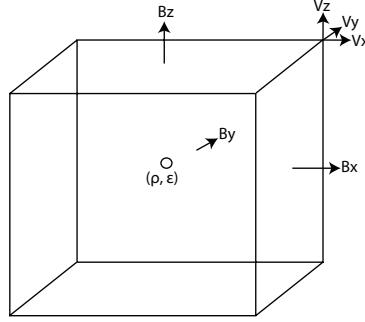


Figure 1.5: Position of variables on a 3D staggered grid in the Lare3D code (based on Arber et al., 2001).

where viscosity is added through the strain rate ε_{ij} ,

$$\varepsilon_{ij} = \frac{1}{2} \left(\frac{\partial v_i}{\partial x_j} + \frac{\partial v_j}{\partial x_i} \right)$$

and the stress tensor S_{ij} . Two forms of viscosity can be applied in Lare3D, a *uniform background viscosity* and an *artificial shock viscosity*, which are given by different forms of the stress tensor S_{ij} ,

$$S_{ij} = 2\nu_3 \left(\varepsilon_{ij} - \frac{1}{3} \delta_{ij} \nabla \cdot \mathbf{v} \right),$$

$$S_{ij}^{shock} = (\nu_1 \rho c_f l + \nu_2 \rho l^2 |s|) \left(\varepsilon_{ij} - \frac{1}{3} \delta_{ij} \nabla \cdot \mathbf{v} \right),$$

where c_f is the fast magnetoacoustic speed, l is the distance across a grid cell normal to the shock front and s is the strain rate normal to the shock front. The shock viscosity in Lare3D does not represent a physical viscosity in the corona but is used to capture the heating from shocks. The uniform viscosity and shock viscosity can be set by the coefficients ν_3 and ν_1, ν_2 , within the shock tensor, respectively. In our experiments, when shock viscosity is included, these parameters are set as $\nu_1 = 0.1$ and $\nu_2 = 0.5$, as suggested in the Lare3D manual.

1.5.3 The Grid

The code uses a staggered grid, which helps to reduce averaging errors. The scalars (density, pressure and internal energy density) are the cell averaged values and are defined at the cell centres, while the velocities are defined at the cell vertices and the magnetic field components at the cell faces. The placement of the magnetic field in the staggered grid also helps to keep the magnetic field divergence-free and the code uses the Evans and Hawley (1988) constrained transport model to maintain $\nabla \cdot \mathbf{B} = 0$ to machine precision. Figure 1.5 shows a visualisation of the position of variables in the cell.

Lagrangian and Remap Steps

The Lagrangian Remap code is a second order scheme in time and space which is fully 3D. The code uses a Lagrangian step followed by a remap step. It is in the Lagrangian step where the MHD equations are solved and all the ‘physics’ takes place and energy is conserved exactly. After the Lagrangian step, the variables have all been updated but the grid has also been deformed, as it was advected with the fluid. The variables must then be remapped back onto the original Eulerian grid. Carrying out this remap at each time step prevents the grid from becoming contorted. For more details we again refer to Arber et al. (2001).

1.6 Outline

The aim of this thesis is to study how the number and distribution of flux sources, when subjected to slow footpoint velocity motions, affect the creation of current concentrations and how this impacts the heating produced through reconnection and Ohmic dissipation. Similar to the tectonics theory by Priest et al. (2002), we construct varying magnetic field distributions and subject them to the same simple driving velocity and analyse the energy evolution of the plasma.

In Chapter 2, we begin by creating an initial two flux tube configuration from prescribed magnetic sources. We compare the numerical set-up with a potential case with the same boundary conditions and assess its initial equilibrium. In Chapter 3, we consider low-resolution test cases subjecting the two flux tubes to footpoint driving motions and compare how the value and form of resistivity impact the results. We then discuss how increasing the resolution can affect the evolution of the experiments in Chapter 4 and, in Chapter 5, compare how doubling the length of the loops (and the numerical domain) impact the evolution of the simulations.

We then go on to examine how the strength and distribution of the sources, when subjected to the same velocity driver alter the timing, magnitude and efficiency of the energy release. In Chapter 6, using the high resolution set-up, we compare the two flux tubes with a four flux tube case, while maintaining the same total flux through the surface. In addition, in Chapter 7 we describe how a background field can impact the comparison.

In Chapter 8, we extend the idea of multiple-source configurations and consider cases where one of the sources is broken into many smaller fragments. The flux tubes created from the fragmented source are subjected to the same footpoint driving velocity and we examine whether this fragmentation of the single source has any impact on the energy release and whether the spread of these source fragments is important.

Finally, in Chapter 9 we summarise our findings and discuss possible future work.

Chapter 2

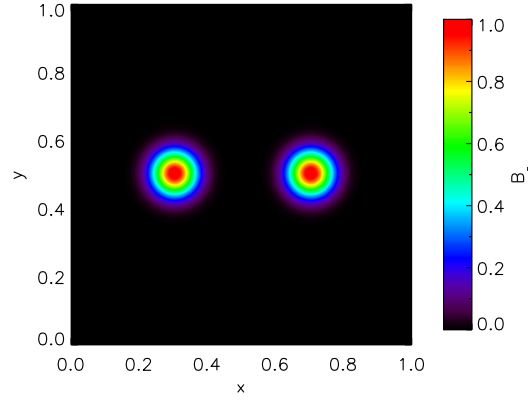
Creating an Initial Two Flux Tube Configuration

2.1 Comparison of Flux Tube Set-ups

In this chapter, we describe the formation of two flux tubes in our numerical domain. We prescribe two positive and two negative sources on the bottom and the top boundaries of the domain, respectively. The sources are initially aligned, creating two distinct vertical flux tubes. In future chapters (Ch. 3 and Ch. 4) this configuration is subjected to a velocity driver on the upper and lower boundaries, to emulate photospheric driving motions. In this chapter we first analyse and compare two approaches or ‘set-ups’ for creating the flux tubes in Lare3D, by specifying only a vertical flux distribution in the domain. In each case, the vertical flux tubes are allowed to relax in the domain, towards numerical equilibrium, with no imposed velocities. The resulting magnetic field, current, velocity and energies of the two cases are considered and compared to the potential field constructed from the same boundary conditions, in order to evaluate which is the most appropriate form from which to begin further experiments.

2.1.1 Numerical Set-up

The domain for each case is a unit cube, with $0 < x, y, z < 1$. The boundaries in x and y are chosen to be periodic while the boundaries in z are line-tied. On the upper and lower boundaries the magnetic field components, the specific internal energy density and the mass density all have zero normal derivative. The velocity is also set to zero on $z = 0$ and $z = 1$. The magnetic field component B_z on the upper and lower boundaries is a summation of Gaussians given by:

Figure 2.1: Contour plot of B_z at $z = 0$.

$$B_z = B_{max} \left[e^{-[(x-x_1)^2+(y-y_1)^2]/r_1^2} + e^{-[(x-x_2)^2+(y-y_2)^2]/r_1^2} \right], \quad (2.1)$$

where $B_{max} = 1.0$, and $r_1 = 0.065$ is the radius of the sources. $(x_1, y_1) = (0.3, 0.5)$ and $(x_2, y_2) = (0.7, 0.5)$ are the centres of the sources on the upper and lower boundaries. The distribution of B_z is shown on the base in Figure 2.1.

Using these boundary conditions, the two approaches we consider to produce two flux tubes in approximate numerical equilibrium are:

- (a) Constructing *straight* flux tubes ($B_x = B_y = 0$) in the domain and letting the magnetic field relax.
- (b) Constructing *straight* flux tubes ($B_x = B_y = 0$) in the domain and letting the magnetic field relax, while artificially maintaining a *constant* density and internal energy density.

These cases shall be compared to the potential, minimal energy state:

- (c) A *potential field* constructed from sources on the boundary and imported into Lare3D.

In cases (a) and (b), the vertical magnetic field component B_z is specified throughout the domain as given on the boundaries (in Equation 2.1), while B_x and B_y are set initially as zero. In case (a) the flux tubes are allowed to evolve naturally in the domain, as the equations are solved in Lare3D. The flux tubes therefore expand and the plasma pressure and density respond. In case (b), the flux tubes are again allowed to expand in the domain, however, the density and internal energy (and hence the pressure) are artificially held constant. In comparison, case (c) has non zero

B_x and B_y components from the start and the initial field is the potential field constructed from the B_z boundary conditions, externally calculated and imported into Lare3D.

In all the experiments described in this thesis we shall use the term ‘flux tubes’ to refer to the flux associated within the specified radius (r_1) of the sources, as opposed to distinct topological features. Moreover, although no additional field is added between the flux tubes on the boundaries, due to the strictly positive (negative) flux prescribed on the lower (upper) boundaries by the exponential distribution (that is strictly greater than zero), we shall refer to the mapping of the field lines on the boundary to be continuous (i.e with a QSL present). However, we note that these numerical experiments are near the computational limit of producing separators.

All three cases are run for 80 normalised time units (which we shall refer as t_{relax}) to allow the flux tubes to expand and then any velocities or waves created to be naturally damped. In this thesis we shall call this process the ‘relaxation’. The flux tubes relax towards a (numerical) equilibrium, with minimal background velocities remaining in the domain (and these should be much smaller than the driving velocity we later want to impose in Section 3).

All the relaxation cases have a normalised uniform viscosity of 0.001 and are ideal (no resistivity apart from the unavoidable numerical resistivity). These comparisons are carried out at relatively low resolutions (128^3), as they are initial test cases. In the following comparisons the cases shall be referred to by their respective letter for ease of reference.

2.1.2 Initial Conditions and Normalisation

Normalisation	Initial Conditions	
$B_0 = 10 \text{ G}$	$\epsilon = 0.001$	Resolution: 128^3
$L_0 = 50 \text{ Mm}$	$\rho = 0.1$	$\eta = 0$ (ideal relaxation)
$n_e = 5 \times 10^{14} \text{ m}^{-3}$		viscosity = 0.001
		$0 < t_{relax} < 80$

These simulations are all carried out with Lare3D and, as described in Section 1.5.1, normalised equations use used. The normalisation values used in these comparisons are: $B_0 = 10 \text{ G}$, $L_0 = 50 \text{ Mm}$ and an electron number density of $n_e = 5 \times 10^{14} \text{ m}^{-3}$, which gives a normalisation density constant of $\rho_0 = 8.3 \times 10^{-13} \text{ kg m}^{-3}$. (A summary of the normalisation, initial conditions and resolutions used in this comparison is displayed in the box above. This format shall be used to outline these values at the start of each section and for each new experiment in this thesis.) These chosen values give normalisation values of $v_0 = 976 \text{ km s}^{-1}$ for velocity, $t_0 = 51 \text{ s}$ for time, $T_0 = 1.15 \times 10^8 \text{ K}$ for temperature and $J_0 = 1.59 \times 10^{-5} \text{ A}$ for current density.

This implies that the flux tubes, which are of unit length in normalised values, correspond to

having a length of 50 Mm. Similarly, the sources with radius $r_1 = 0.065$ on the upper and lower boundaries are equivalent to a radius of 3.25 Mm in real units. On the boundaries, the magnetic field values peak at a maximum of 1.0, which gives the sources on the boundaries a peak field strength of 10 G. As stated in Section 1.5, gravity is neglected in the simulations. The density is therefore uniform throughout the domain and has a normalised initial value of $\rho = 0.1$. In real units this corresponds to a density of $8.3 \times 10^{-14} \text{ kg m}^{-3}$, which may be considered very low for coronal values. The specific internal energy density (ϵ) is initially set equal to 0.001, which gives an initial temperature of 38333 K. (Note, these parameters will be adjusted to closer resemble typical coronal values in Section 2.2.) For the rest of the chapter, all the figures and comparisons between the cases shall be considered in terms of normalised values.

2.1.3 Magnetic Field

After allowing all three simulations to relax, the resulting magnetic fields are compared. Figure 2.2 shows the vertical magnetic field B_z on the upper (red dashed) and lower (solid black) boundaries at $y = 0.5$, after a period of 80 time units. In cases (a) and (b) in Figures 2.2a and 2.2b, the

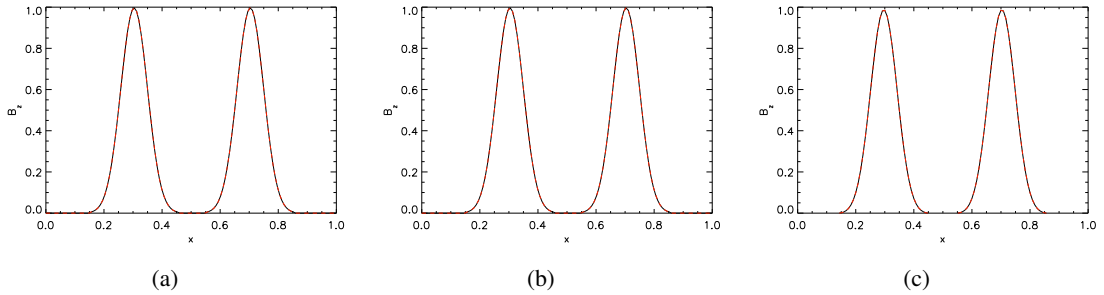


Figure 2.2: Cross section of B_z at $z = 0$ (black, solid line) and B_z at $z = 1$ (red, dashed line), plotted against x , at $y = 0.5$ and at time $t_{relax} = 80$, for cases (a), (b) and (c).

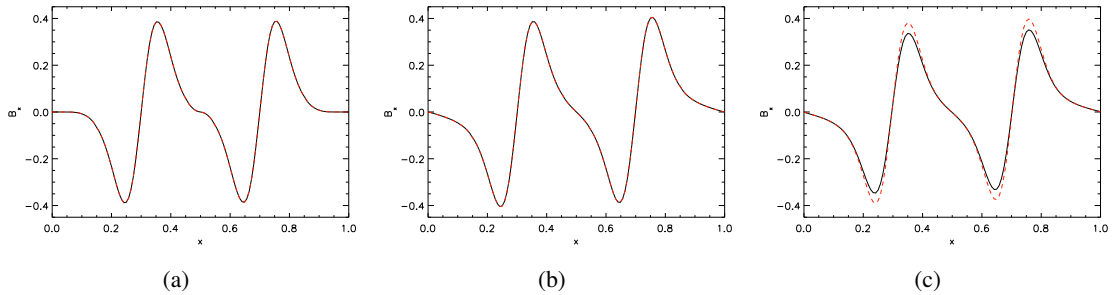


Figure 2.3: Cross section of B_x at $z = 0$ (black, solid line) and $-B_x$ at $z = 1$ (red, dashed line) plotted against x , at $y = 0.5$ and at time $t_{relax} = 80$, for cases (a), (b) and (c).

B_z component maintains a peak magnitude of 1.0 at the centre of the sources at $x = 0.3$ and $x = 0.7$, as we would expect due to the line-tied nature of the boundary conditions. We also note, in case (c), due to the potential field being calculated externally from the boundary conditions before being imported into Lare3D, the resultant magnitude of B_z is slightly less than 1.0 on both the upper and lower boundaries from the start of the simulation.

A similar comparison for B_x is shown in Figure 2.3. At $t_{relax} = 0$ only B_z was specified on the boundary in cases (a) and (b), but as the field expands and relaxes, B_x and B_y components form. Cases (a) and (b) both produce a maximum magnitude of B_x of over 0.35 on the lower

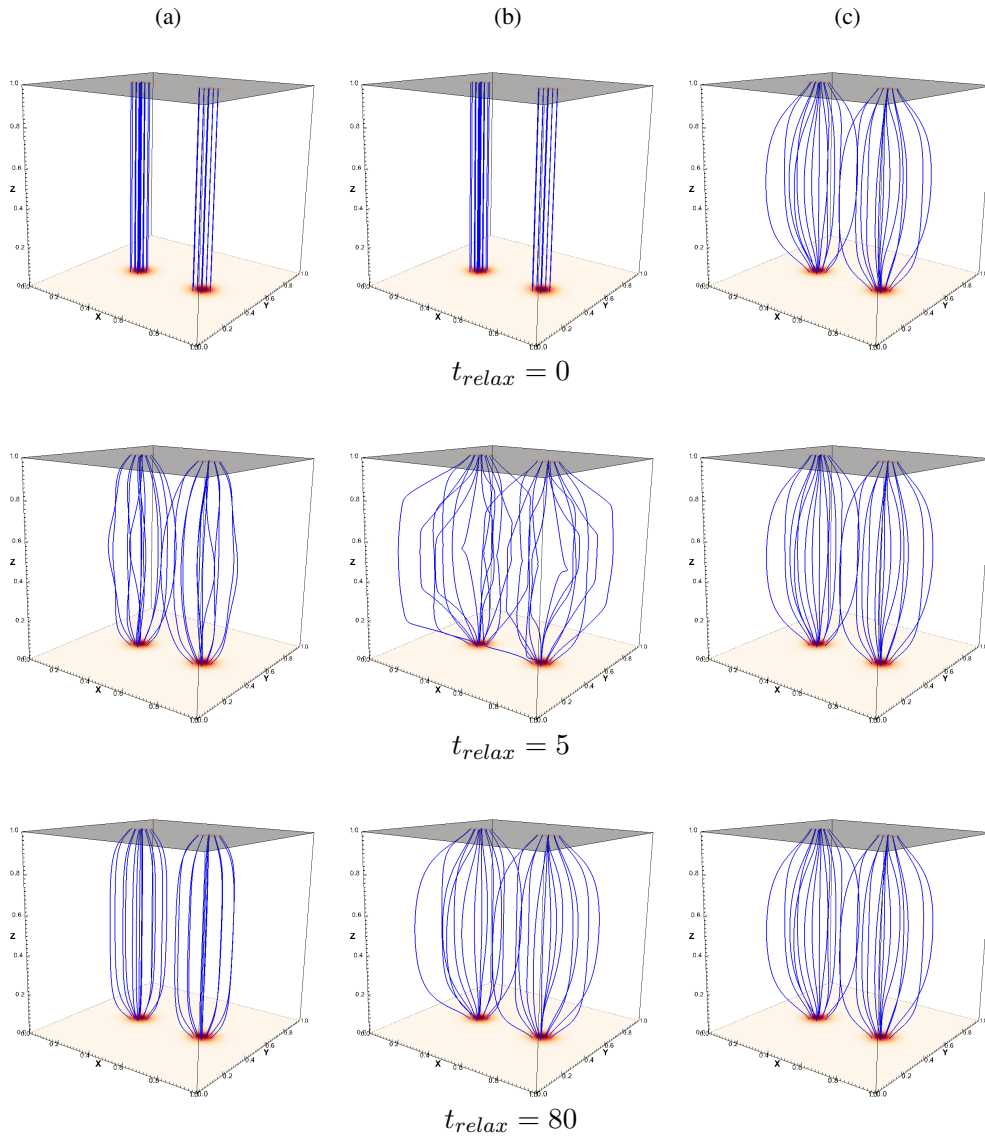


Figure 2.4: Magnetic field lines traced from the same 26 points on the base, at $t_{relax} = 0, 5, 80$, for cases (a), (b) and (c).

boundary. In case (a), B_x remains zero towards the x boundaries, outside of the flux patches, as the field is stopped from expanding fully, due to the gas pressure in the domain. In case (b), on the other hand, there is a small B_x at all values of x along the cut shown, except on the boundaries, as the field has been able to expand further. The distribution of the B_x component of case (b) is also the most similar to the potential case (c) shown in Figure 2.3c. Due to the symmetric boundary conditions of cases (a) and (b), we note that the formed B_x component of the magnetic field are also symmetric in z (i.e the magnitude of B_x at $z = 0$ is the same as at $z = 1$). However, in case (c), where the field is imported, the B_x component appears slightly asymmetrical in z . The field is constructed to be symmetric, but when importing the field into Lare3D the magnitude of B_x on the base is not the same as on the top boundary. This difference is most likely due to numerical issues when importing the field onto the staggered grid that Lare3D uses. As this asymmetry does not appear to affect the general magnetic field and this case is considered only as a comparison to the expanding flux tubes, this discrepancy is not investigated further.

The three-dimensional form of the magnetic field in the three cases can be seen in Figure 2.4, which shows 13 field lines traced from the base of each source at $z = 0$ and shown at times $t_{relax} = 0, 5$ and 80 , respectively. At $t_{relax} = 0$, in cases (a) and (b), the initially straight flux tubes are shown, while in case (c) the potential field flux tubes are already formed. After 5 time units, Figure 2.4a shows that for case (a) the initial expansion of the straight tubes causes oscillations along the field lines, visible by the sudden curvature in the centre. By $t_{relax} = 80$, in case (a) these oscillations are no longer visible and overall the field lines remain fairly compact in comparison with the large spread in cases (b) and (c). This is because, in case (a), the sudden expansion of the magnetic field causes a surrounding increase in gas pressure. The shape of the field lines is therefore due to a balance between the magnetic and gas pressure. In comparison, case (b) in Figure 2.4b also shows initial large oscillations in the magnetic field at $t_{relax} = 5$. By $t_{relax} = 80$ in case (b), there is greater curvature of the field lines than seen in case (a). In this case, the gas pressure and density are overwritten to be constant, at each time step in Lare3D, allowing the field to expand further.

Lastly, Figure 2.4c displays the field lines traced from the same points on the base for the constructed potential field. The field lines for case (c) appear very similar with little change or movement for all the times shown. This is in sharp contrast to the initial rapid expansion of case (b). However, by $t_{relax} = 80$, the relaxation with a constant density in case (b) appears to form a very similar magnetic field structure to the imported potential field in case (c).

2.1.4 Current Density

An electric current is also formed in the domain as the flux tubes are allowed to relax. Figure 2.5 displays the logarithm of the maximum magnitude of the current density ($\max(|j|)$) against height

(z) in the domain, at times $t_{relax} = 30$ and $t_{relax} = 79$, represented by solid and dashed lines, respectively. All three cases show the same high current density values on the upper and lower boundaries of the domain (≈ 13.1). This is due to a combination of the strong field on the boundaries with the rapid expansion of the field lines from the sources (seen in Figure 2.4) and the errors involved in calculating then numerical derivatives of the magnetic field near the boundaries. However, the extremely high values are very localised to the boundaries and a small distance away from the z -boundaries the maximum current reduces significantly in all three cases.

Away from the boundaries, the three cases show relatively different distributions of current with height. For case (a), Figure 2.5a shows that at $t_{relax} = 30$ (solid line), after an initial decrease away from the boundaries to a minimum of 1.3, the maximum current density then increases again towards the mid-plane to ≈ 2.8 and appears fairly constant with height between $0.2 < z < 0.8$. The dashed line in Figure 2.5a also shows at a later time of $t_{relax} = 79$, the relatively high values of current in the middle of the domain persist throughout the experiment. This high current in the centre of the domain is due to the field not being able to fully expand because of the pressure constraints of the plasma. This persistent high current can also be seen in Figure 2.6a, which shows the maximum magnitude of the current density between $0.04 < z < 0.96$ in the domain

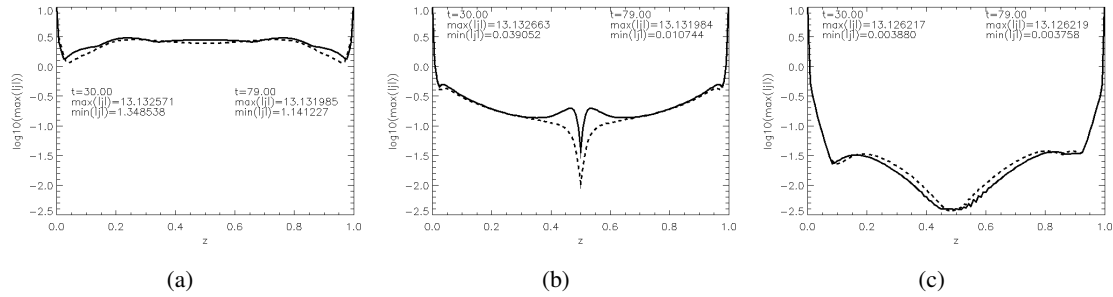


Figure 2.5: Log of maximum current at each height in the domain plotted against z , at $t_{relax} = 30$ (solid line) and $t_{relax} = 79$ (dashed line), for cases (a), (b) and (c).

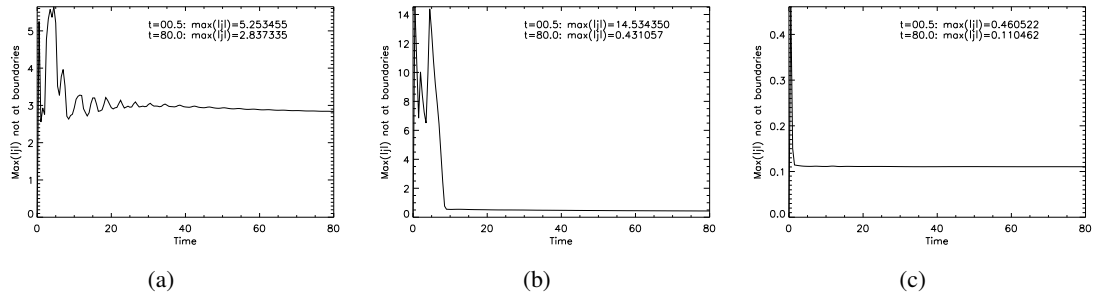


Figure 2.6: Maximum current in domain between $0.04 < z < 0.96$ over time, for cases (a), (b) and (c).

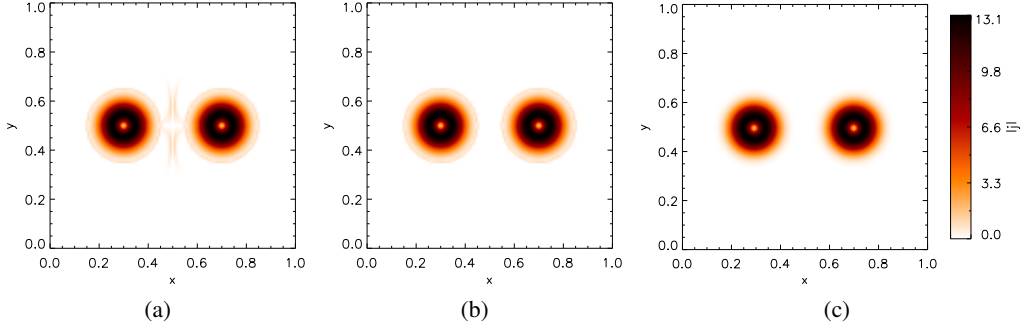


Figure 2.7: Contour plot of the magnitude of the current density on the base ($z = 0$) after relaxation, for cases (a), (b) and (c).

(thereby excluding the large values on the boundaries) plotted against time for case (a). This shows the maximum value of current oscillates and decreases slightly over time. After $t_{relax} = 40$, it still continues to decay very slowly and reaches a final value of approximately 2.8 at $t_{relax} = 80$, a much higher value than in cases (b) and (c). This reduction in current over the simulation is due to numerical dissipation, as, even though the simulation is ideal, there is always a small amount of numerical resistivity.

Figure 2.5b shows that the maximum current with height for case (b) reduces sharply away from the boundaries, but then, unlike case (a), continues to decrease further with height. It reaches a minimum in the mid-plane of ≈ 0.039 at $t_{relax} = 30$. Figure 2.5b shows that, at $t_{relax} = 79$ (dashed line), the distribution of the maximum current with height remains very similar to that at $t_{relax} = 30$, but with the minimum at $z = 0.5$ having reduced by 60% to 0.0107. This is less than 1% of the minimum value in case (a). In Figure 2.6b the maximum current in the domain between $0.04 < z < 0.96$ shows that initially a very large current enters the domain (no longer just at the boundaries) peaking at a value of 14.5, due to the expansion of the field. The maximum current then reduces, levelling off and remaining fairly constant at approximately 0.43. A comparison of this value with the distribution of maximum current with height in Figure 2.5b, suggests that this value of 0.43 is probably from around the edge of the region considered (near $z = 0.04$ and $z = 0.96$), where the current is still slightly higher, rather than towards the middle of the domain.

Despite there being no current present in the potential field of case (c) initially (by definition), due to the less accurate numerical calculation of the current near the boundaries in the code (and the large magnetic field strength at this location) a high current is shown on the domain boundaries in Figure 2.5c. The solid and dashed lines in Figure 2.5c, which display the maximum current against height in the box at times $t_{relax} = 30$ and $t_{relax} = 79$, respectively, appear very similar and both show that the current in the domain is minimal compared to cases (a) and (b). The minimum value has reduced slightly from $t_{relax} = 30$ to $t_{relax} = 79$, but is still approximately

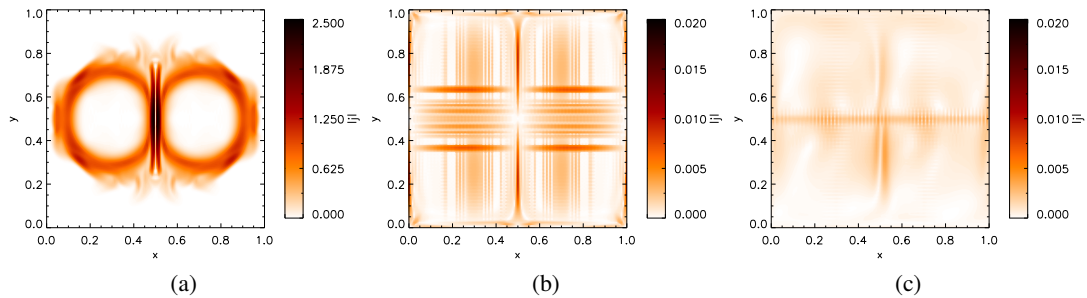


Figure 2.8: Contour plot of the magnitude of the current density on the mid-plane ($z = 0.5$) after relaxation, for cases (a), (b) and (c).

0.0038 at both times. The evolution of the maximum current with time in Figure 2.6c, shows that after a very small initial increase to 0.46, it then decreases very quickly and then remains constant at ≈ 0.1 for $t_{relax} > 2$. This is significantly lower than the maximum current shown for case (a) and a fourth of the maximum current of case (b) in Figure 2.6b. The maximum current remains constant for a large proportion of the simulation in case (c). This suggests the field settles very quickly, as we saw from the field lines in Figure 2.4c.

The distribution of the current in the $x - y$ plane at $t_{relax} = 80$ is shown in Figures 2.7 and 2.8 at $z = 0$ and $z = 0.5$, respectively. The current on the base, shown in Figure 2.7, is practically identical for all three cases as the boundary conditions specify B_z on $z = 0$ to be the same for each simulation. Hence, in all three images in Figure 2.7, circles of high current form around the sources specified on the base of the domain, with a maximum current magnitude of over 13. The same distribution is also observed on the top boundary.

In the centre of the domain (at $z = 0.5$) the structure of the current differs between the three cases. For case (a), shown in Figure 2.8a, current builds up around the edges of the flux tubes and greatly increases between the two flux tubes as they expand towards each other. Two current layers appear to form, but they remain slightly separated as the gas pressure prevents the two flux tubes from fully coinciding (see Section 2.1.5). In cases (a) and (b), as discussed previously, the current in the mid-plane is generally very small (note the change in scale of the colour bar in Figures 2.8b and 2.8c compared to Figure 2.8a). However, apart from a small current built up along $y = 0.5$ the current distributions shown are resolution artefacts that disappear at higher resolutions (see Figure 4.5).

2.1.5 Density, Pressure and Temperature

The magnetic field lines of case (c), in Figure 2.4, do not show any large oscillations, as observed in the other cases. We would, therefore, expect there to be little change to the initial uniform

plasma parameters, such as density and pressure, as the field relaxes. Figure 2.9c shows the density (dashed line) for case (c) at $y = 0.5$ in the mid-plane at a time of $t_{relax} = 80$. The variation in the density at this point is of the order of 10^{-3} and the distribution appears slightly asymmetric. Similarly, there is only a small pressure variation of the order of 10^{-6} . Despite the slight asymmetry, the small scale of the variation, means that the pressure and density would appear fairly uniform (particularly in comparison to case (a)).

The expansion of the initially straight flux tubes in case (a) creates a large variation in the density and pressure in the mid-plane of the domain. Figure 2.9a shows a cross section of the density (dashed line) at $t_{relax} = 80$. Although the simulation begins with a uniform density of 0.1, by this time, the density has formed two minima at $x = 0.3$ and $x = 0.7$, where the flux tubes are centred. Hence, as the magnetic field expands, the density inside the flux tubes decreases and forms 3 peaks; between the two flux tubes and on the boundaries outside the flux tubes. A similar pattern is evident in the cross section of the gas pressure for case (a), shown by the solid line in Figure 2.9a. The difference in pressure inside to outside the flux tubes is ≈ 0.004 , which is three orders of magnitude larger than the potential case, creating a pressure (gradient) force in the domain. In case (b), the density (dashed line) in Figure 2.9b maintains a uniform distribution at 0.1 across the domain, as initially prescribed. This is due to the flux tubes in case (b) being allowed

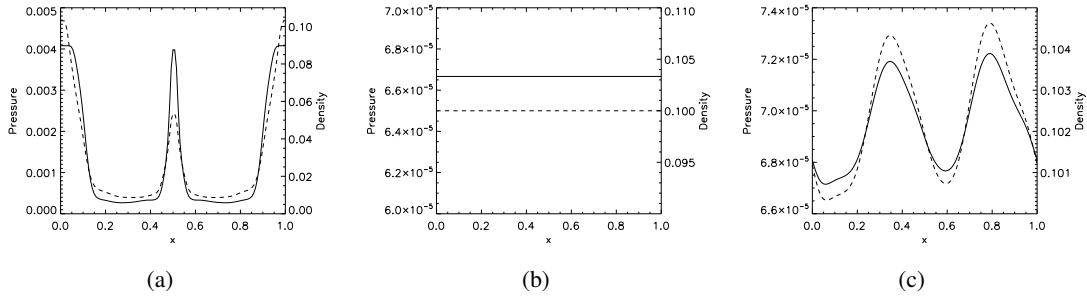


Figure 2.9: Density (dashed line) and gas pressure (solid line) in the mid-plane at $y = 0.5$ at $t_{relax} = 80$, for cases (a), (b) and (c).

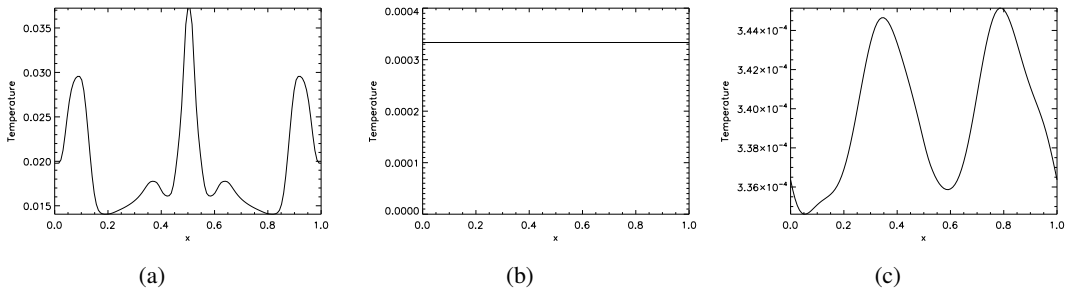


Figure 2.10: Temperature in the mid-plane at $y = 0.5$ at $t_{relax} = 80$, for cases (a), (b) and (c).

to expand while the density is kept artificially constant. The pressure (solid line) in Figure 2.9b is, therefore, also constant in the domain, as it is derived in the code from the density and internal energy density.

The temperature variation with x in the mid-plane is shown for the three cases in Figure 2.10. The temperature is constant for case (b), as the density and internal energy are held constant at the initial values. In panels (a) and (c) of Figure 2.10, the temperature follows similar distributions to the density and pressure shown in Figure 2.9. This shows that, in case (a), due to an increase of pressure around the flux tubes, the plasma is heated at these locations. Therefore, in case (a), the interior of the loops is cooler than the outside of the loops. The variation in pressure and temperature created in case (a) is relatively large (3 orders of magnitude larger), compared to the small variation in case (c).

2.1.6 Velocity

Figure 2.11 shows the maximum velocity in the domain over time for the three cases, but plotted from $t_{relax} = 10$ onwards, to better display the scale of the maximum velocity later in the simulations (at $t_{relax} = 0.5$ there is an initial sharp increase in velocity for all three cases). The maximum velocity values after 0.5 time units and at the end of the relaxation are also printed on each figure. The initial increase in velocity is much greater for cases (a) and (b), which have a maximum velocity of approximately 0.4, as the straight flux tubes expand quickly. In comparison, case (c), which uses an imported potential field, has an initial maximum velocity of 0.026, which is just 6% of the maximum velocity created in cases (a) and (b).

In all three cases, the maximum velocity in the domain decreases quickly, as the initial movement and subsequent oscillations are damped by the viscosity. Figure 2.11a shows rapid oscillations in the maximum velocity for case (a), which appear to occur on a time scale of 1 (in normalised times units). Figure 2.11c also shows an oscillation in the maximum velocity in the

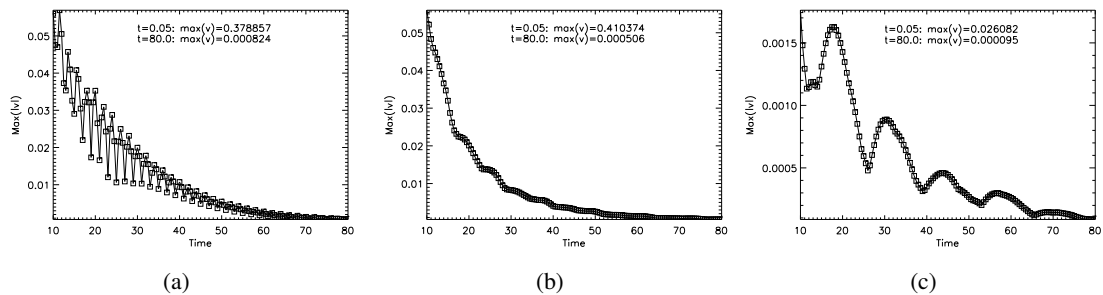


Figure 2.11: Maximum velocity in the domain over time, for $t_{relax} > 10$, for cases (a), (b) and (c).

domain for case (c), though this is of a much smaller magnitude and occurs over a longer time scale of more than 10 time units. A slight oscillation is also visible for case (b), but this appears relatively smooth in comparison to case (a), due to the pressure and density being held constant. The final maximum velocity is smallest for case (c), with a value of $\approx 1 \times 10^{-4}$, in normalised units. The final maximum velocity values in cases (a) and (b) are just over 5 and 8 times larger than case (c), respectively. By the end of the simulations, the maximum velocity in the domain in all the cases has reduced to less than 10^{-3} , as the flux tubes approach a numerical equilibrium.

2.1.7 Evolution of Energy

The evolution of the kinetic, magnetic and internal energies during the relaxations are shown in Figures 2.12, 2.13, and 2.14, respectively. These show the volume integrated energies plotted against time. Similar to the behaviour of the maximum velocity over time (see Figure 2.11), the kinetic energy is very high at the beginning of all three simulations and then decreases rapidly. The peak kinetic energy for cases (a) and (b) is approximately 4 orders of magnitude larger than the peak kinetic energy for case (c). This is due to their rapid initial expansion, in comparison to

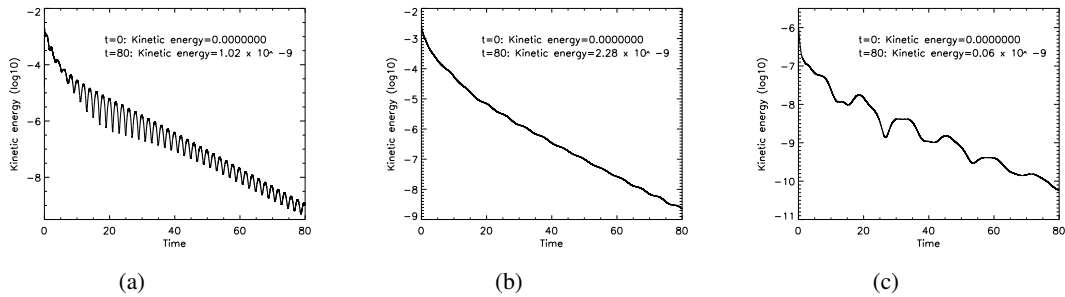


Figure 2.12: Logarithm of the volume integrated kinetic energy as a function of time, for cases (a), (b) and (c).

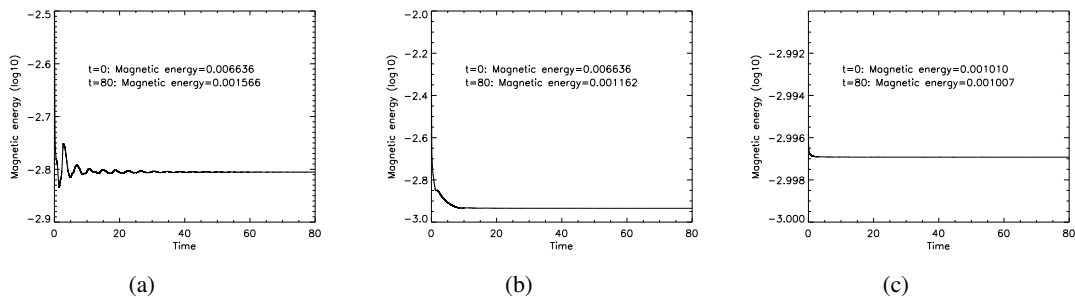


Figure 2.13: Logarithm of the volume integrated magnetic energy as a function of time, for cases (a), (b) and (c).

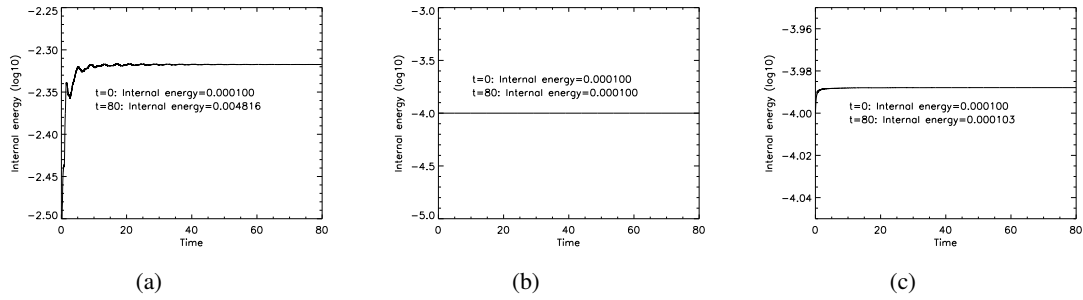


Figure 2.14: Logarithm of the volume integrated internal energy as a function of time, for cases (a), (b) and (c).

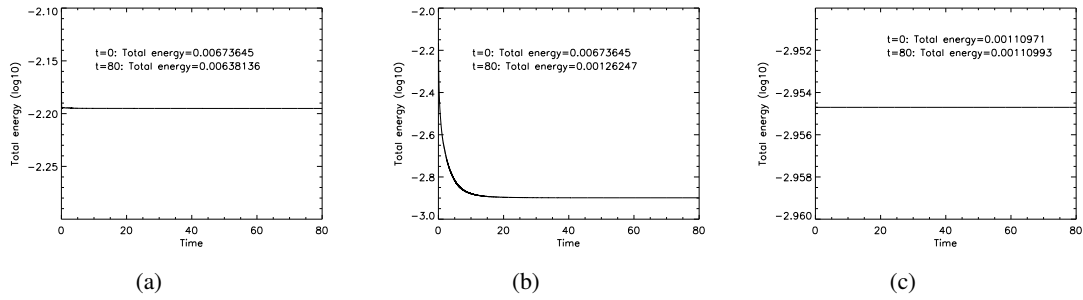


Figure 2.15: Logarithm of the total volume integrated energy as a function of time, from $t_{relax} = 10$, for cases (a), (b) and (c).

the potential field imported in case (c). Figure 2.12a depicts an oscillating kinetic energy for case (a), decreasing over time to a value (in normalised units) of the order of 10^{-6} . In comparison, case (b) in Figure 2.12b shows a gradual reduction to a similar magnitude, with little observable oscillation. The reduced oscillation is due to the gas pressure being held constant and the field is therefore able to expand without an opposing pressure gradient being created. The kinetic energy of case (c) is smaller to begin with and reduces (slightly erratically) to the lowest value, as stated previously.

The magnetic energy over time also differs for the three cases. The total magnetic energy for cases (a) and (b) varies on the order of 10^{-5} , as the straight magnetic field expands. Whereas, the variation of magnetic energy for case (c) is much smaller, of the order of 10^{-8} (see Figure 2.13c). The final values of the magnetic energy in cases (c) and (b) are $\approx 1.0 \times 10^{-3}$ and $\approx 1.2 \times 10^{-3}$. Case (b), therefore, only has a 20% larger initial volume integrated magnetic field than the potential case. This suggests that the two cases form relatively similar magnetic field configurations, as suggested previously by the snapshots of field lines in Figure 2.4. Case (a) has the largest volume integrated magnetic energy ($\approx 1.6 \times 10^{-3}$, which is $\approx 60\%$ larger than the potential field) at the end of the relaxation, shown in Figure 2.13a. This is due to the magnetic field not being able to

fully expand. An increase in the internal energy over time is shown in Figure 2.14 for cases (a) and (c), largely corresponding to the decrease in the magnetic energy. Therefore, the internal energy in case (a) is an order of magnitude greater than in case (c). However, in case (b) the artificially constant density and internal energy density result in a constant internal energy.

In case (b), over-writing the density and internal energy density to remain constant results in a reduction in the total energy in the domain, as the plasma density and temperature are not allowed to evolve in response to the changing magnetic field. Figure 2.15 shows the variation of the total volume integrated energy in each simulation with time. There is an initial sharp decrease at $t_{relax} = 0$ in the total energy for case (a). However, this is assumed to be due to poor resolution of the initial high currents, that have dissipated numerically to reduce the total energy. In contrast, Figure 2.15c shows case (c) mostly conserved the total energy over the relaxation (a small gain of less than 0.01% occurred). The magnetic energy is clearly the largest contribution to the total energy in cases (b) and (c) and therefore, as with the magnetic energy, the final total energy in the case (b) is less than 20% larger than the potential case (c).

2.1.8 Plasma β and Lorentz Force

The corona is generally modelled as a low β plasma, where the plasma β is the ratio of the gas pressure to magnetic pressure. In a low β plasma ($\beta \ll 1$) the magnetic force dominates the evolution of the plasma. In normalised units in Lare3D, the plasma β can be calculated by $\beta = \frac{2P}{B^2}$, where P is the gas pressure and B the magnetic field strength. The plasma beta on the base of the domain at $y = 0.5$ for the three cases is shown in Figure 2.16. In cases (a) and (b) the field in the domain is constructed by expanding initially straight flux tubes, therefore at the edges of the domain the field is very small, as shown previously in Figures 2.2 and 2.3. Hence, there is an extremely high plasma β at the boundaries $x = 0$ and $x = 1$. Inside the flux tubes, on the base (where the field is strongest) there is a very low plasma β of the order of 10^{-4} for all three cases, as shown in Figure 2.16.

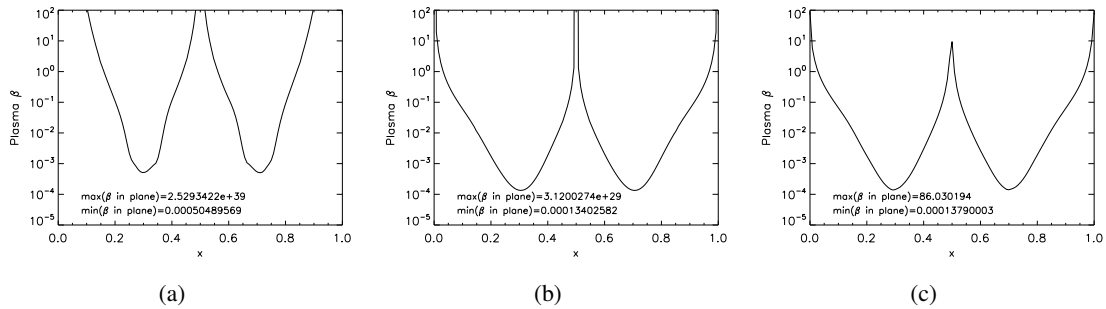


Figure 2.16: The plasma β at $z = 0.0$ and $y = 0.5$ at $t_{relax} = 80$, for cases (a), (b) and (c).

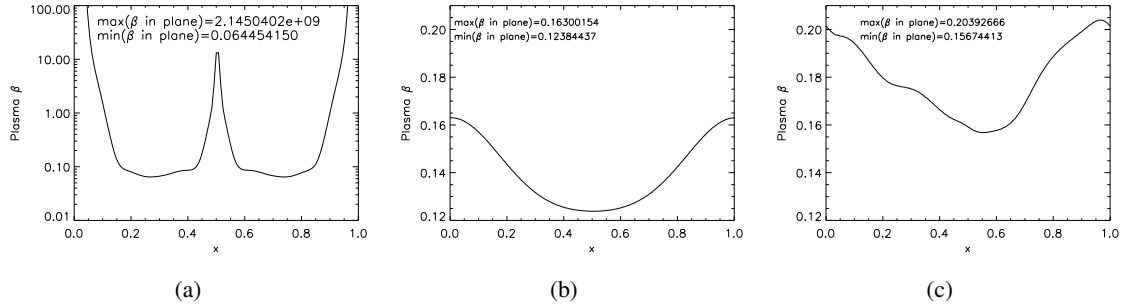


Figure 2.17: The plasma β at $z = 0.5$ and $y = 0.5$ at $t_{relax} = 80$, for cases (a), (b) and (c).

In the mid-plane, where the flux tubes have expanded, the plasma β is shown in Figure 2.17. For case (a) the plasma β in the mid-plane is again very high towards the side boundaries. This is because the magnetic field is constrained by the gas pressure and so the magnetic field is still very weak at the horizontal boundaries. However, in Figure 2.17b, for case (b) there is a relatively small plasma β and along the cut $y = 0.5$ in the mid-plane the plasma β is always less than 0.17. The minimum plasma β in the mid-plane of case (c) is $\approx 30\%$ larger than in case (b) (due to the smaller magnetic field strength). Overall, the plasma β of cases (b) and (c) are generally comparable and both show a gradual decrease towards the centre of the mid-plane, where the magnetic field is strongest. However, the plasma β in the mid-plane of case (b) has a symmetric distribution from the symmetric expansion of the magnetic field and the uniform plasma pressure and density. In comparison, case (c) has a slightly asymmetric distribution, which is assumed to be due to the asymmetric distribution of the gas pressure, previously shown in Figure 2.9c.

Due to the high currents on the boundaries, there is a strong Lorentz force on the upper and lower boundaries of the domain, around the sources. Elsewhere in the domain, the very small current density values in cases (b) and (c) (in Figures 2.5 and 2.8) mean that there is a minimal

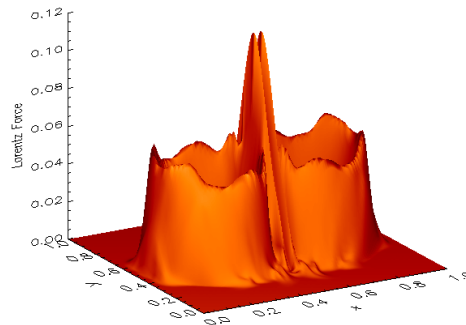


Figure 2.18: Surface plot of the Lorentz force at $z = 0.5$ at $t_{relax} = 80$, for case (a).

Lorentz force. However, in case (a), the high current values produce a fairly strong Lorentz force, which is shown for the mid-plane by the surface of $|\mathbf{j} \times \mathbf{B}|$ in Figure 2.18. The Lorentz force present around the magnetic flux tubes in the mid-plane is of the order of 10^{-1} , whereas cases (b) and (c) have a much smaller Lorentz force of the order of 10^{-4} and a fairly uniform distribution. In case (a) this large Lorentz force is balanced by the large pressure gradient formed, as the magnetic field settles towards a numerical equilibrium.

2.1.9 Summary

We have described two methods of ‘forming’ a two flux tube configuration, by prescribing a vertical magnetic field in the domain. The first, case (a), considers a magnetic field that relaxes, while the plasma (density and internal energy etc.) is allowed to respond naturally. The second, case (b), considers the relaxation of the magnetic field, while the density and internal energy are held constant. The simulations’ evolutions during this relaxation and the final state produced have been compared to the potential field case (case (c)), that is constructed from the same magnetic field boundary conditions and imported and relaxed in Lare3D. The resultant magnetic fields and approximate equilibria that are formed are compared, to assess the suitability of cases (a) and (b) to be used as an initial field configuration, from which we can investigate the effects of imposing footpoint motions on these flux tubes.

By the end of the 80 normalised time units, both cases (a) and (b) have a maximum background velocity of less than 10^{-4} . Although the final velocities in cases (a) and (b) are larger than in the potential case, they are significantly smaller than the driving speed that will be imposed and so both are suitable from this perspective. The general magnetic field formed by the expanding field in case (b), was qualitatively similar to the imported potential field of case (c), with $\approx 20\%$ larger total integrated magnetic energy in the domain. There was also minimal current formed in case (b), of a similar magnitude to the potential field (and much smaller than case (a)), which resulted in a small Lorentz force in the domain, compared to case (a). Due to the expansion of the magnetic field in case (a), a high gas pressure develops and the magnetic field is not able to fully expand. This results in a larger total magnetic energy in the domain. By the end of the relaxation, high values of current were present throughout the domain in case (a), as well as a large Lorentz force opposing a large plasma pressure gradient.

In the following chapters, the chosen flux tube configuration will be subjected to boundary driving motions in order to investigate the formation of current concentrations and associated heating. The initial flux tube configuration should therefore have minimal current present to begin with. Hence, case (b) is chosen as the method of flux tube formation. Its resultant magnetic field is qualitatively similar to the potential case and is shown to reach an adequate numerical equilibrium. This method of creating a flux tube configuration is also very versatile as it can easily be extended

to create an initial configuration with any number of flux tubes, by prescribing the initial source distribution. All the experiments considered in this thesis, shall continue to use this method of relaxing a vertical magnetic field to form the initial flux tube configuration.

2.2 Discussion of Normalisation Values

In the comparisons in Section 2.1, a normalisation value for density of $\rho_0 = 8.3 \times 10^{-13} \text{ kg m}^{-3}$ was chosen, which with an initial density of 0.1 in Lare3D would produce a density of the order of $8.3 \times 10^{-14} \text{ kg m}^{-3}$. This is an extremely low density for the corona, which we wish to model. This chosen normalisation value also leads to low temperature and pressure values. To address this, new normalisation values are used for all future experiments. The new chosen normalisation values are:

$$B_0 = 100 \text{ G},$$

$$L_0 = 75 \text{ Mm},$$

$$n_e = 1 \times 10^{16} \text{ m}^{-3},$$

which give normalisation values:

$$\rho_0 = 1.67 \times 10^{-11} \text{ kg m}^{-3},$$

$$v_0 = 2182.9 \text{ km s}^{-1},$$

$$t_0 = 34.35 \text{ s},$$

$$P_0 = 79.57 \text{ Pa},$$

$$T_0 = 5.76 \times 10^8 \text{ K},$$

$$J_0 = 1.06 \times 10^{-4} \text{ A m}^{-2},$$

$$E_0 = 21829.149 \text{ V m}^{-1}.$$

$$\eta_0 = 2.057 \times 10^8 \text{ } \Omega \text{ m}$$

Hence, the initial conditions of the two flux tube set up described in Section 2.1 are :

$$\begin{aligned} \text{Loop length} = 1.0 & \Rightarrow \text{Loop length} = 75 \text{ Mm}, \\ r_1 = 0.065 & \Rightarrow r_1 \approx 4.8 \text{ Mm}, \\ B_{max} \approx 1.0 & \Rightarrow B_{max} \approx 100 \text{ G}, \\ B_{mid-plane} \approx 0.03 & \Rightarrow B_{mid-plane} \approx 3.0 \text{ G}, \\ \rho = 0.1 & \Rightarrow \rho \approx 1.67 \times 10^{-12} \text{ kg m}^{-3}, \\ \epsilon = 0.001 & \Rightarrow T \approx 1.9 \times 10^5 \text{ K}. \end{aligned}$$

The density and temperature are now of the order of $10^{-12} \text{ kg m}^{-3}$ and 10^5 K , respectively, which are much more realistic for coronal values. The normalised magnetic field strength has also been increased from the previous experiments. The highly concentrated sources have a peak field strength of 100 G on the z -boundaries. The field strength decreases towards the mid-plane of the domain until, in the centre, the magnetic field is approximately 3 G. The normalisation lengths produce loops with a length of 75 Mm and a radius on the boundaries (r_1) of approximately 5 Mm.

2.3 A Comparison of Periodic Boundary Conditions and Neumann and Dirichlet Boundary Conditions

Normalisation	Initial Conditions	
$B_0 = 100 \text{ G}$	$\epsilon = 0.001$	Resolution: 128^3
$L_0 = 75 \text{ Mm}$	$\rho = 0.1$	$\eta = 0$ (Ideal relaxation)
$n_e = 1 \times 10^{16} \text{ m}^{-3}$		viscosity = 0.001
		$0 < t_{relax} < 80$

In the previous comparisons, periodic boundary conditions were used for the x and y boundaries. In this section, case (b) is repeated with Neumann and Dirichlet boundary conditions, where the normal derivatives of the magnetic field, energy and density are zero (Neumann) and the velocity components are zero (Dirichlet) on the x and y boundaries. The z boundary conditions are the same as described in Section 2.1: the velocity components set to zero and the normal derivatives of the magnetic field, energy and density are also zero, so the field is line-tied at the sources. We investigate whether altering the boundary conditions has a significant impact on the relaxation, through examining the magnetic field, velocity and current remaining after relaxing for the same 80 normalised time units (t_{relax}).

The general form of the magnetic field is not altered by the boundary conditions, as shown by the field lines traced from the same points on $z = 0.0$ in Figure 2.19 for both cases. B_z is the largest magnetic field component and its distribution in the mid-plane along the cut $y = 0.5$ is displayed in Figure 2.20. The pink line shows the case with periodic boundaries and the black line is the case with Neumann and Dirichlet boundary conditions. In the centre of the domain at $y = 0.5$ and $x = 0.5$ the maximum B_z is the same for both simulations, with a value of approximately 0.033. Towards the boundaries, the case with the Neumann and Dirichlet boundary

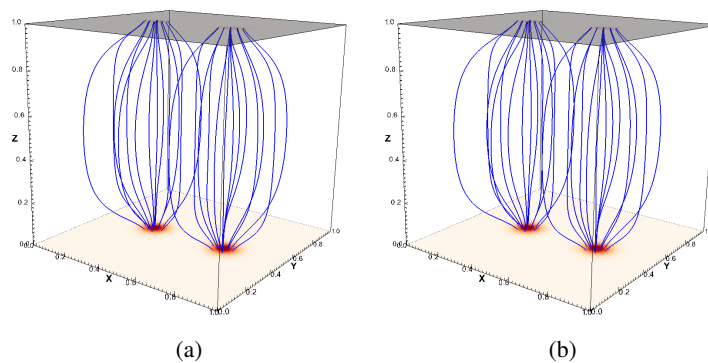


Figure 2.19: Magnetic field lines traced from the same 26 points on the base after relaxation for (a) periodic and (b) Neumann and Dirichlet boundary conditions.

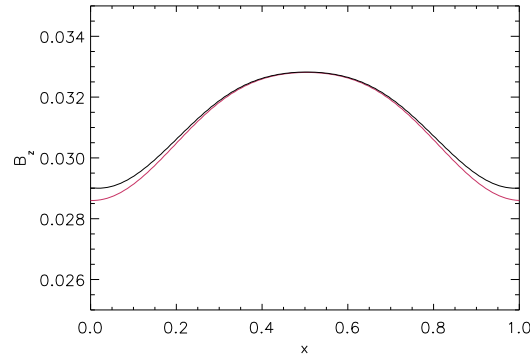


Figure 2.20: Magnetic field component B_z at $z = 0.5$ after relaxation for periodic (pink) and Neumann and Dirichlet (black) boundary conditions.

conditions does not reduce to as low a value of B_z as the periodic case, however, it is only a small difference of approximately 0.4%. This is due to the flux tubes in the periodic case not expanding as far, due to the other ('periodic') expanding flux tubes on both sides in the x direction.

There is a small impact on the background current from the choice of boundary conditions. Figure 2.21b shows the maximum current in the mid-plane with time, as the magnetic field expands and relaxes, with the two types of boundary conditions. Before $t_{relax} = 10$, the maximum current in the two cases behaves almost identically. After this time, the maximum current in the mid-plane for the case with periodic boundary conditions (pink) continues to decrease while oscillating, whereas for the case with Neumann and Dirichlet boundary conditions, the maximum current appears to level off at $t_{relax} \approx 50$. However in Figure 2.21a, the maximum current in a larger area of the domain ($0.3 < x, y, z < 0.7$) is higher than in the mid-plane and the two

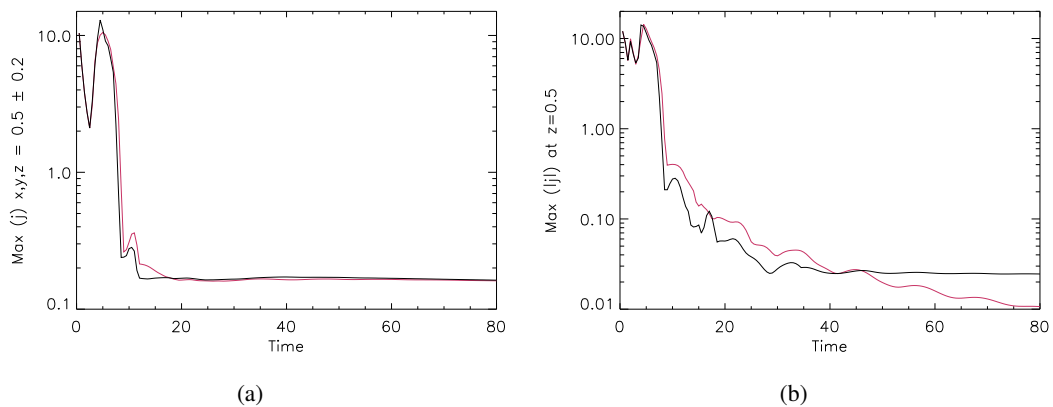


Figure 2.21: Maximum current over time in the domain (a) between $0.3 < x, y, z < 0.7$ and (b) at $z = 0.5$, for periodic (pink) and Neumann and Dirichlet (black) boundary conditions.

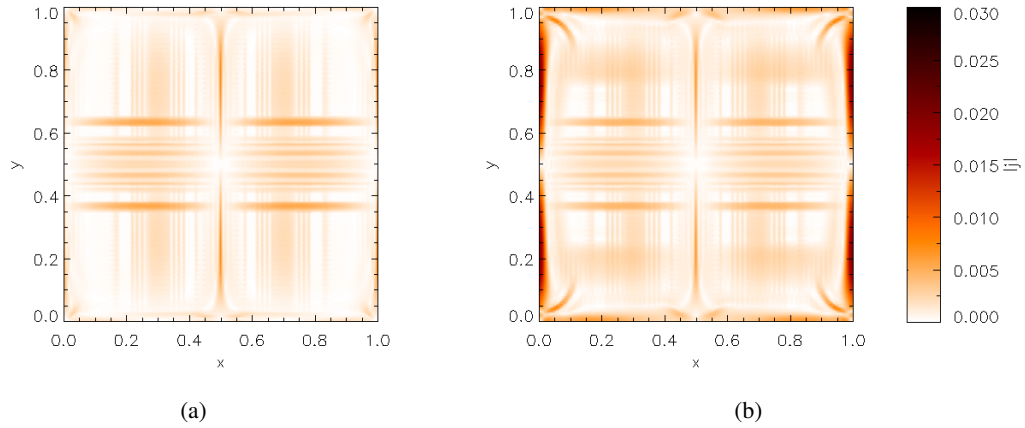


Figure 2.22: Contour of the current magnitude in the mid-plane $z = 0.5$ after relaxation for (a) periodic and (b) Neumann and Dirichlet boundary conditions.

cases show very similar values. The similar evolution suggests that, away from the mid-plane, the amount of current built up is not greatly affected by the boundary conditions. To examine where in the mid-plane the maximum current is occurring, contour plots of the magnitude of the current at $z = 0.5$ are displayed in Figure 2.22. Figure 2.22b shows that the maximum current is actually occurring on the x boundaries for the Neumann and Dirichlet boundary conditions. This current does not build up on the edges for the periodic boundary conditions as the expansion of the flux-tubes balances the field expansion of the ‘neighbouring source’ on the other side of the boundary. This is not the case in (b) and the field expansion continues up to the boundaries leading to a high current forming. In general, the current distribution in and around the centre of the plane is very similar for both cases.

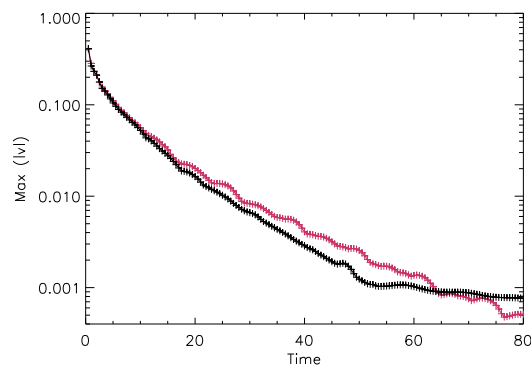


Figure 2.23: Maximum velocity in the domain over time for periodic (pink) and Neumann and Dirichlet (black) boundary conditions.

The maximum velocity in the domain is plotted with time for the two types of boundary conditions in Figure 2.23. The velocities in the domain decrease quickly for both cases, to values of the order of 10^{-4} after 80 time units, with the periodic boundary conditions case (pink) reaching a 30% lower minimum value.

Overall, the flux tubes formed in these two cases are not qualitatively altered by the use of periodic or Neumann and Dirichlet boundary conditions. To decide which boundary conditions to use, we consider the impact they will have on the simulation when a driving velocity is applied to the base of the field lines. Many simulations use periodic boundary conditions, as a periodic simulation is often used to simulate a more realistic coronal set-up, as an active region or flux-tube will never evolve purely in isolation from the surrounding activity. However, the symmetry of periodic boundary conditions can also be considered unrealistic. The choice of Neumann and Dirichlet boundary conditions, also means that reconnection cannot occur through the boundaries (as was the case in the experiment carried out by De Moortel and Galsgaard (2006a)). This reduces the possible locations for reconnection to occur and makes the experiments easier to compare, particularly if more sources are introduced. Hence, the investigations driving the flux-tubes in the following chapters are carried out with Neumann and Dirichlet boundary conditions.

Chapter 3

Driving Two Flux Tubes: Resistivity Test Cases

3.1 Description of Velocity Driver

The initial set up described in Chapter 2 is now subjected to a driving velocity on the lower and upper boundaries at $z = 0.0$ and $z = 1.0$. A rotational velocity is used as in De Moortel and Galsgaard (2006a). The driver on the bottom boundary is described by:

$$\begin{aligned} v_x &= -v_0 r \sin(\theta) \left[1 + \tanh \left(A (1 - B r) \right) \right], \\ v_y &= v_0 r \cos(\theta) \left[1 + \tanh \left(A (1 - B r) \right) \right], \end{aligned} \quad (3.1)$$

where

$$r = \sqrt{(x - 0.5)^2 + (y - 0.5)^2}, \quad \theta = \arctan \left(\frac{y - 0.5}{x - 0.5} \right). \quad (3.2)$$

This produces a rotational driver in the anti-clockwise direction on $z = 0.0$, as indicated by the velocity vectors in the plane in Figure 3.1b. The coefficients A and B describe the steepness and drop off of the driver near the boundaries, respectively, and are set as $A = 16.8$ and $B = 2.8$. The coefficient v_0 impacts the magnitude of the rotation and is chosen to be $v_0 = 0.02$.

The velocity is zero in the centre of the plane and increases linearly away from this point. Figure 3.1a shows the velocity profile varying with x at the cut $y = 0.5$, together with the profile of the magnetic field strength of the sources on the base (normalised to fit axis). The sources are positioned within the linear section of the velocity driver, ensuring minimum distortion of the

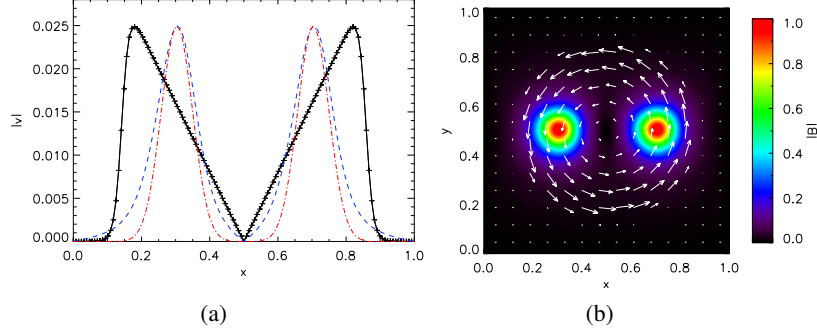


Figure 3.1: (a) Profile of the driving velocity on the base at $y = 0.5$ for resolution 128^3 . The blue dashed line shows the magnitude of the magnetic field ($|B|$) and the red dot-dashed line is the B_z component specified on the boundary. Both magnetic profiles are normalised to fit the axis. (b) Contour plot of $|B|$ on $z = 0.0$ with velocity vectors indicating the imposed velocity.

footpoints on the boundary. Towards the edge of the plane the velocity decreases sharply to reduce shear at the x and y boundaries. In Figure 3.1a the velocity profile is displayed for resolution 128^3 and shows that although the velocity profile reduces very quickly, the reduction is continuous and described by a sufficient number of grid points even at this low resolution.

To start the rotation smoothly, this driver is built up over time using a tanh profile:

$$v = v \left[1 + \tanh \left(\frac{t - t_1}{t_d} \right) \right]. \quad (3.3)$$

This allows the velocity to increase gradually, to help reduce waves and shocks due to a sudden onset of the velocity. The parameters t_1 and t_d are set as 2 and 0.5, respectively. The velocity at $z = 1.0$ has exactly the same magnitude and profile as at $z = 0.0$, but in the opposite direction (clockwise). The sources on the lower and upper boundaries are therefore counter rotated, effectively doubling the twist the field experiences. The simulations are run until $t = 80$ (in most cases), which corresponds to a rotation (θ) of $\approx 2\pi$ on one boundary and a total twist of $\approx 4\pi$.

3.2 Investigating Resistivity

3.2.1 Investigating the Effect of Varying Values of Uniform Resistivity

Normalisation	Initial Conditions	
$B_0 = 100 \text{ G}$	$\epsilon = 0.01$	Resolution: 128^3
$L_0 = 75 \text{ Mm}$	$\rho = 0.1$	$\eta = \eta_0$ (Uniform)
$n_e = 1 \times 10^{16} \text{ m}^{-3}$		$0 < t < 80$

In this section, the behaviour of two flux tubes when rotated by the velocity driver is compared for four values of (normalised) resistivity (η): 0, 10^{-5} , 5×10^{-5} , 10^{-4} (shown in Table 3.1). These resistivity values are applied uniformly throughout the domain. As discussed in Chapter 1, in the solar corona the value of η is expected to be extremely small, of the order of $10^{-6} \Omega \text{ m}$ or less, which would be of the order of 10^{-14} in our normalised values. (Remember here η refers to the resistivity not the diffusivity.) However, this value is not possible to replicate in current numerical experiments and so here we consider how the choice of η can impact the simulation results. One important consideration is that, although η may be set to be zero, the simulation will not be completely ideal due to numerical resistivity and therefore some diffusion will always take place.

The order of magnitude of the numerical diffusivity in Lare3D can be estimated by the expression:

$$V_a(\Delta x)^2/L \quad (3.4)$$

as given by Arber et al. (2007). Here, $\Delta x = \frac{\text{domain width}}{\text{grid resolution}}$ so $\Delta x = \frac{1}{128}$, L is the typical length scale in the dynamical evolution, and V_a is the maximum Alfvén speed in the domain ($\max(B/\sqrt{\rho})$). To estimate (an upper bound of) the numerical resistivity in the domain we shall use $L = 0.1$ as this is the smallest length scale present in the initial configurations and is produced on the z boundaries at the sources. Similarly, the maximum Alfvén speed (≈ 3.16) occurs on the upper and lower boundaries. An upper bound for the numerical diffusivity in the domain is therefore of the order of 2×10^{-3} for a resolution of 128^3 . However this is a maximum estimate and would decrease away from the boundaries, as the field strength decreases with height from the sources.

This is an initial crude estimate of the value of the numerical resistivity, and we also note that as the magnetic field evolves, the length scales considered (i.e. L) will also vary, for example, by the creation of a current layer. This in turn may also increase the numerical resistivity value locally at these regions. It is important to try and understand the impact of resistivity in the simulations, as it is well known that the characteristics of the current layers produced (such as their thickness and maximum values) depend on the resistivity applied and on the resolution of the simulations. However, the details of exactly how they depend on η is still under debate. For example Heerikhuisen and Craig (2004) and Galsgaard and Pontin (2011) found that the maximum current value follows a power law dependence on η . Galsgaard and Pontin also use this scaling as an alternative method to estimate the numerical resistivity present in their simulations, based on the characteristics of the current layer produced.

The effect of the value of resistivity in the experiment is investigated by comparing the evolution of the energy, magnetic field and current. The simulations are run for 80 normalised time units

except for $\eta = 10^{-4}$, which is halted at $t = 50$ due to the time-scale restrictions (discussed later in this section). Note that we now take $\epsilon = 0.01$ (corresponding to $T = 1.9 \times 10^6$ K), compared to $\epsilon = 0.001$ used in Chapter 2, as we found that this initial internal energy density condition allows reconnection to occur sooner in the simulations and hence reduces the computational time needed.

Table 3.1: Uniform Resistivity Comparison: Parameters and colour scheme that will be used throughout this chapter.

$\eta_0 = 0$	$\eta_0 = 1 \times 10^{-5}$	$\eta_0 = 5 \times 10^{-5}$	$\eta_0 = 1 \times 10^{-4}$
--------------	-----------------------------	-----------------------------	-----------------------------

Electric Current Evolution

The evolution of the maximum current density with time around the mid-plane (between $0.46 < z < 0.54$) is shown in Figure 3.2b for the four values of resistivity. The maximum current at first dips very slightly as the flux tubes respond to the presence of the resistivity introduced to the domain. Then the current increases with time and varies between the different cases as the simulations continue. The current for $\eta = 0$ (red) has an initially higher value than the other cases (until $t=60$). This is because this simulation is ideal and therefore the magnetic field is able to be stressed further without diffusing, creating larger currents. Eventually for the $\eta = 0$ case (at $t \approx 70$) the maximum current begins to decrease. This suggests that the current is diffusing numerically and could imply numerical reconnection may be occurring.

For the cases with a value of η specified, the current also increases with time, but initially does not reach as high a value (as $\eta = 0$), due to the presence of resistivity. This allows the field to diffuse when currents have formed and for larger values of η the field is able to diffuse

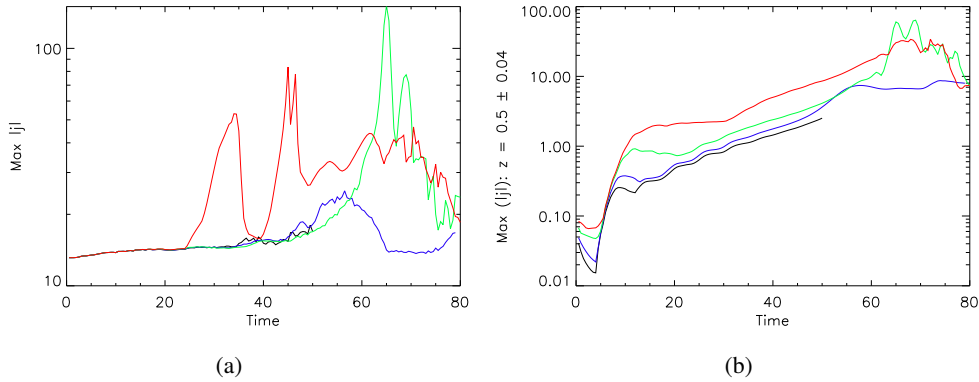


Figure 3.2: (a) Maximum magnitude of current density in the domain and (b) the maximum magnitude of current density between $0.46 < z < 0.54$ for uniform resistivity values of 0, 10^{-5} , 5×10^{-5} and 10^{-4} shown in red, green, blue and black, respectively.

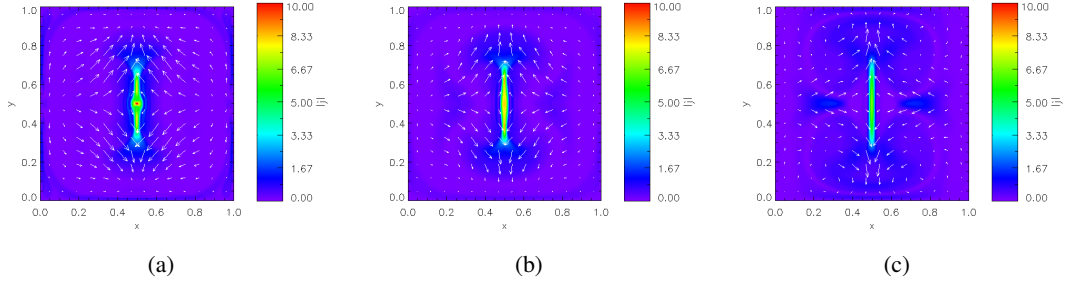


Figure 3.3: Contour plots of the magnitude of the current density in the domain at $z = 0.5$ at $t = 60$ for uniform resistivity values with η as: (a) 0, (b) 1×10^{-5} , (c) 5×10^{-5} . Over-plotted are the velocity vectors in the mid-plane.

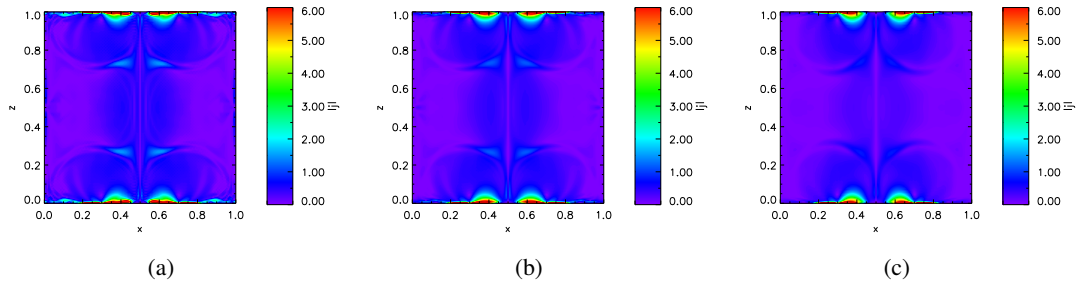


Figure 3.4: Contour plots of the magnitude of the current density in the domain at $y = 0.5$ at $t = 40$ for uniform resistivity values with η as: (a) 0, (b) 1×10^{-5} , (c) 5×10^{-5} .

earlier. The case with $\eta = 5 \times 10^{-5}$ (blue in Figure 3.2b), reaches a peak at the earliest time (≈ 55) and then decreases before building up again. A similar pattern occurs for the lower values of resistivity, however the maximum current density continues to increase for longer and reaches higher maximum values.

Contours plots of the magnitude of the current density ($|\mathbf{j}|$) in the mid-plane are displayed in Figure 3.3 at $t = 60$ for the three simulations that reached this time: (a) $\eta = 0$, (b) $\eta = 10^{-5}$ and (c) $\eta = 5 \times 10^{-5}$. At this time, Figure 3.2b shows that for $\eta = 0$ and $\eta = 10^{-5}$, the current is still increasing and has not yet reached a maximum, whereas the maximum current for $\eta = 5 \times 10^{-5}$ had started to reduce. In Figure 3.3 a central current concentration is shown to occur in all three cases along $x = 0.5$ in the mid-plane, with minimal current in the surrounding area. The arrows represent velocity vectors in the plane, to indicate the motion of the plasma. There is a strong inwards velocity in the x direction towards $x = 0.5$. This inwards velocity is due to the increasing field line tension as the flux tubes are twisted. The inwards velocity then pushes the differently connected field lines towards each other, creating small scales and therefore a high current. Figure 3.5b displays four field lines traced from around the central current formation in the mid-plane at $t = 40$ for the $\eta = 5 \times 10^{-5}$ case. The red and yellow coloured field lines

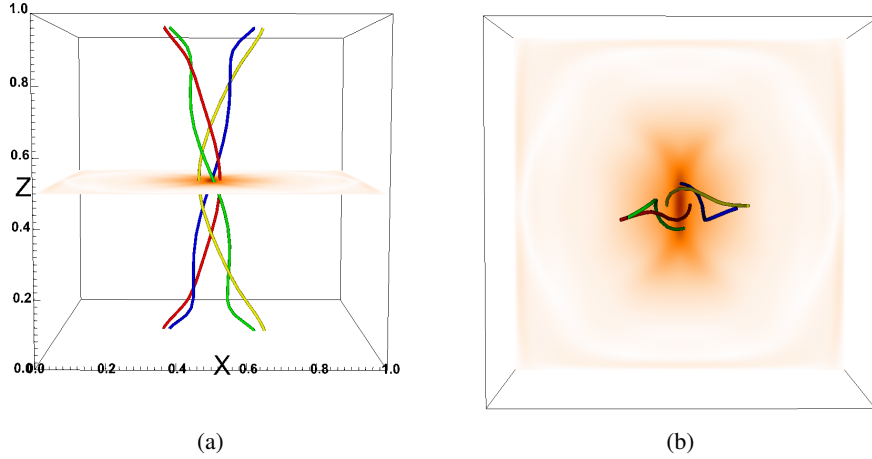


Figure 3.5: (a) Side-view and (b) top-view of field lines traced from the mid-plane at $z = 0.5$ at $t = 40$ for uniform resistivity $\eta = 5 \times 10^{-5}$ plotted over the contour of current in the mid-plane.

intersect the mid-plane on either side ($x > 0.5$ and $x < 0.5$) of the narrow current layer and are approaching it, as indicated by the velocity vectors shown in Figure 3.3c. These field lines have not passed through the current layer and still maintain their original connections to the sources above. The field lines coloured in blue and green are moving away from the current layer and the side-view shown in Figure 3.5a indicates that they have altered their footpoint connections compared to the red and yellow field lines and suggest that they have reconnected. These field lines are shown for $\eta = 5 \times 10^{-5}$, but this is indicative of the field line behaviour for all four cases, as in each case the current layer at $x = 0.5$ forms this ‘reconnection region’.

The current builds up at different speeds for the different resistivity values and therefore, in Figure 3.3 the three contours show current layers at different phases in their evolution. In contour (a) of Figure 3.3, there is the largest value of current at this time, but it is a very small point in the central current layer. In comparison, the peak current is more evenly distributed along the thin current strip in (b) and (c) for non-zero values of η . The current layer is also thinner for larger values of resistivity, however, by $t = 60$, in case (a) the current layer has become so thin that it has approached the limit of the numerical grid and the current layer is shown to fragment.

Figure 3.2a shows the maximum current density magnitude with time for the entire domain and this shows much greater variation between the simulations. Most noticeably, the evolution of the current for $\eta = 0$ is extremely volatile. It rises sharply during the initial stages of the experiment before falling and then greatly increasing once more. In general, we expect higher values of current for smaller η values, as the field cannot diffuse, but in this case, the maximum current occurs just between the footpoints where the flux tubes expand towards each other and it is not properly resolved (see Chapter 4 for resolution discussion). Indeed, the maximum value of current in all the cases always occurs at (or just above) the footpoints of the flux tubes, as discussed

in the comparisons of the flux tube set-ups in Section 2.1. When the velocity driver is applied, it is at this location that we observe the large increase in current over time in the domain for $\eta = 0$. However, the simulations with non-zero resistivity have a more physical current evolution, as the small scales are able to diffuse and a gentle increase in current is observed before slowly decreasing. The peak values of current are greater for the entire domain than in the mid-plane suggesting that, even after rotation, the higher current values occur near the footpoints of the flux tubes. This is supported by Figure 3.4, which displays contours of the current in the x - z plane at $y = 0.5$ at time $t = 40$ and the highest current in this cut clearly occurs just above the footpoints.

Energy: Evolution and Conservation

The evolution of the integrated (a) kinetic, (b) internal, (c) magnetic and (d) total energies in the domain are shown in Figure 3.6 for each resistivity value. The footpoint motions enable energy to be stored in the twisted magnetic field, shown by the increasing magnetic energy in Figure 3.6c. The process of reconnection then allows the magnetic energy to be converted to kinetic and inter-

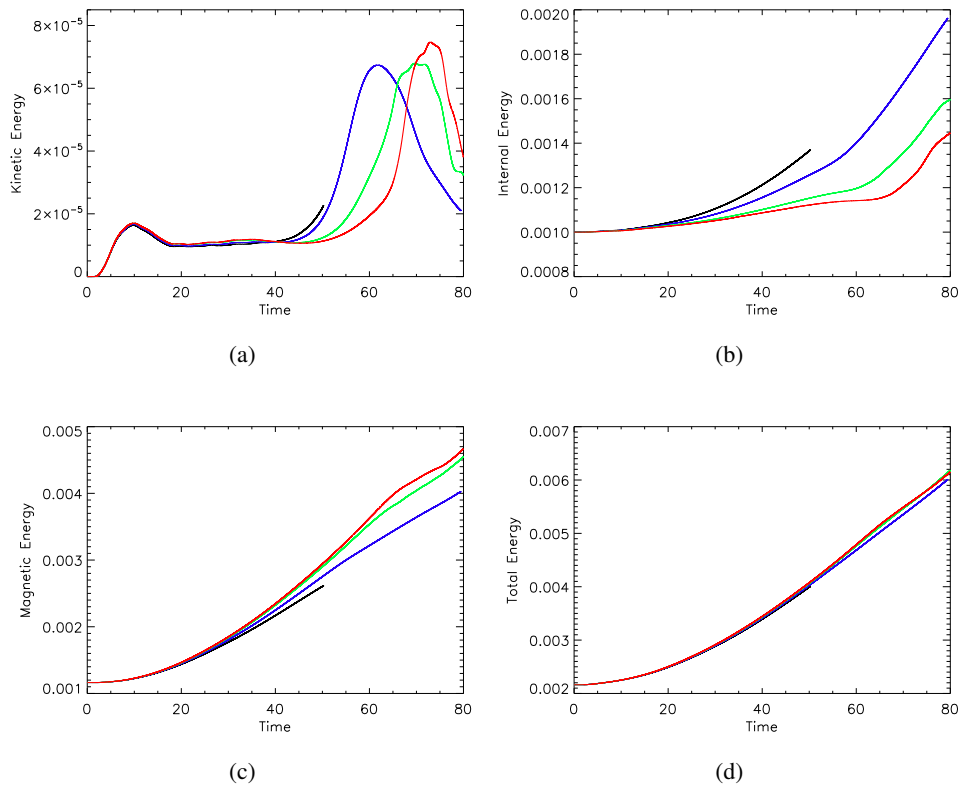


Figure 3.6: (a) Kinetic, (b) internal, (c) magnetic and (d) total volume integrated energies for cases with uniform resistivity values of 0 (red), 10^{-5} (green), 5×10^{-5} , (blue) and 10^{-4} (black).

nal energy. The increase of the internal energy is an order of magnitude greater than the kinetic energy increase, indicating that the majority of the energy is converted to internal energy through diffusion and reconnection. The total energy in Figure 3.6d is continually increasing, as energy is constantly being injected into the domain through the footpoint motions, with only small variations ($\approx 2\%$) between simulations.

For all the energies in Figure 3.6, the different resistivity cases behave very similarly up to approximately $t = 20$. After this time, the magnetic energy continues to increase at a faster rate for $\eta = 0$, with the gradient of the increasing magnetic energy reducing for larger values of η . Correspondingly, the increase in internal energy is greatest for the largest value ($\eta = 10^{-4}$), which had the smallest increase in magnetic energy. Initially, a similar amount of energy for all four cases is being introduced to the domain through the velocity motions on the $z = 0.0$ and $z = 1.0$ boundaries. However, a higher resistivity value means that the diffusion term ηj^2 in the energy equation becomes important at an earlier stage (and will also enable reconnection to occur sooner) converting the magnetic energy into internal and kinetic energy at an earlier time, thus preventing the build up of large magnetic energy. By $t = 80$, the internal energy for $\eta = 5 \times 10^{-5}$ has reached a value of over 0.0019 from a starting internal energy of 0.001. This increase of $\approx 90\%$ is almost double the increase for the $\eta = 0$ case, which rises by only 45%.

The different times for the onset of reconnection are also seen in panel (a) of Figure 3.6, where the peak in kinetic energy occurs earlier in the simulations with higher values of resistivity. This is comparable to the timing of the peaks in the maximum current evolution in Figure 3.2b. The value of the kinetic energy maxima also depends on the value of resistivity. The highest peak is observed for the ideal simulation with η equal to zero (red), which occurs at the latest time. This is due to the magnetic field being twisted for longer before reconnecting (numerically), allowing higher current values to be built up (see Figure 3.2b) and therefore stronger reconnection, with faster flows, occurs. Hence, for higher values of η the reconnection is earlier but weaker, producing smaller flows and hence, less kinetic energy.

In order to discuss the conservation of energy in the domain, we consider the total energy equation (that can be derived from the MHD equations in Section 1.2.1, again neglecting induction and radiation):

$$\frac{\partial}{\partial t} \left(\frac{1}{2} \rho v^2 + \frac{p}{\gamma - 1} + \frac{B^2}{2\mu_0} \right) + \nabla \cdot \left(\frac{1}{2} \rho v^2 \mathbf{v} + \frac{\gamma p}{\gamma - 1} \mathbf{v} + \frac{\mathbf{E} \times \mathbf{B}}{\mu_0} \right) = 0. \quad (3.5)$$

Integrating this equation over the domain and then using Gauss' theorem, Equation 3.5 becomes,

$$\frac{de_{Total}}{dt} = - \int_S \mathbf{Q} \cdot d\mathbf{S}, \quad (3.6)$$

where e_{Total} is the sum of the integrated kinetic, internal and magnetic energy and is therefore the

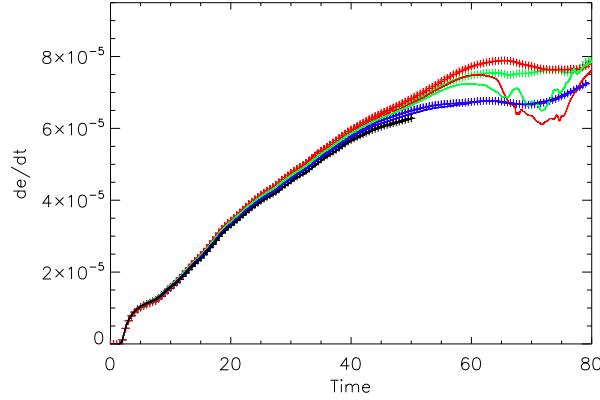


Figure 3.7: The total rate of change of energy de/dt (solid line) and the Poynting flux injected into the domain (crosses) for uniform resistivity values of 0, 10^{-5} , 5×10^{-5} and 10^{-4} shown in red, green, blue and black, respectively.

total volume integrated energy in the domain:

$$e_{Total} = \int \frac{1}{2} \rho v^2 dV + \int \frac{p}{\gamma - 1} dV + \int \frac{B^2}{2\mu_0} dV, \quad (3.7)$$

and

$$\mathbf{Q} = \frac{1}{2} \rho v^2 \mathbf{v} + \frac{\gamma p}{\gamma - 1} \mathbf{v} + \frac{\mathbf{E} \times \mathbf{B}}{\mu_0}, \quad (3.8)$$

which is the energy flux into or out of the domain. As there is no horizontal velocity through the side boundaries and v_z is specified as zero on the upper and lower boundaries, the total flow of energy in/out of the domain reduces to the Poynting flux given (in dimensionless variables) by the integral

$$- \int_S \mathbf{E} \times \mathbf{B} \cdot d\mathbf{S}, \quad (3.9)$$

evaluated on the top and bottom boundaries, where $\mathbf{E} = -\mathbf{v} \times \mathbf{B} + \eta \mathbf{j}$.

Figure 3.7 displays the rate of change of energy ($\frac{de_{Total}}{dt}$, solid line) and the total Poynting flux injected into the domain on the upper and lower boundaries (crosses). There is better agreement between the Poynting flux and the rate of change of total energy for larger values of resistivity. The two smallest values of resistivity, 0 and 10^{-5} , in red and green, respectively, show good agreement between the Poynting flux and rate of change of total energy until an approximate time of $t = 50$. At this point the Poynting flux injected into the domain continues to increase as the footpoints are still being driven, however, the rate of change of energy begins to decrease. The ideal run ($\eta = 0$) has the largest difference between the total rate of change of energy and the Poynting flux. This

difference implies that energy is not being conserved as numerical resistivity is coming into play, thereby reducing the build up of magnetic energy without correspondingly increasing the internal energy. However, the higher uniform resistivity value of 5×10^5 in blue in Figure 3.7 shows the Poynting flux agreeing with the rate of change of energy in the simulation, indicating that energy is conserved throughout the simulation. Similarly, the higher resistivity of 10^{-4} , shown in black in Figure 3.7, also conserves energy until the simulation is halted at $t = 50$.

As discussed by Galsgaard and Parnell (2005b) and Bowness et al. (2013), the total Poynting flux injected into the domain also depends of the value of the resistivity used in the numerical code. The magnitude of the Poynting flux injected into the domain depends on the magnitude of the horizontal magnetic field components on the boundaries where the driving velocity is applied. Each simulation begins with the same magnetic field and has the same velocity on the boundaries and therefore the Poynting flux is initially the same. However, as the magnetic field is twisted and allowed to evolve, reconnection takes place and, as shown in Figure 3.6c, the magnetic field evolution varies between cases. As discussed previously, higher values of resistivity allow reconnection to occur sooner, reducing the twist in the field and hence reducing the magnitude of the horizontal field components. This corresponds with the reduced Poynting flux for larger values of η , shown in Figure 3.7, and supports the slightly larger total energy for smaller values of η shown in Figure 3.6d.

The simulation with $\eta = 0$ should have an ideal evolution and therefore evolve without diffusion or reconnection occurring. However, as discussed, there is always numerical resistivity associated with numerical simulations, which depends on the resolution of the simulations. These comparisons are all carried out at 128^3 resolution. Figure 3.7 shows that before $t = 15$, the $\eta = 0$ (red) case had an ideal evolution (as the Poynting flux and rate of change of total energy are equal) and then gradually start to separate as numerical diffusion occurs. Similarly for the second lowest value of η , $\eta = 10^{-5}$ (green), the numerical resistivity becomes important, causing the rate of change of energy and Poynting flux injected to no longer agree (see Figure 3.7).

The importance of energy conservation was discussed in detail by Bowness et al. (2013) for a case where a simple shearing motion is applied to an initially uniform field. However, in our cases, the initial numerical resistivity varies with height in the domain, due to its dependence on the maximum Alfvén speed and thereby, on the magnetic field strength. As the field evolves the numerical resistivity will also alter depending on the changing Alfvén speed and on the length scale (L) produced by the formed current layer. This variation makes it harder to achieve complete conservation of energy and small losses in energy conservation are expected. In our choice of η we are therefore looking to choose a large enough value to accurately follow and account for the energy evolution in our domain, with minimal numerical errors, while remaining as small as possible to try and realistically model the solar corona. At 128^3 resolution, the maximum numerical resistivity at $t = 0$ was estimated (using Equation 3.4) as 2×10^{-3} on the base, but

for the majority of the domain, where the magnetic field has expanded, the numerical resistivity is below 2×10^{-4} . However, as we consider higher resolutions with subsequent lower numerical resistivities, the energy conservation will improve (see Section 4.1).

Evolution of Field line Connectivity

To observe and quantify the amount and timing of the reconnection that is occurring, we apply a similar analysis to that of De Moortel and Galsgaard (2006a). Figure 3.8 shows snapshots in time of the connectivity of field lines associated with one source at $z = 0.0$ as it is rotated. The source shown in Figure 3.8 is initially centred on $x = 0.7$ and $y = 0.5$ at $t = 0$ (the initial right-hand source). The magnetic field has been traced from points within a radius of $r_1 = 0.065$. Within this radius, 4197 field lines are traced and are coloured according to where they connect to at $z = 1.0$. Any field line that is within $2r_1$ of a source at $z = 1.0$ is said to be connected to that source and is coloured dark blue if it is connected to its original source (namely the source which was at $y = 0.5$, $x = 0.7$ and $z = 1.0$ at $t = 0$) or light blue if it is connected to the other source. If the field line is traced to $z = 1.0$ but is not within $2r_1$ of either source then we say it is unassigned and it is coloured black. The routine may not be able to trace the field line to $z = 1.0$ and then it is coloured red. If this is the case, it suggests that it would be a highly twisted field line, which implies it has probably not changed connectivity.

The highest value of η ($\eta = 10^{-4}$) has the largest number of field lines change connectivity earlier in the simulation, shown in light blue at $t = 30$ and $t = 45$ in Figure 3.8. The snapshot at $t = 45$ for $\eta = 10^{-4}$ shows over a quarter of the flux in the source has reconnected. This amount then decreases for smaller values of η , as reconnection begins at later times. However, this case is halted by $t = 50$ due to numerical reasons. Considering the other cases, by $t = 70$ for $\eta = 5 \times 10^{-5}$ (which is the only one of the cases to conserve energy and run for the entire simulation time), over 90% of the flux from the source is coloured light blue and has reconnected to the other source. This is the maximum percentage of reconnected flux for all the simulations with different η values.

Figure 3.9 shows the evolution of the field line connectivity with time, where the percentage of reconnected flux is the average for both sources at $z = 0.0$. For higher values of η , the flux begins to change connectivity sooner and reaches a larger maximum percentage of flux having changed connectivity. For the two cases where energy was not conserved, $\eta = 10^{-5}$ (green) and $\eta = 0$ (red), the percentage of flux changing connectivity appear very similar. The case with $\eta = 10^{-5}$ increases slightly sooner, but reaches a very similar maximum ($\approx 82\%$ by $t = 74$) to the $\eta = 0$ case.

In general, the peak percentage of reconnected flux occurs for all cases within a few time

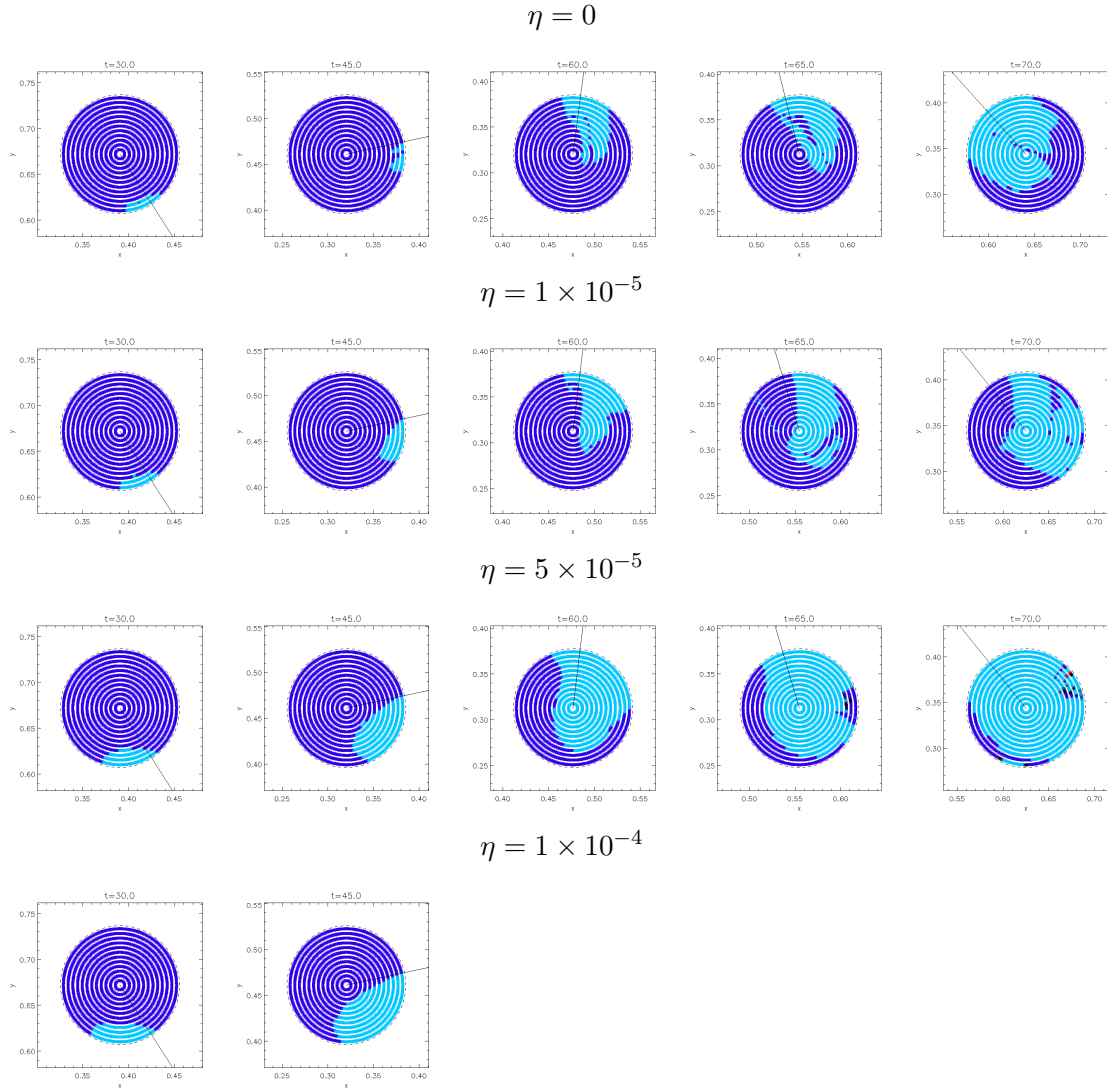


Figure 3.8: The field line connectivity of the right-hand source (at $t = 0$) on $z = 0$ at different times for uniform resistivity of 0, 10^{-5} , 5×10^{-5} and 10^{-4} . The solid black line indicates the direction to the centre of rotation. Dark blue signifies field lines at the original connection, light blue shows field lines that have changed connectivity and are connected to the other flux source on the upper boundary, red corresponds to field lines that cannot be traced to $z = 1$ and black are field lines that are connected to the upper boundary but not associated with either source by our definition (see text).

units of $t = 73$ (over-plotted in Figure 3.9). This is despite the fact that the times of the onset and rate of reconnection for each simulation varies greatly, as shown by the peaks in the kinetic energy graphs in Figure 3.6. This suggests that the time of the maximum reconnected flux does not depend on the resistivity or the amount that has reconnected but on the rotation angle. After the maximum of reconnected flux has occurred in Figure 3.9, the percentage of reconnected flux then decreases for all simulations as the field lines in the sources begin to reconnect back to their

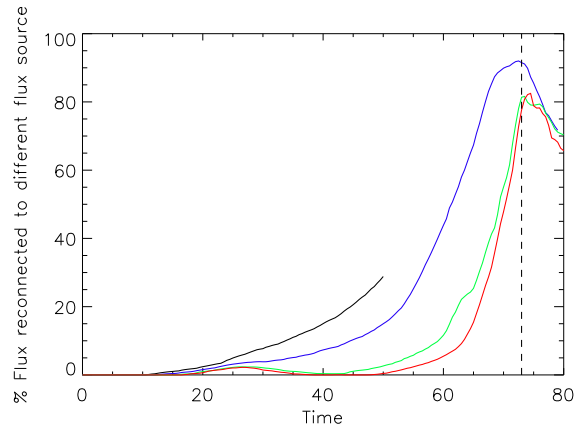


Figure 3.9: The percentage of reconnected flux averaged from both sources at $z = 0.0$ for uniform resistivity of 0 , 10^{-5} , 5×10^{-5} and 10^{-4} shown in red, green, blue and black, respectively. $t = 73$ is over-plotted as a dashed vertical line.

original source. This results in regions of original connectivity (dark blue) appearing among other light blue regions of connectivity in the footpoint connectivity maps at $t = 70$ in Figure 3.8, which are associated with field lines that have reconnected back again.

Plasma Response: Temperature and Density

The minimum density in the domain is plotted as a function of time in Figure 3.10. For the simulations with $\eta = 10^{-4}$ and $\eta = 5 \times 10^{-5}$, the minimum density in the domain decreases rapidly after approximately $t = 20$. These are the two cases shown to conserve energy throughout the simulation (see Figure 3.7) and in which the largest amounts of magnetic energy are converted into internal and kinetic energy.

This large increase in internal energy heats the plasma and therefore, by the gas law, reduces the density where the heating occurs. Figure 3.11 shows a contour plot of the plasma density at $t = 40$ in the plane $y = 0.5$. At this time, the plane $y = 0.5$ cuts through the footpoints of the flux tubes as they have undergone a rotation of approximately π radians (on one boundary). We are able to see that it is just above the footpoints on $z = 0.0$ and $z = 1.0$ that this heating, and a subsequent reduction in density, occurs. Figure 3.11d (for $\eta = 10^{-4}$) shows four large depletions of plasma above the footpoints, with a density in normalised units of less than 10^{-7} at some locations. This is clearly non-physical and is due to the simulation set-up, as there is no vertical velocity through the z boundaries. The plasma is heated by the magnetic field diffusing, causing a velocity flow away from the footpoints, but there is no flow through the boundary to replace the displaced plasma, as would occur in reality in the solar atmosphere.

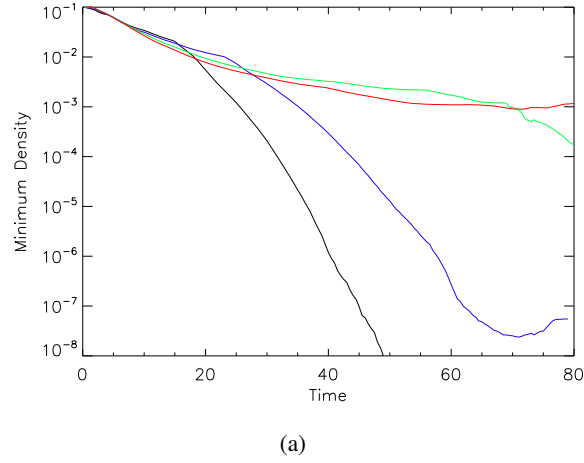


Figure 3.10: Minimum density in the domain with time for uniform resistivity values of 0, 10^{-5} , 5×10^{-5} and 10^{-4} shown in red, green, blue and black, respectively.

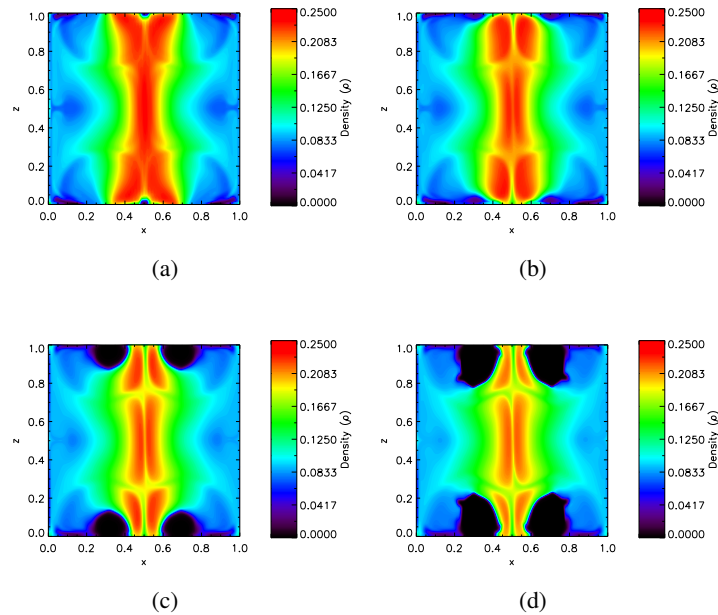


Figure 3.11: Contour plots of the density in the domain at $y = 0.5$ at $t = 40$ for uniform resistivity values of (a) $\eta = 0$, (b) $\eta = 1 \times 10^{-5}$, (c) $\eta = 5 \times 10^{-5}$ and (d) $\eta = 10^{-4}$.

The reduction in density also increases the Alfvén velocity at these points, as (in Lare3D) $v_A = \frac{B}{\sqrt{\rho}}$. The numerical code ensures that the time-step remains smaller than the minimum Alfvén time, therefore, as the Alfvén time continues to decrease rapidly, the simulation for $\eta = 10^{-4}$ is unable to continue to output data with the available numerical resources and is halted at $t = 49$. A large reduction of density is also seen in Figures 3.10 and 3.11c for $\eta = 5 \times 10^{-5}$. However, the diffusion that heats the plasma becomes important at a slightly later time for the

higher value of resistivity, therefore the density does not reach such small values and so it is able to run for the full simulation time, but the non-physical plasma distribution remains.

In comparison, for the smaller values of η where energy is not conserved, the minimum density decreases by just a few orders of magnitude and the contours of density in Figures 3.11a and 3.11b for $\eta = 0$ and $\eta = 5 \times 10^{-5}$ do not show large evacuations of density above the footpoints.

Summary and Discussion

The location of the high current density values and heating suggest that diffusion happens predominantly nearer the footpoints as the field expands. The large expansion of field on the z boundaries, and the high currents this produces, cause the density deficit at the footpoints. Combining the large expansion of the field with the non-stratified atmosphere, modelled for simplicity, means that plasma is expelled from the footpoints. These effects arise due to the simplified approach we take in modelling the atmosphere. Possibilities for future experiments include: using a stratified atmosphere where the gas pressure is larger towards the boundaries, having a larger plasma β in the whole domain, or applying thermal conduction to the code to distribute the heat in the plasma.

The effect of boundary conditions on the plasma distribution is also discussed by Baumann et al. (2013), who model 3D simulations of reconnection with boundary driving velocities. For a non-stratified atmosphere experiment, they also showed these ‘voids’ occurring at the boundaries. Baumann et al. compared a stratified and non-stratified simulation as well as a simulation with open boundary conditions allowing plasma to flow in/out at the boundaries. They found the simulations with a stratified atmosphere, prevented these voids from becoming an issue due to the large amounts of relatively cold gas in the region. Similarly, with open boundary conditions, the exchange of plasma was able to fill these voids.

Another avenue to consider is using a localised resistivity region within the domain, similar to that used by Pontin et al. (2005). This allows reconnection and heating to occur towards the centre of the domain rather than at the footpoints. However, with no resistivity specified near the boundaries, care needs to be taken to ensure there is minimal loss of energy conservation.

3.2.2 Investigating the Effect of Localised Resistivity Regions

Normalisation	Initial Conditions	Resolution: 128^3
$B_0 = 100 \text{ G}$	$\epsilon = 0.01$	$\eta_0 = 5 \times 10^{-5}$
$L_0 = 75 \text{ Mm}$	$\rho = 0.1$	$0 < t < 80$
$n_e = 1 \times 10^{16} \text{ m}^{-3}$		

In Section 3.2.1, the impact of different values of uniform resistivity, when twisting two flux tubes, was considered. We now go on to consider a localised resistivity region of two different forms. The first is of the form:

$$\eta = \eta_0 e^{-\left(\frac{r}{r_0}\right)^2}, \quad (\text{radially dependent})$$

where,

$$r = \sqrt{(x - 0.5)^2 + (y - 0.5)^2 + (z - 0.5)^2} \quad \& \quad r_0 = 0.1.$$

The value of resistivity (η) is exponentially decreasing with radius from the centre of the domain. The second localised resistivity region is of the form:

$$\eta = \eta_0 e^{-\left(\frac{z-0.5}{r_0}\right)^2}, \quad (z\text{-dependent})$$

also with $r_0 = 0.1$. This resistivity distribution is constant in the $x - y$ plane and exponentially decreasing away from the mid-plane. In both of these cases the resistivity is zero at the footpoints of the flux tubes, the location where large currents and heating were found in Section 3.2.1. To examine the effect of a localised resistivity, we compare these forms to the uniform resistivity ($\eta_0 = 5 \times 10^{-5}$) and an ideal simulation with $\eta = 0$ (summarised in Table 3.2).

Table 3.2: Localised Resistivity Comparison: Resistivity form and colour scheme that will be used throughout this chapter.

Ideal $\eta = 0$	Uniform $\eta = \eta_0$	Radially dependent $\eta = \eta_0 e^{-\left(\frac{r}{r_0}\right)^2}$	z -dependent $\eta = \eta_0 e^{-\left(\frac{z-0.5}{r_0}\right)^2}$
---------------------	----------------------------	---	---

Plasma Response: Density Evolution

Figure 3.12 shows the variation of the minimum density with time. The uniform resistivity simulation, discussed in Section 3.2.1, produced voids of plasma above the footpoints of the flux tubes and has a minimum density (shown in green) of less than 10^{-7} . In comparison, for both localised resistivity runs the density decreases slightly over time but remains around 10^{-3} in normalised units. The two cases behave very similarly to each other, and similarly to the ideal case, as there is no resistivity acting on the footpoints. The large heating and associated reduction in density near the boundaries is therefore not present, as shown in the contours of density at $t = 40$ in Figure 3.13. The density distribution in Figure 3.13 is similar for the two localised resistivity cases. In both cases, denser plasma is present towards the central column of the domain, as is also true for $\eta = 0$. The density contours for the cases with localised non-ideal regions in Figures 3.13c

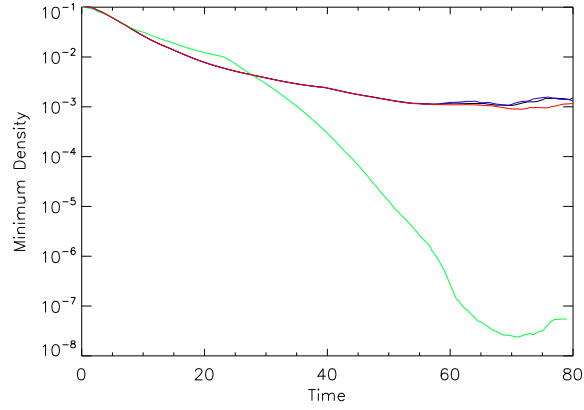


Figure 3.12: Minimum density in the domain with time for simulations with resistivity forms: $\eta = 0$, uniform, radially dependent and z -dependent with $\eta_0 = 5 \times 10^{-5}$ shown in red, green, blue and black, respectively.

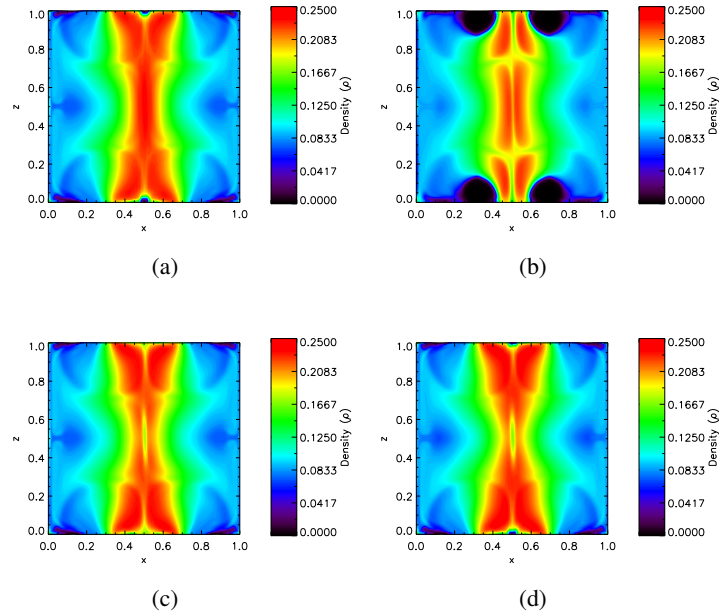


Figure 3.13: Contour plots of density in the domain at $t = 40$ at $y = 0.5$ for simulations with resistivity forms: (a) $\eta = 0$, (b) uniform, (c) radially dependent and (d) z -dependent with $\eta_0 = 5 \times 10^{-5}$.

and 3.13d differ slightly from the ideal case in 3.13a in the centre of the domain. In (c) and (d) there is a slight reduction in density along $x = 0.5$ visible in the plane. This suggests that Ohmic heating is occurring and thereby reducing the density in this central region where η is present.

Energy and Current Evolution

The energy evolution in the domain for the four cases is displayed in Figure 3.14, where the volume integrated energy is plotted separately for the (a) kinetic, (b) internal, (c) magnetic and (d) total energy. As with the uniform resistivity case, the energy evolution is very similar for all forms of resistivity up to approximately $t = 20$. After this time, the internal energy of the uniform resistivity case (green) begins to increase very quickly in comparison to the other cases and this coincides with the magnetic energy gradient reduction. This is what we would expect as the uniform case has an η present in the whole domain, which can act on the high currents near the base to convert the magnetic energy into internal energy earlier. In terms of the magnetic energy evolution, the two localised resistivity regions and the ideal run behave almost identically until $t = 55$, when magnetic energy becomes greater for the ideal case. This is because the current formed in the cases with localised non-ideal regions allows the magnetic field to diffuse. The internal energy evolution is also similar for the cases with localised non-ideal regions and the ideal case until $t = 55$. After which, the cases with a non zero resistivity produce greater internal energy. This suggests that the localised resistivity does not have a large effect until this time and that diffusion occurring in the uniform η case is occurring away from these localised regions.

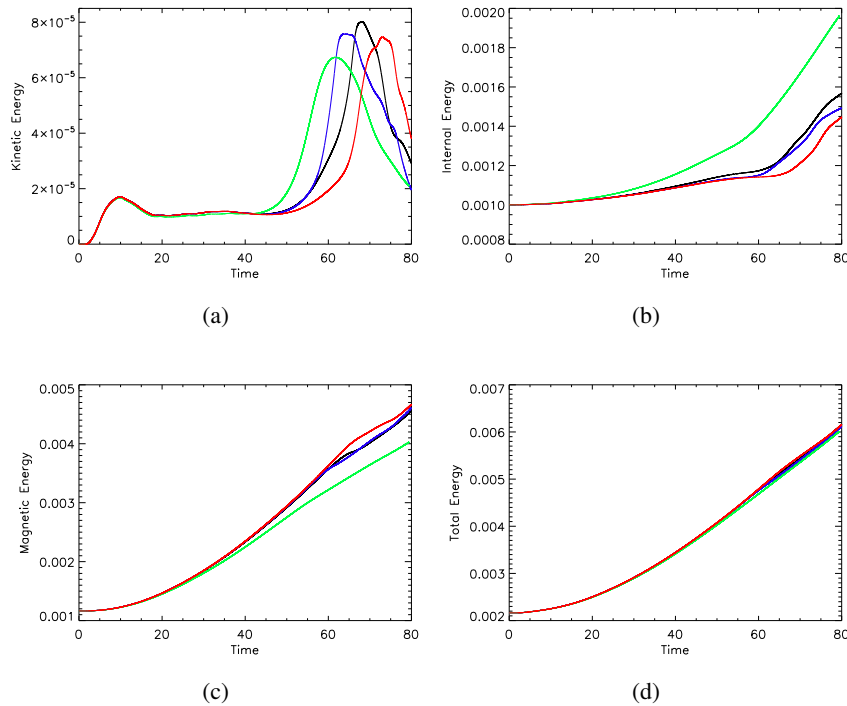


Figure 3.14: (a) Kinetic, (b) internal, (c) magnetic and (d) total volume integrated energies for simulations with resistivity forms: $\eta = 0$, uniform, radially dependent and z -dependent with $\eta_0 = 5 \times 10^{-5}$ shown in red, green, blue and black, respectively.

In Figure 3.14, the case with z -dependent η (black) has slightly larger internal energy than the radially dependent η (blue), but this difference is relatively small ($\approx 5\%$). The magnetic energy evolution is also very similar with minimal difference between them, but the z -dependent η does have a slightly smaller value at the end of the simulation, which corresponds to the larger internal and kinetic energy. This is due to the larger area where Ohmic heating can occur in the z dependent case, and so a larger internal energy is produced. The timing of the increase in kinetic energy is also interesting, as the uniform η case peaks first at $t \approx 61$ in Figure 3.14, but the case with a radially dependent localised non-ideal region increases before the z -dependent η . This suggests that reconnection is occurring earlier in the $\eta = \eta_0 e^{-(\frac{r}{r_0})^2}$ case. This initially appears counter-intuitive as the case with a diffusive term acting on a smaller area produces reconnection earlier.

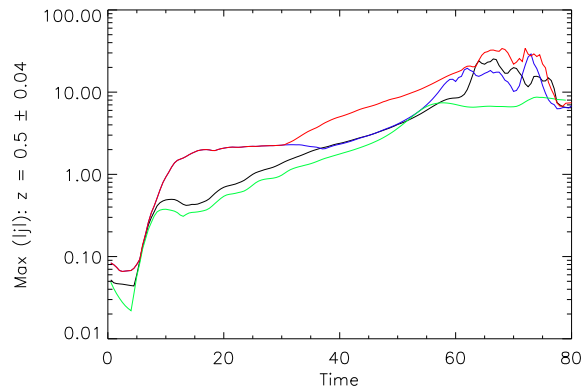


Figure 3.15: The maximum magnitude of current density between $0.46 < z < 0.54$ for simulations with resistivity forms: $\eta = 0$, uniform, radially dependent and z -dependent with $\eta_0 = 5 \times 10^{-5}$ shown in red, green, blue and black, respectively.

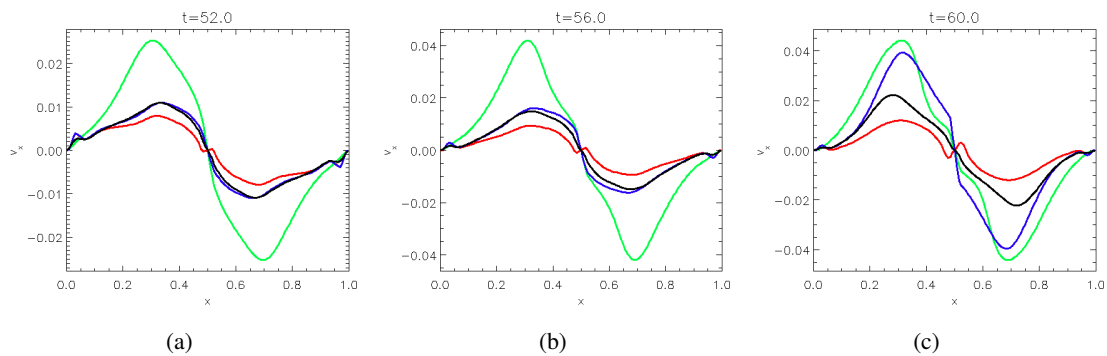


Figure 3.16: Velocity component v_x at $y = 0.5$ in the mid-plane at (a) $t = 52$, (b) $t = 56$, (c) $t = 60$, for cases with resistivity forms: $\eta = 0$, uniform, radially dependent and z -dependent with $\eta_0 = 5 \times 10^{-5}$ shown in red, green, blue and black, respectively.

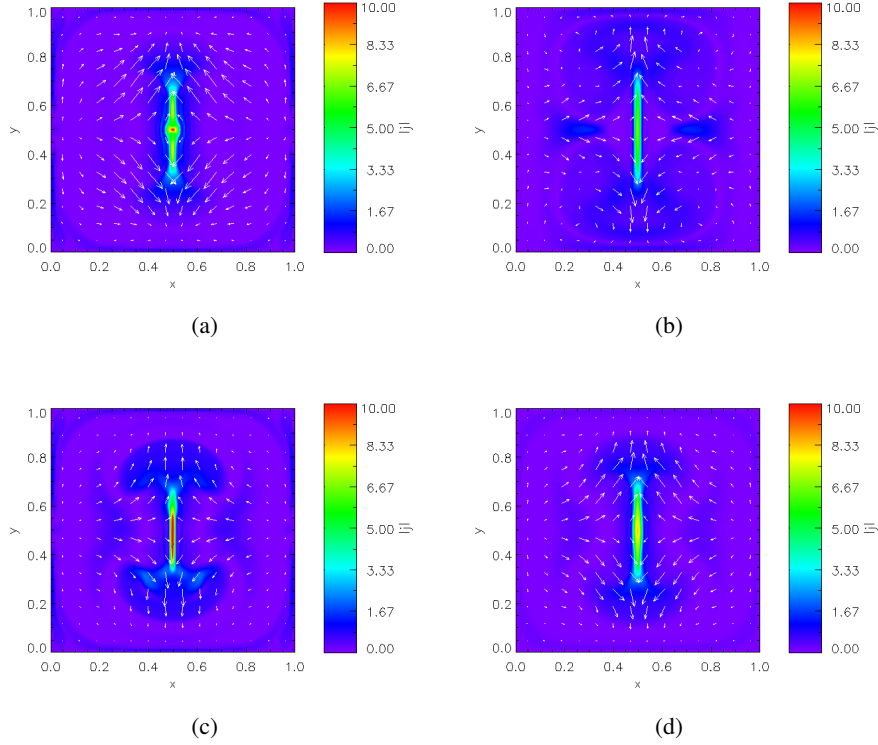


Figure 3.17: Contour plots of the current density in the domain at $y = 0.5$ at $t = 60$ for simulations with resistivity forms: (a) $\eta = 0$, (b) uniform, (c) radially dependent and (d) z -dependent with $\eta_0 = 5 \times 10^{-5}$. Over-plotted are the velocity vectors in the mid-plane.

To explain this, we look at how the presence and shape of the localised resistivity region affect the evolution of the field and the timing of the reconnection. As the resistivity regions are both centred around the mid-plane of the domain, they are the same in the centre of the domain but differ at the boundaries. Therefore, we would expect any difference in the behaviour of the two simulations to begin in this area. Figure 3.15 shows the evolution of the maximum current in the narrow region $0.46 < z < 0.54$ surrounding the mid-plane. Initially the $\eta = \eta_0 e^{-\left(\frac{r}{r_0}\right)^2}$ case (blue) has the same behaviour as the ideal simulation shown in red, with a high maximum current in the mid-plane. In comparison, the z -dependent resistivity has a slightly lower initial maximum current around the mid-plane, before increasing to similar values to the radially dependent case after $t = 35$. This initial current disparity between the cases with localised resistivity regions is due to the maximum current near the x -boundaries. The z -dependent resistivity (black) has a uniform η in the plane and hence acts to diffuse the field and reduce the currents at the x -boundaries initially. There is no resistivity acting here for the radially dependent localised non-ideal region and so the initial higher currents on the boundaries remain, as with the $\eta = 0$ case.

The diffusion of the field at the x -boundaries can also affect the magnetic field evolution later in the simulation, through the Lorentz force. When the field has diffused near the boundaries,

there is a smaller Lorentz force acting towards the centre. The effect of this can be seen in the velocity cut at $y = 0.5$ in the mid-plane in Figure 3.16. In Figure 3.16a at $t = 52$, the v_x velocity component has a very similar shape for both runs with localised resistivity regions (in blue and black), where there is a velocity towards $x = 0.5$ from either side. However, by $t = 60$ in Figure 3.16c, the v_x cut for the radially dependent resistivity region (blue) has a much larger magnitude and steep gradient at $x = 0.5$. This velocity will act to bring the differently connected field lines together, creating a high current at $x = 0.5$. This can be seen in Figure 3.17, where contours of the magnitude of the current density ($|j|$) in the mid-plane are displayed at $t = 60$. The current layer at $x = 0.5$ in contour (c), for the radially dependent resistivity region, is already thinner and stronger than the current layer in contour (d). This is due to the high inwards velocity seen in Figure 3.16 and explains why the maximum current rises earlier (at $t \approx 50$) for the radially dependent resistivity region in Figure 3.15. This also supports the earlier peak in kinetic energy shown in Figure 3.14, as the current layer is formed earlier and hence allows reconnection to occur earlier.

Evolution of Field line Connectivity

The timing of reconnection can also be inferred from the field line connections traced from one of the sources, these are shown at different times in Figure 3.18. The connectivities in Figure 3.18 are found using the same method outlined in Section 3.2.1 and represent one source on $z = 0.0$, as it is rotated by the velocity driver and the flux within it is coloured according to its connectivity at $z = 1.0$. Hence, initially the entire source is dark blue, as all field lines are at their original connection. Then, as they change connectivity, their origin within the source is depicted as light blue. The uniform η case changes connectivity first and has the largest proportion of the source reconnected at all times. Initially, the two cases with localised resistivity regions show very similar evolution until $t = 60$. After this point, the radially dependent form of localised η has a larger percentage of flux changing connectivity than the z -dependent η . All the cases with some form of resistivity show more flux changing connectivity and at an earlier time than for $\eta = 0$, as we would expect as this reconnection is completely numerical.

An estimate of the total percentage of reconnected flux with time is plotted in Figure 3.19. This is estimated using the connections of the field lines traced from both footpoints on $z = 0.0$ and averaged. The peak percentage of reconnected flux occurs slightly later for the z -dependent η (black) than for the radially decaying η (blue), which agrees with the timing of reconnection inferred from the energy and current evolutions previously discussed. The peak percentage of reconnected flux for the z -dependent η is also slightly larger, but still less than the uniform η case. The reconnected flux for all cases (except $\eta = 0$) peaks within a few time-steps of each other, at approximately $t = 74$, even though they reach different maxima.

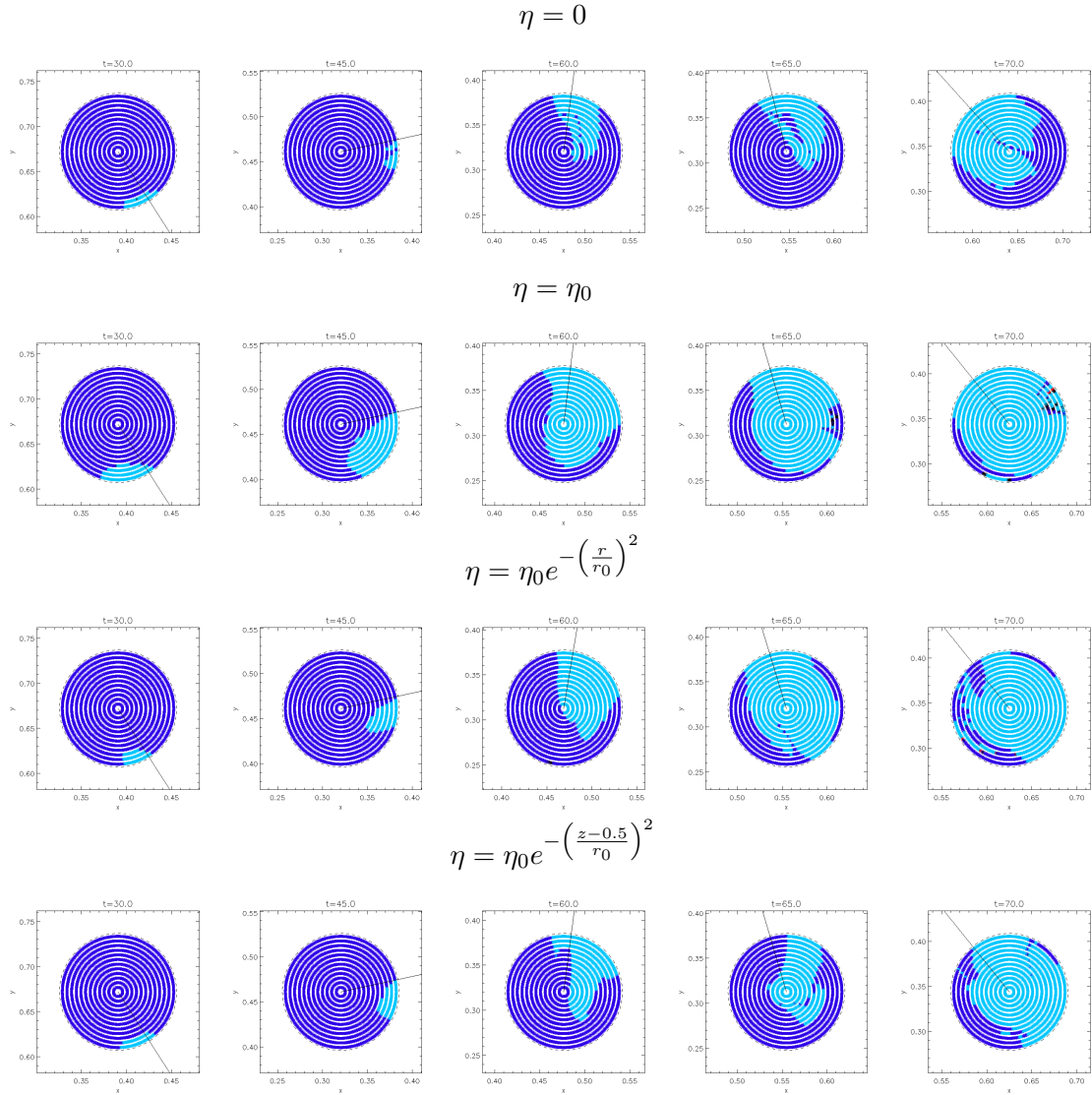


Figure 3.18: The field line connectivity of the right source on $z = 0$ at different times for simulations with resistivity forms: $\eta = 0$, uniform, radially dependent and z -dependent with $\eta_0 = 5 \times 10^{-5}$. The solid black line indicates the direction to the centre of rotation. Colours as in Figure 3.8.

Parallel Electric Field

The condition for reconnection to occur is that $\int E_{\parallel} dl \neq 0$ when evaluated on a magnetic field line passing through a localised region of (one sign of) E_{\parallel} (Schindler et al., 1988). The distribution of the parallel electric field is displayed in the plane $y = 0.5$ in Figure 3.20 at $t = 40$, for the three cases with a non-zero resistivity. The parallel electric field is equal to the parallel current multiplied by the resistivity value: ηj_{\parallel} . The uniform resistivity case in Figure 3.20a, shows the highest values of E_{\parallel} occurring above the footpoints, as well as along $x = 0.5$. This is expected

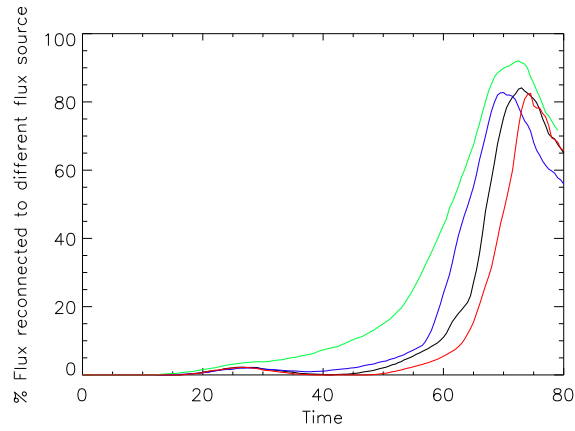


Figure 3.19: The percentage of flux reconnected from sources for simulations with resistivity forms: $\eta = 0$, uniform, radially dependent and z -dependent with $\eta_0 = 5 \times 10^{-5}$ shown in red, green, blue and black, respectively.

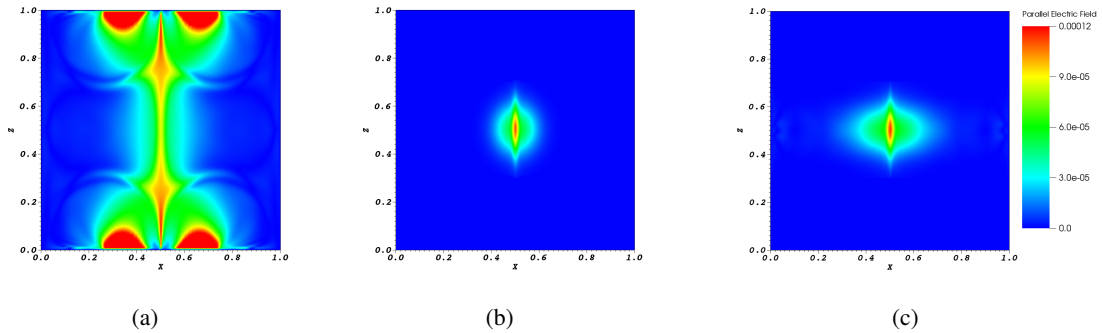


Figure 3.20: Contour plots of the parallel electric field (E_{\parallel}) in the domain at $y = 0.5$ at $t = 40$ for simulations with resistivity forms: (a) uniform, (b) radially dependent and (c) z -dependent with $\eta_0 = 5 \times 10^{-5}$.

as there is always a high current in all the cases at the footpoints and with a uniform resistivity throughout the domain, it is at this location that the highest value of E_{\parallel} occurs.

The two localised resistivity values create localised regions of E_{\parallel} around the centre of the domain in Figures 3.20b and 3.20c. The peak value occurs in the centre where the highest value of η and a relatively large current are located. Both cases have a very similar maximum value of E_{\parallel} (at the time shown) in the centre of the domain. The form of the high E_{\parallel} region is slightly broader for the resistivity that is only z -dependent, due to the η not being restricted in the $x - y$ plane, as it is for the radially dependent η shown in Figure 3.20b. Even though the resistivity is present across the plane in the z -dependent η case, it is only towards the centre of the domain that the E_{\parallel} occurs, as this is where the current forms from the twisted flux tubes. This distribution of E_{\parallel} is shown again in Figure 3.21, where a selection of field lines traced from the centre of the domain

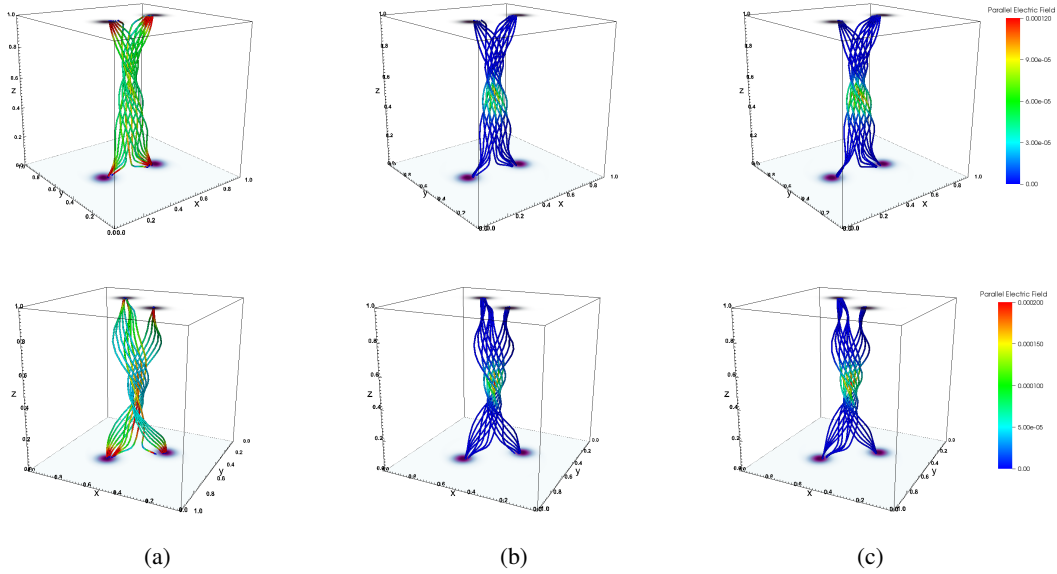


Figure 3.21: Field lines coloured with parallel electric field traced from the mid-plane at $t = 40$ (top row) and $t = 50$ (bottom row) for simulations with resistivity forms: (a) uniform, (b) radially dependent and (c) z -dependent with $\eta_0 = 5 \times 10^{-5}$.

are coloured according to the value of E_{\parallel} along them. As the field lines in images 3.21b and 3.21c enter the localised non-ideal region, high E_{\parallel} values are present along the field lines. At $t = 50$, the uniform resistivity case (in Figure 3.21a) shows high values of E_{\parallel} along longer sections of the field lines, suggesting reconnection may be occurring in a larger area.

Conservation of Energy

As described in Section 3.2.1, the conservation of energy can be considered by comparing the total rate of change of energy in the domain to the Poynting flux injected at $z = 0.0$ and $z = 1.0$ (see Equation 3.6). For the uniform η case, as we have previously discussed, these values align throughout the simulation and hence energy is conserved for $\eta_0 = 5 \times 10^{-5}$. In contrast, the $\eta = 0$ case should allow for an ideal evolution of the magnetic field, but numerical reconnection occurs and hence energy conservation is lost. We now consider the impact of a localised resistivity region on the energy conservation.

In Figure 3.22 we consider the energy conservation in the total domain and within subsections centred around the mid-plane. The subsections we consider (illustrated in Figure 3.22e) are $0.025 < z < 0.975$, $0.125 < z < 0.875$, $0.25 < z < 0.75$ and $0.375 < z < 0.625$, displayed in dark blue, light blue, green and orange, respectively. When we consider energy conservation in these subsections of the domain, the flux through the planes bounding the regions can be compared to the change in the total energy within each of these regions. Contrary to when we consider

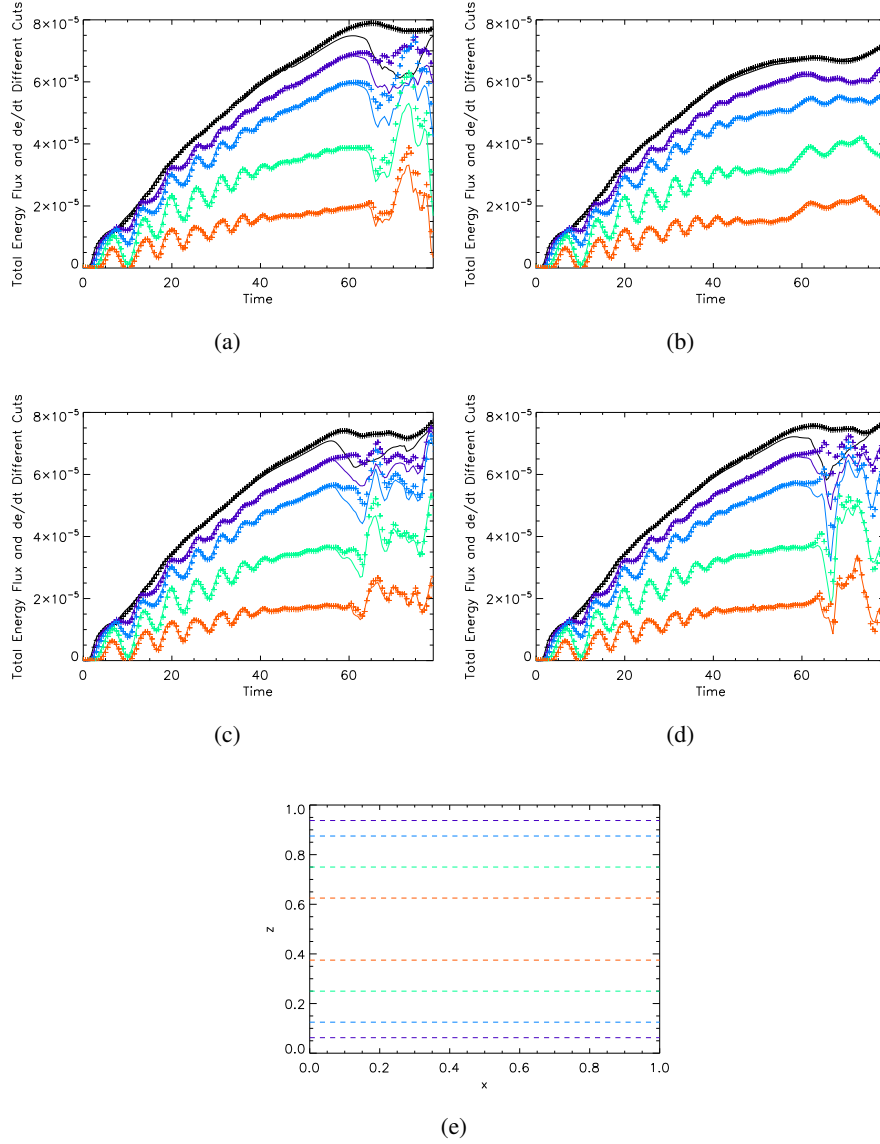


Figure 3.22: Total flux in/out of the domain at cuts $0.025 < z < 0.975$ (dark blue), $0.125 < z < 0.875$ (light blue), $0.25 < z < 0.75$ (green) and $0.375 < z < 0.625$ (orange) for simulations with resistivity forms: (a) $\eta = 0$, (b) uniform, (c) radially dependent and (d) z -dependent with $\eta_0 = 5 \times 10^{-5}$. The subsections of the domain we consider are plotted against height in (e).

the whole domain with boundaries on $z = 0$ and $z = 1$, when considering the flux into these smaller domains, there is a vertical velocity through the plane to take into account. Therefore, as described in Section 3.2.1, the kinetic energy flux and enthalpy flux must also be included as well as the Poynting flux in Equation 3.8. The crosses in Figure 3.22 now depict the total flux (Poynting flux + kinetic energy flux + enthalpy flux) into each of these regions, while the solid line shows the rate of change of total energy in the subregion (calculated from the output at each time-step of the code). In all four simulations, approximately 25% of the Poynting flux into the

whole domain (black crosses) reaches the central (orange) subsection.

At all cuts in the domain, the uniform η case shows energy conservation, as the flux and rate of change of energy align very well. In comparison, for the localised η cases in Figures 3.22c and Figures 3.22d, there is some loss of energy conservation in the whole domain (shown by the difference between the black crosses and the black solid line). However, in the smaller subsections towards the centre of the domain, where the resistivity is present, the energy conservation improves for the localised η cases. This suggests that the loss of energy conservation is occurring near the footpoints where η is zero. Both the cases with localised non-ideal regions, show better energy conservation in all subsections of the domain compared to the ideal case in Figure 3.22a. This is most evident in the smallest central section (orange), which shows substantially better conservation for both the localised η cases in (c) and (d), compared to the ideal $\eta = 0$ case in (a).

Finally, considering the domain as a whole, Figure 3.22 shows that the radially dependent η has a maximum loss of energy conservation of 13% (at $t \approx 62$), compared to $\approx 20\%$ for the z -dependent η (at $t \approx 66$). The z -dependent η , which had the higher maximum current value in Figure 3.15, therefore has the larger loss of energy conservation between the two cases. For both cases, the timing of the maximum loss in energy conservation also coincides with the timing of the initial maximum current (in Figure 3.15) and the peak percentage of reconnected flux in Figure 3.19. The earlier loss of energy conservation therefore supports the previous assertion that the radially dependent η evolves earlier than the z -dependent case. We also note that these comparisons are carried out with low resolution and therefore the percentages of energy loss are relatively high (see Chapter 4).

Summary and Discussion

In this section, we have compared and analysed the effect of localised resistivity regions in our simulations and compared them with the uniform η case, discussed in Section 3.2.1. We have described two localised forms of η (z -dependent and radially dependent) and considered how their distributions affect the evolution of the reconnecting flux tubes.

We have found that some numerical diffusion occurs for both the localised η cases, as there is no η at the footpoints and hence (when considering the full domain) energy conservation is lost. However, in the central region where the η is prescribed, the energy conservation is good for the vast majority of the length of the simulations. Looking at the energy evolution and field line connections, reconnection occurs sooner for the uniform η case. However, we also found that the case with the radially dependent η reconnected sooner than the case with the z -dependent η . This was due to the field near the x and y boundaries of the domain being diffused in the case with the z -dependent η and not for the case with the radially decreasing η . The current on the

boundaries, therefore, created a greater Lorentz force pushing the field lines towards the centre of the domain sooner for the radially dependent η case. This meant, in turn, that the values of the internal and kinetic energy produced were $\approx 5\%$ higher for the z -dependent η , compared to the radially dependent form, as more magnetic energy built up before reconnection occurred.

Overall, the localised η simulations had qualitatively similar reconnection timings and behaviour to the uniform case. The centre of the domain was the key location for reconnection in these simulations, as this is where the localised E_{\parallel} occurs. This also meant that the heating at the footpoints, observed in the uniform η case, does not occur in the simulations with η localised around the mid-plane.

There appears to be very little to choose between the two localised resistivity cases, however, we note that the evolution of the radially dependent η was shown to be influenced by the initial current formed on the boundaries. This could in turn impact future simulations where more intricate initial flux tube distributions could produce varying currents on the boundaries. Whereas, in the z -dependent case these would be diffused away and would not greatly impact any comparisons. Therefore, all future experiments in this thesis shall use the z -dependent form of localised resistivity.

Chapter 4

Resolution Comparison: Two Flux Tubes

So far, in Chapters 2 and 3, all of the simulations have been carried out with 128^3 resolution. In this Chapter, we will compare different resolutions to decide upon an optimal resolution to continue with. In general, higher resolution is preferable for numerical modelling, but a balance must be made between accurately modelling the plasma and minimising the computational time and power. With this in mind, we compare the flux tube relaxations (Section 4.1) and then rotations (Section 4.2) at four different resolutions: 128^3 , 256^3 , 512^3 and $512^2 \times 256$. The first three resolutions are increasing in all directions and the fourth resolution uses 256 for the vertical resolution and 512^2 in the horizontal plane, as this is where we expect the small scales to be created that require higher resolution. A summary of the resolutions used and the colours they shall be represented by in figures is shown in Table 4.1. The following comparisons have been carried out using the normalisation outlined in Section 2.2, with Neumann and Dirichlet boundary conditions and with an initial internal energy density (ϵ) of 0.01.

4.1 Comparing the Two Flux Tube Set-up at Higher Resolutions

Normalisation	Initial Conditions	
$B_0 = 100$ G	$\epsilon = 0.01$	Resolution: 128^3 , 256^3 , 512^3 , $512^2 \times 256$
$L_0 = 75$ Mm	$\rho = 0.1$	$\eta = 0$ (Ideal relaxation)
$n_e = 1 \times 10^{16}$ m ⁻³		viscosity= 0.001
		$0 < t_{relax} < 80$

Table 4.1: Resolution Comparisons: Colour scheme that will be used throughout this chapter.

128 ³	256 ³	512 ³	512 ² × 256
------------------	------------------	------------------	------------------------

As in Chapter 2, the two initially straight flux tubes are allowed to expand for 80 time units. A contour plot of the magnitude of the magnetic field in the mid-plane is displayed in Figure 4.1a for 512³. The variation of the field strength with x in the mid-plane (at $y = 0.5$) is shown for all four resolutions in Figure 4.1b (after the flux tubes have expanded). The magnetic field fills the majority of the plane, with the largest value in the centre. The field strength shows minimal alteration for different resolutions. Figure 4.2 displays a selection of 13 field lines traced from $z = 0.0$ at $t = 0$ and $t = 80$ and also shows minimal difference in the field structure for increased resolution.

One important difference to note is that increasing the resolution will decrease the numerical diffusivity of the code. This is important to be aware of when we begin driving the flux tubes and stressing the magnetic field in a non-ideal simulation. The order of the numerical diffusivity can be estimated by the expression given in Equation 3.4 and is dependent on the maximum Alfvén speed, the grid resolution $\Delta x = \frac{1}{\text{grid resolution}}$ and the typical length scale L . The greater the value of the grid resolution: 128, 256 or 512, the smaller the estimated numerical diffusivity.

In this initial set-up, the maximum magnetic field strength and therefore the largest Alfvén speed occurs on the z boundaries of the domain, where $V_a \approx 1/\sqrt{0.1} = 3.16$ is the maximum Alfvén speed. This gives an upper bound for the numerical diffusivity on the base of the order of 2×10^{-3} for resolution 128³ compared to 1.2×10^{-4} for 512³. Over the height of the box, the

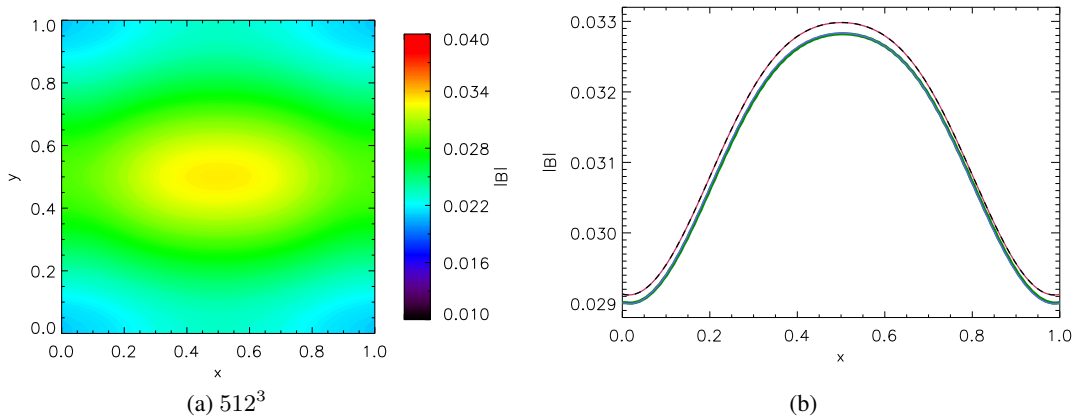


Figure 4.1: (a) Contour plot of magnetic field strength in the mid-plane $z = 0.5$ after relaxation for resolution 512³ and (b) the field strength at $y = 0.5$ in the mid-plane for 128³ 256³, 512³ and 512² × 256 in green, blue, black (dashed) and pink, respectively.

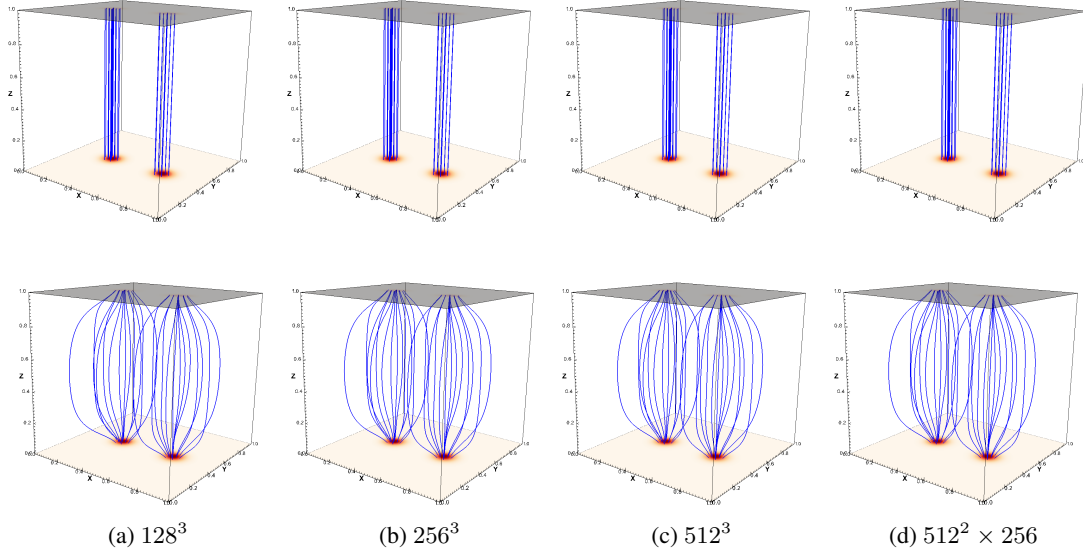


Figure 4.2: Magnetic field lines traced from the same 13 points from each source on the base within a radius 0.05 of the sources, initially (top row) and after 80 time units (bottom row), for resolutions: (a) 128^3 , (b) 256^3 , (c) 512^3 and (d) $512^2 \times 256$.

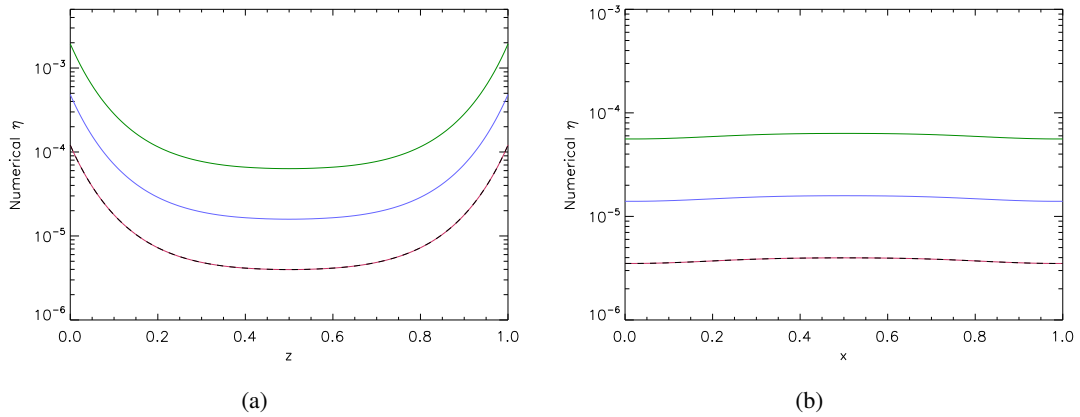


Figure 4.3: (a) The maximum numerical diffusivity calculated at each height and (b) the maximum numerical diffusivity calculated in the mid-plane at each x , for resolutions 128^3 , 256^3 , 512^3 and $512^2 \times 256$ after relaxation, shown in green, blue, black (dashed) and pink, respectively.

estimated numerical diffusivity varies with the field strength. Figure 4.3a shows the variation of the estimated maximum numerical diffusivity with height in the domain for increasing resolution. Towards the mid-plane the maximum field strength reduces, thereby reducing the Alfvén speed and the numerical diffusivity. As expected, the simulations show a similarly shaped distribution with height as they have a similar magnetic field distribution as shown in Figures 4.1 and 4.2. However, the maximum numerical diffusivity reduces by almost an order of magnitude with each increase of resolution. For resistive experiments, the value of the resistivity (η) in Lare3D should

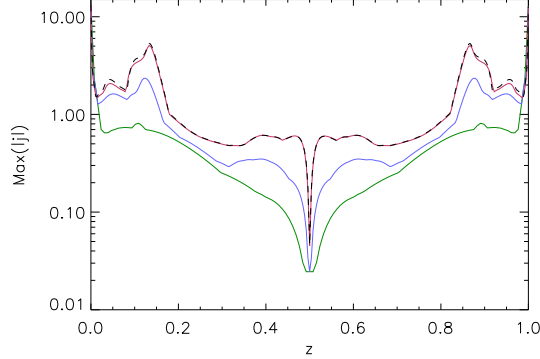


Figure 4.4: Maximum current density for each height in the domain plotted against z (height) after relaxation for resolutions 128^3 , 256^3 , 512^3 and $512^2 \times 256$ shown in green, blue, black (dashed) and pink, respectively.

be chosen to be greater than the numerical resistivity to ensure conservation of energy. However, this is a very simplistic estimate of the numerical resistivity and, as discussed in Section 3.2.1, the formation of a current layer and the subsequent reduction in the length scales created in the domain will also increase the numerical resistivity.

In Figure 4.3, the 512^3 simulation shown in black (dashed) and the $512^2 \times 256$ in pink have identical estimated numerical resistivity as they have the same resolution of 512 in the horizontal plane and only a difference in resolution vertically. The numerical resistivity is calculated using a value of $L = 0.1$ and the grid resolution Δx in the horizontal plane, to consider the resolution across the width of current layers that may form when the magnetic field is twisted and stressed.

When we go on to twist the flux tubes, the mid-plane will be an important site for magnetic field interactions and therefore for current to build up, as the set up is vertically symmetric. With this in mind, we have also examined the behaviour of the maximum numerical diffusivity as a function of x in the mid-plane, as presented in Figure 4.3b. This shows that the difference in magnitude of the numerical diffusivity between the different resolutions is fairly constant across the plane. There is also minimal variation in the numerical diffusivity with x , due to the minimal variation of the magnetic field in this cut for all four resolutions.

Figure 4.4 shows the maximum magnitude of current density with height (z) in the domain after the flux tubes have expanded. The maximum current has a minimum in the mid-plane for all resolutions and increases with resolution at all heights. As discussed in Section 2.1.4, the maximum current occurs on the z boundaries of the domain and there is only a small difference in the maximum current between the different resolution simulations. Between $0.2 < z < 0.8$, in Figure 4.4, the maximum current formed during the relaxations in the domain is less than 1 for all resolutions and can still be considered small. Figure 4.5 displays contour plots of the current

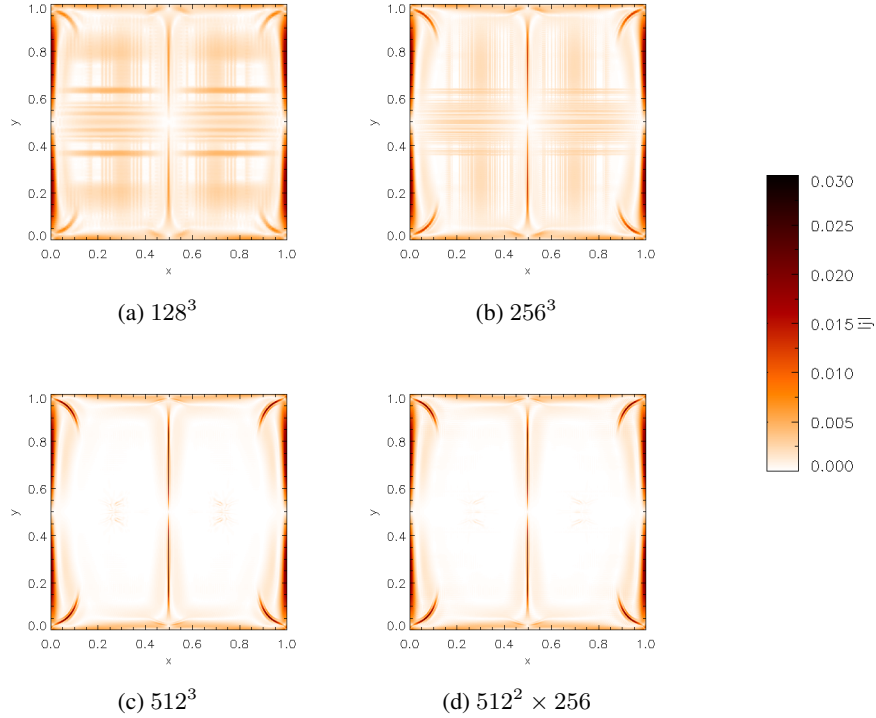


Figure 4.5: Contours of the current magnitude in the mid-plane after relaxation for resolutions (a) 128^3 , (b) 256^3 , (c) 512^3 and (d) $512^2 \times 256$.

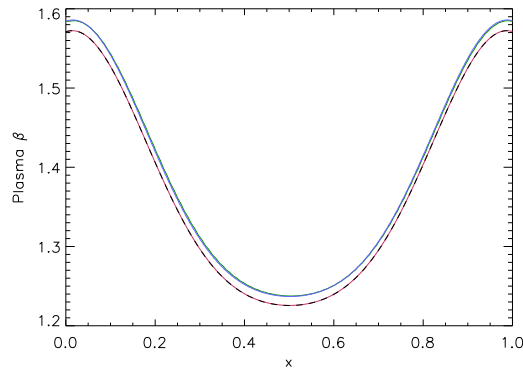


Figure 4.6: Plasma β as a function of x at $z = 0.5$ and $y = 0.5$ after relaxation for resolutions 128^3 , 256^3 , 512^3 and $512^2 \times 256$ resolutions shown in green, blue, black (dashed) and pink, respectively.

magnitude in the mid-plane and shows a very similar spatial current distribution for the different resolutions. The current increases slightly for higher resolutions but the diffuse background distribution of current (away from $x = 0.5$) seen for 128^3 and 256^3 has reduced greatly for 512^3 and $512^2 \times 256$, where the current seems confined to the boundaries and $x = 0.5$, where the expanding

flux tubes meet.

Finally, we look at the plasma β for the different resolutions. The plasma β is calculated numerically and plotted in Figure 4.6 at $y = 0.5$ in the mid-plane. As the gas pressure is constant, the plasma β distribution depends entirely on the magnetic field distribution. Figure 4.1 shows the magnetic field distribution at different resolutions to be almost identical and, as expected, this is also the case for the plasma β . The plasma β is of order 1 in the mid-plane and is greatest at the edge of the domain, where the magnetic field is weakest, and lowest in the centre, where the field is strongest.

4.2 Comparing Rotation of Two Flux Tubes at Higher Resolutions

Normalisation	Initial Conditions	
$B_0 = 100 \text{ G}$	$\epsilon = 0.01$	Resolution: $128^3, 256^3, 512^3, 512^2 \times 256$
$L_0 = 75 \text{ Mm}$	$\rho = 0.1$	$\eta = \eta_0 e^{-\left(\frac{z-0.5}{r_0}\right)^2}$
$n_e = 1 \times 10^{16} \text{ m}^{-3}$		$\eta_0 = 10^{-4}$
		$0 < t < 85$

In Section 4.1 we compared the set-up of the two flux tubes at four different resolutions. We now go on to apply the rotational driving velocity, described in Chapter 3, to the simulations in order to see the impact of the resolution. For these simulations we use a resistivity (η) of the form

$$\eta = \eta_0 e^{-\left(\frac{z-0.5}{r_0}\right)^2},$$

where $\eta_0 = 10^{-4}$ and $r_0 = 0.1$, as in Section 3.2.2.

To begin, for each of the resolutions, we consider the conservation of energy in the whole domain and within subsections of the domain. For the entire domain, the energy entering the simulations simply reduces to the Poynting flux calculated on $z = 0.0$ and $z = 1.0$ (see Section 3.2.1). If energy is conserved, this should align with the rate of change of total energy in the domain. In panels (a) to (d) of Figure 4.7, the Poynting flux (black crosses) and rate of change of total energy (black solid line) in the whole domain is shown for the different resolution simulations. As the resolution increases the rate of change of total energy in the domain and the Poynting flux injected into the domain are closer together, implying better energy conservation. Energy conservation is lost when the numerical resistivity becomes larger than the prescribed value of resistivity and numerical diffusion occurs. The higher the resolution, the lower the numerical resistivity value and therefore as the resolution increases the energy conservation improves.

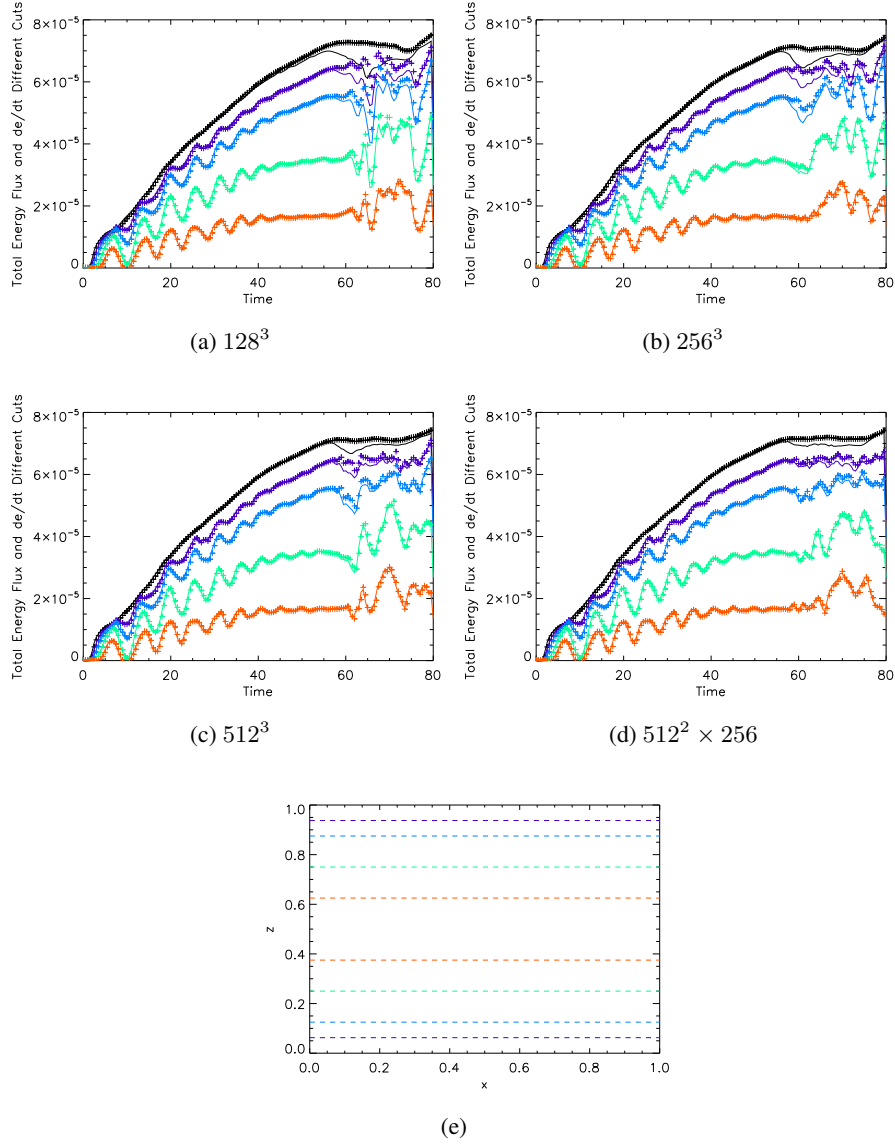


Figure 4.7: Total flux in/out of the domain at cuts $0.0 < z < 1.0$, $0.025 < z < 0.975$, $0.125 < z < 0.875$, $0.25 < z < 0.75$ and $0.375 < z < 0.625$ shown in black, purple, blue, green and orange, respectively, for simulations with resolutions: (a) 128^3 , (b) 256^3 , (c) 512^3 and (d) $512^2 \times 256$.

In Figure 4.7d (for resolution $512^2 \times 256$) the rate of change of energy in the domain remains very close to the Poynting flux injected into the domain until $t = 55$. The higher resolution case (512^3) in Figure 4.7c is also shown to lose energy conservation at a similar time and both cases show a loss of energy conservation of $\approx 8\%$. This suggests the reduction in resolution in the z direction has not affected the energy conservation. This confirms that the small scales that are being created and causing the loss of energy conservation are predominantly in the $x - y$ plane and a reduction in resolution can be applied in the z direction without increasing the error due to

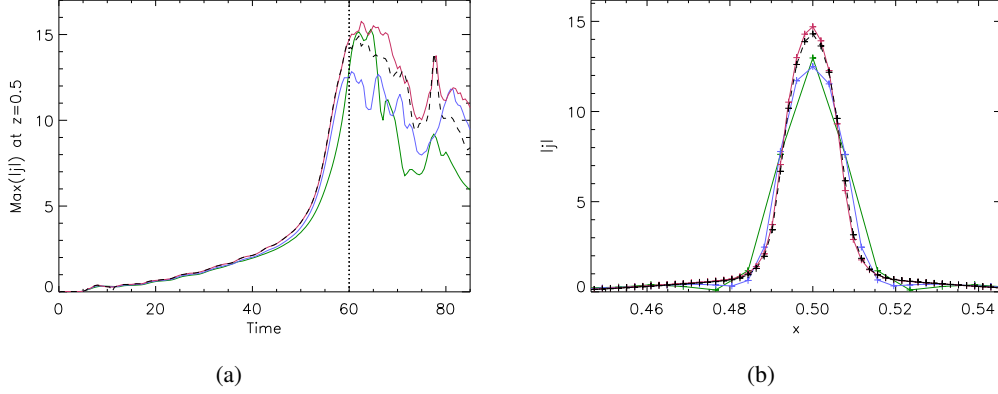


Figure 4.8: Maximum magnitude of the current density (a) in the mid-plane and (b) at $y = 0.5$ and $z = 0.5$ between $0.45 < x < 0.55$ at $t = 60$, for resolutions 128^3 , 256^3 , 512^3 and $512^2 \times 256$ shown in green, blue, black and pink, respectively.

loss of energy conservation.

We can also consider where in the domain the loss of energy conservation is occurring, by calculating the total rate of change of energy in subsections of the domain and the total energy flux entering these subsections. We consider subsections of the domain centred around the mid-plane with reducing height and are between $0.025 < z < 0.975$ (purple), $0.125 < z < 0.875$ (blue), $0.25 < z < 0.75$ (green) and $0.375 < z < 0.625$ (orange), as represented in Figure 4.7e. We consider the flux entering and leaving these subsections of the domain, but as the planes bordering the subsections are no longer on the boundary, there is a vertical velocity present and the flux can be positive or negative and is made up of the Poynting flux, kinetic energy flux and enthalpy flux through each of the boundaries of our subsections (see Equation 3.8). The total flux (crosses) and the rate of change of total energy (solid line) is shown for each of these subsections of the domain in the corresponding colour, for all the resolutions in Figure 4.7.

In the central section between $0.375 < z < 0.625$ (orange), the rate of change of energy (solid line) aligns with the flux in/out of the domain for all resolutions, suggesting that in this region energy is always conserved. However, as we extend the area of the domain we are considering, the impact of the higher resolution becomes more evident. In the section $0.25 < z < 0.75$ (green) the lowest resolution cases (128^3 and 256^3) indicate a loss of energy conservation around $t = 60$. However for the two cases with 512 grid-points in the horizontal plane energy conservation is much better in this section. Therefore the increased resolution cases have larger areas of the domain with total energy conservation.

The maximum current evolution with time in the mid-plane is shown in Figure 4.8a for 128^3 , 256^3 , 512^3 and $512^2 \times 256$ resolutions in green, blue, black (dashed) and pink, respectively. Note

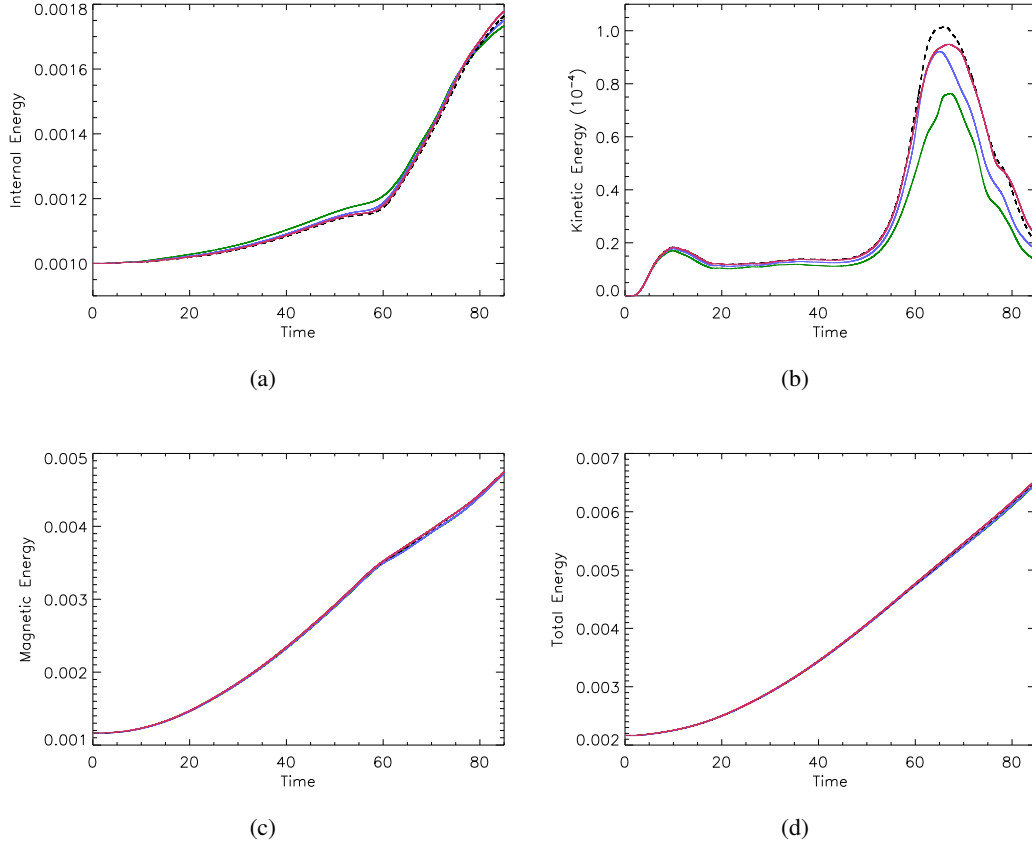


Figure 4.9: (a) Kinetic, (b) internal, (c) magnetic and (d) total volume integrated energies for simulations with resolutions 128^3 , 256^3 , 512^3 and $512^2 \times 256$ shown in green, blue, black (dashed) and pink, respectively.

that the current in the mid-plane is taken as a point of comparison to discuss the difference in the time evolution and the difference between resolutions, but that this is not necessarily the point in the domain with the largest current.

After $t = 40$, the current begins to increase faster for higher resolutions. However, the 512^3 (black) and the $512^2 \times 256$ (pink) cases have a very similar current evolution in the mid-plane, until approximately $t = 58$. At this point, the two values of maximum current begin to separate and the $512^2 \times 256$ case reaches a slightly larger value in the mid-plane. This suggests that the reduced vertical resolution does have some impact on the evolution, but this difference is very small. In Figure 4.8b the current at $(y, z) = (0.5, 0.5)$ is displayed between $0.45 < x < 0.55$, showing the peak in current that is forming along $x = 0.5$ in the plane. The grid points are indicated (plus signs) to show how the current layer is resolved at each resolution. The current layer for the higher resolutions appears smoother and increases more gradually. Once again the 512^3 and the $512^2 \times 256$ appear to behave very similarly, only varying slightly towards the peak

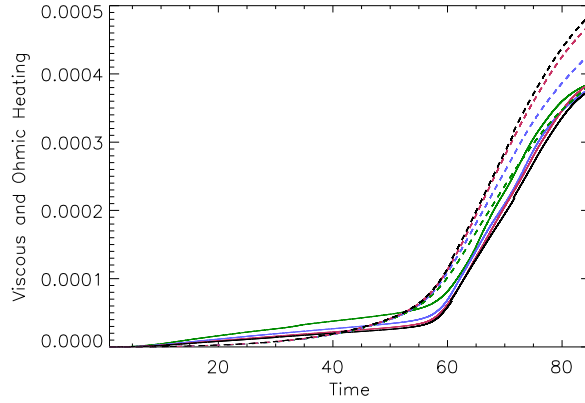


Figure 4.10: The Ohmic (dashed) and viscous (solid) heating for resolutions 128^3 , 256^3 , 512^3 and $512^2 \times 256$ shown in green, blue, black and pink, respectively.

value at the centre.

The evolution of the energy in the domain is shown in Figure 4.9 for the different resolutions. The energy behaviour is qualitatively very similar, as we would expect from simulations with the same initial conditions. The peak values of kinetic energy increase by approximately 40% from resolutions 128^3 to 512^3 . For all cases, the time of the peak kinetic energy occurs between 65 and 67. As with the current evolution in Figure 4.8, the 512^3 and $512^2 \times 256$ behave almost identically until ≈ 58 when the 512^3 kinetic energy continues to increase. The internal energy evolution is relatively similar for all cases, except for a slightly larger value for 128^3 in the early stages of the simulation. At $t = 80$, the internal energies differ by approximately 2% of the maximum value, with the largest value for the higher resolutions.

Similarly, there is a small difference in the peak value of the integrated Ohmic heating occurring by the end of the simulations, shown by the dashed lines in Figure 4.10. The largest value of Ohmic heating occurs for 512^3 and is then less for lower resolution cases. The viscous heating (solid lines) has a slightly larger value for the lowest resolution 128^3 earlier in the simulation, but in general the evolution is comparable for all the simulations.

In Figure 4.11, the connectivity of the source that is located at $(x = 0.7, y = 0.5, z = 0.0)$ at the start of the simulations (right-hand source) is displayed. A large number of points (≈ 5800) within the source are traced (within a radius of 0.065) and are coloured dark blue if the traced field line is still connected to its original source at $z = 1.0$ and light blue if it has changed connectivity to the opposite source. Comparing the field line connectivity in the source allows us to estimate the timing and the amount reconnection occurring in the different resolution simulations. The field lines of the lowest resolution simulation (128^3) are shown to change connectivity first, by $t = 30$, in Figure 4.11. This suggests this early change in connectivity is a numerical effect due to the

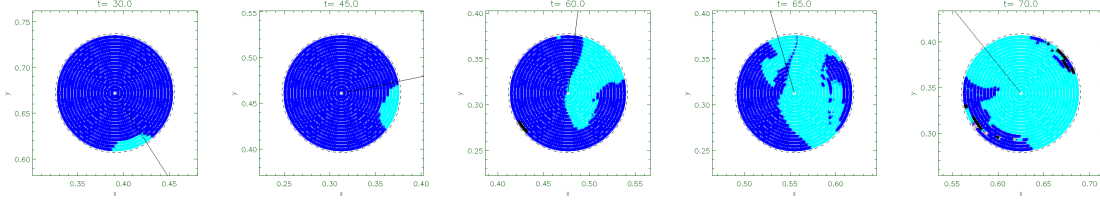
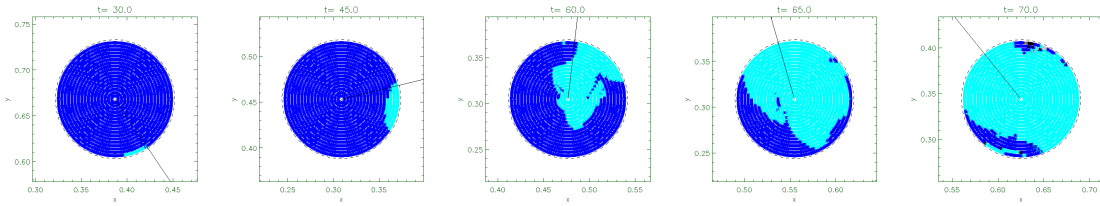
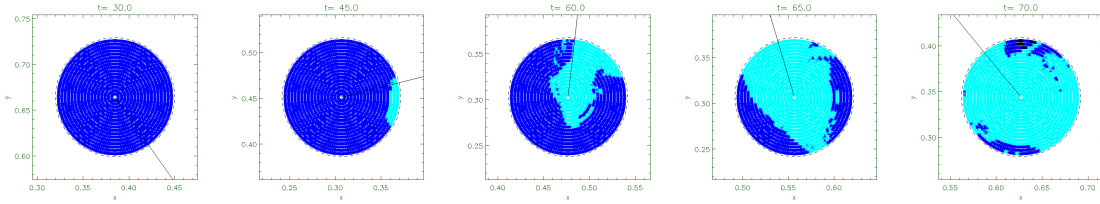
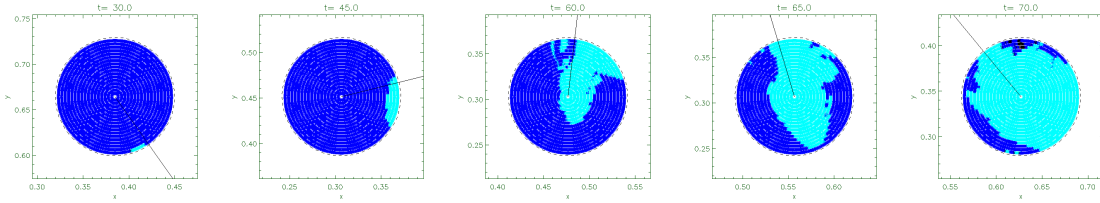
(a) 128^3 (b) 256^3 (c) 512^3 (d) $512^2 \times 256$ 

Figure 4.11: The field line connectivity of the right-hand source (at $t = 0$) on $z = 0$ at different times. The solid black line indicates the direction to the centre of rotation. Dark blue signifies field lines at the original connection, light blue shows field lines that have changed connectivity to the other flux source on the top boundary and black are field lines that are connected to the top boundary but not associated with either source by our definition (i.e are not within $2r_1 = 0.13$) of a source.

low resolution. Figure 4.12 shows the percentage of field lines reconnected to a different source at $z = 1.0$, averaged over both sources on the base. The initial early rise in connectivity for 128^3 is also seen in green in Figure 4.12. In comparison, the higher resolutions do not begin to increase greatly until $t = 35$. After $t = 60$, the increase in the percentage of reconnected flux differs, but only slightly, for the various resolutions, before reaching a very similar maximum of $\approx 90\%$.

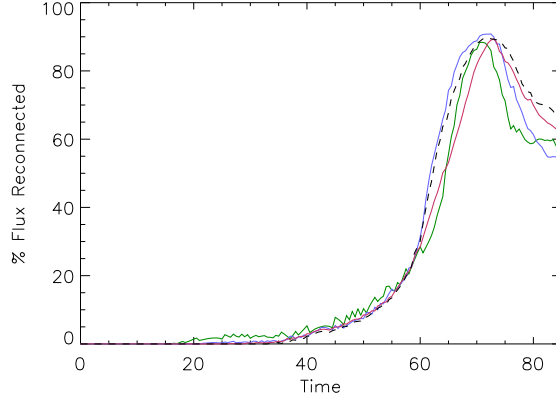


Figure 4.12: The average percentage of flux that has changed connectivity for simulations with resolutions 128^3 , 256^3 , 512^3 and $512^2 \times 256$ shown in green, blue, black (dashed) and pink, respectively.

The connectivity of the two simulations with the same horizontal resolution (512^3 and $512^2 \times 256$) also has some differences, with the percentage of reconnected field lines increasing earlier for the higher resolution (512^3) case. However, the two peaks have similar values and the maximum of both occurs at approximately $t = 74$. Indeed, there is a similar proportion of the source shown to be reconnected at $t = 70$ in Figure 4.11 for 512^3 and $512^2 \times 256$.

Summary

Overall, higher resolution results in better energy conservation, although there is still a slight loss of energy conservation around the footpoints. However, the improvement in energy conservation is not greatly diminished by reducing the vertical resolution as shown by the comparison between 256×512^2 and 512^3 resolution cases. The current layer built up in the horizontal plane is also equally well resolved for the 256×512^2 and 512^3 cases, as they share the same high horizontal resolution.

The plasma energy evolution of the simulations is altered slightly by the resolution. This is seen most clearly in the kinetic energy graph (Figure 4.9b). However, in terms of the total energy of the simulation, these differences are minimal (of the order of a few percent of the maximum values). The timing of the rise and maxima of the internal energy are also very similar for all the cases, particularly for 256×512^2 and 512^3 resolutions, with a difference of less than 5% of the maximum value. The percentage of field lines changing connectivity reached an approximate maximum value of 90% for all resolutions, although the timing of the increase differs slightly.

These comparisons suggest that the improvements to the energy conservation can be achieved

by increasing the resolution to 256×512^2 . It has also been shown that the plasma and magnetic field evolution of the 256×512^2 case is generally comparable with the most accurate high resolution 512^3 simulation, but would require less computational resources. From these comparisons we will therefore continue to use the 256×512^2 resolution for further comparisons of rotating flux tubes in the following chapters.

Chapter 5

Extended Loop Length Comparison

All the experiments so far have been carried out in a unit cube domain. Therefore, the loops had an initial length of 1 in normalised units (the distance between the upper and lower boundary) or 75 Mm in real units, using the normalization outlined in Chapter 2. However, observations of coronal loop structures, summarised in Reale (2010), show varied and complex loop structures with lengths that span two orders of magnitude. Hence, in this chapter we briefly consider the impact of increasing the length of the modelled flux tubes on the evolution of the experiment.

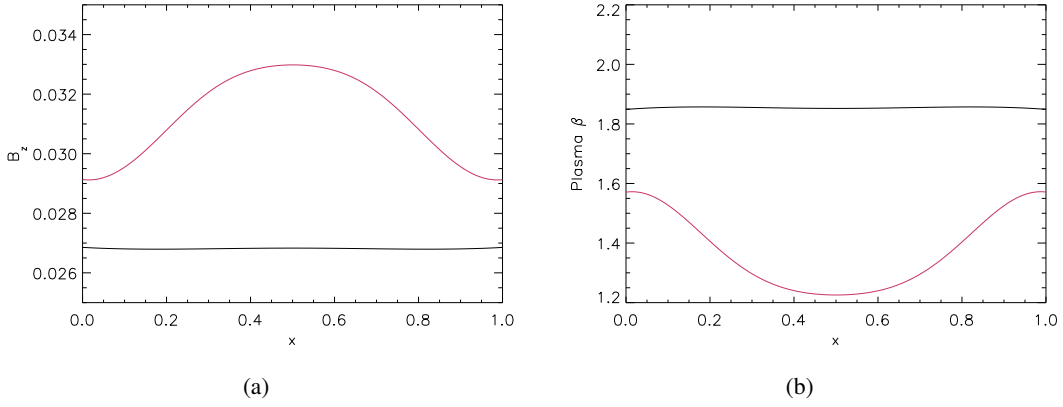
5.1 Comparing the Relaxation of Flux Tubes of Increased Length

Normalisation	Initial Conditions	
$B_0 = 100 \text{ G}$	$\epsilon = 0.01$	Resolution: $512^2 \times 256$ and 512^3
$L_0 = 75 \text{ Mm}$	$\rho = 0.1$	$\eta = 0$ (Ideal relaxation)
$n_e = 1 \times 10^{16} \text{ m}^{-3}$		viscosity = 0.001
		$0 < t_{relax} < 80$

We take the same relaxation approach for creating the initial flux tubes as in the original two source simulation described in Chapters 3 and 4, while doubling the height of the numerical box, giving a domain of $0 < x < 1$, $0 < y < 1$ and $0 < z < 2$. This produces an initial loop of length 2 (150 Mm in real units). The extended domain set-up will be referred to as case (ii) in the following discussions. We will compare the results to the original two source experiment described in Chapter 4 (with resolution $512^2 \times 256$) and refer to it as case (i) (shown in red for comparison, see Table 5.1). For case (ii) we also increase the number of grid points in the vertical direction from 256 to 512 to maintain the same resolution as case (i).

Table 5.1: Domain Height Comparison: Parameters and colour scheme that will be used throughout this chapter.

(i) $z_{max} = 1.0$ Resolution: $512^2 \times 256$	(ii) $z_{max} = 2.0$ Resolution: 512^3
--	--

Figure 5.1: (a) B_z and (b) plasma β in the mid-plane at $y = 0.5$ for runs with for (i) $z_{max} = 1.0$ (red) and (ii) $z_{max} = 2.0$ (black).

The radius of the loop source is specified on the boundary ($r_1 = 0.065$) but the loops are allowed to expand to fill the domain elsewhere, as described in Chapter 2. When the loop length is increased, the initially straight flux tubes expand further and an almost uniform magnetic field is observed in the mid-plane at $z = 1.0$. This is depicted by the plot of B_z in the mid-plane at $y = 0.5$ for case (ii) shown in black in Figure 5.1a. The B_z component in the mid-plane for case (i) ($z_{max} = 1.0$) is over-plotted in red. The variation in field strength and corresponding variation in the initial plasma β has been greatly reduced by doubling the domain height. In addition to being more uniform, the vertical field strength is also approximately 10% smaller in the mid-plane than for case (i), due to the flux tube expansion. The reduction in field strength for case (ii) also results in a corresponding increase in the plasma β in the mid-plane, to ≈ 1.85 , shown in Figure 5.1b.

5.2 Comparing the Rotation of Flux Tubes of Increased Length

Normalisation	Initial Conditions	
$B_0 = 100$ G	$\epsilon = 0.01$	Resolution: $512^2 \times 256$ and 512^3
$L_0 = 75$ Mm	$\rho = 0.1$	(i) $\eta = \eta_0 e^{-\left(\frac{z-0.5}{r_0}\right)^2}$, (ii) $\eta = \eta_0 e^{-\left(\frac{z-1.0}{2r_0}\right)^2}$
$n_e = 1 \times 10^{16}$ m $^{-3}$		$\eta_0 = 10^{-4}$
		$0 < t < 80$

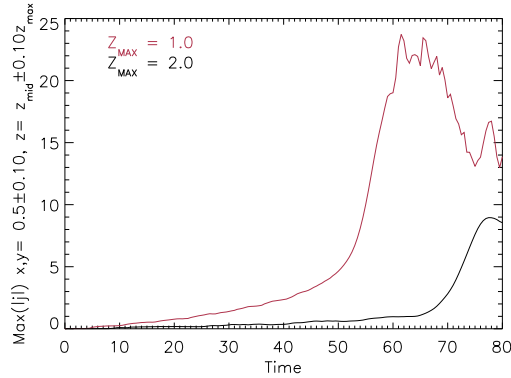


Figure 5.2: The maximum current density magnitude in the central 20% of the domain for case (i) with $z_{max} = 1.0$ (red) and case (ii) for $z_{max} = 2.0$ (black).

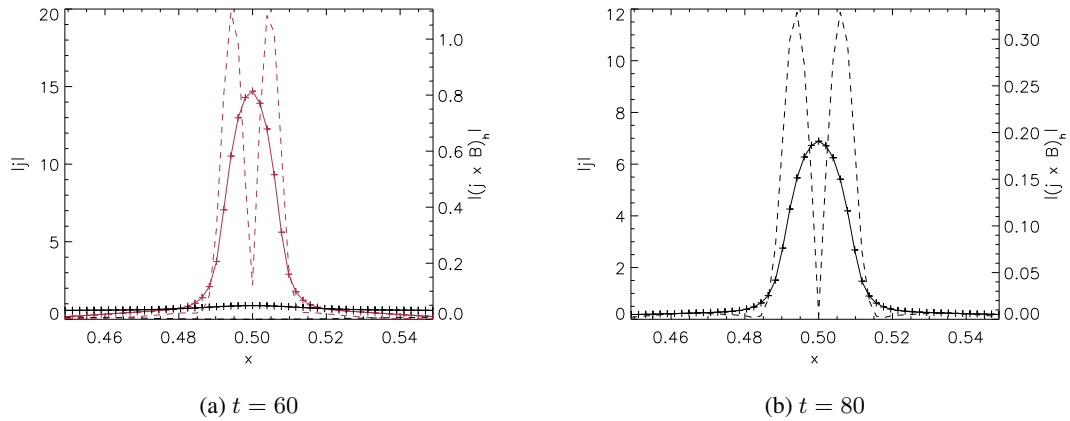


Figure 5.3: The magnitude of the current density (crosses) and the magnitude of the horizontal Lorentz force, $|\mathbf{j} \times \mathbf{B}|_h$ (dashed) in the mid-plane between $0.45 < x < 0.55$ is plotted for case (i) with $z_{max} = 1.0$ (red) and case (ii) $z_{max} = 2.0$ (black) at (a) $t = 60$ and for case (ii) only at (b) $t = 80$.

The flux tubes in the extended domain are driven (for 80 normalised time units) with the same rotational velocity described in Chapter 3. The same form of z -dependent resistivity is applied, with a maximum at the mid-plane, but with double the standard deviation (i.e. $2r_0$), so that the localised non-ideal region covers the same proportion of the domain. For the extended flux tubes it takes longer for small scales in the magnetic field to build up in the mid-plane and hence, as shown in Figure 5.2, the electric current values are smaller. The evolution of the maximum current in the central 20% of the domain (shown in Figure 5.2) indicates that the magnitude of the current density in case (ii) increases sharply after $t = 65$, almost 15 time units after case (i), and reaches a peak value of less than half that of case (i).

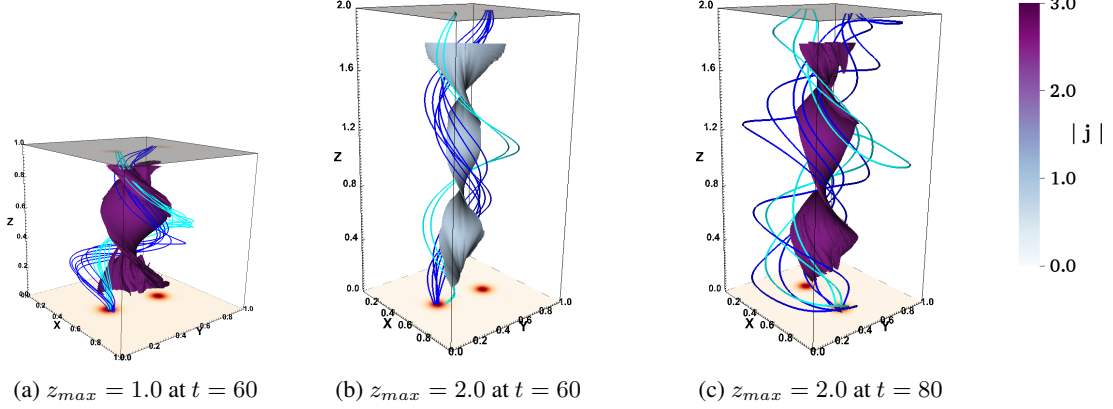


Figure 5.4: A selection of field lines, coloured by their connectivity, traced from original right source on $z = 0$. Shown in (a) at $t = 60$ for case (i) $z_{max} = 1.0$, in (b) at $t = 60$ for case (ii) $z_{max} = 2.0$, and in (c) at $t = 80$ for case (ii) $z_{max} = 2.0$. Over-plotted are the isosurfaces of current density of magnitude 2.5 (in (a) and (c)) and 0.8 in (b), shown within the central region ($0.2 < x, y < 0.8$ and $0.2z_{max} < z < 0.8z_{max}$) of the domain.

The twisted field lines create a magnetic tension force (Lorentz force) that acts to bring oppositely directed field towards the centre of the domain. This creates small scales in the magnetic field between the flux tubes leading to the formation of a current layer. The magnitude of the horizontal component of the Lorentz force (dashed line) is shown in the mid-plane at $t = 60$ in Figure 5.3a for cases (i) and (ii) in red and black, respectively. The horizontal component of the Lorentz force is negligible in case (ii) at this time. By $t = 80$ (in Figure 5.3b) the magnitude of the horizontal component of the Lorentz force for case (ii) has increased substantially to a peak value of 0.33 in normalised units, but this is still less than a third of the peak value shown at $t = 60$ for case (i).

The current density (pluses) that is formed due to the inwards Lorentz force is also plotted in Figure 5.3 in the mid-plane at $y = 0.5$ for the two cases. By $t = 80$, when the Lorentz force and current layer have become more prominent for case (ii), the magnitude of the current density is still less than half the peak value seen in case (i) at its maximum at $t = 60$. Isosurfaces of the current density for cases (i) and (ii) are shown in Figure 5.4. In Figure 5.4a an isosurface of $|j| = 2.5$ for case (i) at $t = 60$ shows the twisted current layer formed throughout the height of the domain. Due to the weaker current present in case (ii) at this time, an isosurface of $|j| = 0.8$ is shown in Figure 5.4b for comparison. The same total twist ($\approx 3\pi$) has been imparted in both cases but in case (ii) there is half the amount of twist per unit length than in case (i). Hence, it is not until later in case (ii) that the Lorentz force increases, allowing the current magnitude to build up substantially. At a later time of $t = 80$ (and total twist of $\approx 4\pi$) an isosurface of $|j| = 2.5$ is shown in Figure 5.4c, displaying an increasingly twisted central current layer for case (ii).

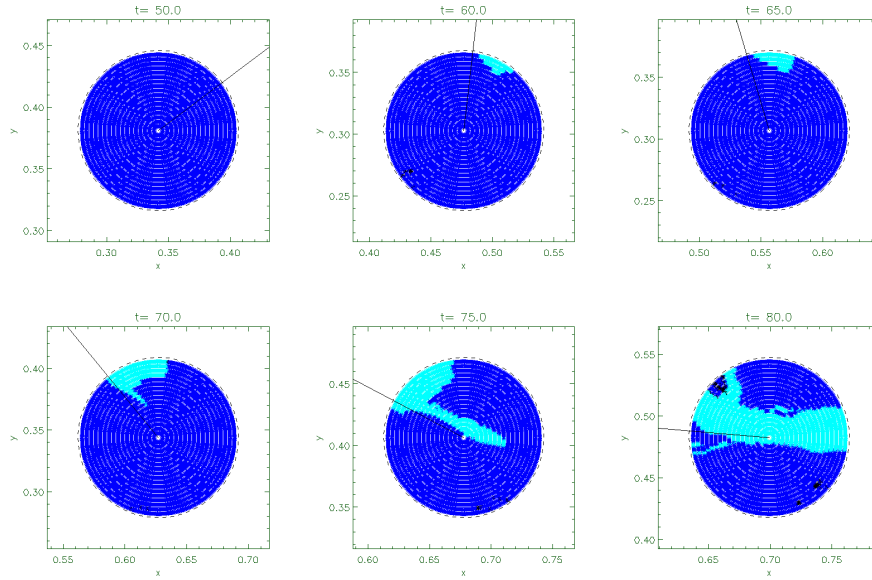


Figure 5.5: The field line connectivity of the source initially at $(x = 0.7, y = 0.5)$ on $z = 0.0$ at $t = 50, 60, 65, 70, 75, 80$ for case (ii) with $z_{max} = 2.0$. The solid black line indicates the direction to the centre of rotation. Dark blue signifies field lines at the original connection and light blue indicates that the field lines that are now connected to the opposite source on the upper boundary. Black represents field lines are not assigned to a source on the upper boundary.

The delay in the build up of the electric current density in the domain also means that reconnection of the field lines is delayed. The evolution of the field line connectivity of the footprint originally at $(0.7, 0.5)$ on the base is displayed in Figure 5.5 for case (ii) (these can be compared to the footprint graphs in Figure 4.11 for case (i)). The entire source remains at its original connection until after $t = 50$ and then gradually some field lines begin to change connectivity. In Figure 5.5, the newly reconnected field lines begin to appear at the front of the source (in terms of the direction of rotation), as seen for case (i). However, the reconnected field lines then appear across the centre of the source, in contrast to the previous simulations (shown in Figure 4.11), where the newly reconnected field lines were more concentrated in one region of the source.

A selection of field lines at $t = 60$ and $t = 80$ traced from the base of the domain are shown in Figure 5.4 to give an indication of the structure of the magnetic field and are coloured light blue and dark blue according to the connectivities described in Figure 5.5. At $t = 60$, the field lines in case (ii) appear much straighter than in case (i), as we would expect from the extended loop length.

The mean percentage of flux (from both sources on the lower boundary) that has changed connectivity to the opposite source on the upper boundary is plotted in light blue for case (i) (crosses) and case (ii) (solid line) in Figure 5.6. This shows the field lines begin to change connectivity almost 20 time units later for case (ii) than in the case where $z_{max} = 1.0$. Both cases also show a

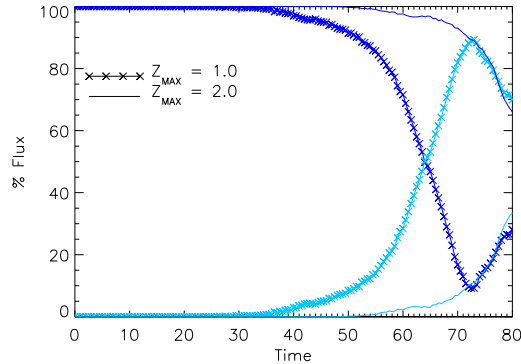


Figure 5.6: Total percentage of flux that has changed connectivity (light blue) and percentage of flux connected to original source (dark blue) for case (i) with $z_{max} = 1.0$ (crosses) and case (ii) for $z_{max} = 2.0$ (solid).

two stage connectivity evolution: an initial slow increase in the percentage of flux changing connectivity, followed by a sharp increase, which coincides with the sudden growth of the maximum current density shown in Figure 5.2.

When the percentage of flux connected to the opposite source begins to increase sharply in Figure 5.6 (after $t = 55$ and $t = 70$ for cases (i) and (ii), respectively), there is a corresponding increase in the viscous heating shown in Figure 5.7 for both cases. This is due to the field lines reconnecting and causing a fast plasma outflow from the ends of the current layer. In Figure 5.7 the integrated viscous and Ohmic heating in the domain are displayed per unit volume. The Ohmic heating for case (ii) (black, dashed line) gradually increases over the simulation but with much smaller values than for case (i) (red), due to the smaller current density. The total Ohmic heating in case (ii) by $t = 80$ is a seventh of the total for case (i).

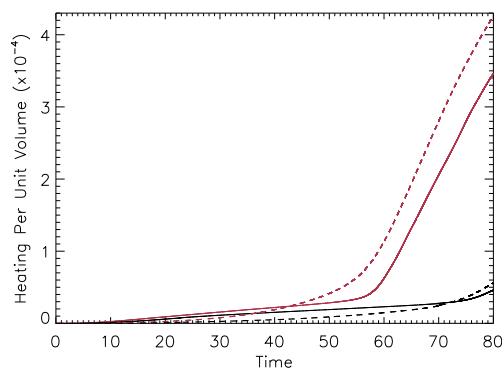


Figure 5.7: The Ohmic (dashed) and viscous (solid) heating per unit volume for cases (i) $z_{max} = 1.0$ (red) and (ii) $z_{max} = 0.2$ (black).

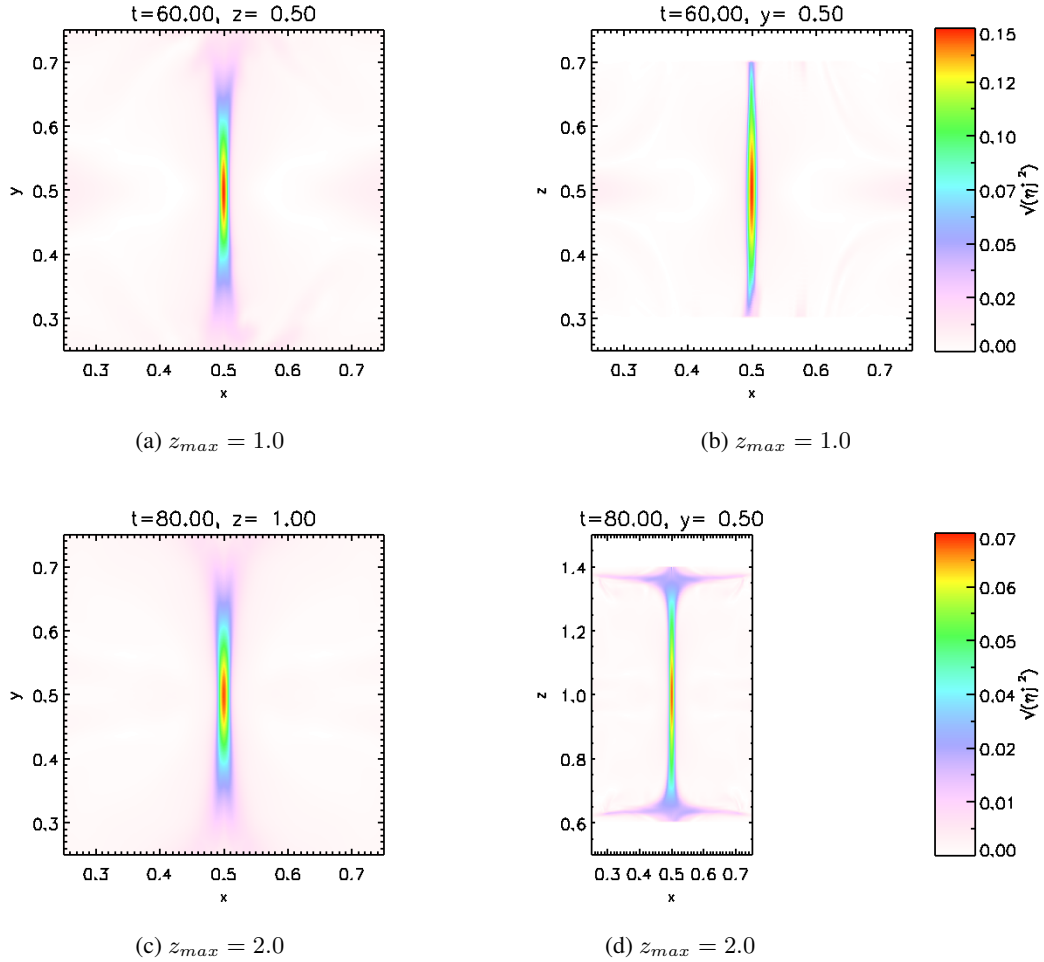


Figure 5.8: Contours plots of $\sqrt{\eta j^2}$ in the central 50% of the domain, shown for case (i) at $t = 60$ (a) in the mid-plane and (b) at $y = 0.5$ and for case (ii) at $t = 80$ (c) in the mid-plane and (d) at $y = 0.5$.

Despite these different values, a similar distribution of Ohmic heating is observed in Figure 5.8. The contours in the mid-plane and the plane $y = 0.5$, displayed in Figure 5.8, show the square root of the Ohmic heating ($\sqrt{\eta j^2}$) at the approximate time of the maximum current in each case (i.e. at $t = 60$ and $t = 80$ for cases (i) and (ii), respectively). In both cases, the heating is concentrated in a narrow layer in the centre of the domain, where the twisted current layer forms. The resistivity (η) covers the same proportion of the domain for both cases and has the same maximum value of $\eta_0 = 10^{-4}$, therefore the distribution of the Ohmic heating with height in case (ii) in Figure 5.8d is proportionally very similar to the heating in case (i) in Figure 5.8b.

Contours plots of the resulting percentage increase in temperature $\left(\frac{T - T(t=0)}{T(t=0)}\right)$ are displayed in Figure 5.9 for the same times. In both cases, some heating at the ends of the current layer (in the $x - y$ plane) is visible, due to viscous shock heating from the fast outflows from reconnection,

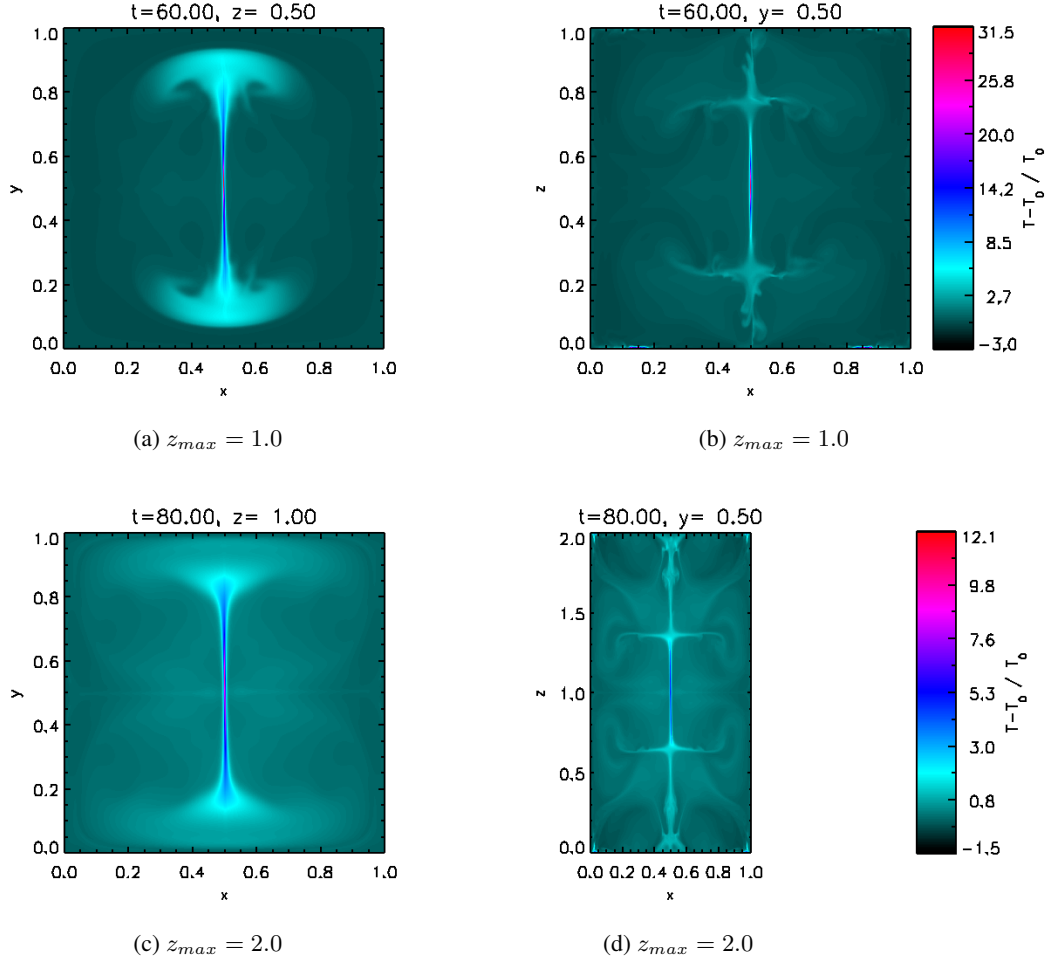


Figure 5.9: Contours plots of $(T - T_0)/T_0$ shown for case (i) at $t = 60$ (a) in the mid-plane and (b) at $y = 0.5$ and for case (ii) at $t = 80$ (c) in the mid-plane and (d) at $y = 0.5$.

with stronger values for case (i). Figure 5.7 also displays the integrated viscous heating over time and shows that by $t = 80$ in case (ii) the viscous heating per unit volume (solid black line) has only reached the value achieved by case (i) at $t \approx 58$. Both experiments in Figure 5.9 also show that the largest temperature increase occurs along the current layer and remains very localised in the centre of the domain, due to the Ohmic heating (this shall be discussed further in Chapter 6).

In these experiments, the same vertical magnetic field component and horizontal velocity driver are imposed on the upper and lower boundaries of the domain for cases (i) and (ii). Therefore we would expect the energy injected into the domain, through the Poynting flux, to coincide for both cases (see Equation 3.9). In Figure 5.10, we see this is true initially (for $t < 10$), however, the Poynting flux (crosses) in Figure 5.10ii for the extended domain does not continue to increase as quickly as it does in case (i). Therefore, the maximum Poynting flux reached for case (ii) is 5.7×10^{-5} in Figure 5.10ii, compared to 7.5×10^{-5} for case (i) in Figure 5.10i. This is due to

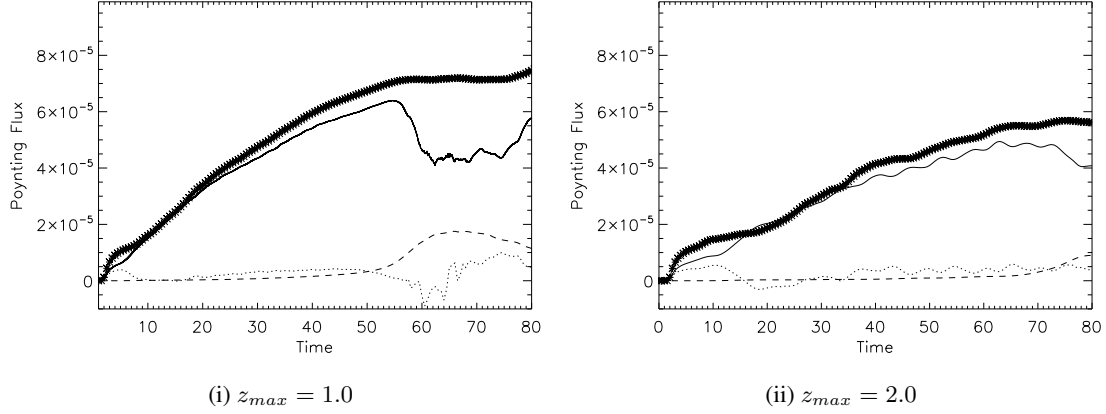


Figure 5.10: The Poynting flux (crosses) with time and the integrated volume contributions of the rate of change of magnetic energy (solid), work done by the Lorentz force (dotted) and Joule dissipation (dashed) with time for case (i) $z_{max} = 1.0$ and case (ii) $z_{max} = 2.0$.

the extended length of the field lines in case (ii). The Poynting flux is proportional to $B_v \mathbf{B}_h \cdot \mathbf{v}_h$ (Klimchuk, 2006), where B_v is the vertical magnetic field component and \mathbf{B}_h and \mathbf{v}_h are the horizontal field and velocity components on the surface. In case (i), with the shorter domain, the imposed twist on the field lines very quickly increases the angle of the field at the boundary and therefore increases the horizontal field component that contributes to the Poynting flux. In contrast, for case (ii) the imparted twist can be distributed over field lines of double the length and therefore the angle of the field on the boundary does not increase as quickly.

The Poynting flux can be divided into the three integrated volume contributions: the rate of change of the magnetic energy, the Ohmic (Joule) dissipation and the work done by the Lorentz force. This can be derived from taking the scalar product of the Induction equation (Equation 1.10) with \mathbf{B}/μ_0 :

$$\frac{\mathbf{B}}{\mu_0} \cdot \frac{\partial \mathbf{B}}{\partial t} = \frac{\mathbf{B}}{\mu_0} \cdot [\nabla \times (\mathbf{v} \times \mathbf{B}) - \nabla \times (\eta' \nabla \times \mathbf{B})],$$

where $\eta' = 1/\sigma\mu_0$. Then using the identities:

$$\begin{aligned} \mathbf{B} \cdot [\nabla \times (\mathbf{v} \times \mathbf{B})] &= \nabla \cdot ((\mathbf{v} \times \mathbf{B}) \times \mathbf{B}) + (\mathbf{v} \times \mathbf{B}) \cdot (\nabla \times \mathbf{B}), \\ \mathbf{B} \cdot [\nabla \times (\eta' \nabla \times \mathbf{B})] &= \nabla \cdot ((\eta' \nabla \times \mathbf{B}) \times \mathbf{B}) + (\eta' \nabla \times \mathbf{B}) \cdot (\nabla \times \mathbf{B}), \end{aligned}$$

this becomes:

$$\begin{aligned} \frac{\partial}{\partial t} \left(\frac{B^2}{2\mu_0} \right) &= \frac{1}{\mu_0} \left(\nabla \cdot ((\mathbf{v} \times \mathbf{B}) \times \mathbf{B}) + (\mathbf{v} \times \mathbf{B}) \cdot (\nabla \times \mathbf{B}) \right) \\ &\quad - \frac{1}{\mu_0} \left(\nabla \cdot ((\eta' \nabla \times \mathbf{B}) \times \mathbf{B}) + (\eta' \nabla \times \mathbf{B}) \cdot (\nabla \times \mathbf{B}) \right), \end{aligned}$$

which can be re-arranged to form:

$$\frac{\partial}{\partial t} \left(\frac{B^2}{2\mu_0} \right) = \frac{1}{\mu_0} \nabla \cdot ((\mathbf{v} \times \mathbf{B}) \times \mathbf{B} - (\eta' \nabla \times \mathbf{B}) \times \mathbf{B}) + ((\mathbf{v} \times \mathbf{B}) - (\eta' \nabla \times \mathbf{B})) \cdot \left(\frac{\nabla \times \mathbf{B}}{\mu_0} \right).$$

Replacing $\mu_0 \mathbf{j} = \nabla \times \mathbf{B}$:

$$\frac{\partial}{\partial t} \left(\frac{B^2}{2\mu_0} \right) = \frac{1}{\mu_0} \nabla \cdot \left((\mathbf{v} \times \mathbf{B}) \times \mathbf{B} - \frac{\mathbf{j}}{\sigma} \times \mathbf{B} \right) + \left((\mathbf{v} \times \mathbf{B}) - \frac{\mathbf{j}}{\sigma} \right) \cdot \mathbf{j}.$$

Finally, using $(\mathbf{v} \times \mathbf{B}) - \mathbf{j}/\sigma = -\mathbf{E}$, the rate of change of magnetic energy can be described by:

$$\frac{\partial}{\partial t} \left(\frac{B^2}{2\mu_0} \right) = -\nabla \cdot \left(\frac{\mathbf{E} \times \mathbf{B}}{\mu_0} \right) - \mathbf{v} \cdot (\mathbf{j} \times \mathbf{B}) - \frac{j^2}{\sigma}.$$

Integrating over the volume of the domain and using Gauss' Theorem this becomes,

$$\begin{aligned} \int_V \frac{\partial}{\partial t} \left(\frac{B^2}{2\mu_0} \right) dV &= - \int_S \left(\frac{\mathbf{E} \times \mathbf{B}}{\mu_0} \right) d\mathbf{S} - \int_V \mathbf{v} \cdot (\mathbf{j} \times \mathbf{B}) dV - \int_V \frac{j^2}{\sigma} dV \\ \Rightarrow - \int_S \left(\frac{\mathbf{E} \times \mathbf{B}}{\mu_0} \right) d\mathbf{S} &= \int_V \frac{\partial}{\partial t} \left(\frac{B^2}{2\mu_0} \right) dV + \int_V \mathbf{v} \cdot (\mathbf{j} \times \mathbf{B}) dV + \int_V \frac{j^2}{\sigma} dV. \end{aligned} \quad (5.1)$$

The term $-\int_S \left(\frac{\mathbf{E} \times \mathbf{B}}{\mu_0} \right) d\mathbf{S}$ is the Poynting flux evaluated on the boundaries of the domain, and is equal to the sum of the total volume integrated rate of change of magnetic energy $\left(\int_V \frac{\partial}{\partial t} \left(\frac{B^2}{2\mu_0} \right) dV \right)$, total volume integrated work done by the Lorentz force in the domain $\left(\int_V \mathbf{v} \cdot (\mathbf{j} \times \mathbf{B}) dV \right)$ and the volume integrated Ohmic/Joule dissipation $\left(\int_V \frac{j^2}{\sigma} dV \right)$. The evolution of each of these terms with time is plotted in Figures 5.10i and 5.10ii, for cases (i) and (ii), respectively.

The rate of change of the magnetic energy for the case (ii) (black-solid line) in Figure 5.10i accounts for the majority of the Poynting flux entering the domain up to $t = 55$, as the energy is stored in the twisted magnetic field. After this time, the rate of change of the magnetic energy decreases sharply, as the magnetic field changes connectivity and the Joule dissipation (dashed line) increases. In case (ii), shown in Figure 5.10ii, the decrease in the rate of change of the magnetic energy, and associated increase in the Joule dissipation, occurs much later (after $t = 70$). The timing of the increase in Joule dissipation in each case coincides with the build up of current observed in Figure 5.2.

In order to compare the efficiency of the energy release in the two cases, given that the amount of energy injected into the simulations varies, we consider these integrated contributions as percentages of the integrated Poynting flux over time in Figure 5.11. By the end of the simulations, for case (ii) 88% of the Poynting flux that has entered the domain is attributed to the change of

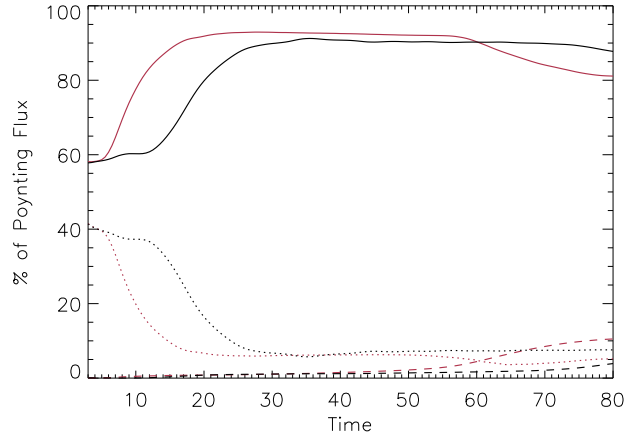


Figure 5.11: The volume and time integrated rate of change of magnetic energy (solid), work done by the Lorentz force (dotted) and Joule dissipation (dashed) shown as a percentage of the integrated Poynting flux at each time, for cases (i) $z_{max} = 1.0$ and (ii) $z_{max} = 2.0$ shown in red and black, respectively.

the magnetic energy (black, solid line), while it is 82%, by the same time, for case (i) (red, solid line). Similarly, the total Joule dissipation accounts for 4% and 11% of the total Poynting flux into the domain by the end of the experiments, for cases (i) and (ii), respectively. This difference can be attributed to the combination of the delay in the current evolution and the smaller current values reached for case (ii). Therefore, this reduction in the efficiency of converting the Poynting flux into Joule dissipation combined with the decreased total energy entering the domain through Poynting flux both contribute to the reduction in the total Ohmic heating from case (i) to case (ii) shown in Figure 5.7.

The rate of change in magnetic energy and the work done by the Lorentz force clearly show oscillations in Figure 5.10ii for case (ii). The period of these oscillations appears to decrease slightly over the length of the simulation, consistent with the increase in the magnetic field strength and therefore the Alfvén speed. This suggests that these oscillations are due to waves occurring in the extended domain and are likely due to some combination of Alfvén waves and fast waves.

Summary

Doubling the domain height and therefore the loop length, while maintaining the same initial pressure and density, results in a more uniform, but weaker field in the centre of the domain. The extended loop length prevents the field lines from becoming as curved, thereby reducing the magnetic tension force between the flux tubes that acts to build up the twisted current layer in the domain. Hence, the timing of reconnection and its associated heating is delayed by approximately

15 normalised time units (≈ 8.5 minutes in real units) in case (ii) compared to case (i). The values of the Ohmic heating are also reduced but the locations of current formation and associated heating are distributed similarly (proportionally) in the domain for both cases.

The comparison presented in this chapter suggests that, in a coronal context, shorter magnetic loops require less footpoint advection (i.e. less energy input by the Poynting flux) in order for magnetic stress to increase quickly and reconnection and Ohmic heating to occur. However, the time-scales and comparative values of heating produced in this comparison are dependent on the parameters, such as resistivity, that are used.

Chapter 6

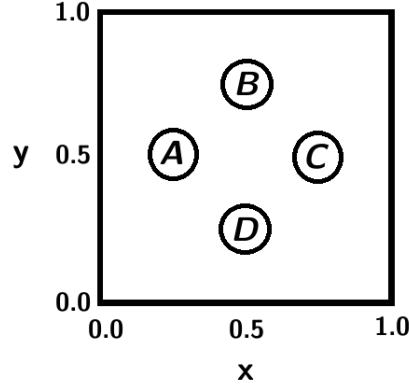
Comparison of Two and Four Flux Tubes

In Chapters 2, 3 and 4 we have considered a model with two flux tubes, connecting flux sources on the upper and lower boundaries. In this chapter, we extend this model to consider a larger number of magnetic flux sources on the boundaries, where the total flux remains unchanged from the previous two source model. This will allow us to examine how the distribution of magnetic flux impacts the reconnection process and therefore the energy release. A simple extension of the two source case is to consider four sources. We will consider two cases with four sources, where the constant total magnetic flux is achieved by varying either the peak magnitude or the radius of the sources. In Section 6.1, we describe the process of relaxing the four sources to compare the initial field configuration with the two source case. We then go on, in Section 6.2, to compare the dynamical evolution, using the same driving velocity.

6.1 Comparing Two and Four Flux Tubes Set-up

Normalisation	Initial Conditions	
$B_0 = 100 \text{ G}$	$\epsilon = 0.01$	Resolution: $512^2 \times 256$
$L_0 = 75 \text{ Mm}$	$\rho = 0.1$	$\eta = 0$ (Ideal relaxation)
$n_e = 1 \times 10^{16} \text{ m}^{-3}$		viscosity= 0.001
		$0 < t_{relax} < 80$

To extend the two flux tube simulation to a four flux tube case, we will position the sources so they have rotational symmetry about $(x, y) = (0.5, 0.5)$, as in the two flux tube case. The four sources will now be located at $(x_A, y_A) = (0.3, 0.5)$, $(x_B, y_B) = (0.5, 0.7)$, $(x_C, y_C) = (0.7, 0.5)$,

Figure 6.1: The magnetic source labels on $z = 0.0$.

and $(x_D, y_D) = (0.5, 0.3)$, which we shall call sources A, B, C and D, for ease of reference (see Figure 6.1). The sources A and C are in the same position as the original two source case discussed in previous chapters.

We will consider two distributions of magnetic field with four sources, which both retain the same total magnetic flux through the surfaces at $z = 0.0$ and $z = 1.0$. The magnetic field component B_z on the upper and lower boundaries is described by a summation of Gaussians and is given by:

$$B_z = B_{max} \left[e^{-[(x-x_A)^2+(y-y_A)^2]/r_1^2} + e^{-[(x-x_B)^2+(y-y_B)^2]/r_1^2} + e^{-[(x-x_C)^2+(y-y_C)^2]/r_1^2} + e^{-[(x-x_D)^2+(y-y_D)^2]/r_1^2} \right]. \quad (6.1)$$

This boundary condition can describe both four source cases where different B_{max} and r_1 are specified. The first case uses the parameter values $B_{max} = 0.5$ and $r_1 = 0.065$. The radius of the sources remains the same as in the two source case but the peak magnitude (B_{max}) is halved. The second case retains the same peak magnitude but the radius is reduced by a factor of $\sqrt{2}$, where $B_{max} = 1.0$ and $r_1 = 0.065/\sqrt{2}$ (see Table 6.1). This enables us to compare the original two source case with four more concentrated sources (case iii) as well as with four weaker sources of the same size (case ii).

Table 6.1: Multiple Source Cases: Parameters and colour scheme that will be used throughout this chapter.

(i) Two Sources	(ii) Four Sources: Weak	(iii) Four Sources: Compact
$B_{max} = 1.0,$	$B_{max} = 0.5,$	$B_{max} = 1.0,$
$r_1 = 0.065$	$r_1 = 0.065$	$r_1 = 0.065/\sqrt{2} \approx 0.046$

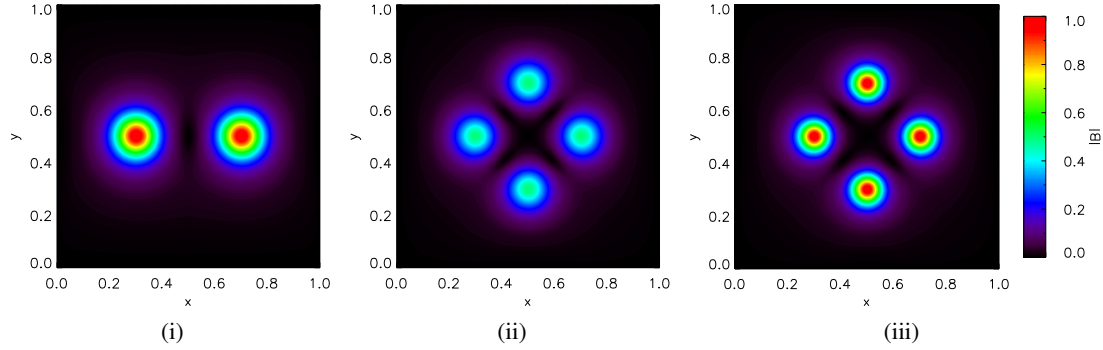


Figure 6.2: Contour plots of $|B|$ after relaxation at $z = 0.0$ for cases with (i) 2 sources, (ii) 4 sources (weak) and (iii) 4 sources (compact).

In order to create the four aligned, distinct flux tubes, this distribution of B_z is specified at all heights throughout the domain and the flux tubes are allowed to relax and expand for 80 time units. In the four source cases, the positioning of the sources on the boundaries now produces four regions of connectivity, which, using the same terminology as in Chapter 2, we shall refer to as being divided by QSLs, that intersect in the centre of the plane.

We will now briefly describe how the number and strength of the sources affects the expanded flux tubes and discuss any implications that the initial configuration will have on the subsequent dynamical evolution. In this chapter all of the relaxations and rotations are carried out at $512^2 \times 256$ and with the boundary and initial conditions as described in Chapter 4.

The strength and distribution of the magnetic field at $z = 0.0$ is shown in the contours of the magnitude of the field in Figure 6.2. The B_z component described in Equation 6.2 is plotted on the lower boundary in Figure 6.3a for all three cases at $y = 0.5$. The original two source case is displayed in red and the four source case (iii), with the same peak magnitude of 1, is plotted in black. The field strength of case (iii) reduces more steeply due to the reduction in the parameter r_1 . The four source case (ii), with the reduced magnitude ($B_{max} = 0.5$), is over-plotted in blue and has the same wider Gaussian distribution as the two source case. The B_x component that forms when the flux tubes are allowed to expand is shown in Figure 6.3b. The B_x component for case (iii) has a similar magnitude to case (i), which has the same specified B_{max} , but reduces faster between the sources. This demonstrates the field is not able to expand as fully as the two source case, due to the two extra flux tubes in the domain.

The field components B_z and B_x at $y = 0.5$ are also shown in the mid-plane in Figures 6.3c and 6.3d after relaxation. All three simulations have a similar peak value of B_z in the mid-plane of ≈ 0.033 , however this B_z then drops off much more steeply for the four source cases shown in blue and black. This is also due to the fact that including two extra flux tubes in the

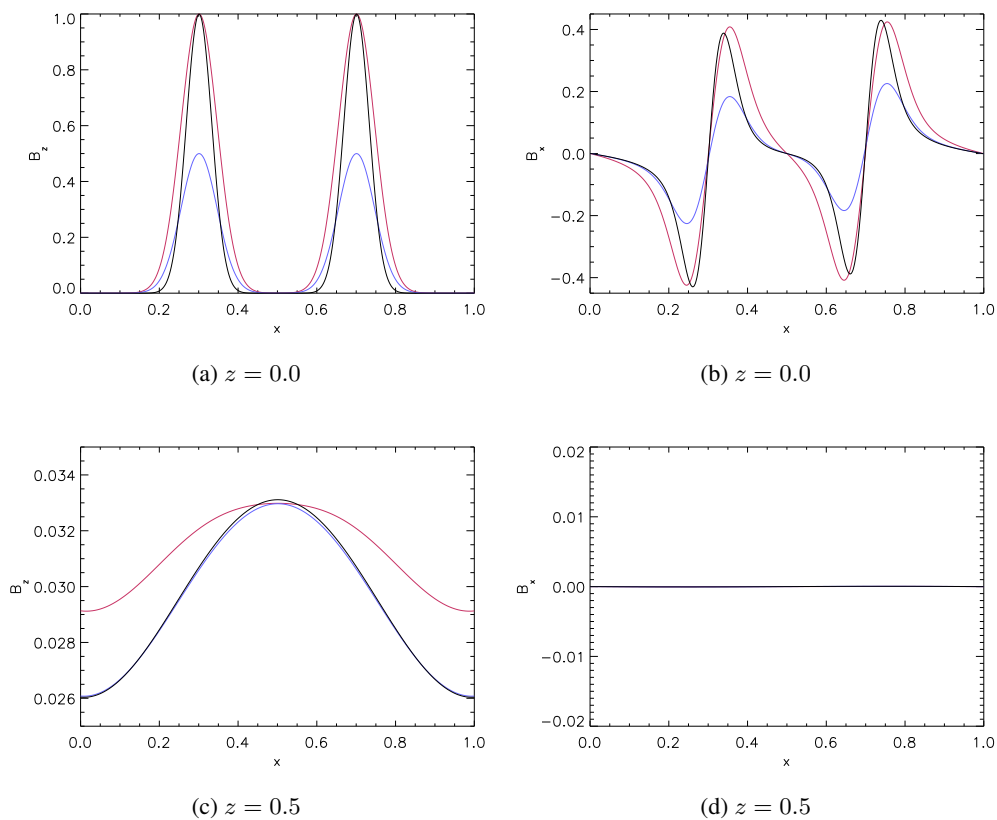


Figure 6.3: Magnetic field components (a) B_z , (b) B_x at $z = 0.0$ and (c) B_z , (d) B_x at $z = 0.5$ at $y = 0.5$ after the flux tubes have expanded, for cases with (i) 2 sources, (ii) 4 sources (weak) and (iii) 4 sources (compact) shown in red, blue, and black, respectively.

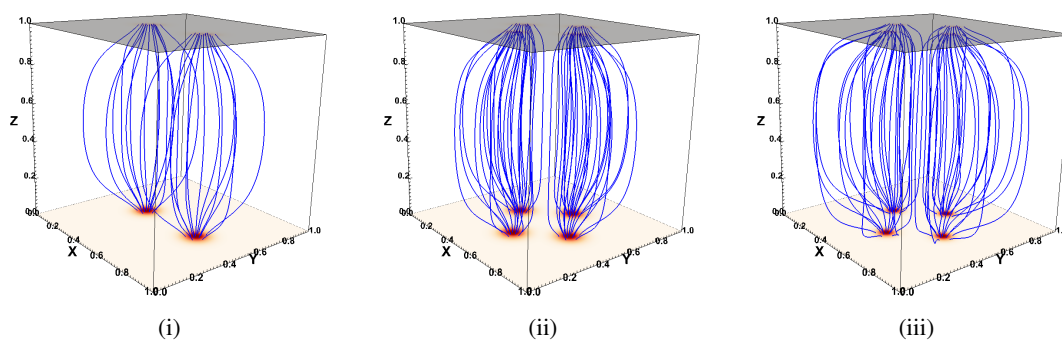


Figure 6.4: A selection of field lines traced after relaxation from $z = 0.0$ for cases (i) 2 sources, (ii) 4 sources (weak) and (iii) 4 sources (compact).

domain prevents the field from expanding as far as the two flux tube case and so the field lines are straighter and there is a weaker field towards the boundaries. This is also visible in Figure 6.4,

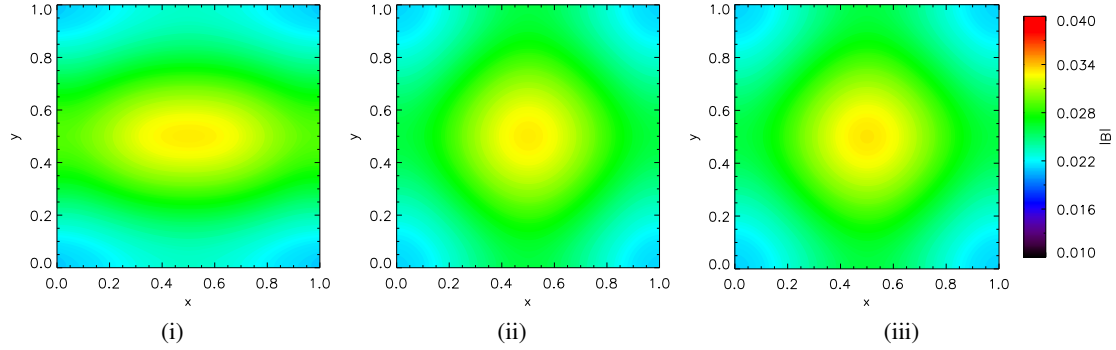


Figure 6.5: Contour plots of $|B|$ after relaxation at $z = 0.5$ for cases (i) 2 sources, (ii) 4 sources (weak) and (iii) 4 sources (compact).

which shows a selection of field lines traced from the sources at $z = 0.0$ for the three cases after relaxation. The field lines are traced from the same positions in Figures 6.4ii and 6.4iii, but due to the smaller radius of the sources in case (iii) the field expands more quickly from the upper and lower boundaries.

In the mid-plane, however, the four source cases have a very similar magnetic field strength and distribution, as shown in Figures 6.5ii and 6.5iii. In comparison to the two source case in Figure 6.5i, the field strength is slightly more spread out in the y -direction. This difference is due to the placement of the extra two sources in cases (ii) and (iii), where the distributions in y and x are now symmetric. However, the peak magnitude of the field strength in the plane for all three cases is approximately 0.03 in normalized units and occurs in the centre of the plane at $(0.5, 0.5)$.

The identical peak magnetic field strength at the centre of the mid-plane also means that, due to the constant pressure and density in the relaxation, the minimum plasma β value in the mid-

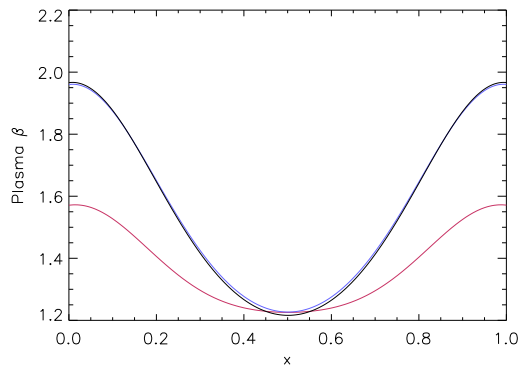


Figure 6.6: Plasma β at $y = 0.5$ and $z = 0.5$ for cases (i) 2 sources, (ii) 4 sources (weak) and (iii) 4 sources (compact) shown in red, blue, and black, respectively.

plane will be the same in all three cases. The plasma β , calculated at $y = 0.5$ in the mid-plane, is plotted as a function of x in Figure 6.6 and shows the minimum value for the two and four source cases occurs at $x = 0.5$ with a value of ≈ 1.25 . The plasma β then increases away from the centre of the domain, where this increase is greater for the four source cases, shown in blue and black, which have a maximum of approximately 1.95 compared to a value of 1.57 for the two source case. This higher plasma β value at the edges is due to the weaker magnetic field strength. However, this difference is not great as both are of the same order of magnitude and are similar in the centre of the domain, where we expect the majority of the field interaction to occur.

Through the Alfvén speed, the difference in the magnetic field strength also affects the numerical resistivity, as discussed in Chapters 3 and 4 (see Equation 3.4). This can be seen in the estimate of the numerical resistivity in the mid-plane in Figure 6.7a, where the four source cases (blue and black) have a lower value of numerical resistivity at the edges of the domain, in line with the weaker field strength. The estimated maximum numerical resistivity in the domain with height is also displayed in Figure 6.7b. This shows that the numerical resistivity is 10^{-4} at the footpoints ($z = 0.0$ and $z = 1.0$) for the two cases with the same maximum field strength ($B_{max} = 1.0$) plotted in red and black and is slightly greater than the maximum for the four source case with $B_{max} = 0.5$ (blue). However, these differences are small compared to the values being considered and should not impact the evolution of the field when a velocity driver is applied. In addition, these are initial estimates only. The actual numerical η will evolve depending on the typical length scales (L) produced and will therefore vary between the different simulations.

When the field expands and relaxes, a small current is produced in the domain. For the two source case (red), we previously discussed that the highest value of the current is formed near the z -boundaries of the simulation due to the rapid expansion of the field from the sources on

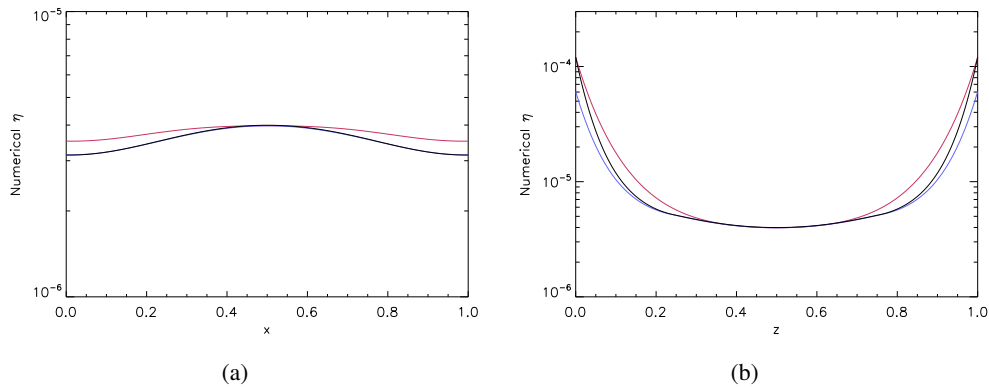


Figure 6.7: Estimated maximum numerical resistivity (a) in the mid-plane along $y = 0.5$ and (b) with height (z) for cases (i) 2 sources, (ii) 4 sources (weak) and (iii) 4 sources (compact) shown in red, blue, and black, respectively.

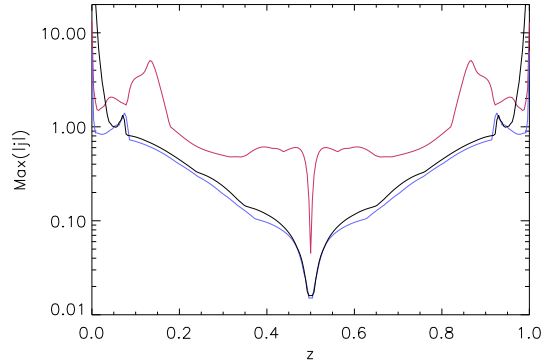


Figure 6.8: Maximum current magnitude with height (z) for cases (i) 2 sources, (ii) 4 sources (weak) and (iii) 4 sources (compact) shown in red, blue, and black, respectively.

the boundaries. This is also true for the four flux tube cases (blue and black), as indicated in Figure 6.8, which shows the maximum current value with height in the domain. The case with four compact sources, with the same field strength of $B_{max} = 1.0$, has the highest current value at the boundaries. This is what we would expect as it has the greatest expansion. The maximum current value with height has its minimum in the mid-plane for all three cases, where the field has expanded the most and therefore the field strength is weakest.

It is also important to take into account the final energy state after the flux tubes have expanded and relaxed before we begin driving the system. As discussed previously, the relaxation is carried out with a uniform density and pressure and therefore the internal energy is constant throughout the process. In comparison, the kinetic energy varies greatly as the initial flux tubes expand quickly, inducing a velocity into the domain that slowly decreases over time. The volume integrated kinetic energy density with time, in Figure 6.9a, decreases by six orders of magnitude for all three cases. The oscillations clearly visible in the two source case (red) are not apparent for the four source cases (blue and black) and the four source cases also decrease to a smaller value of less than 10^{-9} . However, the volume integrated kinetic energy density values are very small compared to the other energy contributions. In particular, the volume integrated magnetic energy (Figure 6.9c) is approximately six orders of magnitude larger at the end of the relaxation.

The volume integrated magnetic energy depends on the field strength and, as we saw in Figures 6.3 and 6.4, when four flux tubes are present they are not able to expand as fully. Therefore, the magnetic energy is consistently slightly lower than the two flux tube case. The difference in the volume integrated total energy (Figure 6.9d) can be attributed to the difference in the magnetic energy, as it is by far the largest energy contribution.

It is interesting that although an equal amount of magnetic flux (B_z) is prescribed on the boundaries, the resulting volume integrated magnetic energy in the domain differs. This high-

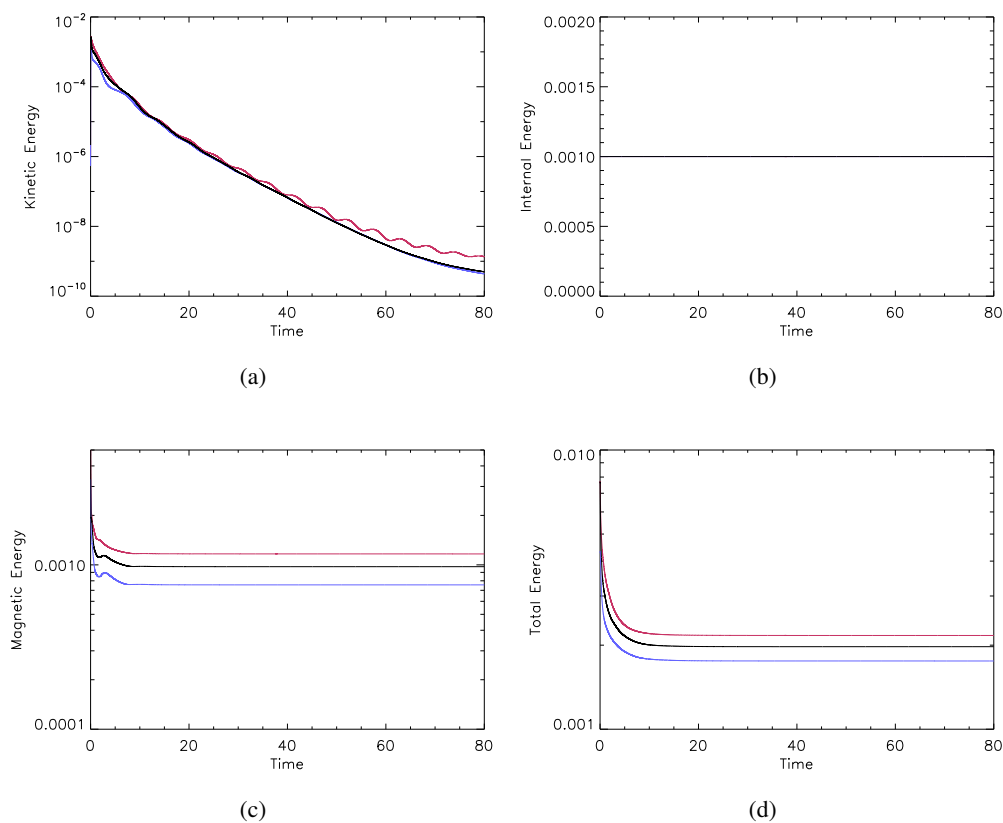


Figure 6.9: (a) Kinetic, (b) internal, (c) magnetic and (d) total volume integrated energy densities for cases (i) 2 sources, (ii) 4 sources (weak) and (iii) 4 sources (compact) shown in red, blue, and black, respectively.

lights the importance of understanding the field configuration in the entire domain and not just the surface flux distribution. If we consider this in terms of the coronal field of the Sun, active regions examined on the photosphere, which contain the same total observed line of sight magnetic flux, will invariably be associated with coronal structures with varying amounts of magnetic energy. This relates to the difficulty in modelling the coronal field from magnetogram observations and is discussed comprehensively in the review by Mackay and Yeates (2012) and references within.

Overall, the relaxations of the four and two flux tube distributions behave very similarly, but the field distribution alters the expansion of the flux tubes which will have implications for the magnetic field strength, plasma beta and background current. However, these differences appear to occur largely towards the boundaries of the simulations. Due to these magnetic field differences towards the boundaries of the domain, the total volume integrated magnetic energy does differ slightly for the three cases. However, in the centre on the domain, where the resistivity will be localised in the following driven experiments, the distribution of magnetic field and its magnitude are comparable for the three cases.

6.2 Comparing Two and Four Flux Tubes Under Rotation

Normalisation	Initial Conditions	
$B_0 = 100 \text{ G}$	$\epsilon = 0.01$	Resolution: $512^2 \times 256$
$L_0 = 75 \text{ Mm}$	$\rho = 0.1$	$\eta = \eta_0 e^{-\left(\frac{z-0.5}{r_0}\right)^2}, \eta_0 = 10^{-4}$
$n_e = 1 \times 10^{16} \text{ m}^{-3}$		$0 < t < 75$

We now go on to rotate the four flux tube cases with the same velocity driver specified in Equations 3.1 and 3.2. We will consider the dynamical evolution of the four source cases in comparison to the two source case. We will also directly compare the four source cases to investigate if there is any effect due to the different magnitude and radius of the magnetic sources. In Section 6.2.1 we discuss the evolution of the magnetic flux connectivity before going on to discuss in more detail the forces acting on the field and the current evolution in Section 6.2.2. Finally, in Sections 6.2.3 and 6.2.4 we describe the effect on the energetics and associated heating.

6.2.1 Magnetic Flux Connectivity and Evolution

At the start of the experiment, the positive sources on $z = 0.0$ and negative sources on $z = 1.0$ are positioned directly above each other, as shown in Figure 6.4. This produces two or four aligned flux tubes, depending on the case. In this initial arrangement, all of the field lines from each source at $z = 0.0$ are connected to the associated negative source directly above at $z = 1.0$. For reference, the sources on the base shall be referred to as A, B, C and D and the sources on the upper boundary as a, b, c and d . These sources are located in the $x - y$ plane at $(0.3, 0.5)$, $(0.5, 0.7)$, $(0.7, 0.5)$, $(0.5, 0.3)$, respectively (see Figure 6.10). We can therefore describe the initial connectivity as Aa, Bb, Cc and Dd . In the two source case, only sources A and C on the lower boundary and a and c on the upper boundary are present and thus the initial flux connectivities are Aa and Cc .

First, we will examine the behaviour of the connectivity associated with only source C on $z = 0.0$ as the flux tubes are rotated. In Figure 6.11 5815 field lines have been traced from within the radius r_1 of source C over the simulation. It is important to note that, although there is no η specified on the boundaries, we expect some numerical diffusion and therefore we are not following the exact evolution of individual field lines but the overall connectivity associated with the source. Each of these field lines is traced to the upper boundary to determine its connectivity. If the field line is within $2r_1$ of a source on the upper boundary then we consider it to be associated with that source and its starting point in the source on the base is coloured accordingly. If the field lines in Figure 6.11 are associated with source c on the upper boundary (the original connection) then they are coloured dark blue. Otherwise, if they are traced to sources a, b or d on the upper

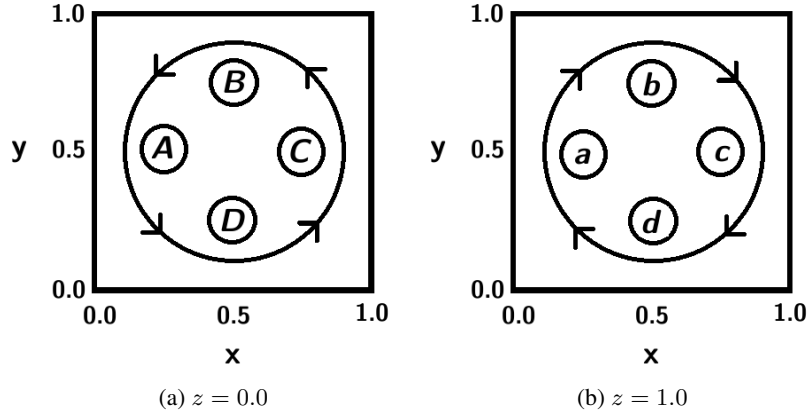


Figure 6.10: The magnetic source labels at $t = 0$ for cases (ii) and (iii) on (a) $z = 0.0$ and (b) $z = 1.0$. The direction of rotation is also indicated.

boundary then they are coloured light blue, green or red, respectively.

In Figure 6.11i, the connectivity of source C for the two source case is displayed. There are only two sources present on each boundary (A and C) and therefore when the flux tubes are rotated the amount of flux with the original connectivity Cc (dark blue) begins to decrease as the connections Ca (light blue) begin to occur, as was discussed in detail in previous chapters. In comparison, in the four (weak) source case (ii) shown in Figure 6.11ii, the total flux with the original connectivity Cc begins to reduce and field lines with connectivity Cb (green) begin to appear as shown at $t = 50$ ($\theta \approx 3.9$ rad). The field lines are now connected to the source (b) on the upper boundary that is the neighbour of its original connection (c) in the anti-clockwise direction. As the sources continue to be counter-rotated on the upper and lower boundaries, the amount of flux with connectivity Cb (green) increases. After this, another magnetic flux connectivity, Cd , begins to appear in red. These red field lines are associated with source d , which is the clockwise neighbour of the original connection on the upper boundary.

The magnetic flux connectivity for the compact four source case (iii) is also shown for source C on the lower boundary in Figure 6.11iii. The initial flux connectivity evolution appears very similar to that of case (ii). However, the Cd connectivity shown in red appears slightly earlier and is visible by $t = 60$ in Figure 6.11iii. Despite this slight difference, the general evolution of the magnetic flux connectivities is very similar for both of the four source cases. The new flux connectivities at source C for all three cases, can also be seen in Figure 6.12, which displays a selection of field lines traced from source C on the lower boundary at $t = 60$. By this time the sources have been rotated by $\approx 3\pi/4$ on the base and similarly for the upper boundary. Figure 6.12 also displays an isosurface of current in the centre of the domain, which appears more compact for cases (ii) and (iii). We will discuss the evolution and importance of current in the domain in more detail in Section 6.2.2.

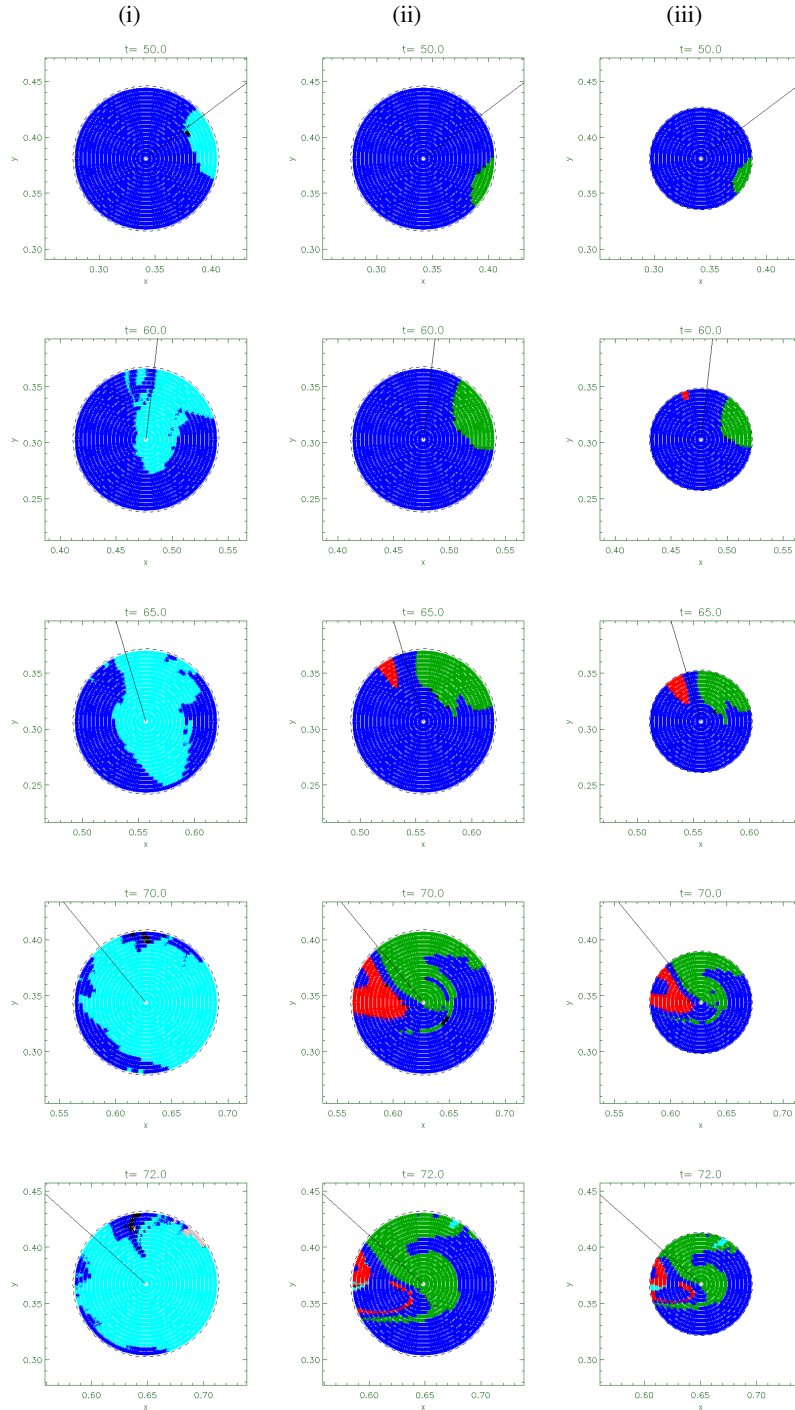


Figure 6.11: The field line connectivity of source C on $z = 0.0$ at $t = 50, 60, 65, 70, 72$ for cases (i) 2 sources, (ii) 4 sources (weak) and (iii) 4 sources (compact). The solid black line indicates the direction to the centre of rotation. Dark blue signifies field lines at the original connection (Cc). The colours light blue, green and red indicate that the field lines have connectivity Ca , Cb and Cd , respectively. Pink corresponds to field lines that cannot be traced to $z = 1.0$ and black are field lines that are connected to the top boundary but not associated with a source by our definition.

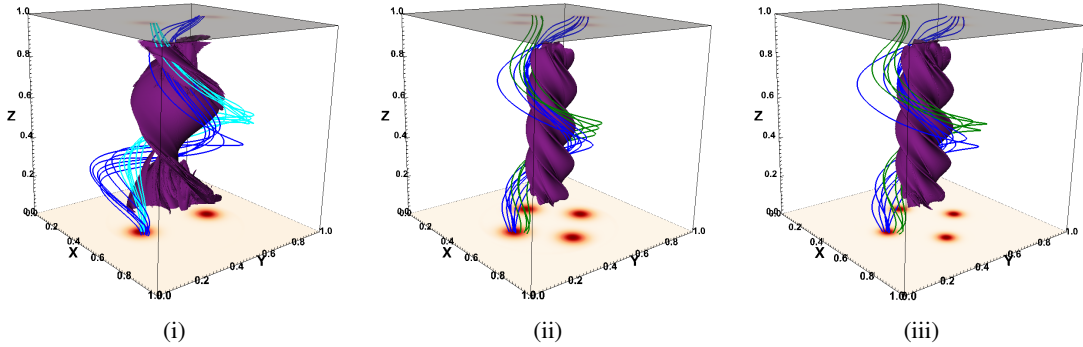


Figure 6.12: A selection of field lines traced from source C on $z = 0$ at $t = 60$ for cases (i) 2 sources, (ii) 4 sources (weak) and (iii) 4 sources (compact), coloured according to their connectivity as described in Figure 6.11. Over-plotted are the isosurfaces of the current density of magnitude 2.5 within the central box ($0.1 < x, y, z < 0.9$) in the domain.

In cases (ii) and (iii), the flux with connectivity Cb (green) occurs in front of the solid black line that indicates the direction to the centre of rotation, while the flux with connectivity Cd is initially behind it. Here ‘ahead’ and ‘behind’ are given in terms of the direction of the rotation of the sources on the base. This division becomes less strict in the later stages of the simulations.

By $t = 72$, another type of magnetic flux connectivity (Ca) has occurred in cases (ii) and (iii) and can be seen in light blue. These field lines are now connected to source a on the upper boundary, that is the source furthest from their original connection c . The amount of magnetic flux with connectivity Ca is very small for both four source cases. This new connectivity (Ca) appears at two separate locations within the source for both cases, as shown at $t = 72$ in Figure 6.11ii and Figure 6.11iii. The Ca field lines appear towards the top right of the source amongst other Cb flux (green), as well as at the far left of the source amongst Cd flux (red). This is different to the appearance of the other flux connectivities shown in red (Cd) and green (Cb) that began to appear from one area of the source and increase in number.

The images in Figure 6.11 only show the field line connectivity evolution for source C . However, due to the rotationally symmetric set-up of the sources and the rotational velocity driver, we expect similar (rotationally symmetric) flux connectivity behaviour for sources A , B and D on the base.

Each source on the lower boundary is originally connected to the source positioned directly above on the upper boundary with the flux connectivities described as Aa , Bb , Cc and Dd . The flux connectivity shown in green in Figure 6.11 for source C can be extended to an arbitrary source on the base by considering flux connectivities formed to the neighbouring source anticlockwise on the upper boundary. This would produce connectivities Ad , Ba , Cb and Dc for each of the four sources and these would be comparable. Similarly, we can consider the new flux connectivities

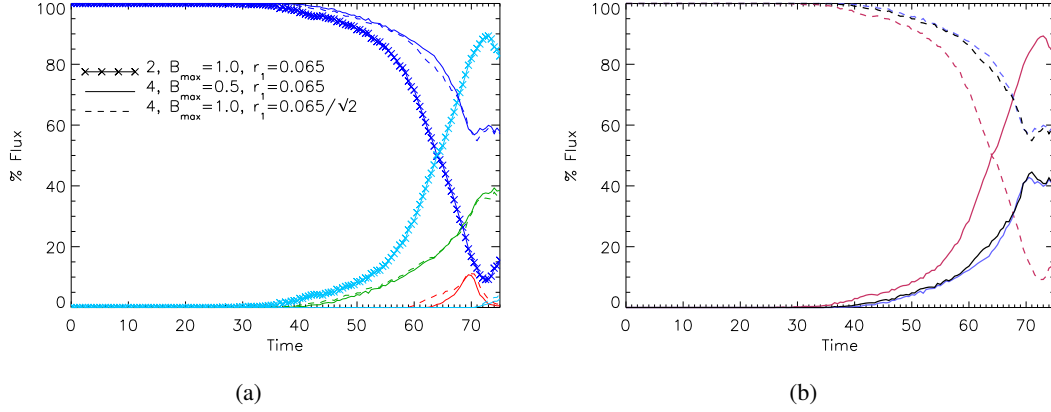


Figure 6.13: (a) Average percentage of flux connected to the original, anticlockwise, clockwise, and opposite sources on the upper boundary shown in dark blue, green, red and light blue, respectively. (b) Total percentage of flux connected to sources other than the original source on upper boundary (solid line) and percentage of flux connected to original source (dashed line) for cases (i), (ii) and (iii) shown in red, blue, and black, respectively.

formed to the neighbouring source clockwise on the upper boundary such as Ab, Bc, Cd and Da and as for source C in Figure 6.11 these can be shown in red. Finally, the sources on the base may connect to the source that was originally across the diameter of the plane (shown in light blue in Figure 6.11) and the connectivities Ac, Bd, Ca and Db are formed.

We carry out the same analysis, as described for source C , on all the sources on the lower boundary to discuss the complete flux behaviour from the lower boundary. The percentage of each source connected anticlockwise, clockwise and opposite can be calculated. We then take the average of these percentages over all the sources on the lower boundary. The average percentage of flux is therefore split into four connectivity groups: original (dark blue), anticlockwise (green), clockwise (red) and opposite (light blue) connections. The evolution of these average flux percentages with time is plotted for cases (i), (ii) and (iii) in Figure 6.13a.

For all cases, at $t = 0$, 100% of the flux from the sources on the lower boundary is associated with its original source on the upper boundary and is shown by dark blue in Figure 6.13a. For case (i) this remains true until $t \approx 35$, when the percentage of flux associated with the opposite source (light blue crosses) begins to increase slowly and then more rapidly until it peaks at $\approx 90\%$ at $t = 73$. After $t = 73$, the percentage of flux at its original connection (dark blue crosses) begins to increase again, suggesting that the field lines are beginning to reconnect back to their original source.

The percentage of flux connected to its original source (dark blue) for cases (ii) (solid) and (iii) (dashed) are plotted in Figure 6.13a and remain at 100% for slightly longer than for case (i), before

reducing at a slower rate. As seen for source C in Figure 6.11, the first new flux connectivities that form are to the anticlockwise (green) neighbouring source on the upper boundary. The increase in this percentage of anticlockwise flux connectivity is practically identical between cases (ii) and (iii), shown by solid and dashed green lines, respectively.

However, there is a slight difference in the evolution of the percentage of flux changing connectivity clockwise for cases (ii) and (iii), shown in red. The percentage of clockwise flux for the compact sources in case (iii) (red, dashed line) begins to increase a few time steps sooner at $t = 60$ compared to case (ii) (red, solid line), but they produce a similar peak value at $t \approx 70$. At its peak value a maximum of 12% of the flux is connected clockwise, which is significantly less than the percentage of flux connected anticlockwise, which reaches a maximum of almost 40%. For cases (ii) and (iii), the percentage of flux connected clockwise (red) begins to decrease as the percentage of flux connected to the opposite source (light blue) begins to increase at $t = 70$. This also coincides with a slower increase in the percentage of anticlockwise flux (green) for the four source cases.

In Figure 6.13b, the percentage of flux at the original connection is shown again, now as a dashed line, while the percentage of total flux with all other connectivities is plotted as a solid line, in red, blue and black for cases (i), (ii) and (iii), respectively. This allows us to compare the total amount of flux changing connectivity. The two source case shows a much larger gradient in the increasing percentage of flux changing connectivity compared to the four source cases, which begin to change connectivity later and do not increase as quickly. For case (i) (red) almost 90% of the magnetic flux is no longer connected to its original connection by $t = 73$. The percentage of flux no longer at the original connection for the four source cases (ii) and (iii) has some slight differences with time, however, they reach similar peak values of only 42% and 45% by $t = 70$ and $t = 71$, respectively. This can be considered as a minimum estimate for the total percentage of flux that has changed connectivity. The actual value may be greater than this, given that flux may have reconnected back to its original connection or gone through multiple reconnection events (see e.g Parnell et al., 2011).

We now go on to examine how these different connectivities manifest themselves in the mid-plane. The original flux connectivity in the mid-plane at $t = 0$ for the two source case (i) is shown in Figure 6.14a. The mid-plane is divided at $x = 0.5$ by a QSL between the two connectivities Aa and Cc . Figure 6.14b shows the original flux connectivities for the four source cases (ii) and (iii) and there are now two QSLs between the different flux connectivity regions, which intersect at the centre of the mid-plane.

We consider a large number of points in the mid-plane from which we trace magnetic field lines. Depending on where the field line is connected to on the lower and upper boundaries, the point on the mid-plane is coloured accordingly. As previously described for Figures 6.13a

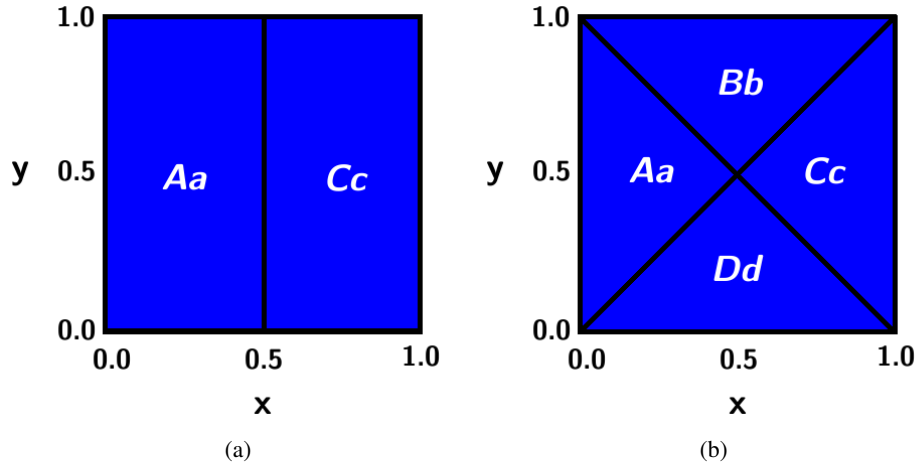


Figure 6.14: The magnetic flux connectivities in the mid-plane at $t = 0$ for the (a) 2 source and (b) four source cases.

and 6.11, the flux connectivities can be divided into flux that has its original connection or that has reconnected to the anticlockwise, clockwise or opposite source on the upper boundary, relative to its original connection. These connectivities are again shown in Figure 6.15 as dark blue, green, red and light blue in the mid-plane, respectively, for those associated with source C on the lower boundary.

Note that we focus on the central region within $0.25 < x, y < 0.75$ in the mid-plane, as this is the key region where the magnetic field is being concentrated and a lower plasma β is present. This allows us to focus on the flux connectivities away from the artificial x and y boundaries of the simulation. Contours of the parallel current density are also over-plotted in black, which we will discuss in detail later.

In Figures 6.15ii and 6.15iii, at $t = 50$ the flux with connectivity Cb (green) appears at the interface of the flux regions with connectivity Cc and Bb (see Figure 6.14b). The contours of parallel current density over-plotted in black show the build up of current at this interface, as the current begins to form an ‘x’ shape.

As the experiment continues, the amount of flux reconnecting anti-clockwise continues to increase, as shown by the regions of green flux connectivity expanding towards the corners of the domain in the mid-plane in Figures 6.15ii and 6.15iii. While this is occurring, flux reconnecting clockwise (red) also begins to appear. This clockwise connectivity region occurs at the other boundary of connectivity for source C , between regions of connectivity Cc and Dd , and is concentrated towards the centre of the domain.

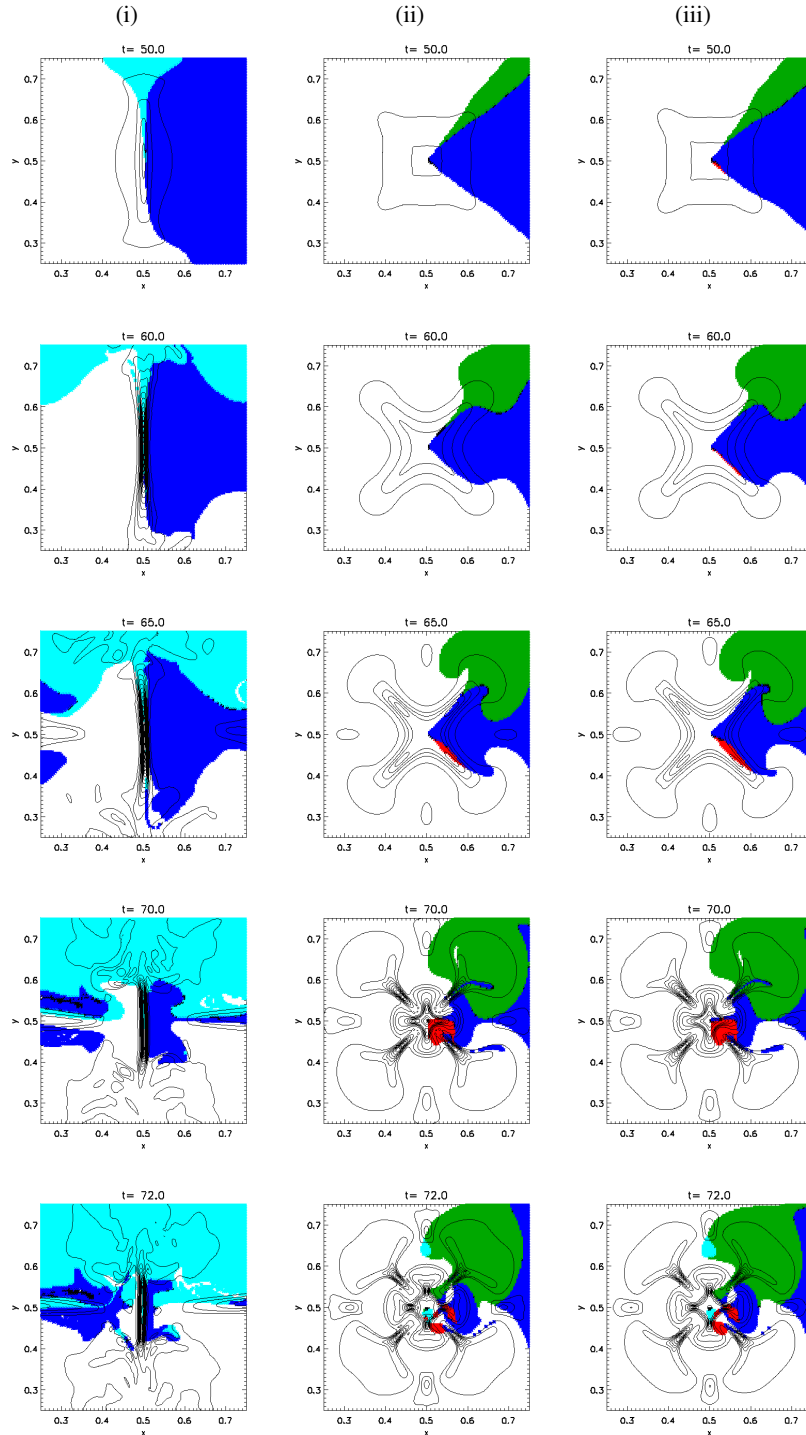


Figure 6.15: The field line connectivity associated with source C , traced from the mid-plane for $0.25 < x, y < 0.75$ for cases (i) 2 sources, (ii) 4 sources (weak) and (iii) 4 sources (compact). Flux with connectivity C_c , C_a , C_b and C_d is shown in dark blue, light blue, green and red, respectively. Over-plotted are the contours of parallel current density (j_{\parallel}) in the same plane.

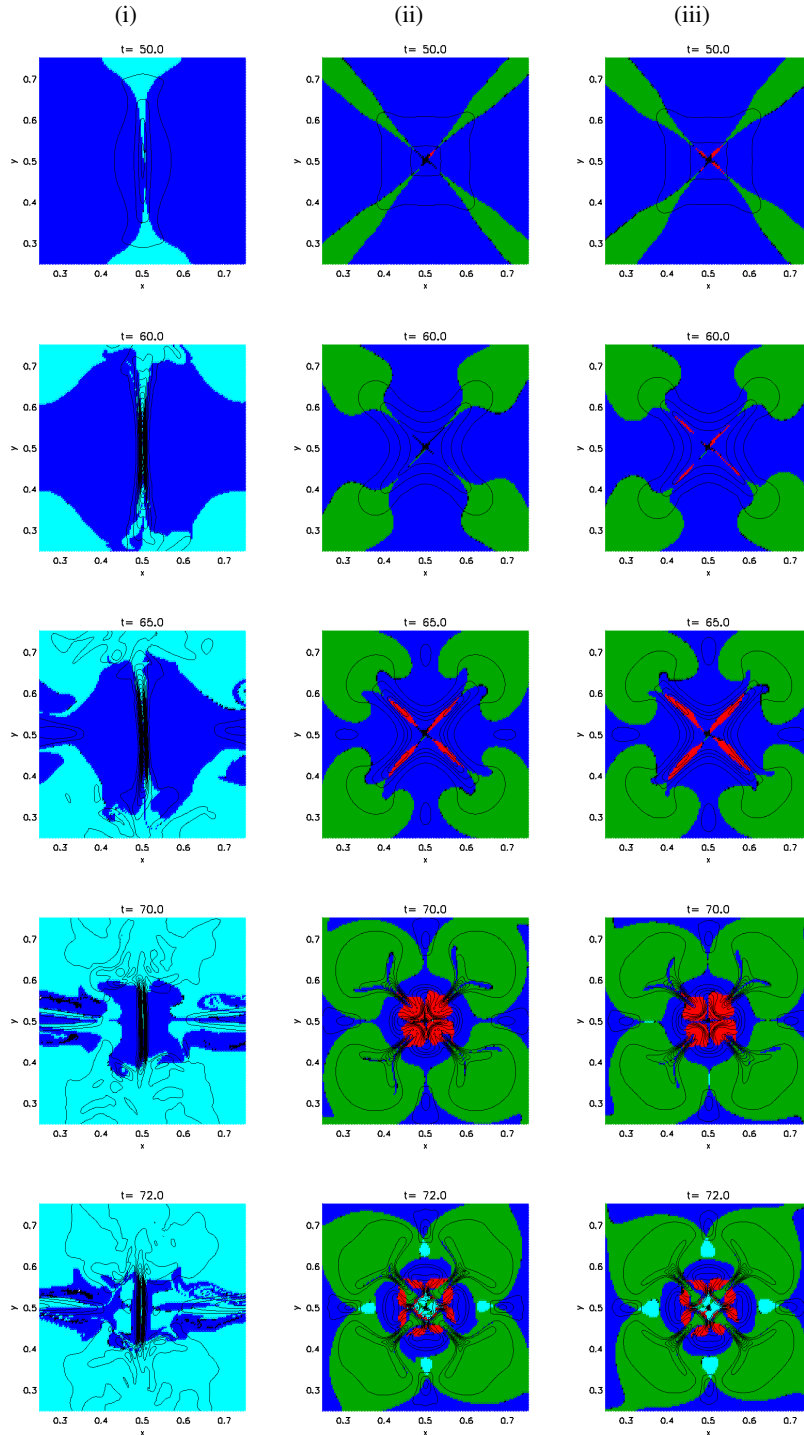


Figure 6.16: The same as in Figure 6.15 but for field lines traced to all sources on $z = 0$, where flux with connectivity original, opposite, anticlockwise and clockwise is shown in dark blue, light blue, green and red, respectively.

The final change in connectivity to occur for flux connected to source C is to the opposite source (Ca) on the upper boundary and appears at $t = 72$ (light blue in Figure 6.15). This ‘opposite’ flux occurred in two locations in source C on the lower boundary, as shown by the light blue in Figure 6.11. Correspondingly, the ‘opposite’ connectivity (light blue) flux occurs at two distinct locations in the mid-plane. One location is adjacent to the anti-clockwise reconnected flux (green) at $x = 0.5$ and the second is adjacent to the clockwise reconnected flux (red) towards the centre of the mid-plane, as seen in Figures 6.15ii and 6.15iii at $t = 72$.

Figure 6.16 shows the mid-plane connectivity for all four sources and it is clear that the connectivity changes we have described for source C happen symmetrically for all four sources. From Figures 6.16ii and 6.16iii, we see that the ‘opposite’ connectivity (light blue) occurs where two regions of differently connected flux expand into each other. Two previously reconnected flux regions are pushed together and a high current is built up, leading to this flux reconnecting again. For example, for cases (ii) and (iii) in Figure 6.16, the flux with connectivity Cb and Ba (both green) are pushed against each other and reconnect to form the light blue Ca flux that occurs at approximately $(0.5, 0.65)$ in the mid-plane. A similar process occurs where the clockwise reconnected flux meets. For example, flux with connectivities Cd and Da (red) are brought together at the centre of the mid-plane and a high current is formed between them, allowing the field to reconnect and form the flux connection Ca .

Therefore, the field lines are reconnected multiple times and as discussed in Parnell et al. (2011), reconnection does not occur in the most efficient way, but where the high current is formed.

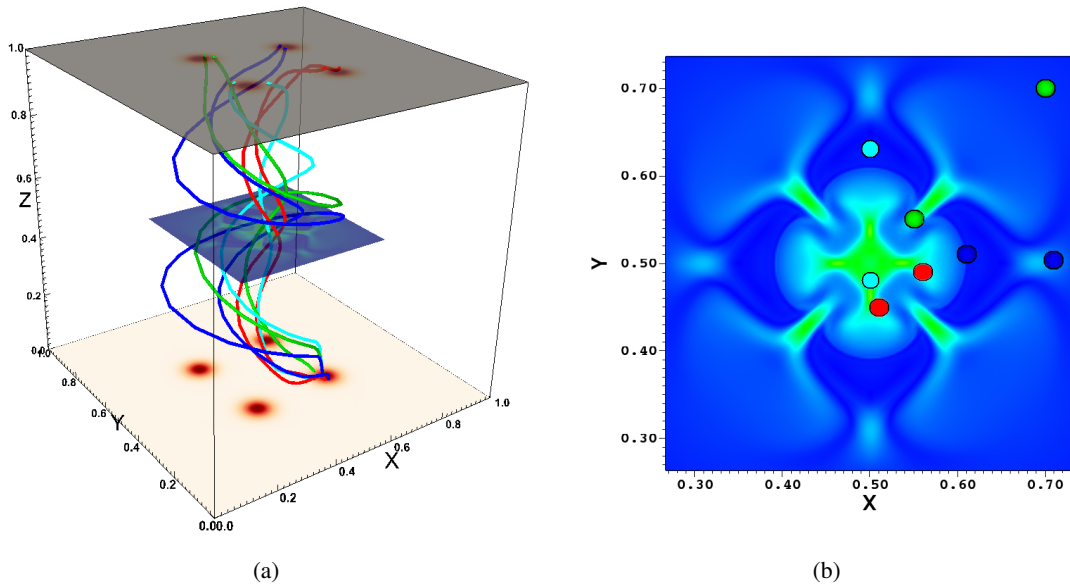


Figure 6.17: (a) A selection of field lines associated with source C traced from the mid-plane. (b) The positions from which the field lines are traced on the mid-plane, plotted on a contour of the current density, at $t = 72$ for case (iii).

The colour code of flux connectivities in the mid-plane does not allow us to see a different colour for flux that has already changed connectivity once, before reconnecting back to its original connection. However, this can be inferred from the percentage of flux with time in Figure 6.13a. We observe that at $t = 70$ the percentage of flux with its original connectivity (dark blue) begins to increase again for cases (ii) and (iii). This coincides with the appearance of the percentage of flux with opposite connectivity and with the decrease in the percentage of anticlockwise and clockwise flux. From the description above, this implies that the reconnection of the anticlockwise and clockwise flux produces both flux with opposite and original connectivity.

A selection of field lines with different connectivities associated with source C on the base is displayed at $t = 72$ for case (iii) in Figure 6.17a. The points from which each of the field lines are traced are also shown in the mid-plane by their corresponding connectivity colour in Figure 6.17b. The dark blue field lines appear highly twisted and helical in shape with a large radius, whereas the field lines that have reconnected to other sources appear slightly straighter.

The flux connectivities in the two source rotational case has been discussed in previous chapters and by De Moortel and Galsgaard (2006a) in similar experiments. The current increases along the current layer, seen at $x = 0.5$ in the mid-plane, and the two regions of connectivity Aa and Cc reconnected to produce two new regions of connectivity Ca and Ac . The percentage of flux connected to its original source is shown to decrease over time in Figure 6.13b. As the flux tubes rotation is continued for a greater angle, we see that the field lines also begin to reconnect back to their original connection after $t = 73$, due to the newly reconnected flux expanding and forming new current concentrations visible at $t = 70$ in the black contours at $y = 0.5$ in Figure 6.16i.

The connectivity evolves much faster and from an earlier time for case (i) with two sources. Although there are more possible sources to reconnect to, a larger percentage of the flux remains at its original connectivity for the four source cases (ii) and (iii) for the duration of the simulations.

6.2.2 Current Formation and Forces

Through the rotation of the sources on the boundaries, the magnetic field becomes twisted and a shear forms across the QSLs. As the magnetic field is twisted, small length scales are produced and a twisted current layer is formed in all three cases. The central current formation is shown in Figure 6.12 for cases (i), (ii), and (iii) at $t = 60$, after a total rotation of $2\theta \approx 3\pi$. Note, in these images, only the current within a central box in the domain ($0.1 < x, y, z < 0.9$) is displayed, to allow us to see the central current formation without the current on the boundary. The isosurfaces of the magnitude of current density are drawn for the same value of 2.5 (in normalised units) and the current layer in case (i) appears slightly larger, suggesting a higher current is present. The current layers appear more twisted in the four source cases (ii) and (iii) due to there being four

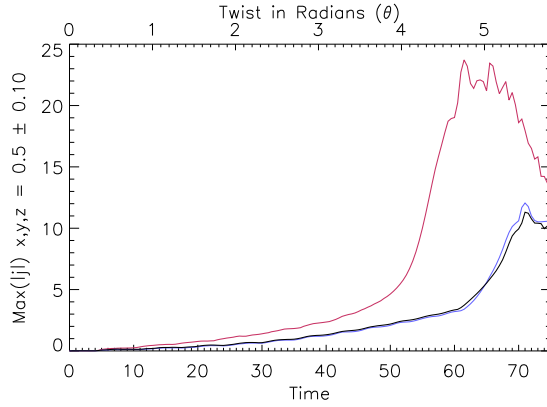


Figure 6.18: Maximum magnitude of current density in $0.4 < x, y, z < 0.6$ for cases (i) 2 sources, (ii) 4 sources (weak) and (iii) 4 sources (compact) shown in red, blue, and black, respectively.

‘wings’ of current that extend from the centre of the domain, shown in Figure 6.20.

The maximum magnitude of the current density in a central box of width 0.2 in the domain is plotted with time in Figure 6.18. The current density begins to increase earlier for case (i) (shown in red) compared to the others and at $t \approx 50$ begins to increase sharply, reaching a value of ≈ 24 in normalised units at $t = 61$. This is almost 50% more than the peak value that is reached by the four source cases (ii) and (iii) (≈ 12) ten time units later at $t = 71$, shown in blue and black in Figure 6.18. The maximum current density behaves very similarly with time for both four source cases (ii) and (iii). The strength and radius of the sources appear to have little impact as there is only a 4% difference in their peak values and both occur at $t = 71$. However, this is due to the maximum current being taken from the central region in the domain, whereas nearer the footpoints

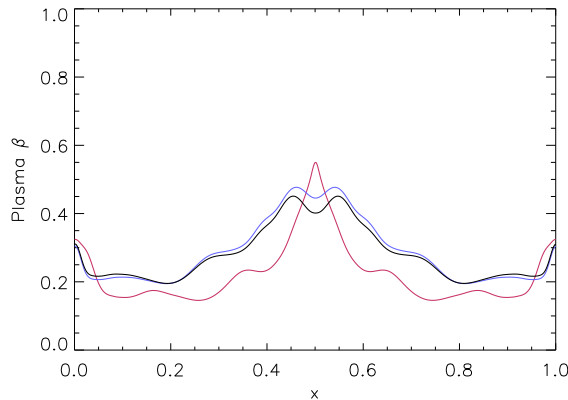


Figure 6.19: Magnitude of plasma β in the mid-plane at $y = 0.5$ at $t = 50$ for cases (i) 2 sources, (ii) 4 sources (weak) and (iii) 4 sources (compact) shown in red, blue, and black, respectively.

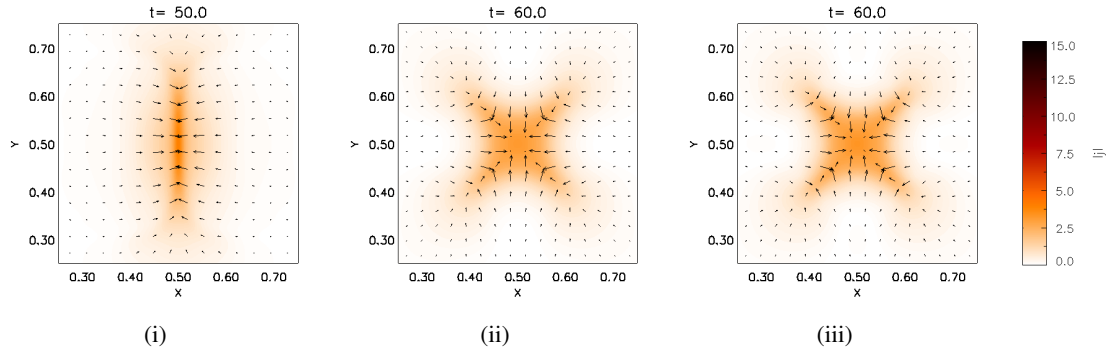


Figure 6.20: The arrows show the projected Lorentz force in the plane over plotted on contours of the magnitude of the current density in the mid-plane $0.25 < x, y < 0.75$ at $t = 50$ for case (i) 2 sources, and at $t = 60$ for cases (ii) 4 sources (weak) and (iii) 4 sources (compact). (Note, that the arrows are not normalised between the simulations and therefore show the direction but not the relative size of the forces between the cases.)

we expect there to be a larger difference in the current formed in the four source cases.

The formation of these current layers is due to oppositely connected field being driven together causing large gradients over small scales. For the majority of the run time of the simulations, away from the boundaries, the plasma β value is of the order of 10^{-1} , as shown in Figure 6.19. Therefore, as described in Chapter 1 the evolution of the field can be considered to be mainly attributed to the Lorentz force ($\mathbf{j} \times \mathbf{B}$), which can be divided into the magnetic pressure ($\nabla(B^2/2\mu_0)$) and the magnetic tension ($(\mathbf{B} \cdot \nabla)\mathbf{B}/\mu_0$) forces, which when calculated in normalised units from Lare3D this is equal to:

$$\mathbf{j} \times \mathbf{B} = (\mathbf{B} \cdot \nabla)\mathbf{B} - \nabla \left(\frac{B^2}{2} \right). \quad (6.2)$$

The Lorentz force in case (i) creates a stagnation point flow pushing the oppositely connected field towards the centre of the domain at $x = 0.5$ in the mid-plane, shown by the projected vectors of the Lorentz force in the mid-plane in Figure 6.20i. De Moortel and Galsgaard (2006a), in their original two source rotational experiments, found that this was mainly due to the magnetic tension force building up as the rotated field became highly twisted. This can also be seen in our two source experiment, where the initial Lorentz force is clearly due to the inward magnetic tension force, as shown by the arrows in Figure 6.21i (bottom row), while the magnetic pressure force acts outwards from the centre of the plane in Figure 6.21i (top row) at $t = 50$.

However, as the change in connectivity and current begin to increase sharply after $t = 50$, the magnetic pressure force locally around the current layer begins to change direction to act inwards. This is due to the magnetic field that builds up in the centre of the domain beginning to reconnect

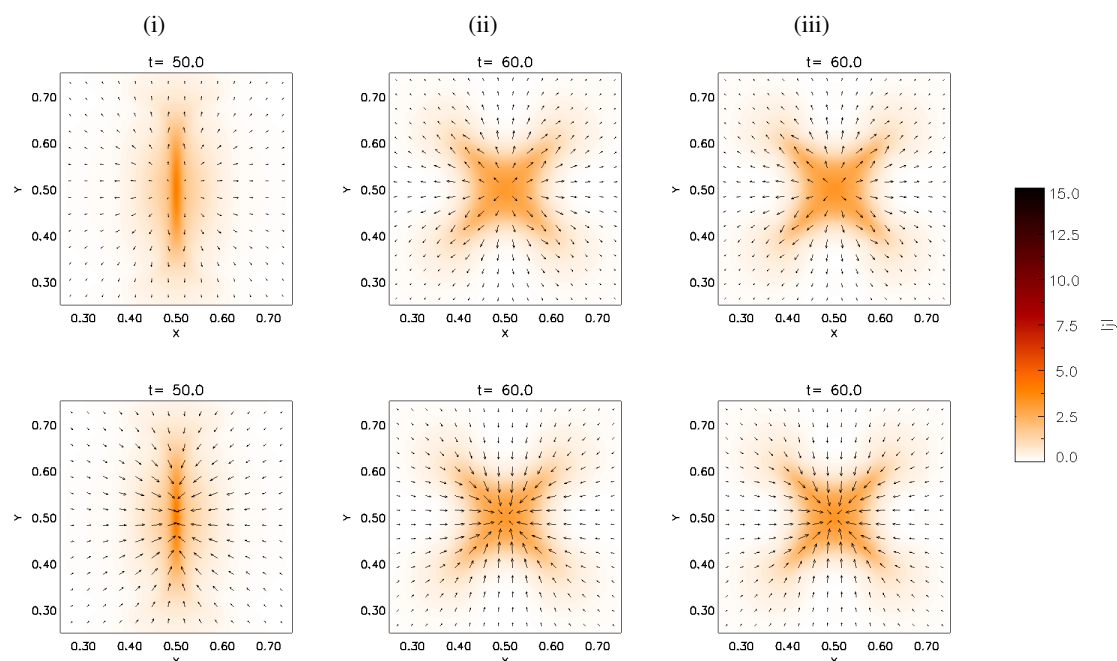


Figure 6.21: The arrows show the magnetic pressure (top row) and magnetic tension (bottom row) over plotted on contours of the magnitude of the current density in the mid-plane $0.25 < x, y < 0.75$ at $t = 50$ for case (i) 2 sources, and at $t = 60$ for cases (ii) 4 sources (weak) and (iii) 4 sources (compact). (Note, that the arrows are not normalised between the simulations and therefore show the direction but not the relative size of the forces between the cases.)

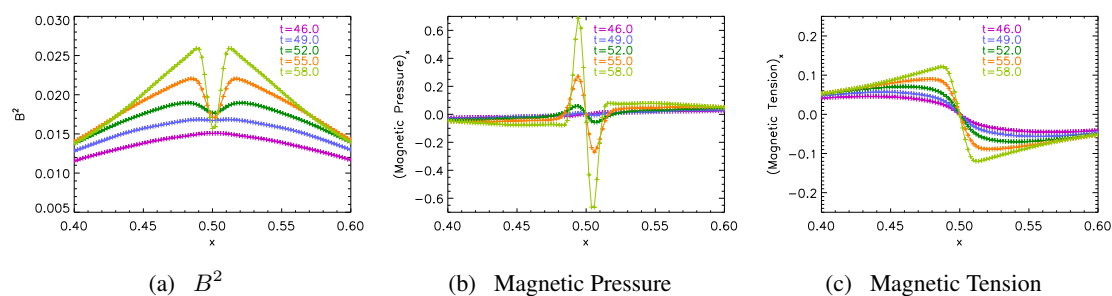


Figure 6.22: (a) B^2 and the x -components of the (b) magnetic pressure and (c) magnetic tension along $y = 0.5$ in the mid-plane. Displayed for various times for two flux tube case (i).

and hence the field strength along $x = 0.5$ reduces. This can be seen in Figure 6.22a, which shows B^2 across the current layer at $y = 0.5$. The gradient in B^2 creates the inwards magnetic pressure force around the current layer, shown in Figure 6.22b, while further away from $x = 0.5$ the magnetic pressure continues to act outwards.

In the four source cases, the forces build up in a similar way. For cases (ii) and (iii), the Lorentz force, the magnetic pressure and magnetic tension are displayed in Figures 6.20 and 6.21

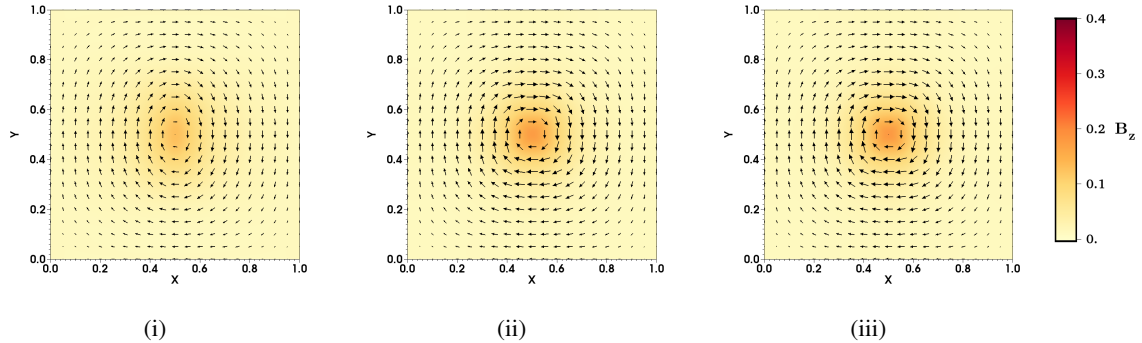


Figure 6.23: The arrows show the projected horizontal field components in the mid-plane, over plotted on contours of B_z , at $t = 50$ for case (i) 2 sources, and at $t = 60$ for cases (ii) 4 sources (weak) and (iii) 4 sources (compact). (Note, the arrows are not normalised between the cases.)

at time $t = 60$. This is 10 time units later than shown for case (i) and is the time just before the sharp increase in the magnitude of the current density for cases (ii) and (iii). This is a similar stage in their evolution as for the two source case at $t = 50$. Similarly to case (i), the curvature of the field from the boundary driving motions creates a magnetic tension force. However, for the four source cases the tension force in Figures 6.21ii and 6.21iii acts towards the centre of the domain equally in the x and y directions. As a high concentration of field is pushed towards the centre, an outwards magnetic pressure force also builds up in cases (ii) and (iii). The magnetic tension force begins to dominate the magnetic pressure, producing an overall inwards Lorentz force (in x and y), visible in Figures 6.20ii and 6.20iii.

The inwards Lorentz force in case (i), which is greatest in the x direction towards $x = 0.5$, causes the initially curved field structure to become elongated in the y direction around the centre of the plane. This is shown by the projection of the horizontal field in the mid-plane in Figure 6.23i and this shear in the B_y component of the field creates the high currents observed in case (i). In comparison, for cases (ii) and (iii) the Lorentz force is equally strong in both the x and y direction in the mid-plane. This in turn creates an almost ‘square’ horizontal field projection in the mid-plane (see Figures 6.23ii and 6.23iii). Therefore, initially, in cases (ii) and (iii) it is not directly in the centre of the mid-plane that the greatest shear in the magnetic field (current) builds up, but at the corners of this square along the locations of the QSLs.

The Lorentz force and its magnetic pressure and tension components that act to push the field towards the QSLs between the different flux tubes (as well as directly towards the centre of the mid-plane) can be seen in Figure 6.24 for case (ii) (case (iii) behaves similarly). The direction of the forces are shown at $t = 65$ for the localised area of the mid-plane between $0.5 < x, y < 0.65$, focused around one wing of current that forms between regions of different connectivity. As in the two source case, the magnetic tension is acting inwards towards the centre of the plane, but also towards the line $y = x$. It is this initial tension that allows the current to build up at the

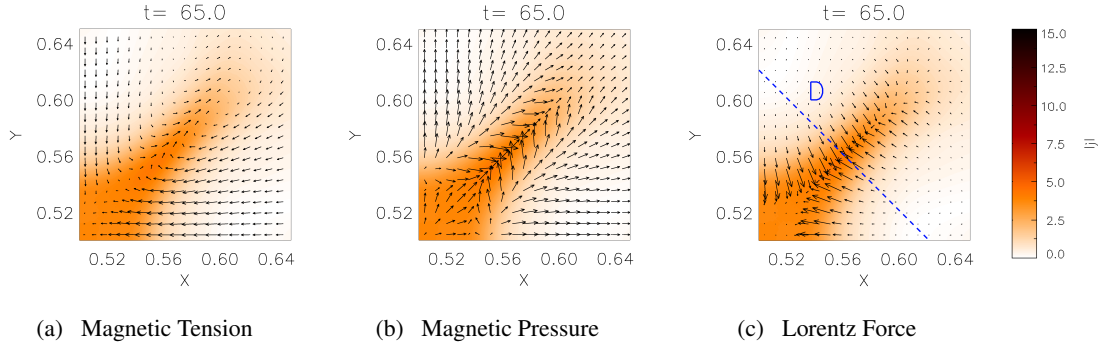


Figure 6.24: The arrows show the (a) magnetic tension, (b) magnetic pressure and (c) Lorentz force and are plotted on contours of the magnitude of the current density in the section of the mid-plane, $0.5 < x, y < 0.65$ at $t = 65$ for case (ii).

centre and along $y = x$. As the field begins reconnecting, the magnetic pressure that is acting outwards from the centre of the plane, also begins to act locally inwards towards the line $y = x$ in the mid-plane, seen in Figure 6.24c. This behaviour is symmetric for the other four wings of current in the mid-plane.

The peak current density in the mid-plane for cases (ii) and (iii) initially occurs at the location of the QSLs along $y = x$ and $y = -x$. Therefore, in order to compare the magnitude and the timing of the build up of the Lorentz force in the two and four flux tube cases, we have taken a cut (labelled ‘D’ in Figure 6.24c) normal to the current formed along $y = x$ and plot the Lorentz force, acting normal to the current layer, along ‘D’. We then compare this to the x -component of the Lorentz force that acts normal to the current layer in case (i) at the cut $y = 0.5$. The calculated normal component of the Lorentz force across a current layer for cases (i), (ii) and (iii) is shown in Figure 6.25.

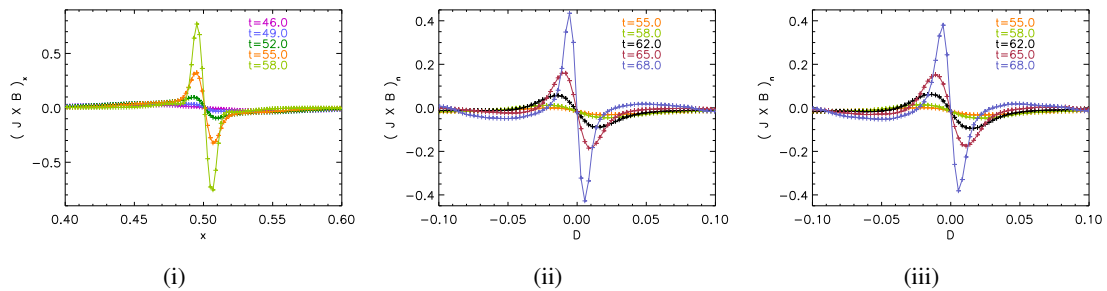


Figure 6.25: The normal component (to the current layer) of the Lorentz force for case (i) along $y = 0.5$ and cases (ii) and (iii) along cut D (shown in Figure 6.24c) centred on $(x, y) = (0.56, 0.56)$ in the mid-plane. Note the different times displayed in panel (i) compared to panels (ii) and (iii).

The Lorentz force begins to increase much earlier for the two flux tube case, in line with the earlier increase in current. By $t = 55$, the Lorentz force grows quickly and has a maximum normal component to the current layer at this time (shown in orange) of 0.32 in Figure 6.25i. In comparison, in Figures 6.25ii and 6.25iii the Lorentz force acting across the current layer at $t = 55$ for cases (ii) and (iii) has barely begun to increase and is approximately 0.05. After this time, the Lorentz force does increase for the four flux tube cases but reaches less than half the magnitude observed for case (i).

Overall, the location of the sources in the two flux tube case means that, when a rotational driver is applied, the oppositely directed field of the flux tubes is brought directly towards the centre of the domain and a single large shear in B_y is produced. This means that the current is able to increase earlier and to higher values. This set-up, described analytically by Priest et al. (2005), is highly idealised to produce this concentrated single current layer. In comparison, in the four source case, the regular distribution of the sources in the circle of rotation, means that flux tubes first create a shear between the neighbouring flux tubes, which due to the relative angles of the magnetic field lines will always be less than that induced in the two source case.

6.2.3 Energetics

Figure 6.26 shows the evolution of the volume integrated energy densities for the three cases. We can qualitatively describe the overall energy evolution for all three cases as follows: When the driving velocity acts on the field, the field lines are ideally advected and the magnetic field becomes twisted, gradually increasing the magnetic energy in the domain. Due to the twisted field lines and induced Lorentz force (seen in Fig 6.20) small scales begin to form, creating locations of high current values. These locations of high current are shown in the mid-plane at a series of times in Figures 6.27 and 6.28. As the high currents occur, the diffusion term becomes important, converting the built up magnetic energy into internal energy, as seen in Figure 6.26b. The build up of magnetic energy continues to occur until the onset of reconnection, when the increase of the magnetic energy slows down slightly and energy is converted more rapidly into internal energy and a sudden increase in kinetic energy occurs from the outflow of the reconnected field lines.

This general behaviour can describe the evolution of all three cases, however, as discussed in Section 6.2.2, the timing and magnitudes vary between the simulations. The two flux tubes in case (i) develop a higher current value earlier than cases (ii) and (iii) and reconnection begins to occur at approximately $t = 50$, when a sharp increase occurs in the kinetic energy, tripling the value in 10 time units. This is also when the percentage of flux changing connectivity begins to increase at a faster rate, increasing from 10% to almost 90% between $t = 50$ and $t = 60$. The rise in kinetic energy for cases (ii) and (iii) occurs later, at approximately $t = 60$, though its maximum value is only 25% of the peak kinetic energy of case (i).

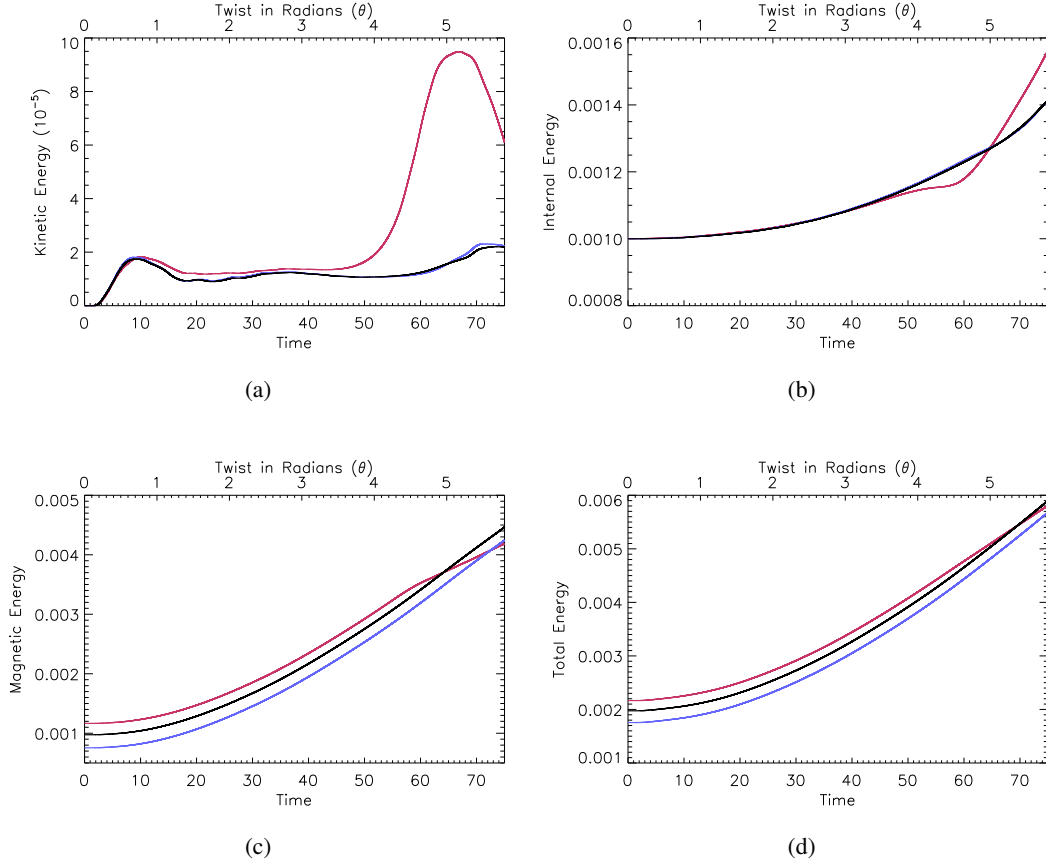


Figure 6.26: (a) Kinetic, (b) internal, (c) magnetic and (d) total volume integrated energies for cases (i), (ii) and (iii) shown in red, blue, and black respectively.

The magnetic energy is the dominating contribution to the total energy evolution in Figure 6.26d. It is more than three times the internal energy and almost two orders of magnitude larger than the kinetic energy. As discussed in Section 6.1, the initial volume integrated magnetic energy density differs between the three cases on the order of 10^{-4} , approximately a 30% variation. However, although cases (ii) and (iii), shown in blue and black, have different magnetic energies to begin with, their kinetic and internal energy evolutions are almost identical. There is only a slightly greater kinetic energy value occurring a few time-steps sooner for case (ii) than case (iii).

The peak in kinetic energy in case (i) occurs at $t = 67$ and the source of this kinetic energy can be seen in Figure 6.27, where the white arrows show the projected velocity vectors in the mid-plane. At $t = 60$ there is a large outward velocity along the line $x = 0.5$ from the centre of the plane with maximum magnitude at $t = 62.5$ (in the mid-plane) of $0.27v_A$ of the maximum Alfvén velocity in the mid-plane, a clear sign of reconnection occurring. The magnetic field is 3D and reconnection is not confined to the mid-plane, but the current contours and velocities shown

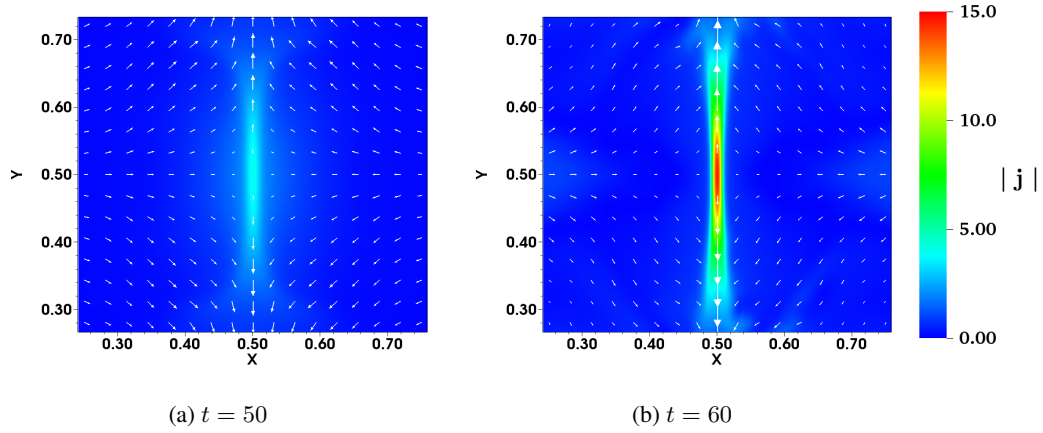


Figure 6.27: Contours of the magnitude of the current density in the mid-plane $0.25 < x, y < 0.75$ at (a) $t = 50$ and (b) $t = 60$ for case (i). The arrows show the projected velocity in the plane.

in the plane can be used to illustrate the differences between the cases.

Figure 6.28 displays the velocity vectors for cases (ii) and (iii) at $t = 65$ and $t = 70$ in the mid-plane, when there is an increase in kinetic energy shown in Figure 6.26a. Note that these vectors are not drawn on the same scale as the velocity vectors in Figure 6.27. At $t = 65$ an ‘X’ shape current concentration has formed between the regions of different connectivity and outflows towards the corners of the plane are clearly visible in both case (ii) and case (iii). By $t = 70$ in Figure 6.28b, the concentrations of current have separated and reduced in length and the outflows now also act towards the centre of the plane. It is these outflows that lead to the formation of further current layers, now seen as a ‘+’ in the centre of the mid-plane. As these newly formed current concentrations allow reconnection to occur, we expect that, if the simulations were to continue, further outflow velocities could lead to the creation of smaller scales, symmetrical about the centre of the plane. The velocity outflows in cases (ii) and (iii) are much smaller than the outflows observed in case (i). In terms of the maximum Alfvén velocity in the mid-plane, the maximum velocity (in the mid-plane) for cases (ii) and (iii) are $0.05v_A$ and $0.04v_A$, respectively, and occurs at $t \approx 74$. This is much smaller than in case (i) and agrees with the reduced kinetic energy maximum for cases (ii) and (iii), compared to case (i), and suggests the reconnection is weaker.

We have so far considered the evolution of the individual energies in the domain. We now consider the Poynting flux injected into the domain and the resulting energy into the system from this. The evolution of the Poynting flux (see Figure 6.29) behaves very similarly for all three cases initially, as we would expect from having the same total surface magnetic flux and driving velocity. The Poynting flux can be divided into the three integrated volume contributions: the rate of change of the magnetic energy, the Ohmic (Joule) dissipation and the work done by the Lorentz

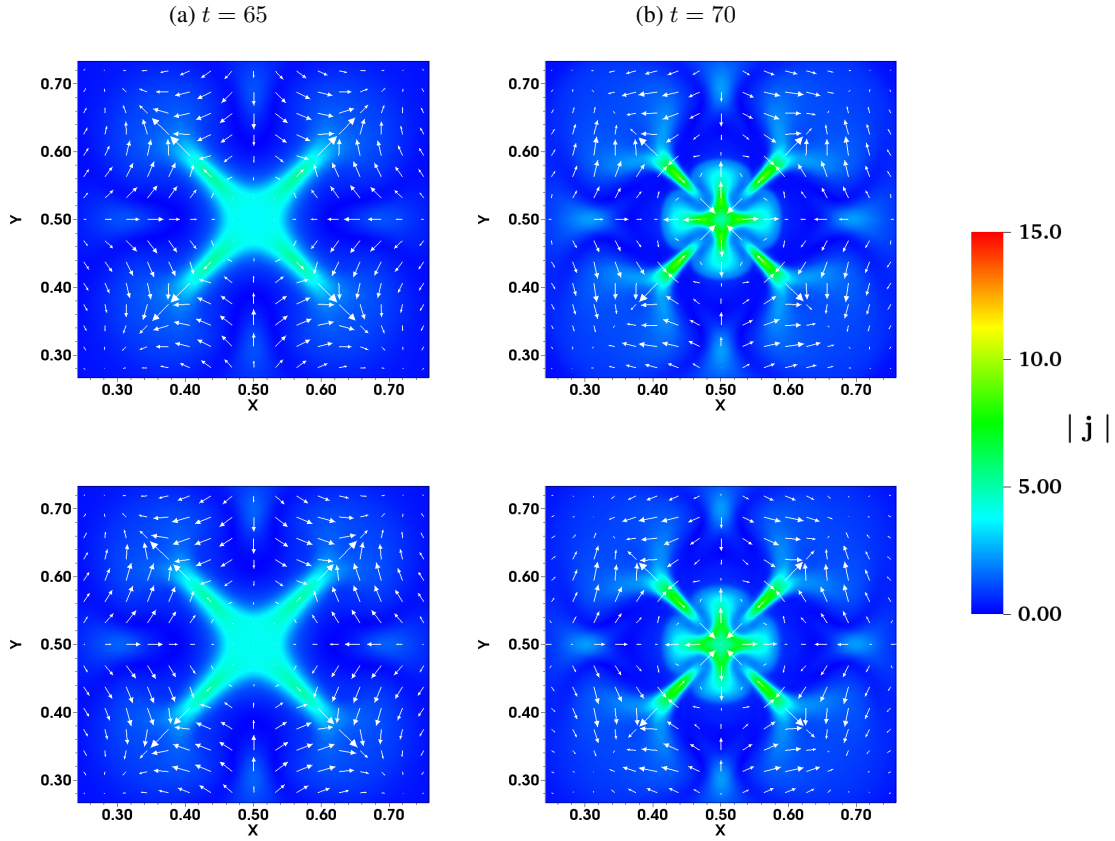


Figure 6.28: Contours of the magnitude of the current density in the mid-plane $0.25 < x, y < 0.75$ at (a) $t = 65$ and (b) $t = 70$ for cases (ii) (top row) and (iii) (bottom row). The arrows show the projected velocity in the plane.

force (see Equation 5.1). The evolution of each of these terms is plotted in Figures 6.29i, 6.29ii and 6.29iii for cases (i), (ii) and (iii), respectively.

Initially, as the Poynting flux increases, most of the energy goes directly into the magnetic field and the rate of change of the magnetic energy increases. There is also a slight increase in the work done by the Lorentz force near the start of all three cases that reduces after 10 time units. This can be attributed to an initial wave induced in the field, which increases the kinetic energy in the domain and is visible as the small oscillations in the work done on the plasma by the Lorentz force.

For the majority of all three simulations, the bulk of the Poynting flux injected into the domain is seen as the change in the magnetic energy as the field becomes highly twisted. As the magnitude of the current density gradually increases in the domain, as seen in Figure 6.18, this allows the Joule dissipation (dashed line, in Figure 6.29) to build up slowly in all cases. When the magnitude of the current density increases sharply, which occurs first in case (i), we see a corresponding faster

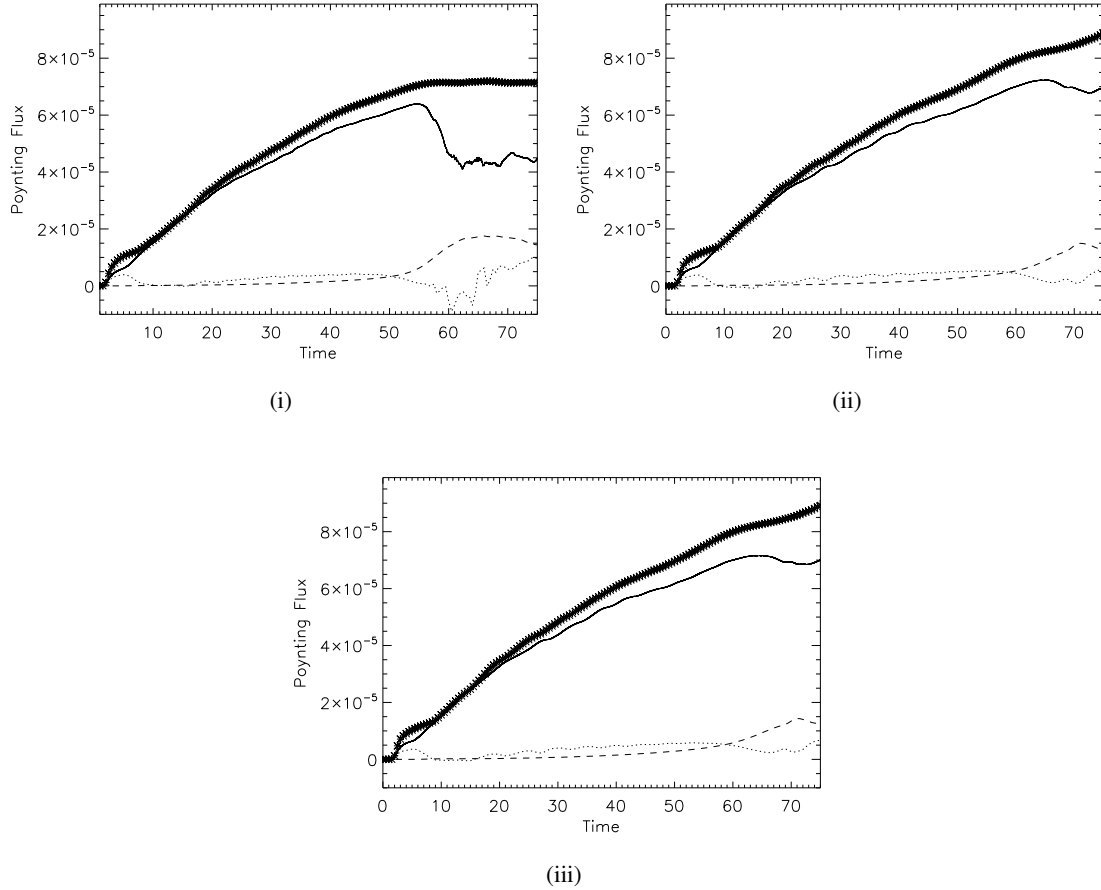


Figure 6.29: The Poynting flux (crosses) with time, for cases (i), (ii) and (iii). The solid line shows the rate of change of magnetic energy, the dotted line work done by the Lorentz force and the dashed line represents the Joule dissipation.

rise in the Joule dissipation in Figure 6.29. This occurs at $t = 50$ for case (i) and approximately 10 time units later in Figures 6.29ii and 6.29iii for cases (ii) and (iii). The Joule dissipation has a maximum value of 1.8×10^{-5} by $t = 65$ in case (i). This is similar for cases (ii) and (iii) which peak at 1.5×10^{-5} , but at a later time of $t = 71$.

After the increase in the Joule dissipation, the rate of change in the magnetic energy begins to decrease in all cases, as the magnetic energy is converted through reconnection into kinetic and internal energy. The change in magnetic energy reduces by approximately 5×10^{-6} (7%) for both cases (ii) and (iii), before beginning to increase again. In other words, the magnetic energy injected into the system by the continuous driving velocity must be greater than the magnetic energy released through diffusion and reconnection.

For case (i), the rate of change in magnetic energy reduces by 1.7×10^{-5} (26%), which is more than three times the reduction in cases (ii) and (iii). After $t = 56$ we are unable to fully resolve

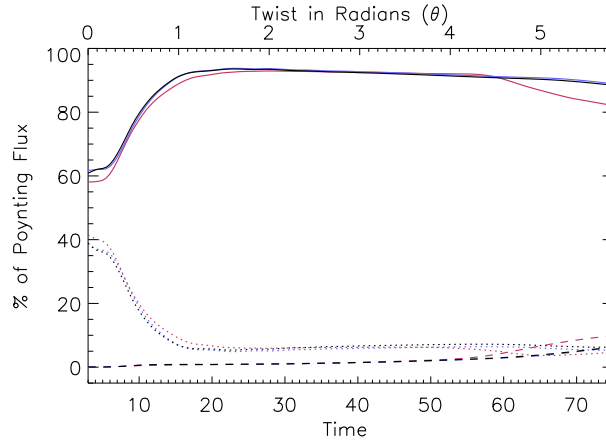


Figure 6.30: The integrated volume contributions of change of magnetic energy (solid), integrated work done by the Lorentz force (dotted) and integrated Joule dissipation (dashed) as a percentage of the integrated Poynting flux at each time, for cases (i), (ii) and (iii) shown in red, blue, and black, respectively.

the current layer and this causes a small loss of energy conservation of approximately 4% of the total Poynting Flux. This loss of energy conservation implies that the change in magnetic energy is reduced through numerical diffusion without the corresponding increase in the Joule dissipation or work done by the Lorentz force. The value of the Joule dissipation in Figure 6.29i can therefore be considered as a lower bound.

The timing of the reduction in the rate of change in magnetic energy for case (i) coincides with the increase in the current density evolution at $t = 50$ and the earlier increase in the percentage of reconnected flux seen in the connectivity plots in Section 6.2.1. Due to this reconnection taking place in case (i) at an earlier stage in the simulation, the magnetic field diffusion and rearrangement from reconnection alters the angle of the field at the upper and lower boundaries and thereby alters the amount of energy introduced by the Poynting flux. The total Poynting flux injected into the domain overall is therefore reduced compared to cases (ii) and (iii). This is clearly visible in Figure 6.29, where, by the end of the experiment, the Poynting flux entering the domain is approximately 7.2×10^{-5} . For cases (ii) and (iii) the Poynting flux entering the domain continues to increase and is over 20% larger than the final value for case (i).

Due to the different values of Poynting flux injected into the domain, it is useful to consider the components as a percentage of the integrated Poynting flux over time (see Figure 6.30). For case (i), in red, by the end of the simulation 10% of the Poynting flux has gone into Joule dissipation (dashed line). However, as discussed, this can be considered a minimum estimate. A slightly smaller value ($\approx 6\%$), of the Poynting flux goes into Joule dissipation for both of the four source cases. This suggests that the two source case is more efficient at Ohmic heating, as we would

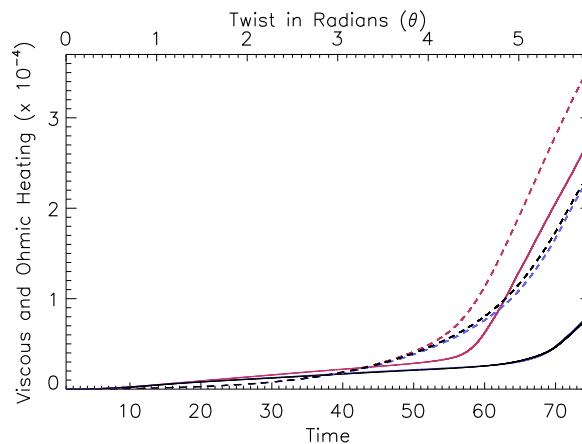
assume from the high current values.

In these experiments, the Joule dissipation never becomes larger than the rate of change in magnetic energy. In other words, there is always more energy being injected through the boundary driving than being dissipated. This is in contrast to the experiments carried out by De Moortel and Galsgaard (2006a) and Wilmot-Smith and De Moortel (2007), where for a similar two flux tube experiment the dissipation exceeded the injected magnetic energy due to the fast reconnection occurring. However, the current evolution and therefore Joule dissipation and reconnection are strongly dependent on the resistivity used in the simulations.

The work done by the Lorentz force is very small for most of cases (ii) and (iii) in Figure 6.29. In case (i), however, it becomes slightly larger and negative when the reconnection occurs. A negative work done results from the Lorentz force acting in the opposite direction to the plasma velocity. This occurs due to the large outflow velocities from the ends of the current layer acting in the opposite direction to the inwards Lorentz force. This negative value does not occur in cases (ii) and (iii) as the outflow velocities are much smaller, as shown by the kinetic energy in Figure 6.26.

6.2.4 Distribution and Magnitude of Heating

The volume and time integrated Ohmic heating and viscous heating are both displayed as a function of time in Figure 6.31. In our experiments, there is no uniform viscosity present but shock viscosity is used and contributes to the heating. For all the simulations, the total Ohmic heating exceeds the viscous heating in the domain. Cases (ii) and (iii) have very similar heating evo-



(a)

Figure 6.31: The integrated Ohmic (dashed) and viscous (solid) heating for cases (i), (ii) and (iii) shown in red, blue, and black, respectively.

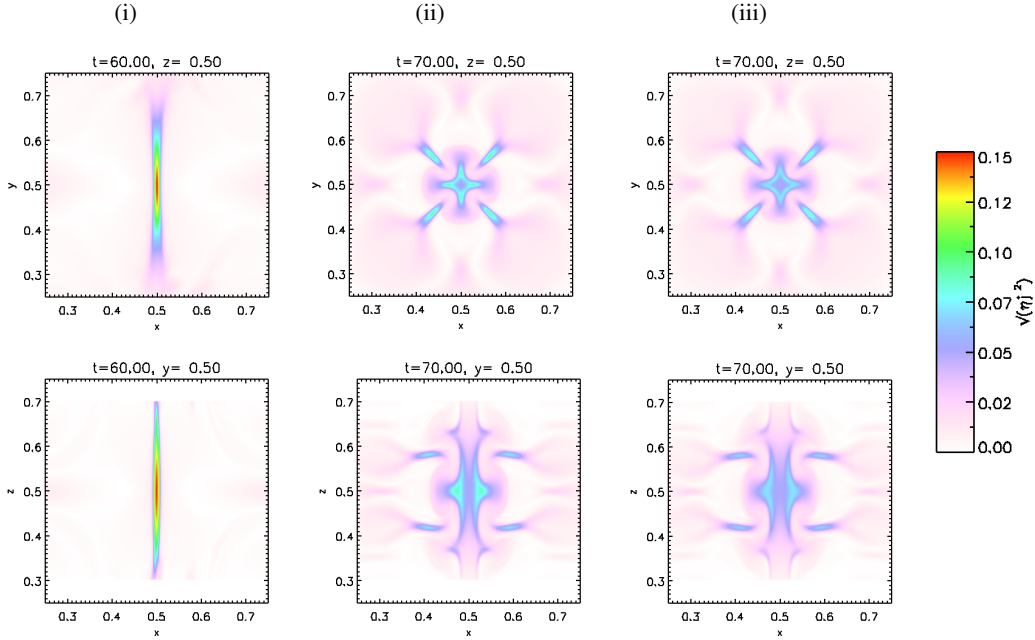


Figure 6.32: Contours of $\sqrt{\eta j^2}$ in the mid-plane between $0.25 < x, y < 0.75$ (top row) and at $y = 0.5$ with $0.25 < x, z < 0.75$ (bottom row), at $t = 60$ for case (i) and at $t = 70$ for cases (ii) and (iii).

lutions. By the end of the simulations, the total viscous heating is approximately a third of the Ohmic heating for both cases (ii) and (iii). In contrast, the total viscous heating is approximately three quarters of the total Ohmic heating in case (i) by $t = 75$.

The viscous and Ohmic heating begin to increase sooner for the two source case. In all cases there are two stages of Ohmic heating: a gradual increase, followed by a rapid increase coinciding with the experiments rapid rise in current values, shown in Figure 6.18. Similarly, there are two distinct stages of viscous heating. The viscous heating increases slightly and then a sudden increase occurs at the same time we saw the peak values in the kinetic energy. There is a delay between the increase in Ohmic heating and the viscous heating for each experiment, but this delay is shorter for case (i).

To consider the distribution of heating, contours of the square root of the Ohmic heating, $\sqrt{\eta j^2}$, are displayed in Figure 6.32 in the mid-plane (top row) and in the plane $y = 0.5$ (bottom row). These are shown at $t = 60$ for case (i) and $t = 70$ for cases (ii) and (iii) to coincide with the times of most intense heating for the different simulations.

The high Ohmic heating in the two flux tube case is concentrated along the single current layer built up between the flux tubes. It is highly localised between $0.3 < y < 0.7$ and around $x = 0.5$ in the mid-plane and is strongest in the centre. The bottom image of Figure 6.32i shows

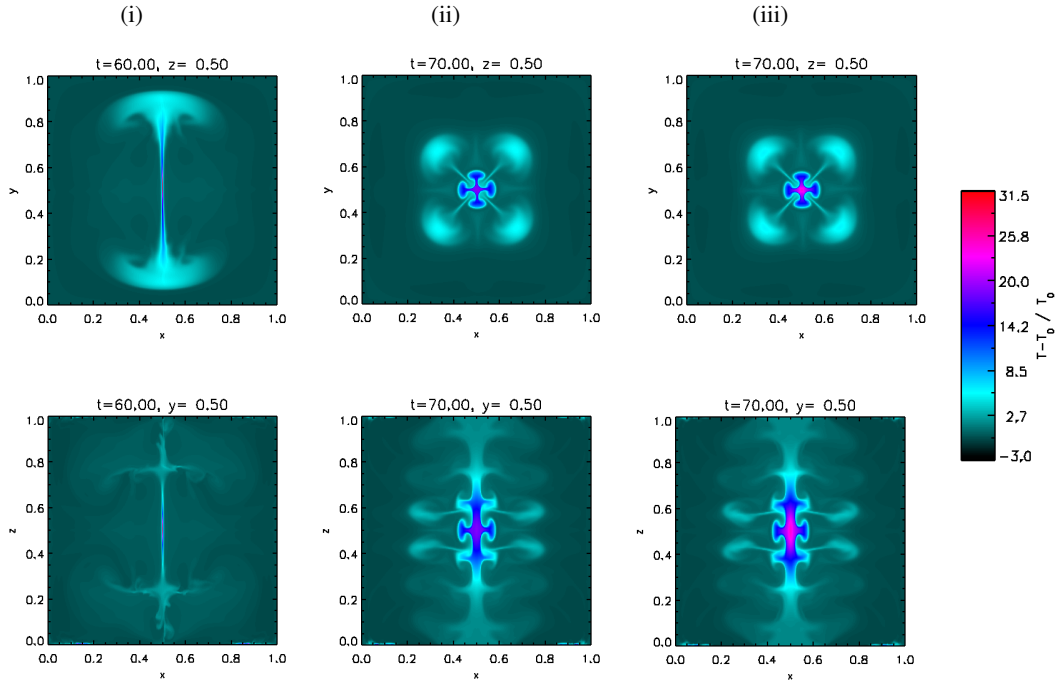


Figure 6.33: Contours of $(T - T_0)/T_0$ in the mid-plane (top row) and at $y = 0.5$ (bottom row) at $t = 60$ for case (i) and at $t = 70$ for cases (ii) and (iii). Note the different extent of the domain displayed compared to Figure 6.32.

the distribution with z . There is extended Ohmic heating between the flux tubes as reconnection occurs over a broad interval in z between 0.3 and 0.7. The heating is strongest in the mid-plane, although this might be an artificial development, due to the resistivity that decreases exponentially from the mid-plane (see Section 3.2.2).

In the cases with four flux tubes, the Ohmic heating distribution reflects the current build up, as expected. There is therefore a much larger area undergoing heating compared to the two source case but with a smaller peak value. The Ohmic heating is slightly greater for case (ii) than case (iii) at $t = 70$, in line with the slightly higher peak magnitude of current density seen in Figure 6.18.

We can further consider the distribution of total heating by examining the temperature difference contours in Figure 6.33 for cases (i), (ii) and (iii). These show $(T - T_0)/T_0$ (the proportional increase from the original temperature at $t = 0$) in the mid-plane (top row) and in the plane $y = 0.5$ (bottom row). The locations of strong Ohmic heating clearly show a temperature increase, but Figure 6.31 showed that a large proportion of the heating was also due to viscous shock heating, particularly for case (i). The locations of this viscous heating can be inferred from the contours of the temperature difference in Figure 6.33. Broader more diffuse areas of heating occur where we observed the large velocities from reconnection outflows, as shown in Figures 6.27 and 6.28, implying shocks are occurring. Due to the larger number of QSLs in cases (ii) and (iii), there

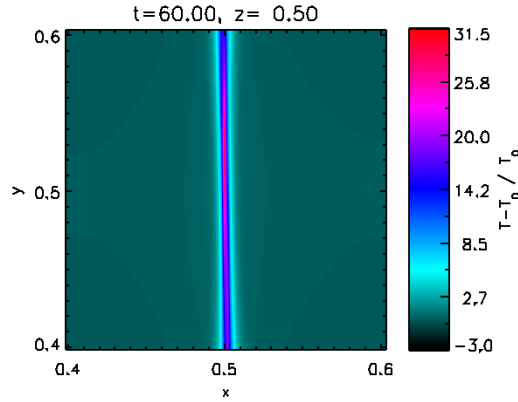


Figure 6.34: Contour of $(T - T_0)/T_0$ for $0.4 < x, y < 0.6$ in the mid-plane (top row) at $t = 60$ for case (i).

are more locations of reconnection outflows and therefore more distributed viscous heating in the mid-plane in Figures 6.33ii and 6.33iii. In Section 6.2, the field lines that had already reconnected in cases (ii) and (iii) were pushed towards the centre of the mid-plane and began to reconnect to the ‘opposite’ source. The strong outflows in the centre of the domain can therefore be seen as the result of this second stage of reconnection.

In cases (ii) and (iii) the temperature increase at $y = 0.5$ in Figure 6.33 (bottom row) also shows a broader area of heating between $0.3 < z < 0.7$. At the time shown, the maximum temperature increase for case (iii) occurs towards the centre of the domain and is 25% greater than the maximum temperature increase in case (ii).

Overall, the heating remains fairly localised towards the central regions of the domain and the peak values occur around the mid-plane. The largest temperature increase actually occurs in case (i), in a very small, barely visible region in Figure 6.33, but it is clearer in the enhanced contour (around $x = 0.5$ of the mid-plane) shown in Figure 6.34. The maximum increase in the temperatures (as a proportion of the initial temperature T_0) occurring at the centre of the domain are 30.5 (at $t = 60$), 19.1 and 24.4 (at $t = 70$) for cases (i), (ii) and (iii). Using the normalisation value of $T_0 = 5.76 \times 10^8$ K, given in Section 2.2, the illustrative maximum values of temperature are about 6.0×10^7 K, 3.8×10^7 K and 4.8×10^7 K for cases (i), (ii) and (iii), respectively, compared to an initial temperature of 1.9×10^6 K. These are generally high temperatures, but similar to those found by Bowness et al. (2013) when considering a uniform shear and the heating produced due to reconnection. (Further comparable temperature and heating values at the end of the experiments are given in Table 6.3.)

It is important to note, however, that in these experiments thermal conduction and radiation are not present and would normally act to distribute the heating and reduce the maximum temperature

value. Botha et al. (2011) found that when examining the kink instability in coronal loop models, using Lare3D, the inclusion of thermal conduction produces temperatures of an order of magnitude lower than occurs without it.

6.2.5 Summary

We have compared three simple numerical experiments in which flux tubes with different sizes and different maximum magnetic flux values are rotated by footpoint driving motions. The slow ($< v_A$) footpoint driving velocity acts to gradually twist the field through a series of equilibria to form layers of high current. The simulations are carried out for 75 time units for the two and four flux tube experiments. This is equivalent to a rotation of $\theta \approx 7\pi/4$ on one boundary and a total twist of double this value.

In case (i), with two flux tubes, a strong Lorentz force creates a central twisted current layer along the QSL between areas of different connectivity. The tension force acts to bring oppositely connected field together along the QSL and reconnection occurs. In cases (ii) and (iii), the Lorentz force acts to build up current in an ‘x’ shape layer in the mid-plane, that is again twisted with height. The current build up is slower in comparison to case (i) and a smaller maximum value is achieved. The onset of reconnection therefore occurs later for cases (ii) and (iii) and is weaker, with smaller outflow velocities. The presence of the extra two flux tubes in cases (ii) and (iii) mean that it is between adjacent flux tubes that the high current first begins to form and where reconnection first occurs.

The reconnection in case (i) is comparable to the experiments carried out by De Moortel and Galsgaard (2006a), where initially there are two regions of connectivity increasing to four after reconnection occurs. In comparison, for cases (ii) and (iii), there are initially four regions of connectivity and by the end of the experiment there are sixteen different connectivities. The changes in connectivities are not trivial and due to reconnection outflows and multiple smaller current concentrations, multiple reconnection occurs. In cases (ii) and (iii) field lines become connected to the ‘opposite’ source only through multiple reconnection with neighbouring sources. However, we speculate that with longer simulations the current structure would become highly fragmented and concentrated towards the centre of the plane, allowing direct reconnection to the opposite source eventually. A summary of the percentage of flux reconnected for increasing twist θ for the three cases is presented in Table 6.2.

The Ohmic heating associated with the diffusion and reconnection of the magnetic field is highly localised between the two flux tubes for case (i). In comparison, the four flux tube set-up in cases (ii) and (iii) allows for more locations (along QSLs) for current and therefore Ohmic heating to occur, although this is in general weaker. Due to the fast outflow velocities, in case

Table 6.2: Overview of the angle θ (rotated on one boundary and given in radians) at which different stages of reconnection occur for cases (i), (ii) and (iii).

	(i) Two Sources	(ii) Four Sources	(iii) Four Sources
Onset of reconnection	2.18	2.90	2.66
10 % reconnected flux	3.94	4.43	4.43
25 % reconnected flux	4.51	5.07	5.00
50 % reconnected flux	4.91	—	—
75 % reconnected flux	5.28	—	—
Max % reconnected flux	89%, $t = 73$, $\theta = 5.64$	43%, $t = 70$, $\theta = 5.39$	45%, $t = 71$, $\theta = 5.48$

(i) $\approx 45\%$ of the heating produced is due to viscous shock heating, compared to just 25% in cases (ii) and (iii). However, these comparative values of viscous heating are clearly dependent on the choice of numerical parameters, as is the case for the resistive heating. The shock viscosity parameters in Lare3D, are chosen to be $\nu_1 = 0.1$ and $\nu_2 = 0.5$ as discussed in Section 1.5.2. Although we do not consider the impact of altering these parameters in this thesis, we note that in the corona $\nu \gg \eta$ and viscosity is expected to play an important role in heating the plasma. Indeed, many numerical investigations (e.g. Armstrong and Craig, 2014) have shown that viscous dissipation should dominate resistive dissipation and account for a large fraction of energy release in flares. Therefore although a comparison of the amount of viscous heating can be made between the different cases, the relative importance of viscous and Ohmic heating may be considered as unrealistic.

Directly comparing cases (ii) and (iii), there is minimal qualitative or quantitative difference in the evolutions. In the early stages, case (iii), with more concentrated stronger sources, appears to evolve slightly faster with higher current values to begin with and reconnection occurs earlier, but only by a few time-steps. However, later in the simulation, case (ii) with broader weaker sources reaches a 5% higher peak value of current density and produces 5% higher maximum velocities. This suggests that due to the slower build up of current and the later reconnection, the heating is stronger though over a shorter time. Interestingly, it is case (iii) which evolves faster that has the slightly greater Ohmic heating summed over the simulation (see Figure 6.31), resulting in a 20% larger maximum temperature for case (iii) compared to case (ii). However, although the difference in heating is very small, due to the heating occurring in the same few locations the increase in temperature is enhanced.

So far, we have compared the simulations using the normalised values from the non-dimensional Lare3D simulations. If we wish to consider the simulations in terms of the coronal values (using the normalisation outlined in Section 2.2 and the initial values given at the start of this chapter) we have:

Time unit :	≈ 34.35 s
Loop length :	≈ 75 Mm,
Velocity driver (max) :	≈ 48 km s ⁻¹
$\rho(t = 0)$:	$\approx 1.67 \times 10^{-12}$ kg m ⁻³ ,
$T(t = 0)$:	$\approx 1.9 \times 10^6$ K,

Using these values a table of comparative coronal values for the three cases is given in Table 6.3.

Finally, we briefly note a few of the shortcomings of these experiments (discussed further in Chapter 9). We have not included thermal conduction or radiation in these models, which would act to both spread and counter the temperature increase. The experiments also use closed boundaries and therefore there is a constant stream of energy being introduced through the Poynting flux that cannot leave, which may create very high energy and temperature values. Similarly, the amount of reconnection and energy dissipated will also depend greatly on the resistivity in the simulations. In Section 3 we discussed the dependence of the value and spacial distribution of η , but Mellor et al. (2005) also showed that using uniform or hyper resistivity impacts the reconnection and subsequent plasma heating. In the next section (Section 6.3) we also go on to briefly discuss the impact of increasing the resistivity for this four and two source comparison.

Table 6.3: Comparison of heating and velocities with corresponding coronal values.

	(i) Two Sources	(ii) Four Sources	(iii) Four Sources
Source Strength & Radius:	$B_{max} \approx 100$ G, $r_1 \approx 4.8$ Mm	$B_{max} \approx 50$ G $r_1 \approx 4.8$ Mm	$B_{max} \approx 100$ G, $r_1 \approx 3.4$ Mm
Total Time of Experiment:	$t = 75 \approx 43$ min	$t = 75 \approx 43$ min	$t = 75 \approx 43$ min
Total Ohmic Heating:	$\approx 3.6 \times 10^{-4}$ $\Rightarrow 1.1 \times 10^{22}$ J	$\approx 2.38 \times 10^{-4}$ $\Rightarrow 7.99 \times 10^{21}$ J	$\approx 2.41 \times 10^{-4}$ $\Rightarrow 8.09 \times 10^{21}$ J
Total Viscous Heating:	$\approx 2.8 \times 10^{-4}$ $\Rightarrow 9.4 \times 10^{21}$ J	$\approx 8.30 \times 10^{-5}$ $\Rightarrow 2.78 \times 10^{21}$ J	$\approx 8.19 \times 10^{-5}$ $\Rightarrow 2.75 \times 10^{21}$ J
Maximum Temperature (T_{max}):	0.333 at $t = 73$ $\Rightarrow 1.9 \times 10^8$ K	0.210 at $t = 75$ $\Rightarrow 1.2 \times 10^8$ K	0.253 at $t = 75$ $\Rightarrow 1.46 \times 10^8$ K
Maximum Velocity in Mid-Plane:	0.21 = $0.27v_A$ at $t = 62.5$ $\Rightarrow v_{max} = 458$ km s ⁻¹	0.075 = $0.05v_A$ at $t = 74.0$ $\Rightarrow v_{max} = 164$ km s ⁻¹	0.071 = $0.04v_A$ at $t = 74.5$ $\Rightarrow v_{max} = 155$ km s ⁻¹

6.3 Impact of Resistivity

6.3.1 Unstable Behaviour at Later Time

In the previous section, the numerical experiments were carried out with a maximum resistivity value of $\eta_0 = 10^{-4}$. The simulations were run for 75 time units and a rotation angle of ≈ 6 radians on one boundary. However, after $t = 75$ both cases involving four flux tubes show indications of becoming kink unstable. The central field line (shown in Figure 6.35), which so far remained straight, begins to kink and forms a helical structure and a large increase in kinetic energy is observed. This suggests that, as the field is being continually rotated, it is not able to reconnect fast enough to release the twist that builds up. We shall not investigate this behaviour in detail, however we note that an introduction of a background field to the four source case (see Chapter 7) results in this helical behaviour occurring earlier and before any significant reconnection is able to take place. Increasing the value of resistivity used in the simulations will allow reconnection to occur earlier. Therefore, in the next chapter (Chapter 7), when we go on to discuss the impact of including a background field in our simulations, we use an increased resistivity value of $\eta_0 = 10^{-3}$.

In this section, the impact of increasing the resistivity to $\eta_0 = 10^{-3}$, in the multiple source

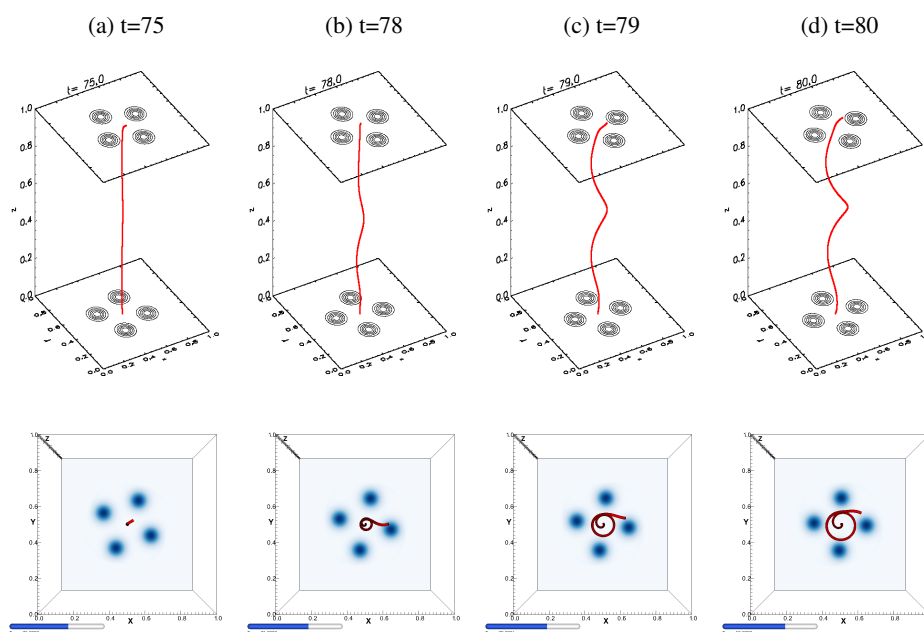


Figure 6.35: Side (top row) and top (bottom row) view of the central field line traced from $(x, y) = (0.5, 0.5)$ on the lower boundary for the four source case (ii) described in Section 6.2 at $t = 75, 78, 79$ and 80 .

cases without background field, shall first be discussed. The two source case (i) and the four source case (ii), previously described, are considered, but case (iii) is omitted, as the previous discussion showed it to behave very similarly to case (ii). In Chapter 3, we have previously discussed the impact of different resistivity values in the two flux tube case (for lower values of η) and therefore many of the general effects we described can also be observed here.

6.3.2 Increasing $\eta_0 = 10^{-4}$ to $\eta_0 = 10^{-3}$

Normalisation	Initial Conditions	
$B_0 = 100$ G	$\epsilon = 0.01$	Resolution: $512^2 \times 256$
$L_0 = 75$ Mm	$\rho = 0.1$	$\eta = \eta_0 e^{-\left(\frac{z-0.5}{r_0}\right)^2}$
$n_e = 1 \times 10^{16}$ m $^{-3}$		$\eta_0 = 10^{-4}$ and $\eta_0 = 10^{-3}$
		$0 < t < 70$

A higher value of resistivity, as discussed in Chapter 3.2.1 for two flux tubes, reduces the threshold of current needed for reconnection to occur. This means that reconnection and the general dynamical evolution will occur after a smaller rotational angle and therefore over a shorter time-scale. This can be seen in the earlier increase in the percentage of flux with different connectivities, shown in Figure 6.36. The percentages were calculated as described for Figure 6.13.

Increasing the resistivity by an order of magnitude enables the field lines to begin to change connectivity over 10 normalised time units earlier for the two flux tube case (see Figure 6.36a) and the gradient quickly increases to produce a larger total percentage of the reconnected flux, and at

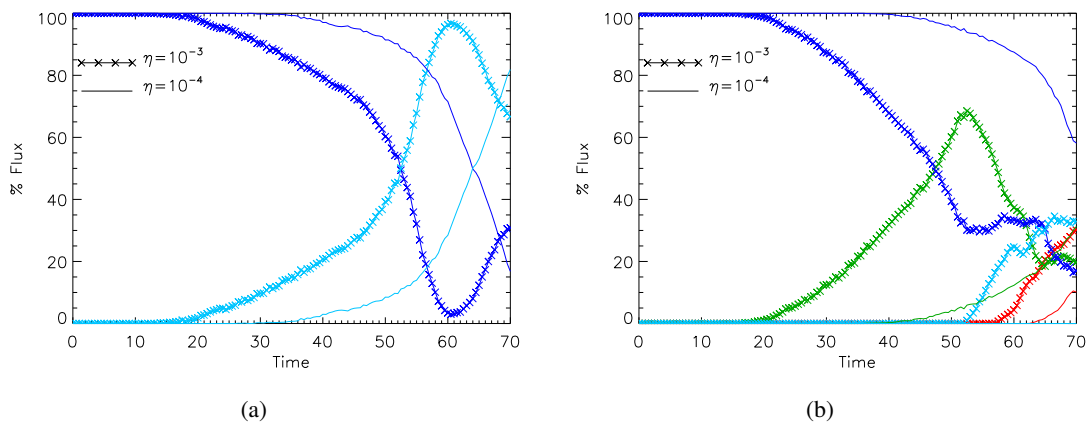


Figure 6.36: Average percentage of flux connected to the original (dark blue), anticlockwise (green), clockwise (red) and opposite (light blue) sources on the upper boundary. (a) Two and (b) four flux tube cases for $\eta_0 = 10^{-4}$ (solid) and $\eta_0 = 10^{-3}$ (crosses) .

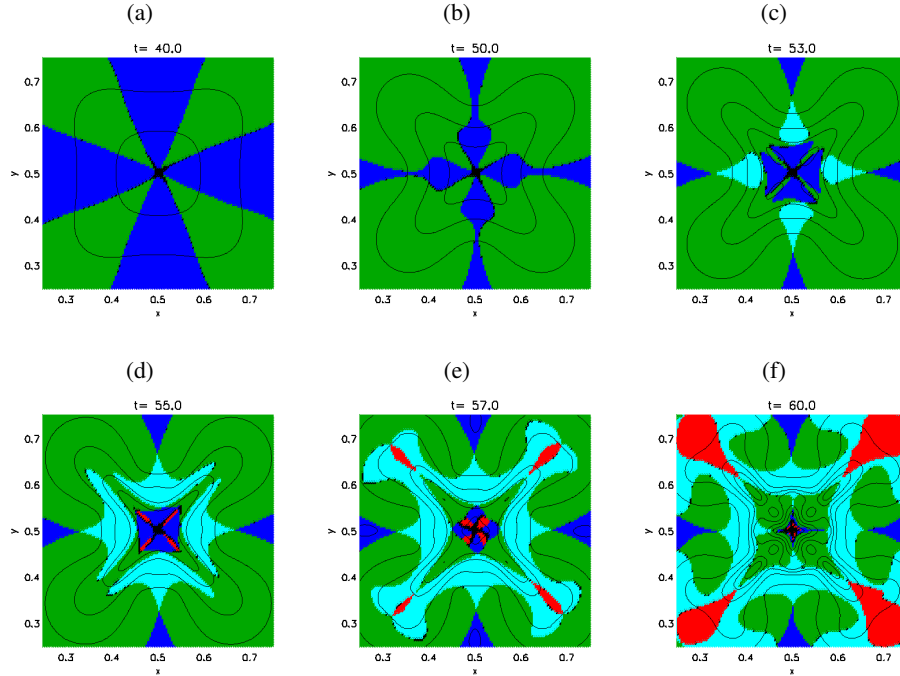


Figure 6.37: The field line connectivity in the mid-plane between $0.25 < x, y < 0.75$ for four flux tubes with $\eta_0 = 10^{-3}$. Over-plotted are the contours of parallel current density ($j_{||}$) in the same plane. Connectivity colours are as in Figure 6.36.

an earlier time than for $\eta_0 = 10^{-4}$.

In the four flux tube case, the field lines also begin to change connectivity earlier (by approximately 20 time units, in Figure 6.36b). The order of the connectivity evolution of field lines also changes slightly from the $\eta_0 = 10^{-4}$ case. In Figure 6.36b, the increased resistivity allows some field lines to reconnect to the ‘opposite’ source on the upper boundary (light blue, crosses) before any are reconnected to the clockwise source on the upper boundary (red, crosses). This is in contrast to the order of connectivities for $\eta_0 = 10^{-4}$, where the ‘clockwise’ (red, solid) connections occur before the ‘opposite’ (light blue, solid). This difference can be better understood from the field line connectivities when traced from the mid-plane, shown in Figure 6.37 for $\eta_0 = 10^{-3}$. These can be compared to the original four source case with $\eta_0 = 10^{-4}$ in Figure 6.16ii. The earlier onset of reconnection produces a large proportion of flux reconnected anticlockwise (green) at an earlier time, seen at $t = 50$ in Figure 6.37b. These newly reconnected flux regions expand towards each other, causing current to build up along the lines $x = 0.5$ and $y = 0.5$ in the mid-plane and allowing the field to reconnect again to the ‘opposite’ source (light blue), visible in Figure 6.37c at $t = 53$. This is the same process observed in the $\eta_0 = 10^{-4}$ case previously (see Figure 6.16), but on a much faster time-scale. Therefore, this secondary change in connectivity occurs before any field lines begin to reconnect to the clockwise source (red) in the centre of the

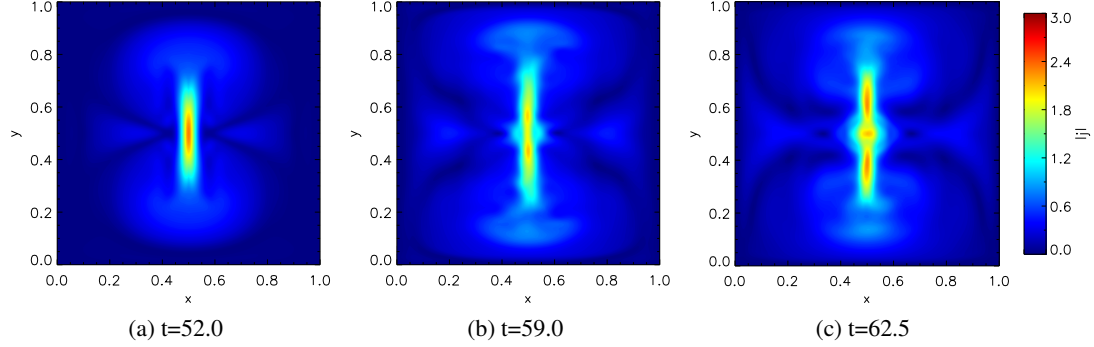


Figure 6.38: Contours of the magnitude of the current density in the mid-plane at (a) $t = 52$, (b) $t = 59$ and (c) $t = 62.5$ for two flux tubes with $\eta_0 = 10^{-3}$.

plane visible at $t = 55$ in Figure 6.37d.

The higher resistivity and subsequent earlier reconnection also implies that the current building up in the domain is reduced slightly, as the stressed field is able to diffuse earlier. This can be observed by the slightly weaker and broader current layer forming in the mid-plane for the two flux tube $\eta_0 = 10^{-3}$ case in Figure 6.38a, compared to Figure 6.27 for $\eta_0 = 10^{-4}$. The current layer for $\eta_0 = 10^{-3}$ also appears to break up as the simulation continues, forming two peak current values in the plane, shown in Figure 6.38b. This can be explained by looking at the forces in more detail. Previously, we described how the central current layer is formed by an inwards Lorentz force towards the centre of the $x - y$ plane. In the mid-plane, this force can be seen in the x -component of the Lorentz force that acts to build up the current along the line $x = 0.5$ (the y -component of the Lorentz force in the two flux tube case at this cut is minimal in comparison). Contours of the x -component of the Lorentz force ($(\mathbf{j} \times \mathbf{B})_x$) are shown in the top row of Figures 6.39 and 6.40 for $\eta_0 = 10^{-4}$ and 10^{-3} , respectively. In Figure 6.39 the Lorentz force acts towards the line $x = 0.5$ and is fairly uniform between $0.4 < y < 0.6$. Whereas for the increased resistivity case in Figure 6.40, the Lorentz force does not increase uniformly between $0.4 < y < 0.6$ and appears weaker around $y = 0.5$.

The Lorentz force can be separated into contributions from the magnetic pressure and magnetic tension (see Equation 6.2). Due to the curvature of the field lines, there is an inwards magnetic tension force from relatively early in the simulations. As the magnetic field is pushed towards $x = 0.5$ in the mid-plane, there is a build up of field strength in the centre of the plane, creating an initial outwards magnetic pressure in the x -direction. However, once reconnection begins to occur, the field strength across the current layer begins to reduce. This can be seen on the plots of B^2 along $y = 0.5$ in the mid-plane in Figure 6.41a from $t = 52$ for $\eta_0 = 10^{-4}$. The large gradient in B^2 around the current layer then creates an inwards (towards $x = 0.5$) magnetic pressure force, that increases until it forms the dominant part of the Lorentz force. This can be seen in snapshots

of the magnetic pressure along $y = 0.5$ in Figure 6.42a (middle row).

Initially, the $\eta_0 = 10^{-3}$ two source case behaves similarly, but evolves at an earlier time and therefore the magnetic pressure begins to act inwards earlier (at $t \approx 36$), as shown in Figure 6.42b. This is due to the higher resistivity value allowing the magnetic field to diffuse earlier and reduce the value of B^2 across the current layer (see Figure 6.41b). The magnetic pressure then begins to increase, as for $\eta_0 = 10^{-4}$ case (although an order of magnitude less). However, for $\eta_0 = 10^{-3}$, after $t = 51$ the magnetic pressure at $y = 0.5$ in the mid-plane then starts to decrease again (shown in Figure 6.42b - middle row). This suggests that the earlier and more efficient reconnection from a higher resistivity prevents the large build up of magnetic field either side of the current layer, as the gradient of B^2 formed across the current layer reduces from $t = 51$ in Figure 6.41b and hence the inwards magnetic pressure force is reduced. Therefore, the x component of the Lorentz force decreases after $t = 51$ for $\eta_0 = 10^{-3}$ at $y = 0.5$, as shown in Figure 6.42b (top row).

This explains the evolution of the $(\mathbf{j} \times \mathbf{B})_x$ component shown in the top row of Figure 6.40 in the mid-plane, for $\eta_0 = 10^{-3}$. The initial ‘inwards’ Lorentz force is focused at $y = 0.5$ and therefore it is at this location that the initial peak current value forms, enabling reconnection to occur. In response to this, the outwards gas pressure force also builds up (see bottom row Figure 6.40) due to the heating in the reconnection region. The sum of the Lorentz force and negative pressure gradient is shown for the mid-plane at $t = 50$ in Figure 6.43a and shows minimal variation around the current layer at $x = 0.5$ implying that the forces are somewhat balanced. However,

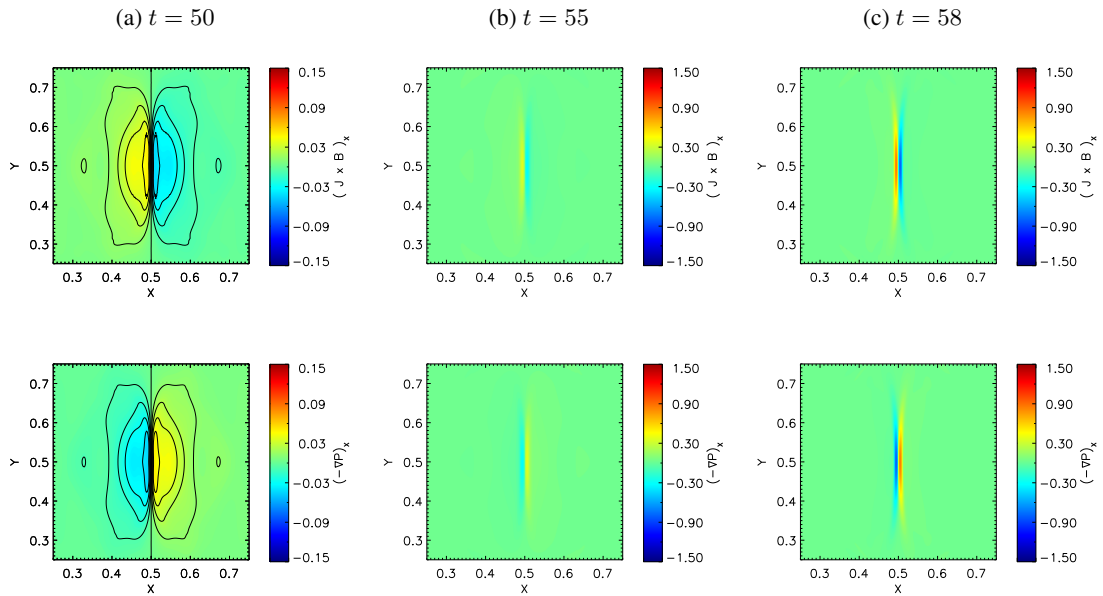


Figure 6.39: Contour plots of the x -component of Lorentz force (top row) and the negative pressure gradient (bottom row) in the mid-plane, for two flux tubes with $\eta_0 = 10^{-4}$. Note the change of magnitude in the colour bar after $t = 50$.

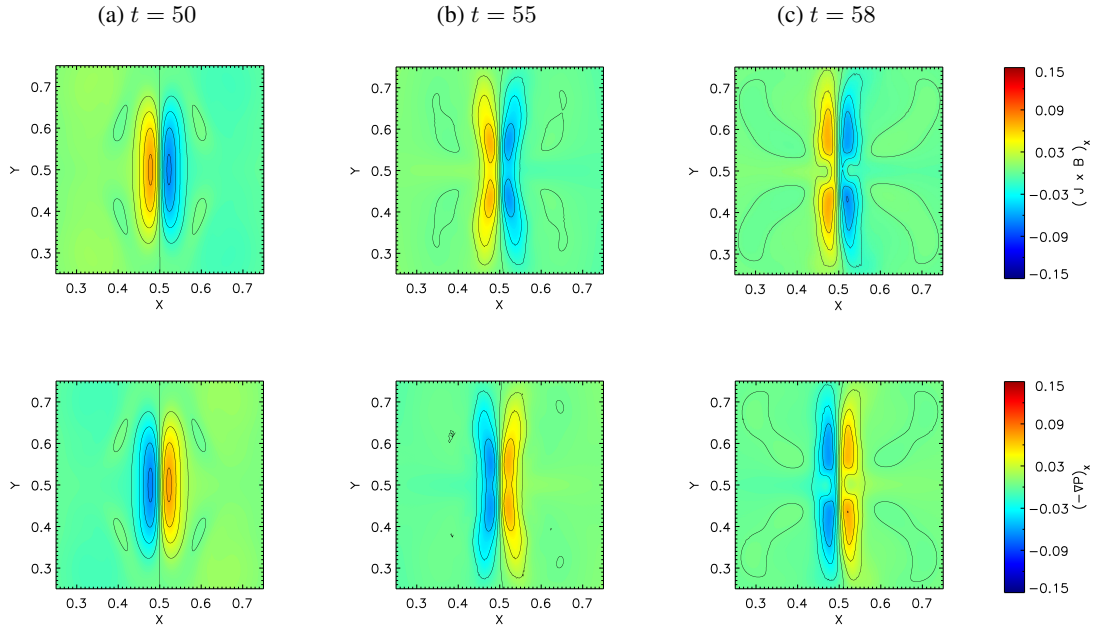


Figure 6.40: Contour plots of the x -component of Lorentz force (top row) and negative pressure gradient (bottom row) in the mid-plane, for two flux tubes with $\eta_0 = 10^{-3}$.

when the Lorentz force then decreases in the centre of the mid-plane (due to the increased η value reducing the magnetic pressure) there is still an outwards gas pressure gradient force at the centre of the mid-plane. This outwards pressure gradient force then begins to dominate, as shown by the contour plot of the summed forces in Figure 6.43b at $t = 55$. This shows an outwards force from the centre of the current layer around $y = 0.5$, but above and below in y there is still a weak force acting inwards towards the current layer.

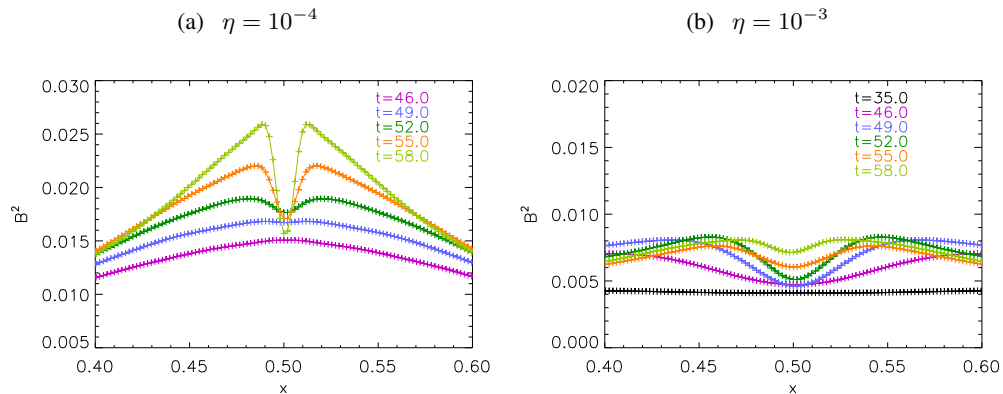


Figure 6.41: B^2 along $y = 0.5$ in the mid-plane for various times for the two flux tube case with (a) $\eta_0 = 10^{-4}$ and (b) $\eta_0 = 10^{-3}$

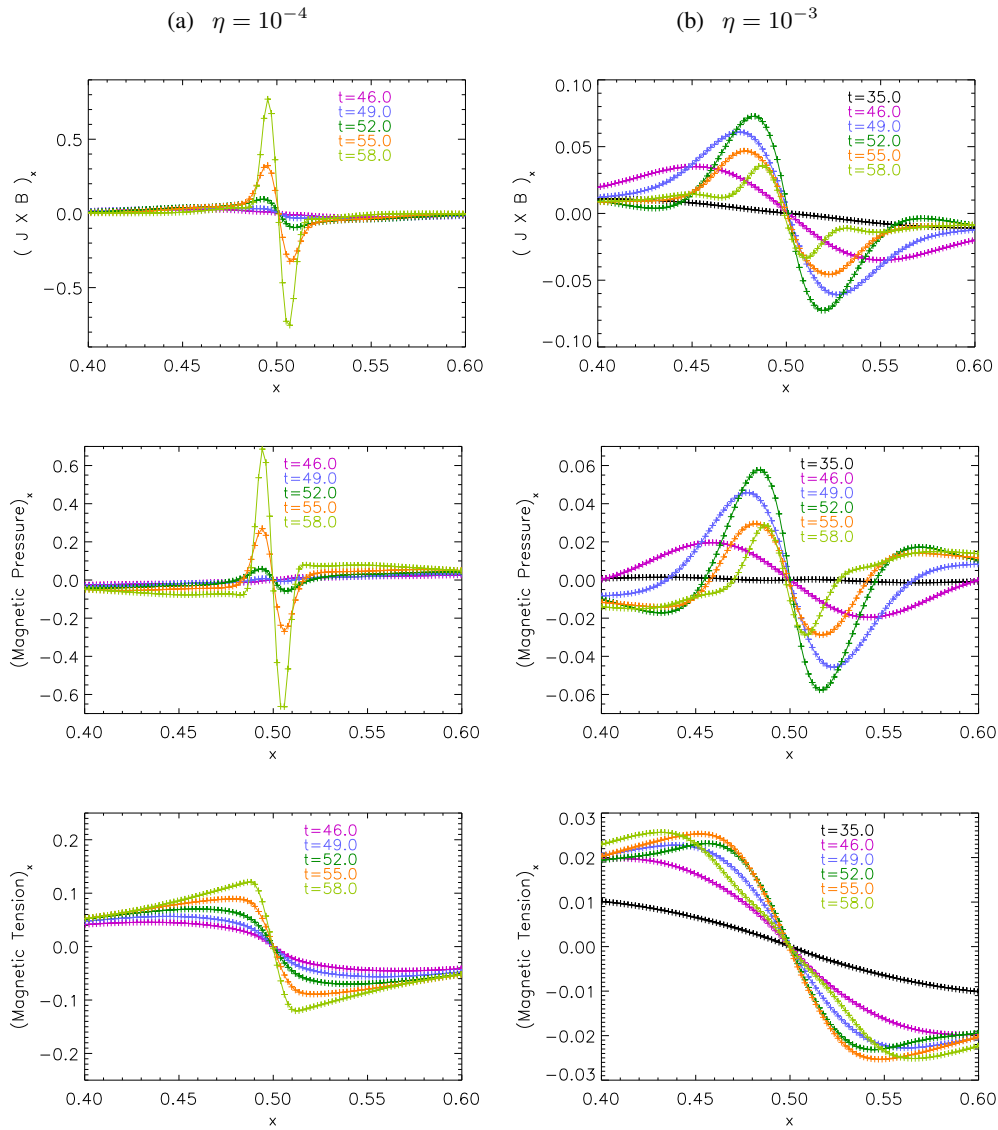


Figure 6.42: The x -components of the Lorentz force ($\mathbf{j} \times \mathbf{B}$) (top row) and its magnetic pressure (middle row) and magnetic tension (bottom row) contributions along $y = 0.5$ in the mid-plane, for various times for the two flux tube case with (a) $\eta_0 = 10^{-3}$ and (b) $\eta_0 = 10^{-4}$.

The field is therefore no longer advected into the centre of the plane but continues to be brought in above and below $y = 0.5$. This causes the current layer to fragment and two reconnection sites to occur at $y > 0.5$ and $y < 0.5$ in the mid-plane, as shown in Figure 6.38b. Hence, as the reconnection continues at these locations, newly reconnected flux is directed towards the centre of the plane from two directions creating a third current formation in the centre, as seen in Figure 6.38c. The field line connectivity in the mid-plane, displayed in Figure 6.44d at this time, correspondingly shows increasing dark blue flux as the newly reconnected field lines are pushed together to form this current concentration, allowing them to reconnect again to their original

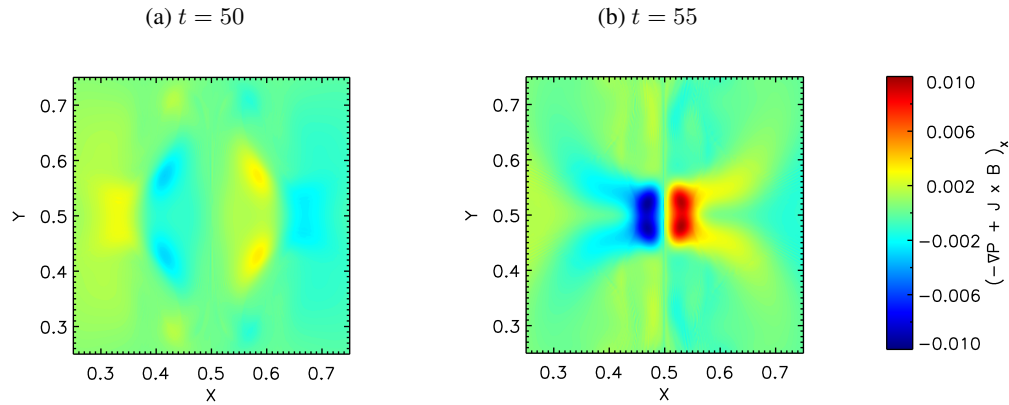


Figure 6.43: Contour plots of the x -component of the sum of the Lorentz force and negative plasma pressure gradient in the mid-plane, for two flux tubes with $\eta_0 = 10^{-3}$.

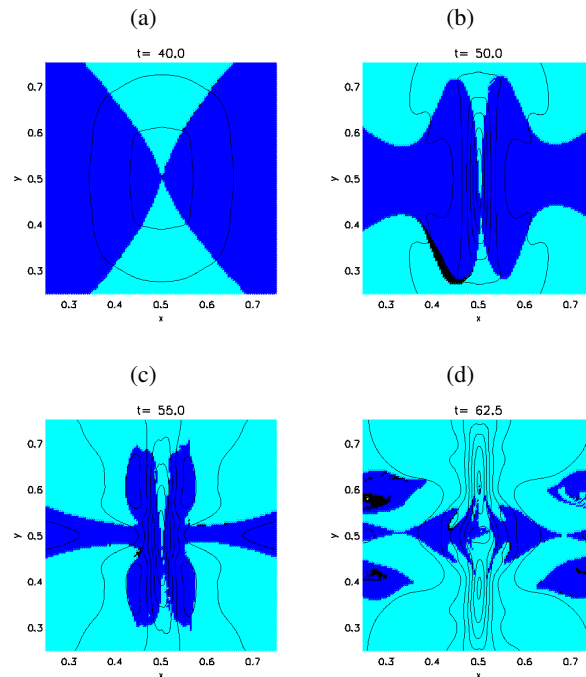


Figure 6.44: The field line connectivity in the mid-plane between $0.25 < x, y < 0.75$ at $t = 40, 50, 55, 62.5$ for two flux tubes with $\eta_0 = 10^{-3}$. Over-plotted are the contours of parallel current density ($j_{||}$) in the same plane. Connectivity colours are as in Figure 6.36.

source. A corresponding increase in the percentage of flux connected to its original source is also shown in Figure 6.36 at $t = 61$.

For the $\eta_0 = 10^{-4}$ two source case the x -component of the Lorentz force and the pressure gradient are shown in contour plots in Figure 6.39. Unlike the $\eta_0 = 10^{-3}$ case, the Lorentz force

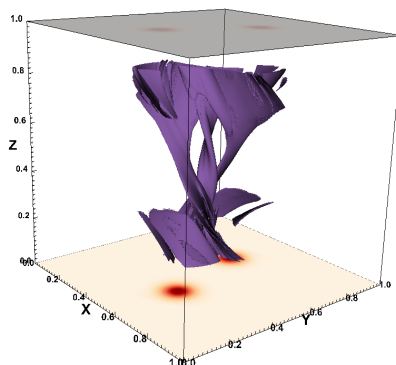


Figure 6.45: Isosurface of the current density of magnitude 2.0 within the central box $0.2 < x, y, z < 0.8$ of the domain, for two flux tubes with $\eta_0 = 10^{-3}$ at $t = 65$.

continues to build up fairly uniformly and is very concentrated in x along the current layer and the outwards pressure gradient matches where the Lorentz force occurs. This enables the single current layer to continue to increase in strength for the length of the simulation.

For our explanation we have only shown the forces in the mid-plane, where the force that acts normal to the current layer is in line with the x -axis. However, the twisted current layer extends vertically throughout the domain and the forces and current break up of the layer we describe are indicative of similar behaviour occurring along the current layer at multiple heights in the domain, as shown by the isosurface of current density in Figure 6.45.

Summary

In this section we have outlined the main impact of increasing the resistivity value from $\eta_0 = 10^{-4}$ to $\eta_0 = 10^{-3}$. These differences include: reducing the current built up, earlier reconnection occurring, the break up of the current layer in the two source case and a change to the timing of multiple reconnection of field lines in the four source case. These changes will also have consequences such as reducing the Ohmic heating (due to the reduced current values) and decreasing the Poynting flux injected into the domain, as the field lines are able to reconnect sooner.

Chapter 7

Comparison of Two and Four Flux Tubes with a Background Field

7.1 Comparing the Flux Tube Set-up with a Background Field

Normalisation	Initial Conditions	
$B_0 = 100 \text{ G}$	$\epsilon = 0.01$	Resolution: $512^2 \times 256$
$L_0 = 75 \text{ Mm}$	$\rho = 0.1$	$\eta = 0$ (Ideal relaxation)
$n_e = 1 \times 10^{16} \text{ m}^{-3}$	$B_{bg} = 0.05, 0.01, 0.00$	viscosity= 0.001
		$0 < t_{relax} < 80$

In the previous chapters, the flux tubes have been modelled as isolated magnetic field structures with no additional background field between them, but in a solar context, this is not very realistic. We now go on to investigate how the presence of a background field impacts the results. To include a background field, an additional constant vertical background flux (B_{bg}) has been added to the (initial) vertical magnetic field component:

$$B_z = B_{max} \left[e^{-[(x-x_A)^2+(y-y_A)^2]/r_1^2} + e^{-[(x-x_B)^2+(y-y_B)^2]/r_1^2} + e^{-[(x-x_C)^2+(y-y_C)^2]/r_1^2} + e^{-[(x-x_D)^2+(y-y_D)^2]/r_1^2} \right] + B_{bg}. \quad (7.1)$$

This will increase the total flux, as well as increasing the peak values of the magnetic sources.

De Moortel and Galsgaard (2006a) and following papers afterwards (De Moortel and Galsgaard, 2006b; Wilmot-Smith and De Moortel, 2007) investigated the rotation of two flux tubes and the impact of including a background field. In the present chapter, we have chosen similar values of background field to compare the results of our two flux tube case with De Moortel and

Galsgaard (2006a). Furthermore, we shall consider whether the introduction of the background field has the same effect on the four flux tube case discussed in the previous chapter. We include a background flux of $B_{bg} = 0.01$ (solid) and $B_{bg} = 0.05$ (dashed) and shall consider two of the cases we previously described; a two flux tube case (orange) and a four flux tube case (green), whose field parameters are given in Table 7.1. For brevity, we have not included the more concentrated four flux tube initial set-up, as the dynamical behaviour was found to be very similar for both four flux tube cases in the previous chapter.

The flux tubes are formed in the same manner described in detail in Chapters 2 and 6, where the vertical magnetic field is prescribed and the initially straight, aligned flux tubes are allowed to expand and relax in a uniform density and pressure domain. The vertical magnetic field component on the lower boundary at $y = 0.5$ is shown in Figure 7.1a. The presence of a background field will constrain the expansion of the flux tubes, so they will appear more compact and there will be less curvature in the field lines, as seen in the field lines drawn in Figure 7.2, after the relaxation.

Table 7.1: Background Field Cases: Parameters and colour scheme that will be used throughout this chapter.

<p>(i) Two Sources - - -</p> <p>$B_{max} = 1.0, B_{bg} = 0.05, r_1 = 0.065$</p>	<p>(ii) Four Sources - - -</p> <p>$B_{max} = 0.5, B_{bg} = 0.05, r_1 = 0.065$</p>
<p>(iii) Two Sources —</p> <p>$B_{max} = 1.0, B_{bg} = 0.01, r_1 = 0.065$</p>	<p>(iv) Four Sources —</p> <p>$B_{max} = 0.5, B_{bg} = 0.01, r_1 = 0.065$</p>
<p>(v) Two Sources —</p> <p>$B_{max} = 1.0, B_{bg} = 0.00, r_1 = 0.065$</p>	<p>(vi) Four Sources —</p> <p>$B_{max} = 0.5, B_{bg} = 0.00, r_1 = 0.065$</p>

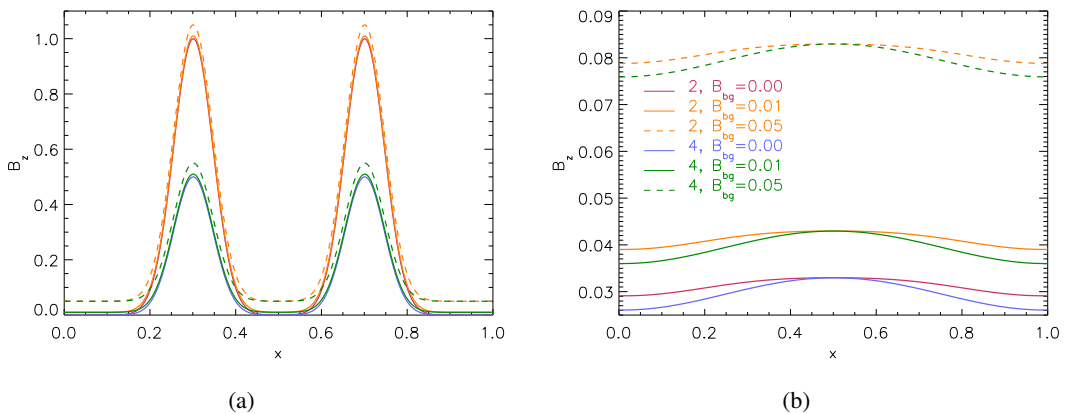


Figure 7.1: B_z at $y = 0.5$ (a) on the lower boundary and (b) in the mid-plane for cases (i) to (vi).

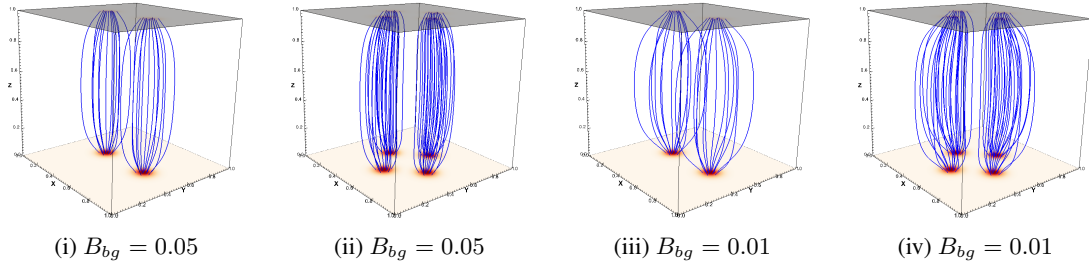


Figure 7.2: A selection of field lines traced from $z = 0.0$ within a radius 0.05 of the sources for cases with (i) 2 sources $B_{bg} = 0.05$, (ii) 4 sources $B_{bg} = 0.05$, (iii) 2 sources $B_{bg} = 0.01$ and (iv) 4 sources $B_{bg} = 0.01$.

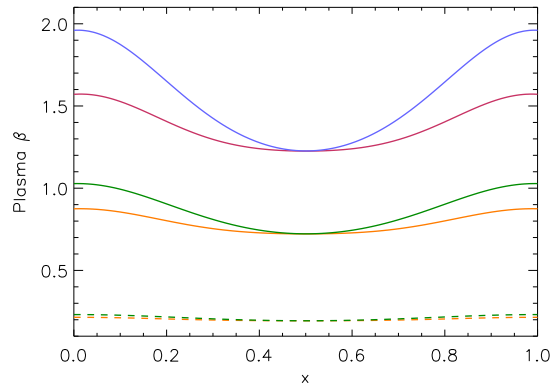


Figure 7.3: Plasma β in the mid-plane at $y = 0.5$ for cases (i) to (vi).

The presence of the additional background flux and the more concentrated flux tubes also means that there will be an increased field strength in the centre of the domain. In Figure 7.1b, the B_z component of the field, which is the strongest field component, is shown in the mid-plane at $y = 0.5$. As with the non-background field experiments, both the two and four source cases have a similar peak strength in the centre of the domain of approximately 0.083 and 0.043 for $B_{bg} = 0.05$ and $B_{bg} = 0.01$, respectively. These values are larger than the maximum B_z in the mid-plane from the non background cases of 0.033 in Figure 7.1. Therefore, the plasma β value shown in Figure 7.3 will also be smaller (less than 1) in the domain, due to this increased field strength.

Due to the added background field, the change in the magnetic field mapping is less steep between regions of differing connectivity and the Quasi Separatrix Layers (QSLs) have smaller values of the squashing factor Q (Démoulin et al., 1996; Démoulin, 2006a). As in Chapter 6, we use the term flux tube to refer to the flux associated within the specified radius (r_1) of the sources. The presence of a background field means that the flux tubes will be separated by regions of flux

associated with this background field.

7.2 Comparing Flux Tubes with a Background Field Under Rotation

Normalisation	Initial Conditions	
$B_0 = 100 \text{ G}$	$\epsilon = 0.01$	Resolution: $512^2 \times 256$
$L_0 = 75 \text{ Mm}$	$\rho = 0.1$	$\eta = \eta_0 e^{-\left(\frac{z-0.5}{r_0}\right)^2}$, $\eta_0 = 10^{-3}$
$n_e = 1 \times 10^{16} \text{ m}^{-3}$	$B_{bg} = 0.05, 0.01, 0.00$	$0 < t < 70$

We now go on to discuss the evolution of the flux tubes with a background field (cases (i) to (iv)) compared to the flux tubes without a background field when the same rotational driver is applied. The non-background field cases shall be plotted in red and blue for two and four sources and shall be labelled cases (v) and (vi), respectively. A z -dependent resistivity with $\eta_0 = 10^{-3}$ is used (as discussed in Section 6.3) and a summary of the parameters of the cases is shown in Table 7.1. The simulations with larger values of background field are halted earlier due to computational restrictions and are therefore displayed until $t = 60$ for both cases (i and ii) with $B_{bg} = 0.05$ and until $t = 67$ for case (iii) with two sources and $B_{bg} = 0.01$.

7.2.1 Dynamical Evolution

The dynamical behaviour of the cases with a background field is qualitatively similar to that of the non-background field cases described in detail in Chapter 6. The solid body rotation of the flux tubes allows the flux tubes to form an interlinking helical structure and the curvature of the field lines leads to an inwards Lorentz force that brings the field towards the centre of the $x - y$ plane. This creates a shear in the magnetic field towards the central column of the domain forming a twisted current layer for the two flux tube case and a twisted current ‘x’ shape to form for the four flux tube case.

When a background field is introduced the flux tubes do not expand as fully and therefore the field is stronger in the domain, as shown in Figure 7.1b. As the Lorentz force acts on the flux tubes, the increased field strength also causes higher current values to be formed. This can be seen in Figure 7.4, where the highest current values are achieved by the cases with $B_{bg} = 0.05$. Initially, the increase in the maximum current in the central box of the domain is gradual, but later there is a sharp increase. The timing of this sharp increase alters between the different cases. In the non background field cases, case (v) with two flux tubes rises 5 time-units earlier than the four source case (vi). For larger background field strengths, the timing of the increase for the two and four source cases occurs closer together. However, for each background field strength the current

in the two source cases always increases before the comparable four source case.

For the non-background field cases, the maximum current in Figure 7.4 is higher for the two source case (red) than the four source case (blue) and this is also true for $B_{bg} = 0.01$. However, for $B_{bg} = 0.05$ it is the four source case that reaches the highest current value. The current for case (i) does not increase as we may have expected, but this may be due to the break up of the single current layer, shown in the contours of the current density in the mid-plane in Figure 7.5. This current

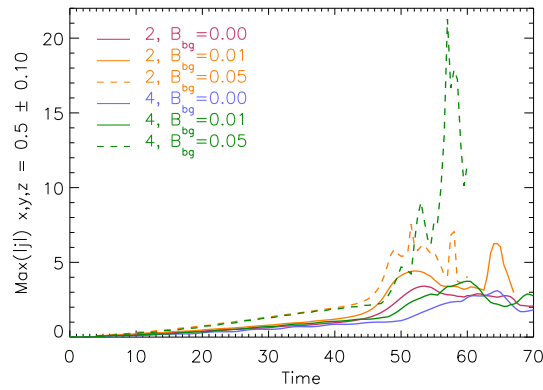


Figure 7.4: Maximum magnitude of the current density in $0.4 < x, y, z < 0.6$ for cases (i) to (vi).

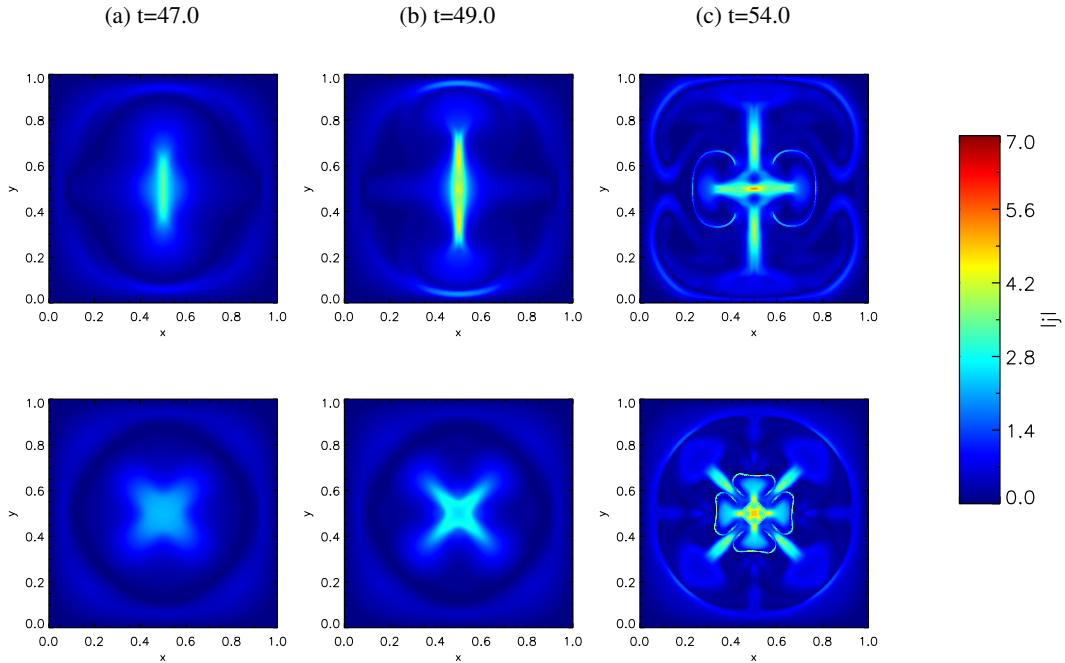


Figure 7.5: Contours of the magnitude of the current density in the mid-plane at (a) $t = 47$, (b) $t = 49$ and (c) $t = 54$ for two flux tubes (top row) and four flux tubes (bottom row) with $B_{bg} = 0.05$. (Cases (i) and (ii), respectively.)

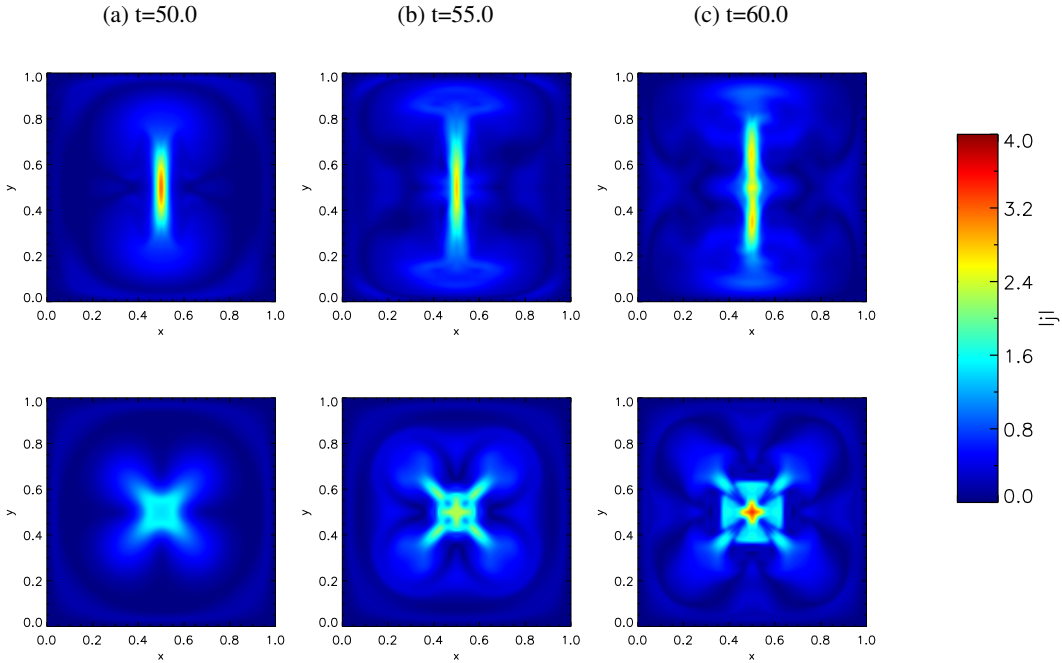


Figure 7.6: Contours of the magnitude of the current density in the mid-plane at (a) $t = 50$, (b) $t = 55$ and (c) $t = 60$ for two flux tubes (top row) and four flux tubes (bottom row) with $B_{bg} = 0.01$. (Cases (iii) and (iv), respectively.)

layer fragmentation was also described for the non-background field case (v) in Section 6.3, but occurred towards the end of the simulation. In Figure 7.5 for $B_{bg} = 0.05$, the current starts to fragment at $t = 49$ and this earlier break up of the single current layer could prevent a large peak value of current building up. The current contours in Figure 7.6 (top row) for case (iii), with two sources and $B_{bg} = 0.01$, also show that towards the end of the experiment ($t = 60$) the current layer breaks up, but it occurs much later, after the current layer has built up for longer.

Despite the different peak values and altered timing of the maximum current, the locations of the current formation in Figures 7.5 and 7.6 are generally similar to those described in detail in Chapter 6 for the non-background cases. In Figures 7.5 and 7.6, the presence of a background field also creates faint rings of current where outflows of reconnection occur. This is due to the newly reconnected field lines being accelerated into the existing background field. This is particularly evident for the larger background field value ($B_{bg} = 0.05$) cases and seen at $t = 54$ in Figure 7.5.

7.2.2 Connectivity Evolution

The presence of a background field also affects the field line connectivity evolution. Using the same method described in Chapter 6, the percentage of flux associated with the different sources

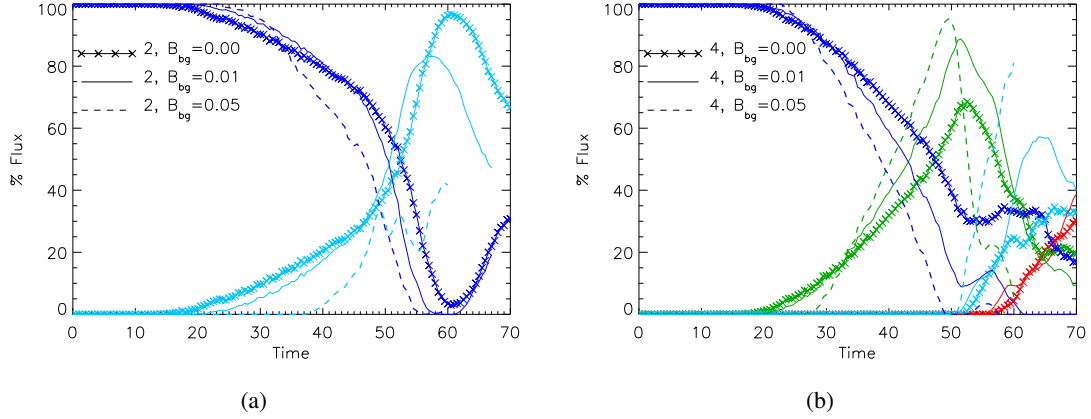


Figure 7.7: Average percentage of flux connected to the original (dark blue), anticlockwise (green), clockwise (red), and opposite (light blue) sources on the upper boundary, for (a) two and (b) four flux tube cases for $B_{bg} = 0$ (crosses), $B_{bg} = 0.01$ (solid) and $B_{bg} = 0.05$ (dashed).

on the upper boundary is plotted in Figure 7.7. The percentage of flux traced from the sources on the base that remains connected to its original source is shown in dark blue for all the cases. The introduction of a background field delays the flux associated with the sources reconnecting, due to the confining effect of the background field. As the current builds up, the background field between the flux tubes must first reconnect before flux associated with the sources can change connectivity. The field lines from the sources first change connectivity to the ‘opposite’ source (light blue) in the two flux tube cases and to the anti-clockwise source (green) in the four flux tube cases.

In the cases without background field (crosses), as the percentage of flux connected to the new sources increases, the corresponding flux associated with the original source (dark blue crosses) decreases. However, for the background field cases in Figure 7.7, there is a delay between the flux being no longer associated with the original source and it being assigned to another source. Due to the presence of the background field, the field lines traced from the sources on the lower boundary are able to reconnect multiple times, appearing to connect across the upper boundary to background field locations before being associated with another source. This is again most pronounced in the stronger background field case and can be seen in the footpoint connectivity graphs for $B_{bg} = 0.05$ in Figures 7.9i and 7.9ii, where regions of field lines that are unassigned (black) to a source appear between regions of different connectivity, when traced from the sources on the base. The unassigned (black) field lines are also shown in the mid-plane connectivity plots (Figures 7.10i and 7.10ii) and can be seen at earlier times at the locations between regions of different connectivity (i.e the QSLs).

After the initial delay in field lines (associated with the sources) changing connectivity, the

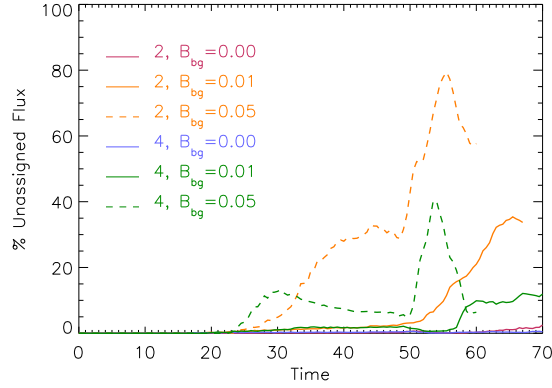


Figure 7.8: Average percentage of unassigned flux for cases (i) to (vi).

cases with background field show steeper gradients in the increase of the percentage of reconnected flux. This suggests that when the reconnection does occur, it is more efficient for larger background field cases, which agrees with the increased current density values in Figure 7.4. For all the background field cases, Figure 7.7 shows that 100% of the flux from the sources on the lower boundary has changed connectivity (percentage of dark blue gone to zero). This did not occur for the non-background field cases. Therefore, despite the initial delay, the change in connectivity in these cases is so fast that the percentage of flux changing connectivity peaks earlier for larger background field values.

The increased rate of the field lines reconnecting is most noticeable when comparing the four flux tube cases with $B_{bg} = 0$ and $B_{bg} = 0.05$ in Figure 7.7b. The amount of flux connected anti-clockwise for $B_{bg} = 0$ (green crosses) reaches a maximum of approximately 68%, before flux begins to reconnect to other sources on the upper boundary. In comparison, for $B_{bg} = 0.05$ this increases to over 95% (green dashed). This rapid change of connectivity can be associated with the initial delay in reconnection. As the background field prevents the flux associated with the sources from diffusing, when the reconnection begins, they produce a higher rate of reconnection (see also De Moortel and Galgaard, 2006a).

For two flux tubes, a large percentage ($\approx 97\%$) of the flux of the original non-background field case reconnects. When a background field is introduced, the rate of change in connectivity increases, but we do not see the corresponding increase in the maximum percentage of flux connected to the opposite source, as we did in the four source cases. Instead, it appears to decrease. This is due to a large percentage of the source being labelled ‘unassigned’ as it connects to other parts of the upper boundary, as seen in the footpoints in Figure 7.9. The percentage of unassigned flux with time for all the cases is shown in Figure 7.8. In the four flux tube case, the larger number of sources on the upper boundary means that there is a larger area where field lines will be considered to be associated with one of the sources and so generally these cases have less unassigned

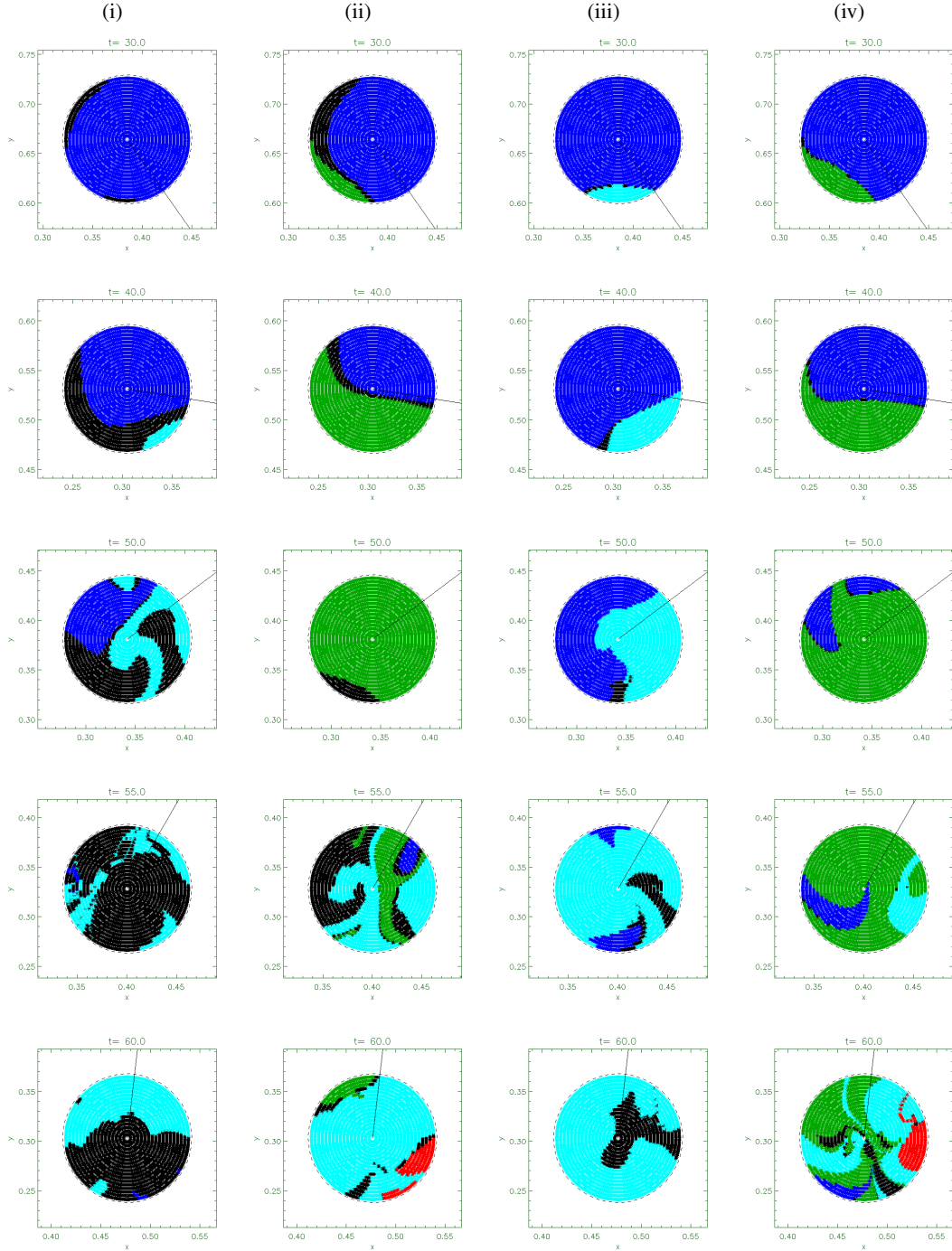


Figure 7.9: The field line connectivity of source C on $z = 0.0$ at $t = 30, 40, 50, 55, 60$ for cases with (i) 2 sources with $B_{bg} = 0.05$, (ii) 4 sources for $B_{bg} = 0.05$, (iii) 2 sources with $B_{bg} = 0.01$ and (iv) 4 sources for $B_{bg} = 0.01$. The solid black line indicates the direction to the centre of rotation. Dark blue signifies field lines at the original connection (C). Light blue, green and red indicate connectivity C_a , C_b and C_d , respectively.

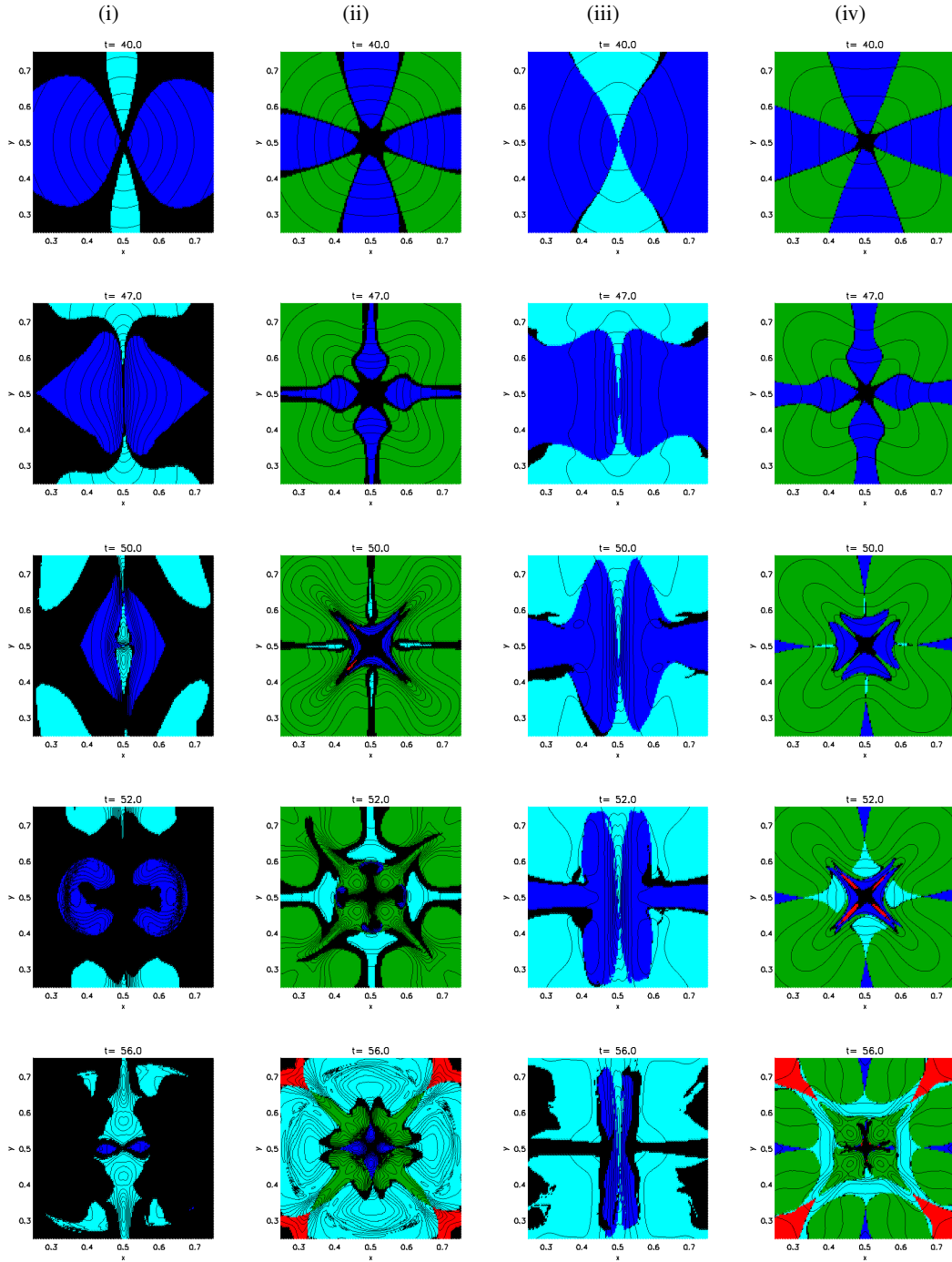


Figure 7.10: The field line connectivity in the mid-plane for $0.25 < x, y < 0.75$ at $t = 40, 47, 50, 52, 56$ for cases with (i) 2 sources with $B_{bg} = 0.05$, (ii) 4 sources for $B_{bg} = 0.05$, (iii) 2 sources with $B_{bg} = 0.01$ and (iv) 4 sources for $B_{bg} = 0.01$. Flux with original, opposite, anticlockwise and clockwise connectivity is shown in dark blue, light blue, green and red, respectively. Over-plotted are the contours of parallel current density ($j_{||}$) in the same plane.

flux than the two source cases.

Despite the large percentage of unassigned flux for the two source cases (see Figure 7.8), the decreasing percentage of flux at its original connection (dark blue) in Figure 7.7 behaves similarly to the four source cases. This suggests that although the field lines are not all being associated with the ‘opposite’ source above, the rate at which they change from their original connectivity (shown by the reduction in dark blue) also occurs at faster rates for increasing values of background field.

This behaviour for both the two and four source cases is similar to the findings for the two flux tube rotation considered by De Moortel and Galsgaard (2006a), carried out using a different numerical code, who also observed an increased rate of reconnection for higher values of background field. However, we note that the exact timing and interplay of the flux changing connectivity between sources will depend on the form and value of the resistivity.

The evolution of the current layer in the domain also impacts how the connectivity changes. This is particularly evident for the two flux tube case with a large background field ($B_{bg} = 0.05$). In Figure 7.5b, the twisted current layer formed in the centre of the domain (along $x = 0.5$ in the mid-plane) is seen to break up, as two localised peaks of current density form either side of $y = 0.5$ along the line $x = 0.5$ in the mid-plane. This causes reconnected field to be ejected in both the positive and negative y direction towards the centre of the plane, shown by the light blue connectivity occurring in the centre of the mid-plane in Figure 7.10i at $t = 50$. The newly reconnected field lines then meet in the centre of the plane and create a central current layer along $y = 0.5$ (see Figure 7.5c), which allows the field lines to change connectivity again. The percentage of flux connected to the opposite source for the $B_{bg} = 0.05$ case in Figure 7.7a (light blue, dashed line) is therefore seen to oscillate as the field lines begin to change connectivity again and a large proportion becomes unassigned.

The current layer eventually breaks up into two localised regions of high current density for all the two flux tube cases with $\eta = 10^{-3}$, as shown in Figures 6.38, 7.6 and 7.5 for $B_{bg} = 0.0$, $B_{bg} = 0.01$ and $B_{bg} = 0.05$, respectively. (This process was described in detail in Section 6.3 for $B_{bg} = 0.0$.) However, this current layer break up occurs later for decreasing values of background field. Therefore, the percentage of flux reconnecting to the opposite source (light blue) in Figure 7.7a is able to reach higher values for cases with smaller background field values.

7.2.3 Efficiency of Heating and Energetics

In Figure 7.11, the evolution of the Poynting flux and the associated volume contributions for all six cases are shown to be qualitatively similar. However, the total energy going into the domain, through the Poynting flux (crosses), increases for larger values of background magnetic field, as the boundary velocity drivers act on a larger area and strength of magnetic field. The Poynting

flux entering the system with time more than doubles between the $B_{bg} = 0.0$ and $B_{bg} = 0.05$ cases. When reconnection begins to occur, the decrease in the rate of change of magnetic energy (solid) and corresponding increase in Joule dissipation (dashed) also occur slightly later and more rapidly for increased background field values. This is in agreement with the initial delay and then

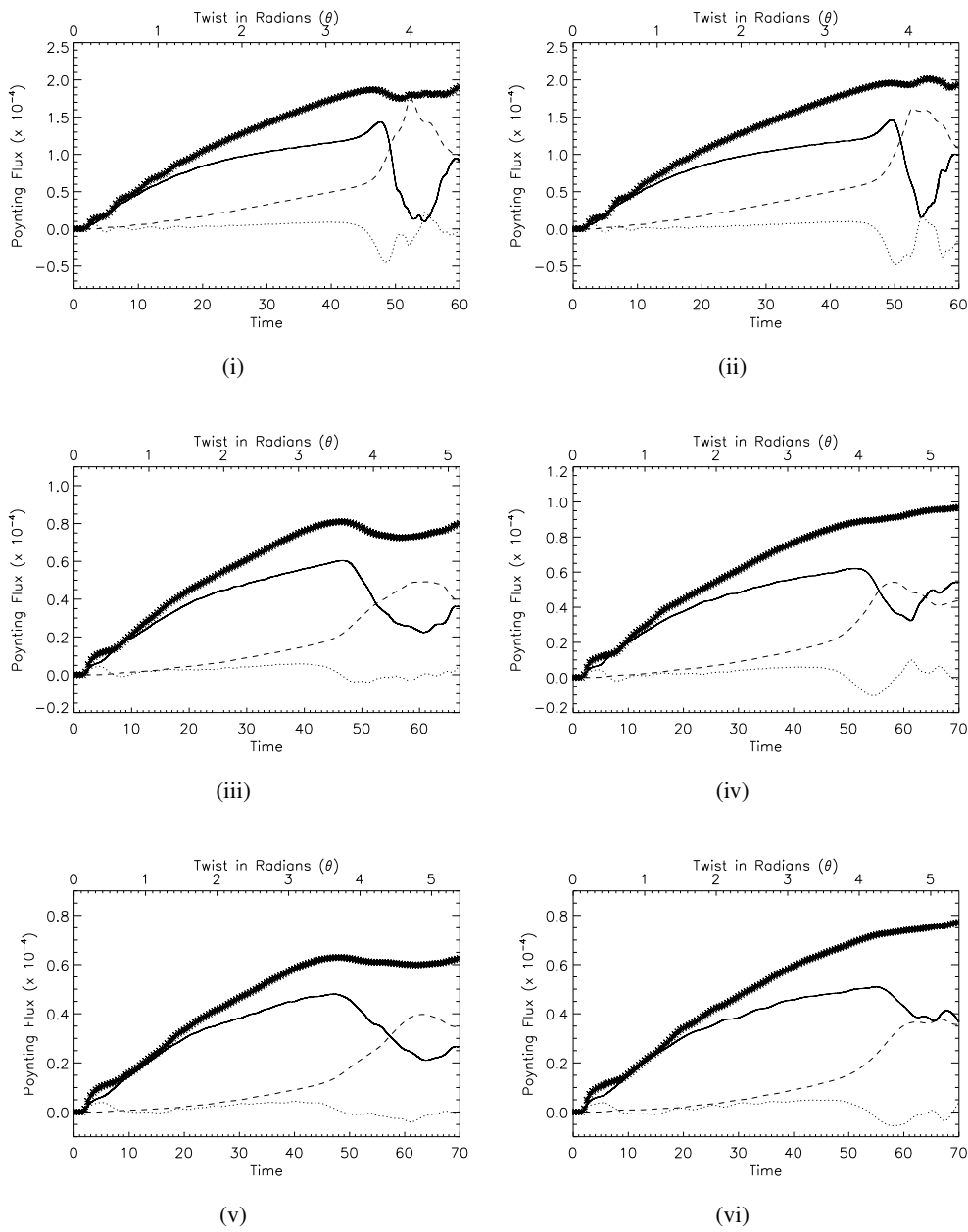


Figure 7.11: The instantaneous Poynting flux (crosses), the rate of change of magnetic energy (solid line), work done by the Lorentz force (dotted line) and Joule dissipation (dashed line), for 2 sources with (i) $B_{bg} = 0.05$, (iii) $B_{bg} = 0.01$ and (v) $B_{bg} = 0.0$ and 4 sources with (ii) $B_{bg} = 0.05$, (iv) $B_{bg} = 0.01$ and (vi) $B_{bg} = 0.0$.

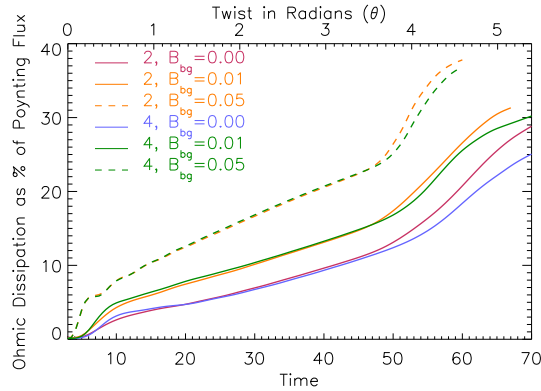


Figure 7.12: The volume and time integrated Ohmic dissipation, shown as a percentage of the time integrated Poynting flux for cases (i) to (vi).

steep gradient observed in the percentage of reconnected flux in Figure 7.7.

The different amounts of Poynting flux entering the domain make it harder to directly compare the efficiency of the heating in the different cases. In the cases with an additional background field there is a lot more energy injected into the system through the Poynting flux and consequently we would expect a greater amount of heating. Therefore, in Figure 7.12 we consider the volume and time integrated Ohmic (Joule) dissipation in each of the cases as a percentage of the time integrated Poynting flux entering the domain. This shows that the percentage of Poynting flux into Ohmic heating also increases for cases with a larger background field, as we would expect due to the larger current density values. After a twist of 4.5 radians (a time when all simulations are still running) the percentage of Poynting flux into Ohmic dissipation reaches values of 20%, 26%, 37% for $B_{bg} = 0, 0.01, 0.05$ for the two flux tubes and 17.5%, 25%, 36.5% for the four flux tube cases. We note that, although the two source cases continue to convert a larger percentage into Ohmic heating, when the background field value is increased the two and four source cases become more comparable.

We can also consider the different energy volume contributions (see Figure 7.13) as a percentage of the integrated Poynting flux into the domain (i.e. as a percentage of the total increase in energy during the simulations). Figure 7.13c shows that the majority of the energy injected into the domain goes into the magnetic energy and the evolution is generally very similar early in the simulations for the cases with and without background field. When the current begins to increase sharply in Figure 7.4 after $t \approx 43$ and reconnection begins to produce a sharp increase in the Ohmic heating, there is a reduction in the gradient of the magnetic energy in Figure 7.13c that is increasingly evident for larger values of magnetic field. This corresponds to an increasing amount of magnetic energy being converted into internal energy in Figure 7.13b. The evolution of the internal energy behaves very similarly to the Ohmic heating in Figure 7.12, as the majority of

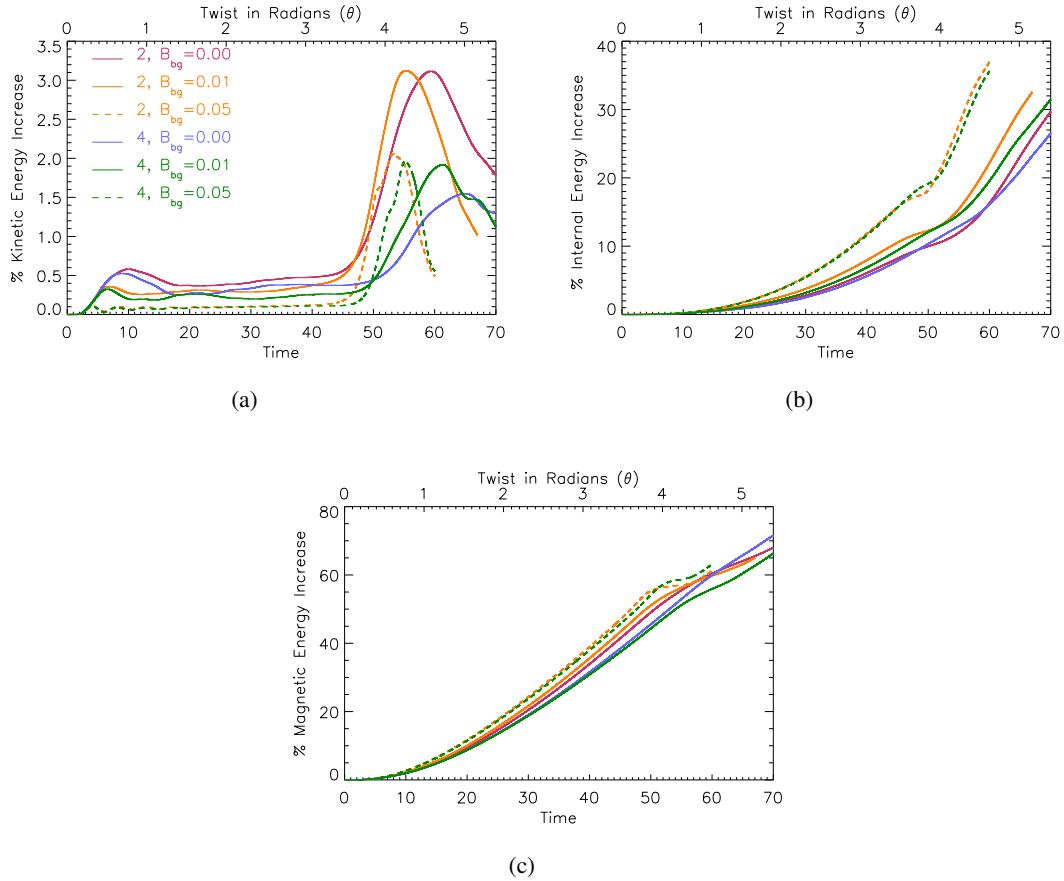


Figure 7.13: The increase of the volume integrated (a) kinetic, (b) internal and (c) magnetic energy as a percentage of the increase in the volume integrated total energy for cases (i) to (vi).

the internal energy increase occurs through Ohmic dissipation with the addition of some viscous shock heating.

The kinetic energy makes up the smallest contribution to the total energy, of just a few percent, for all the simulations. However, the gradient and timing of the peaks also show the slightly altered timing and evolution of the simulations when a background field is present. The peak in kinetic energy in the four flux tube cases occurs at twists of 4.3 radians and 5.0 radians for $B_{bg} = 0.05$ (green, dashed line) and $B_{bg} = 0.00$ (blue line), respectively. Therefore, the maximum kinetic energies (for four flux tubes) occur after less rotation for higher values of background field. The four flux tubes cases with higher values of background field also produce higher peak values of kinetic energy. The case with $B_{bg} = 0.05$ (case (ii)) also had the steepest gradient in the change in connectivity in Figure 7.7b. This suggests that the initially delayed reconnection is stronger and produces faster outflows.

In contrast, the two flux tube cases show only a slight decrease in the twist at which the peak

Table 7.2: Summary of comparison of 2 source cases with increasing background field values.

	(v) 2 Sources, $B_{bg} = 0.00$	(iii) 2 Sources, $B_{bg} = 0.01$	(i) 2 Sources, $B_{bg} = 0.05$
Time of experiment:	$0 < t < 70$ (≈ 40 minutes)	$0 < t < 67$ (≈ 38 minutes)	$0 < t < 60$ (≈ 34 minutes)
Total angle rotated (2θ) :	10.78 rad	10.31 rad	9.19 rad
First $ j $ maxima value: (in $0.4 < x, y, z < 0.6$)	3.4 at $t = 53.5$	4.4 at $t = 52.0$	5.8 at $t = 49.0$
Total viscous heating:	$\approx 1.8 \times 10^{-4}$	$\approx 2.7 \times 10^{-4}$	$\approx 5.6 \times 10^{-4}$
Total Ohmic heating:	$\approx 9.0 \times 10^{-4}$	$\approx 1.2 \times 10^{-3}$	$\approx 2.9 \times 10^{-3}$
Total Poynting flux: (en- ergy into the domain)	$\approx 3.1 \times 10^{-3}$	$\approx 3.7 \times 10^{-3}$	$\approx 7.5 \times 10^{-3}$
% of total Poynting flux as Viscous heating:	$\approx 5.8\%$	$\approx 7.2\%$	$\approx 7.5\%$
% of total Poynting flux as Ohmic heating:	$\approx 29\%$	$\approx 32\%$	$\approx 38\%$

Table 7.3: Summary of comparison of 4 source cases with increasing background field values.

	(vi) 4 Sources, $B_{bg} = 0.00$	(iv) 4 Sources, $B_{bg} = 0.01$	(ii) 4 Sources, $B_{bg} = 0.05$
Time of experiment:	$0 < t < 70$ (≈ 40 minutes)	$0 < t < 70$ (≈ 40 minutes)	$0 < t < 60$ (≈ 34 minutes)
Total angle rotated (2θ) :	10.78 rad	10.78 rad	9.19 rad
First $ j $ maxima value: (in $0.4 < x, y, z < 0.6$)	2.4 at $t = 58.5$	2.9 at $t = 54.5$	4.7 at $t = 50.0$
Total viscous heating:	$\approx 1.5 \times 10^{-4}$	$\approx 2.7 \times 10^{-4}$	$\approx 5.0 \times 10^{-4}$
Total Ohmic heating:	$\approx 8.5 \times 10^{-4}$	$\approx 1.3 \times 10^{-3}$	$\approx 2.8 \times 10^{-3}$
Total Poynting flux: (en- ergy into the domain)	$\approx 3.4 \times 10^{-3}$	$\approx 4.3 \times 10^{-3}$	$\approx 7.7 \times 10^{-3}$
% of total Poynting flux as Viscous heating:	$\approx 4.4\%$	$\approx 6.3\%$	$\approx 6.5\%$
% of total Poynting flux as Ohmic heating:	$\approx 25\%$	$\approx 30\%$	$\approx 37\%$

kinetic energies occur for stronger background field and, unlike the four flux tube cases, the peak values of the relative kinetic energy do not increase with larger background field. In fact, the kinetic energy for the two source case with $B_{bg} = 0.05$ is a much smaller percentage of the total energy increase than for the other two source cases. This again needs to be considered in light of the current layer evolution discussed in Section 7.2.1. The current values in case (i) are not able to increase for as long as in the non-background field case (as the current layer divides to form two maximum locations), therefore the peak Ohmic heating and the reconnection outflows are not as

large as we may have expected. However, we note that despite this, the two flux tube $B_{bg} = 0.05$ case (i) still showed a significant increase in the percentage of total energy into internal energy and heating compared to the other two source cases.

7.2.4 Summary

The presence of a background field delays the field lines associated with the sources from reconnecting, where the amount of delay increases with the strength of the background field. However, when reconnection does occur, the percentage of flux changing connectivity from its original source increases faster for cases with a stronger background field. This means that cases with increasing background evolve faster and release more of the energy injected into the domain as internal energy for the same amount of rotation applied.

In these experiments, the difference between the values of heating for two flux tube and four flux tube cases becomes less significant as the value of the background field increases. The cases with two flux tubes always produce greater heating and faster velocities than their four flux tube counterparts, however, the increase for the four flux tube cases is proportionally larger. Therefore, the energetics of the two and four flux tube cases become quantitatively more comparable. A comparison of the values of heating produced by each case is summarised in Tables 7.2 and 7.3, for the two and four source cases, respectively.

We also note that the current layer in the two source cases appears to fragment earlier for cases with larger background field values. This behaviour was also shown to be dependent on the value of resistivity (in Section 6.3) and may impact the values of heating produced.

Chapter 8

Fragmented Sources

So far, we have considered how increasing the number of sources and therefore flux tubes in our model influenced the evolution and energetics of the simulations. In these previous comparisons, the sources were of a similar radius and positioned an equal distance apart. In this Chapter, we consider whether dividing these sources into a cluster of smaller flux fragments will impact the field evolution and energetics.

8.1 Creating a Fragmented Source Flux Tube Set-up

Normalisation	Initial Conditions	
$B_0 = 100 \text{ G}$	$\epsilon = 0.01$	Resolution: $512^2 \times 256$
$L_0 = 75 \text{ Mm}$	$\rho = 0.1$	$\eta = 0$ (Ideal relaxation)
$n_e = 1 \times 10^{16} \text{ m}^{-3}$	$B_{bg} = 0.01$	viscosity = 0.001
		$0 < t_{relax} < 80$

The two source case with a background field ($B_{bg} = 0.01$) described in Chapter 7 as case (iii) is used as the initial case from which the fragmented sources are constructed. For our comparison, one source is left unchanged and the second is redistributed into six smaller fragments of varying size. As with previous comparisons, the total flux through the upper and lower boundary is kept constant, and this constrains the size and magnitude of the source fragments.

The vertical field distribution on the upper and lower boundaries is given by

$$B_z = B_{max} \left[e^{-[(x-x_1)^2+(y-y_1)^2]/r_1^2} + \sum_{n=1}^6 e^{-[(x-(x_s)_n)^2+(y-(y_s)_n)^2]/(r_s)_n^2} \right] + B_{bg},$$

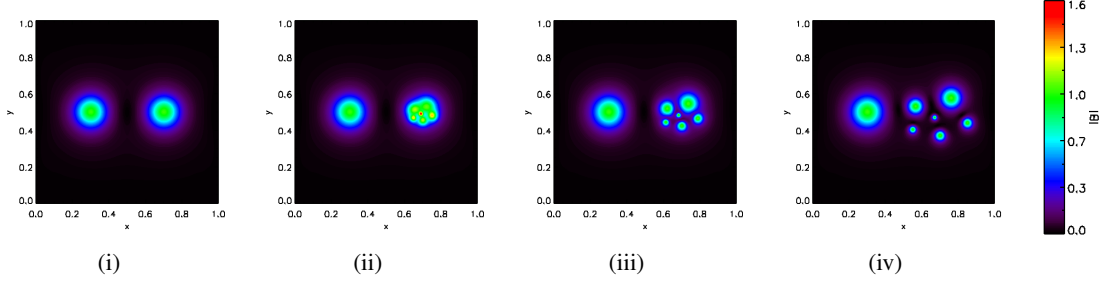


Figure 8.1: Contour plots of $|B|$ after relaxation at $z = 0.0$ for cases (i) to (iv).

where $B_{max} = 1.0$ and $B_{bg} = 0.01$, as in Chapter 7. The first term describes the strength and position of the unaltered left hand source, that remains centred on $x_1 = 0.3$, $y_1 = 0.5$ with radius $r_1 = 0.065$. The second term is a sum of six Gaussians that represent individual source fragments. The x and y positions of the fragmented sources are given by the arrays $(xs)_n$ and $(ys)_n$, respectively, described by

$$\begin{aligned} (xs)_n &= (xm_n - xc)f + xc, \\ (ys)_n &= (ym_n - yc)f + yc. \end{aligned}$$

The fragments are centred around the position $xc = 0.7$ and $yc = 0.5$, which is the location of the right hand source in the original two source case. The arrays xm and ym are an arbitrary series of positions around this location, which are chosen as

$$\begin{aligned} xm &= [0.655, 0.72, 0.75, 0.7, 0.69, 0.65], \\ ym &= [0.51, 0.525, 0.48, 0.457, 0.49, 0.468]. \end{aligned}$$

The parameter ‘ f ’ alters the spread of the fragments, where increasing f increases the distance from the central position of the original single source (xc, yc) . The fragments at each of these locations are also assigned a radius, given by

$$rs_n = [0.0325, 0.0433, 0.0216, 0.0216, 0.0108, 0.0077].$$

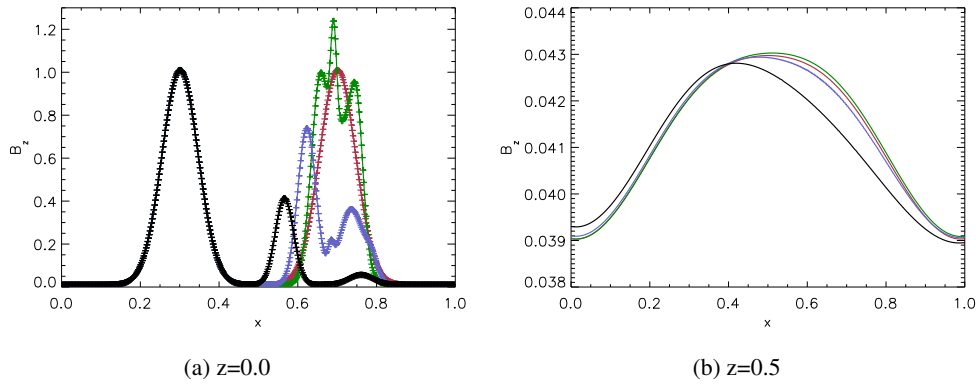
These radii are chosen to ensure that the same total flux is maintained as in the original two source case.

Three cases with increasingly spread fragments shall be considered and compared to the original two source case (now referred to as case (i)). The three cases are given by values for f of (ii) $f = 1.0$, (iii) $f = \sqrt{3} \approx 1.7$ and (iv) $f = 3.0$ and are summarised in Table 8.1.

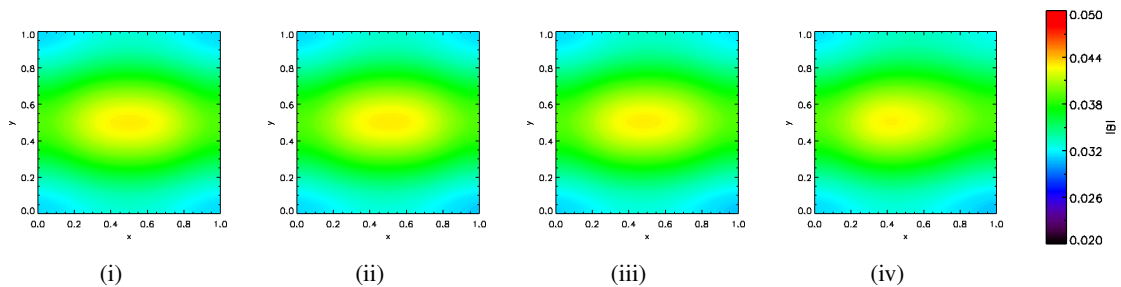
The vertical magnetic field is input into Lare3D and the initially straight flux tubes that form are allowed to expand in the domain and relax towards a numerical equilibrium, as discussed

Table 8.1: Fragmented Source Cases: Parameters and colour scheme that will be used throughout this chapter.

(i) Two Sources See Chapter 7	(ii) Fragments $f = 1.0$	(iii) Fragments $f = \sqrt{3.0} \approx 1.7$	(iv) Fragments $f = 3.0$
----------------------------------	-----------------------------	---	-----------------------------

Figure 8.2: B_z (a) on the lower boundary and (b) in mid-plane after relaxation for cases (i) to (iv) in red, green, blue and black, respectively.

previously (see Chapter 2). Contour plots of the resultant magnetic field strength on the lower boundary of the domain are displayed in Figure 8.1 for the four cases. The flux fragments of case (ii) remain very close together and are within a radius similar to the size of the single source of case (i). However, unlike in case (i), a series of (very strong) peaks are visible in case (ii), associated with the six overlapping fragments. For cases (iii) and (iv), the flux fragments are visibly distinct from each other and remain mostly within the ‘right half’ of the domain. A cross section of B_z along $y = 0.5$ on the lower boundary in Figure 8.2a shows how B_z is resolved with grid points for the four cases and displays the multiple maxima present in cases (ii) to (iv).

Figure 8.3: Contour plots of $|B|$ after relaxation in the mid-plane for cases (i) to (iv).

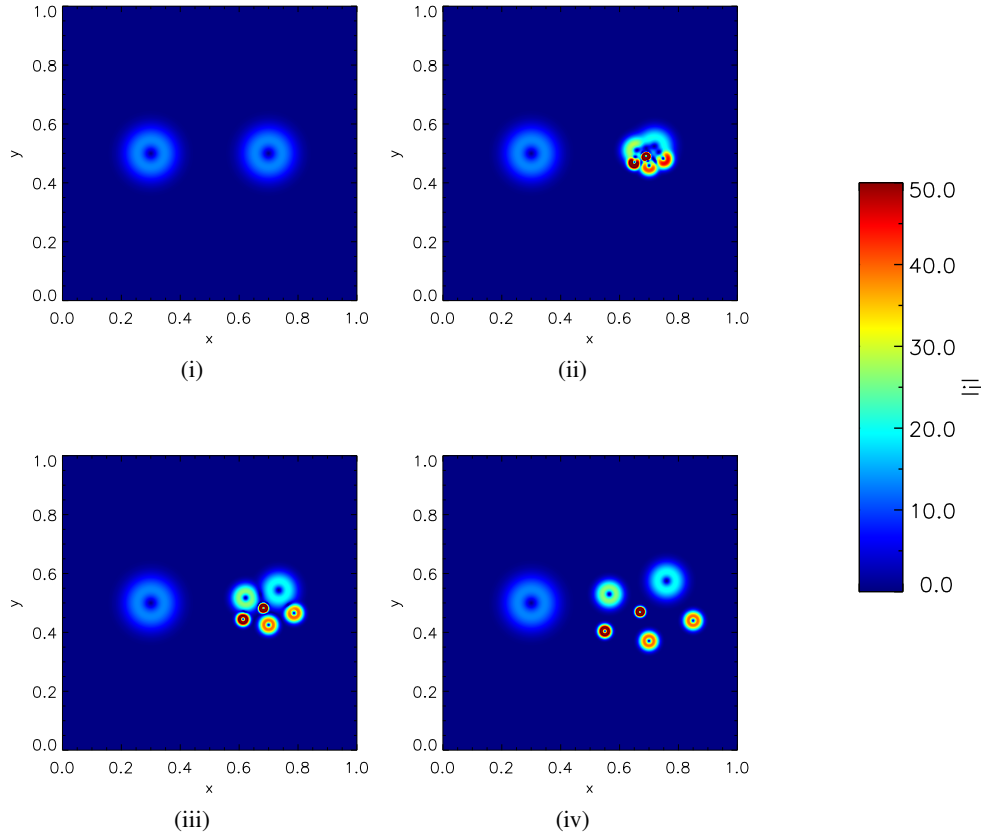


Figure 8.4: Contour plots of the magnitude of the current density ($|j|$) on the lower boundary after relaxation for cases (i) to (iv).

The magnetic field strength formed in the mid-plane by the relaxation of the flux tubes is displayed by the contour plots in Figure 8.3 and by a cross section of B_z in the mid-plane in Figure 8.2b. Both Figures show that, despite the fragmented structure of the magnetic field on the boundaries, the field formed in the mid-plane has a similar distribution and maximum field strength for all the cases. However, there is a slight asymmetry introduced by case (iv) (shown in black in Figure 8.2b). The large spread of the source fragments in case (iv) has altered the balance of total flux either side of the central line $x = 0.5$. The maximum field strength is therefore slightly off centre in Figure 8.3iv.

Figure 8.4 shows contour plots of the magnitude of the current density for the four cases on the lower boundary. The contours indicate that the fragmentation of the sources leads to higher currents forming at the boundaries. This is due to the rapid expansion of the field and the inaccuracy associated with the derivatives calculated near the upper and lower boundaries of the domain (see Chapter 2) and this effect is exaggerated further in cases where the fragments are completely separated. However, we note that the high current remains very close to the boundaries and has

reduced to a value of $|j_{max}| \approx 1.5$ a few grid points into the domain.

8.2 Comparing Fragmented Sources under Rotation

Normalisation	Initial Conditions	
$B_0 = 100 \text{ G}$	$\epsilon = 0.01$	Resolution: $512^2 \times 256$
$L_0 = 75 \text{ Mm}$	$\rho = 0.1$	$\eta = \eta_0 e^{-\left(\frac{z-0.5}{r_0}\right)^2}$
$n_e = 1 \times 10^{16} \text{ m}^{-3}$	$B_{bg} = 0.01$	$\eta_0 = 10^{-3}$
		$0 < t < 70$

The rotational velocity driver (see Chapter 3) is applied to the cases detailed above and the magnetic field is slowly twisted. The same z -dependent resistivity is applied as in Chapter 7, with $\eta_0 = 10^{-3}$. The maximum current formed around the centre of the mid-plane is plotted in Figure 8.5 and shows that the general evolution with time for the fragmented cases is very similar to the two source case previously described. The current values gradually increase until a time of $t \approx 46$ when they begin to increase more quickly. An initial maximum is then achieved in all cases around $t \approx 52$ and after this time there is a more perceivable difference in the current evolution for the different cases as they become more erratic.

There is a twisted current layer formed that is almost identical for the different cases and a cut through the mid-plane is shown in Figure 8.6. The only perceivable difference in the current layers occurs for case (iv), for which the large spread of the flux fragments, creating an asymmetric initial magnetic field distribution, leads to an asymmetric current layer. Figure 8.6iv shows that, although the maximum occurs towards the centre of the plane and with a similar value to the other

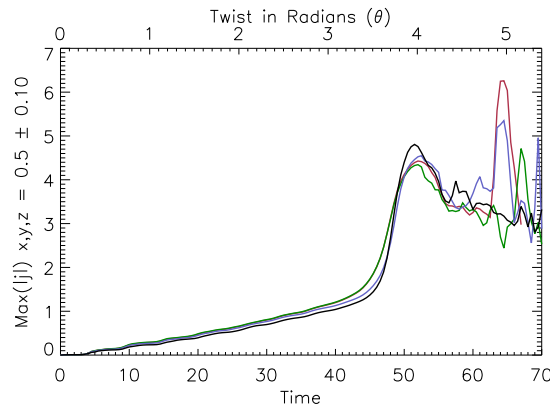


Figure 8.5: Maximum magnitude of the current density between $0.4 < x, y, z < 0.6$ for cases (i) to (iv) in red, green, blue and black, respectively.

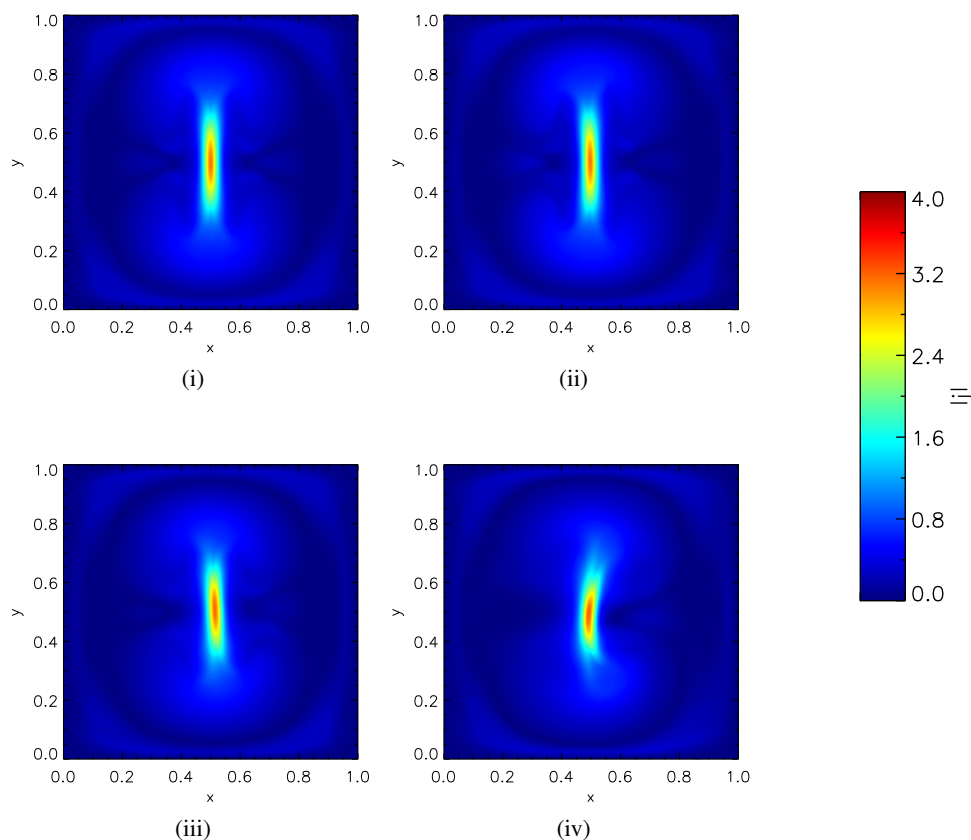


Figure 8.6: Contour plots of the magnitude of the current density in the mid-plane at $t = 50$ for cases (i) to (iv).

cases, the layer appears slightly warped.

Overall, the distribution of the flux into fragments on the boundaries appears to have very little impact on the evolution of the field in the domain. This is due to the driver on the boundaries producing a solid body rotation that moves the fragments cohesively, similar to how they would move if they were one source. This means that there is very little magnetic shear built up between the magnetic field of the flux fragments themselves. Instead, the tension force that is created, due to the curvature in the field, acts to bring the differently connected field lines from the ‘left’ and ‘right’ sides of the domain towards the centre at $x = 0.5$ to form a single strong current layer.

Case (iv) where $f = 3$, has the most spread out flux fragments and is therefore the greatest contrast to the original case (i) with two sources. However, even for these two cases the general shape of the field, shown by a selection of field lines traced from the mid-plane in Figure 8.7, is remarkably similar. Despite the large spread of fragments in case (iv), the field lines for the majority of the domain follow the same general trend as in case (i) and only differ very close to the boundaries, where the field lines diverge to connect to the separate fragments. For cases (ii)

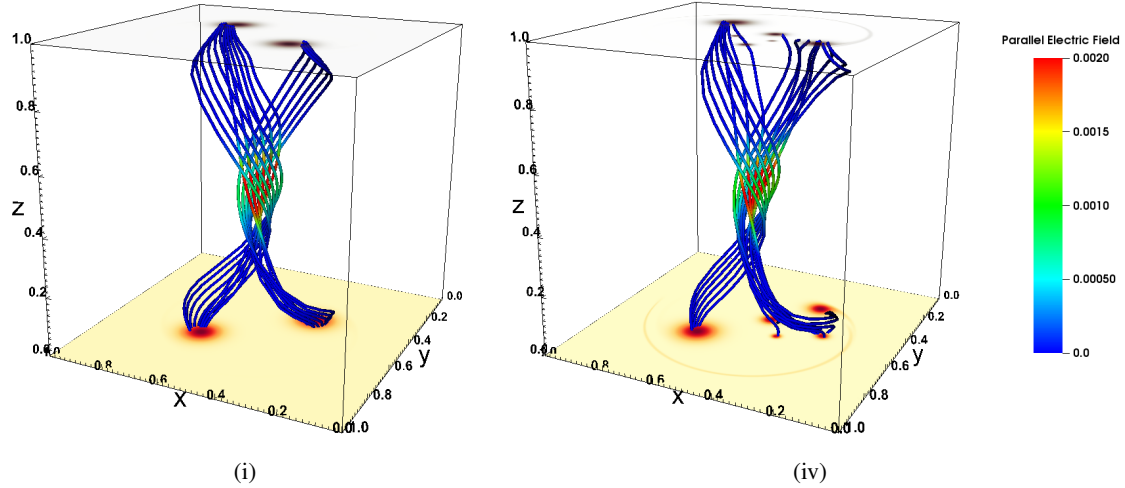


Figure 8.7: Field lines traced from the centre of the mid-plane at $t = 50$ and coloured by the value of E_{\parallel} for cases (i) and (iv).

and (iii) (not shown) the same it true but with a less drastic divergence of the field lines towards the boundaries, as the fragments are closer together. The values of parallel electric field along the field lines in Figure 8.7 are also almost identical in the two cases shown, suggesting that the change in connectivity will also follow the same trend for the two cases. This is supported by Figure 8.8, which shows the percentage of flux (traced from the initial left source) that is connected to its original source on the upper boundary. The percentage of flux at its original connection begins to decrease between 21 and 24 time units for all the cases. Case (iv) is the latest to begin the change of connectivity but the delay is very small and in all the cases 100% of the flux associated with the initial left source on the lower boundary has changed connectivity by $t = 61$.

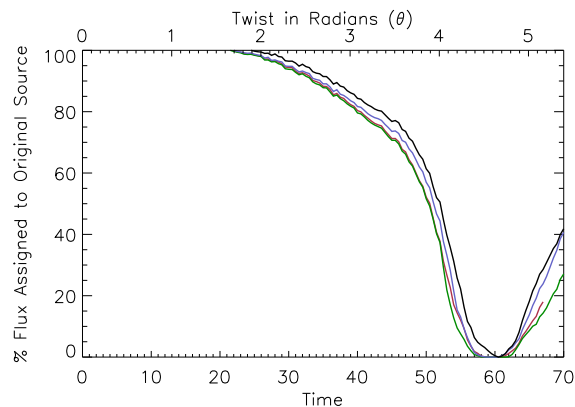


Figure 8.8: Percentage of flux assigned to its original connection from the 'left' source at $x = 0.3$ and $y = 0.5$ on the lower boundary for cases (i) to (iv) in red, green, blue and black, respectively.

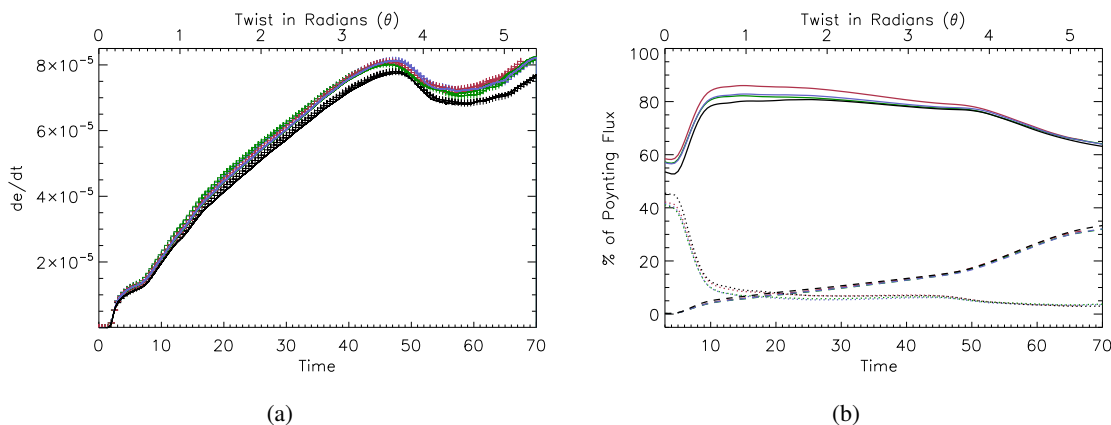


Figure 8.9: (a) The Poynting flux (crosses) and the total change of energy in the domain (solid line). (b) The integrated time and volume contributions of rate of change of magnetic energy (solid), work done by the Lorentz force (dotted) and Joule dissipation (dashed) as a percentage of the integrated Poynting flux at each time, for cases (i) to (iv) in red, green, blue and black, respectively.

The broadly similar behaviour of the magnetic field evolution is also true for the plasma and energy evolution. The total Poynting flux entering the domain (crosses) is plotted with the rate of change of total energy in the domain (solid line) in Figure 8.9a for all cases. The Poynting flux begins to increase as the driver is applied and cases (i), (ii) and (iii) increase at a very similar rate and produce almost identical maxima. In case (iv), which has the furthest spread fragments, the Poynting flux also behaves qualitatively similarly to the other cases, but reaches a slightly smaller maximum. This may be due to part of the flux fragments on the boundaries falling outside of the

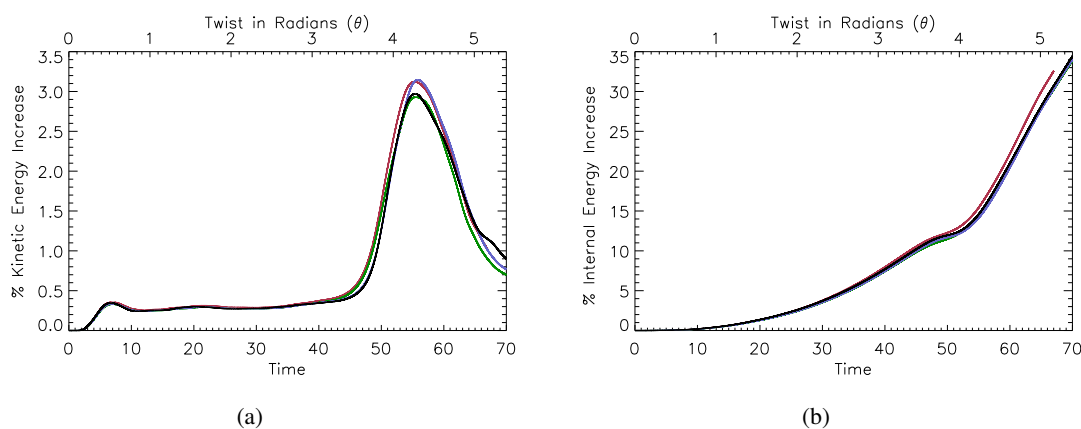


Figure 8.10: (a) Kinetic and (b) internal volume integrated energies as a percentage of the change in total energy (i.e. the time integrated Poynting flux) for cases (i) to (iv) in red, green, blue and black, respectively.

rotational velocity driver and therefore being left behind, which can be seen on the lower boundary in Figure 8.7iv. The rate of change of energy (solid) in the domain is also consistently slightly less than the Poynting flux (crosses) in Figure 8.9a for cases (ii), (iii) and (iv) for the first 50 time units of the simulations. This indicates that energy is not being conserved and suggests the field may be diffusing numerically due to the high currents present in the fragmented source. This could also reduce the amount of Poynting flux entering the domain, as the field diffusing would reduce the angle of the field through the boundaries.

Despite the slight reduction in energy conservation, the general evolution of the plasma is quantitatively similar for all the cases. The integrated Joule dissipation (Ohmic heating), work done by the Lorentz force and the rate of change in the magnetic energy are all shown as a percentage of the integrated Poynting flux in Figure 8.9b. The Ohmic heating, in particular, shows that the efficiency of heating is practically the same for all the cases. The increase in the volume integrated kinetic and internal energies are also shown as a percentage of the Poynting flux for the four cases in Figure 8.10. The original two source case (i) appears to have slightly larger values of internal energy, however this difference is very small and otherwise the evolutions overall show four cases with minimal observable difference.

The integrated domain values of the energy and heating have been shown to be quantitatively similar and, in Figure 8.11, the location of the Ohmic heating is also shown to concur between the cases. Isosurfaces of 10% (grey), 30% (light blue), 50% (green) and 70% (yellow) of the maximum values of Ohmic heating (ηj^2) are shown in Figure 8.11, for the cases with the most different initial flux distributions (i.e. cases (i) and (iv)). These show broadly similar shapes, with

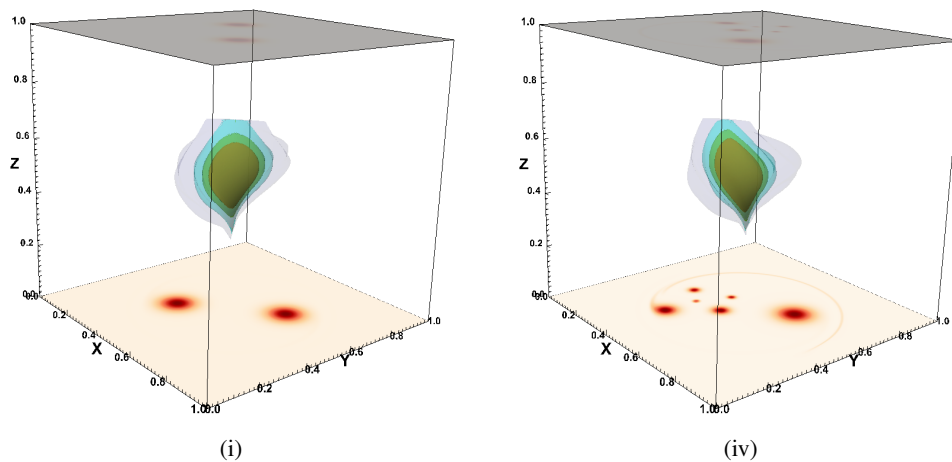


Figure 8.11: Isosurfaces of the Ohmic heating (ηj^2) at $t = 50$ for values of 10% (grey), 30% (light blue), 50% (green) and 70% (yellow) of the maximum at this time (0.007) for cases (i) and (iv).

the Ohmic heating concentrated in the centre of the domain along the twisted current layer. The strongest heating is at the centre of this layer, where the highest current is formed and where the largest value of resistivity is present. As shown in the current contour, there is a slight asymmetry in the magnetic field in case (iv), which creates a current layer that is slightly warped and tilted from the vertical, and this can also be seen in the isosurface of the Ohmic heating in Figure 8.1 iv. Despite this slight angle in the current layer, the efficiency of the simulations to convert the injected Poynting flux into Ohmic dissipation was shown to be practically identical in Figure 8.9b.

Summary

In summary, breaking up one of the flux sources into smaller flux fragments of various sizes, appeared to have very little impact on the plasma and magnetic field evolution. Similarly, exaggerating this fragmentation by increasing the spread of the sources also appeared to have little impact on the field configuration or the subsequent current formed in the domain. When the rotation is applied, the magnetic field behaves very similarly for the majority of the domain for the cases described. It is only near the boundaries that the field lines separate to connect to the individual flux fragments.

These findings seem to contrast to the significant difference that was found in the comparison of the two source case to the four source case in Chapters 6 and 7. However, in those comparisons the sources considered were generally of equal size and of equal distance from each other, maintaining the circular symmetry of the two source case. The increased number of flux sources in Chapters 6 and 7 changed the form of the magnetic field produced during the relaxation stage and, when rotated, the forces acting in the domain were also altered. In contrast, in this chapter, the fragments remained located around the same position. Subsequently, when the flux tubes expanded, virtually the same magnetic field distribution was created away from the boundaries. Therefore, when the solid body rotation was applied, the magnetic field evolution and hence the current formation and heating were not greatly impacted by the flux fragmentation.

These final simulations imply that the scales of the velocity driver and scale of the flux sources and their separation play an important role in the field evolution. The ‘large scale’ velocity driver acted on the flux fragments as one entity and therefore there was little interaction between the fragments. However, this suggests that if smaller scale drivers are applied, that do not create this solid body rotation, the fragmentation of the source may become more important.

The two source configuration is acknowledged to be a simple and idealised flux distribution (unlike the realistic solar surface). However, these results imply that the two source case appears to portray the same evolution and features as a more realistic complex magnetic flux distribution, as long as the scales of the driver are significantly larger than the separation of the flux fragments.

Chapter 9

Conclusions and Future Work

In this thesis, we have investigated how the number and distribution of flux sources impacts the heating and the evolution of the magnetic field and plasma in numerical simulations of coronal tectonics. To begin, in Chapter 2, an initial magnetic field configuration of two flux tubes is created; two magnetic flux sources are prescribed on the upper and lower boundaries of the domain and two magnetic flux tubes are formed, extending between the two planes. The magnetic field is then allowed to relax towards a numerical equilibrium, before a simple rotational velocity driver is introduced in Chapter 3. Using the two flux tube configuration under this velocity driver, a number of test cases considering the effect of different parameters are discussed. These include: the impact of resistivity in Chapter 3; the effect of increasing the resolution in Chapter 4; and the importance of the chosen loop length in Chapter 5.

Having examined the two flux tube case in detail, the flux distribution on the boundaries is altered to create four flux tubes in Chapter 6. The sources are situated symmetrically around the centre of rotation, as with the two flux tube case. Two cases with four sources on the boundaries are considered, where the sources have different radii and peak strengths but are positioned at the same locations. The cases with four flux tubes are created to have the same total flux through the boundaries as the original two sources case. In Chapter 6, the cases with four sources of different radii are shown to behave qualitatively and quantitatively similarly and therefore, in the discussion below, the ‘four source case’ we refer to can be considered to refer to both of the simulations.

In the two source case there are initially two regions of different connectivity present, which increases to four in the four source case. Under the rotational footpoint motion, a single twisted current concentration is created in the centre of the domain, forming between the two regions of differing connectivity in the two source case. Similarly, in the four source case the current builds up along the divide between regions of differing connectivity, which forms an ‘x’ shape in the horizontal plane and appears as a layer that is highly twisted with height in the domain.

The values of current density do not increase as quickly for the four source case as for the two source case and reach much smaller peak values. This leads to reconnection occurring later, after a total rotation on both boundaries of 5.80 rad in the four source case, compared to 4.36 rad for the two sources. Once the field lines begin to change connectivity, the rate at which the flux changes connectivity is also faster for the two flux tube case and produces much larger velocity outflows of $0.27v_A$, compared to $0.05v_A$ for the four source case. The change in connectivity is highly non-trivial for the four source case, with 16 possible connectivities created and flux is shown to reconnect multiple times. However, the field line connectivities traced from the footpoints are shown to behave symmetrically, as we would expect given the symmetric initial flux distribution and the applied driver.

In the two source case the maximum current values are double those found in the four source cases, but are localised in the centre of the thin central current layer. In comparison, in the four source cases there are more locations (i.e. between different regions of connectivity) where current concentrations are forming, though these are generally weaker. The reduced current density values and weaker reconnection outflows in the four source case lead to a reduction in the percentage of the Poynting flux being converted into Ohmic and viscous heating

The relative positioning of the two sources with the velocity driver, that is focussed at the central point between them, means that the forces are naturally focussed towards the centre of the domain. The separation of flux into two sources can be seen as the limiting case and suggests that any increased number of sources (with a similarly symmetric distribution, such as four source case) will create further current concentrations, but each of these would be weaker. The idealised positioning of the sources and velocity driver we use are not likely to occur, particularly with such symmetry, on the solar surface. However, despite these limitations, our findings show that the distribution of the magnetic sources affects the location and amount of Ohmic heating. The results also show that, upon comparison with the uniform field case in Appendix A, the allocation of the magnetic flux into localised sources greatly increases the value of current density created, compared to the uniform field under the same rotation. This supports the suggestion that geometrical (and topological) features in the magnetic field are important to heating, as proposed by Priest et al. (2002) in the coronal tectonics model. However, the simulations of driven uniform magnetic field in Appendix A also show the heating which occurs is surprisingly efficient, despite the small current values. This is attributed to the application of a constant resistivity with time, which allows continuous diffusion to occur without strong current concentrations needing to be built up (this is further evidence of the importance of resistivity in simulations and should be investigated further).

In Chapter 7, an additional background field is included in the comparison, and the general qualitative magnetic field and plasma evolution of the two and four source flux distributions do not change greatly. However, the presence of the background field between the sources does delay the onset of reconnection in all cases. The presence of an increased background field also created

stronger reconnection and produced more efficient Ohmic heating. This supports the findings by De Moortel and Galsgaard (2006a), who also analysed two flux tubes under rotation with different background field values. Interestingly, the delay created by the background field was greater for the two source than the four source case, while the efficiency of heating increased more in the four source case. These two results mean that for increasing values of background field the evolutions became more comparable for the cases with two and four flux tubes. For example, the Ohmic dissipation as a percentage of the Poynting flux differs by $\approx 4\%$ for the cases with no background field, compared to $\approx 1\%$ in the cases with an additional background field value of 0.05 in Chapter 7. Similarly, the timing of the peak outflows and kinetic energies observed were closer together for the two and four source cases with larger values of background field.

Finally, in Chapter 8 we consider whether breaking up one of the sources in the two flux tube case into smaller flux fragments has any effect on the build up of the current concentrations. The smaller, stronger flux fragments are positioned at the same location as the original single source. Therefore, when the same rotational velocity driver is applied, the fragments are advected in a similar manner as the single source. Hence, the general behaviour of the field and the current concentrations in the centre of the domain are unchanged by the fragmentation. The effect of increasing the spread of the fragments is also examined, but (for the spreads considered) the general quantitative behaviour in all the cases is remarkably similar. These results, when compared with the two and four source cases previously discussed, suggests that the spatial scale of the driver with respect to the flux separation scales may be important. We conjecture that a smaller scale driver would increase the interaction between the separate flux fragments and hence impact the current formed in the domain.

In the future, it would therefore be interesting to analyse the impact of velocity drivers of different scales. Previous comparisons by De Moortel and Galsgaard (2006b) touched upon this question, when they compared the spinning of individual flux tubes to the large scale rotation of two flux tubes. Circular and vortex flows have been predicted as a natural consequence of solar convection in models by Vögler et al. (2005) and Carlsson et al. (2010), and have also been directly observed (e.g. Bonet et al., 2008). Therefore, although it is very simplified, the rotational driver used can be seen to emulate some of the velocity patterns observed on the Sun. Using the normalisation outlined in Section 2.2, the rotational velocity driver we use has a radius of 30 Mm and in Chapter 6 acts on flux sources with a radius of 4.8 Mm. These scales are very large compared to the vortex type velocities observed by Bonet et al. (2008). The normalisation values used also result in a velocity in real units of $\approx 50 \text{ km s}^{-1}$, which is very fast. However, Galsgaard and Parnell (2005a) found that the heating by Joule dissipation depended on the distance travelled by the sources and not the magnitude of the velocity. Therefore, as long as the velocity remained less than the Alfvén speed, the magnetic field is able to move through a series of MHD (quasi-) equilibria and the magnitude of the velocity should not greatly impact the results.

As well as altering the scale of the velocity driver, future investigations could extend the comparison of different velocity drivers by applying a driver that will break the unrealistic symmetrical behaviour that our model currently employs. Furthermore, a comparison with non-rotational drivers would also show whether the results we see are robust to a change in the footpoint driving motions. It is also important to bear in mind that actual photospheric velocity motions will not always act to increase the stress in the field. The complex nature of the velocity on the photosphere will produce much more variation (than a simple one directional rotation we have considered) that could also act to untwist the magnetic field and thereby reduce the energy in the domain.

In addition to the simplified velocity driver, the simulations we have shown are underpinned by a number of assumptions which could be relaxed. For example, the atmosphere in our model has an initially uniform pressure and density. This produces a plasma β value that is greater than predicted in the solar corona. In future experiments, a stratified atmosphere with gravity could be introduced to create a more realistic plasma β value. The reduction in the plasma β may also affect the plasma and field evolution and the heating from reconnection (Birn et al., 2009) and it has been suggested by Galsgaard (2002) that the introduction of a gravitationally stratified atmosphere can impact the location of heating.

Our simulations model ‘straight’ coronal loops, extending between two horizontal planes, in contrast to the large arched structures observed. Another avenue to consider in future experiments would be to include the curvature of the field, which may also impact the evolution of the experiments and the current formed. Bareford et al. (2016) showed that the location of heating was impacted by modelling an arched loop compared to a straight model, however, they were primarily investigating heating due to the kink instability, where the presence of curvature is likely to be more important.

In our comparisons, the simulations are discussed in terms of normalised variables as we are chiefly concerned with the comparison between the simulations. However, it may also be useful to examine the heating and energy values produced by the simulations in a solar context. Using the normalisation values outlined in Section 2.2, the cases described in Chapter 7 produce total dissipated energy values of about $(3-9) \times 10^{29}$ ergs, for the cases with a 0–5% background field. These are the values at the end of the simulations after 35 – 40 minutes in real time and a total rotation of 9.2 – 10.8 rad. The presence of a background field is considered more ‘realistic’, but these cases also have the largest amount of energy entering the domain. These dissipation values are very large, particularly compared to the small scale nanoflare concept discussed in Chapter 1. However, the values are clearly dependent on the chosen normalisation and initial conditions, and the initial internal energy density we use is also very high in the experiments. The sources we model are large (with radius of 4.8 Mm) compared to the small fragments of flux associated with predicted nanoflare heating events, and these heating values would therefore be scaled down when considering smaller magnetic features.

We also note that the heating values and energies given for our simulations are highly dependent on the chosen parameter values, such as resistivity and shock viscosity. The importance of the resistivity value for our two source case was considered in more detail in Chapter 3. In our experiments, a localised resistivity region was used, where the resistivity reduced to zero at the footpoints. This was chosen to prevent the large heating and density evacuations from occurring at the footpoints. However, we note that the introduction of a gravitationally stratified atmosphere would help to circumvent the numerical issues that arose from the footpoint heating in our simulations. In reality, the heating is not likely to be confined purely to the middle (i.e. the apex) of the loop (as our resistivity implies) and the current between flux sources and fragments nearer the footpoints may be important. Therefore, it would be beneficial to consider different methods of applying the resistivity, such as anomalous resistivity, in future experiments. It is expected that these resistivity choices would not only impact the location of heating, but could also alter the timing and values of energy produced.

In our simulations, for simplicity, thermal conduction and radiation were neglected. However, this produced extremely high temperature values ($> 10^8$ K) in the simulations, as the heating was not able to be distributed and energy was also continually being added without being able to leave the domain. In future investigations, the presence of conduction and radiation should be considered, especially in simulations using a stratified atmosphere which attempt to model the self consistent evolution of the heated plasma.

Our simulations show some interesting results on the impact of the distribution of flux in these elementary flux tube interactions and associated heating. These ideas can, in turn, help our understanding of the general behaviour of larger and more complex models, where the resolution does not allow for the small scale energy events to be analysed in detail. Our results also lead to many further questions and possibilities to explore, from reducing the symmetry and regularity of the flux tube distribution, to varying the form and scale of the velocity driver. In the future, models should gradually increase the complexity of these elementary heating events in these ways, in order to fully understand the impact of each contribution. Similarly, there is still much work to be done in systematically analysing exactly how these increasingly complex simulations depend on the many numerical parameters and chosen initial conditions.

Appendix A

Uniform Magnetic Field

In the experiments described in this thesis, we have analysed the effect of altering the number and distribution of flux sources. Here we briefly display some of the same key plots and diagnostics for the evolution of a uniform magnetic field (i.e uniform B_z distribution, with no sources) under the same rotational driver. We have carried this out for two cases, the first (case a) has the same total flux as the non-background field cases discussed in Chapter 6 and the second (case b) has the same total flux as the cases with the 1% background field in Chapter 7. The simulations are each run using the same parameters as their comparable cases in Chapters 6 and 7 (see Table A.1). Although we do not analyse these simulations in detail, we present them here for comparison with our simulations.

Normalisation	Initial Conditions	
$B_0 = 100 \text{ G}$	$\epsilon = 0.01$	Resolution: $512^2 \times 256$
$L_0 = 75 \text{ Mm}$	$\rho = 0.1$	$\eta = \eta_0 e^{-\left(\frac{z-0.5}{r_0}\right)^2}$
$n_e = 1 \times 10^{16} \text{ m}^{-3}$		

Table A.1: Uniform Magnetic Field Cases

	(a)	(b)
Initial field strength (B_z)	0.0265465	0.036585559
Resistivity (η_0)	10^{-4}	10^{-3}
Time of simulation	$0 < t < 75$	$0 < t < 70$
For comparable cases see	Ch. 6	Ch. 7

The two cases with uniform field behave qualitatively similarly, with increased values of energy for case (b), as expected due to the stronger magnetic field and the increased resistivity. It takes longer for the current values to increase in simulations with a uniform field, acted on by the rotational velocity driver, compared to the sources of flux in previous cases. The maximum values

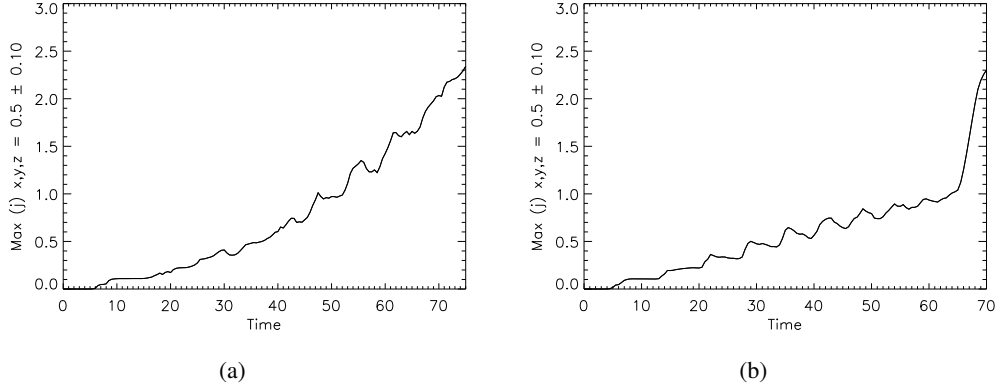


Figure A.1: Maximum magnitude of current density in $0.4 < x, y, z < 0.6$ for cases (a) and (b).

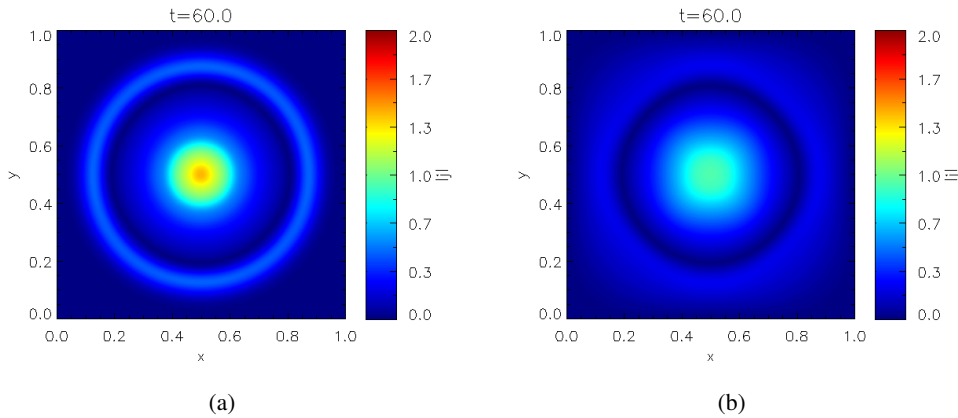


Figure A.2: Contour plots of the magnitude of the current density in the mid-plane at $t = 50$ for cases (a) and (b).

of current density are also much smaller overall (see Figure A.1). Instead of a twisted current layer, as in the cases with magnetic sources, the high current forms in a central circular region, shown in Figure A.2. This produces cylindrical isosurfaces of current, as shown in Figure A.3. The highest values of current are at the centre of the domain and this is therefore where the largest Ohmic heating takes place. Although the maximum value of current density produced is generally small compared to the cases with sources, the contour plots in Figure A.2 show there is a larger area with some value of current density created.

The Poynting flux (and maximum current) entering the domain is shown to increase in a series of ‘steps’ in Figure A.4, unlike the smooth increase we saw in previous chapters. This is due to an Alfvén wave being introduced by the footpoint motions and as it propagates, it is reflected off the boundaries, creating this ‘step’ formation in the Poynting flux (and the maximum current). This was also seen in numerical simulations of shearing by Mellor et al. (2005) and further examined

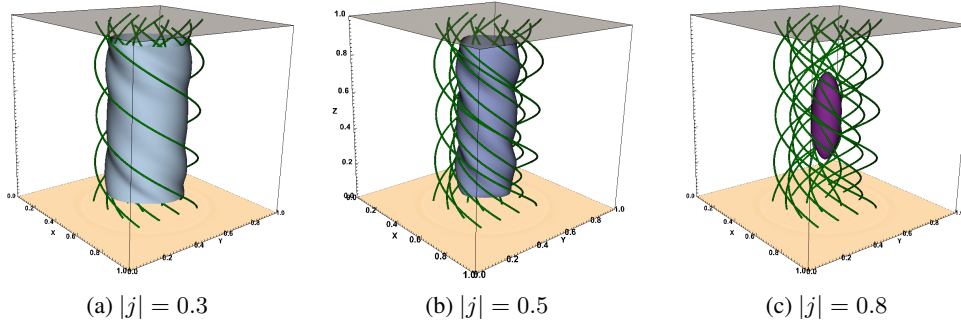


Figure A.3: A selection of field lines at $t = 60$ with isosurfaces of current at values of $|j|$ of 0.3, 0.5 and 0.8, for case (b).

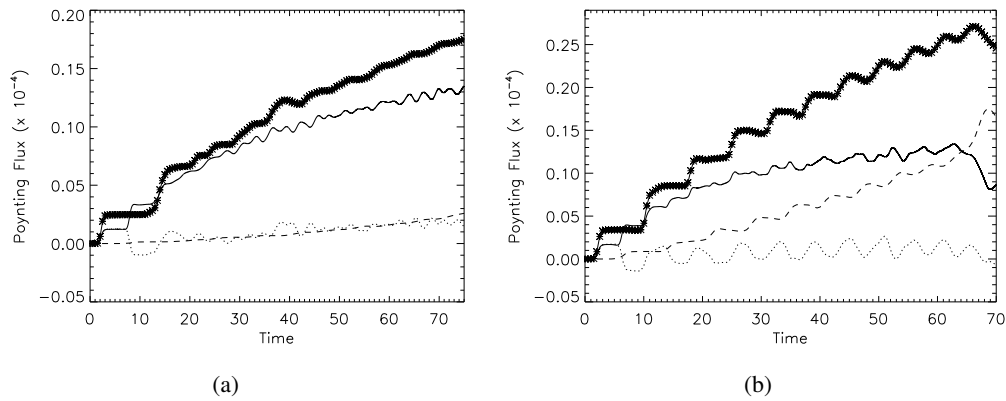


Figure A.4: The Poynting flux (crosses) with time. The solid line shows the rate of change of magnetic energy, the dotted line work done by the Lorentz force and the dashed line represents the Joule dissipation for cases (a) and (b).

analytically by these authors. Diffusion is shown to eventually smooth out these ‘steps’ in their experiments. The normalised value of the velocity acting on the boundaries of the domain remains the same as the cases with the sources in previous chapters, however, the uniform magnetic field is generally weaker and therefore the maximum Alfvén speed on the boundaries (and the average in the domain) is much smaller. This means it takes longer for information to propagate through the domain and hence the ‘step’ behaviour lasts longer and is more prominent in these cases.

The Ohmic dissipation in Figure A.5 is shown to increase from very early in the simulations. This continual dissipation prevents the current values from continuing to build-up. The total amount of Poynting flux entering the domain is also reduced compared to the magnetic source cases. Due to the smaller amount of energy entering the domain, the heating and energy values are greatly diminished compared to the cases with flux sources. However, as a percentage of the energy entering the domain, the Ohmic dissipation values are surprisingly comparable with

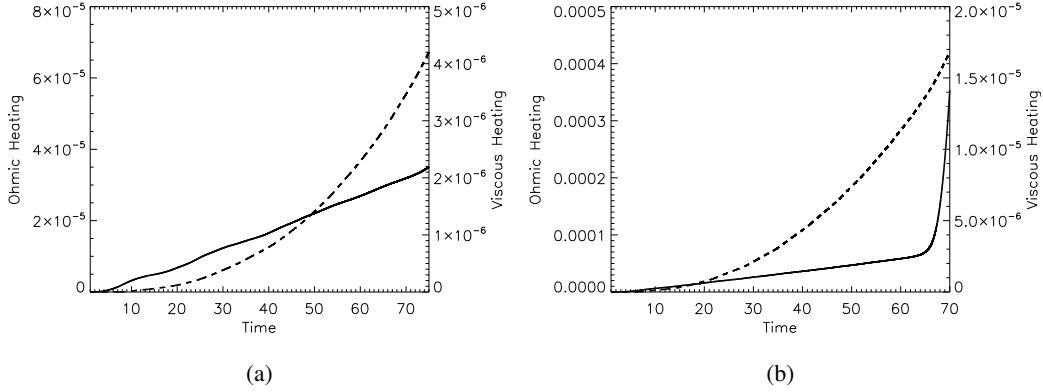


Figure A.5: The Ohmic (dashed) and viscous (solid) heating for cases (a) and (b).

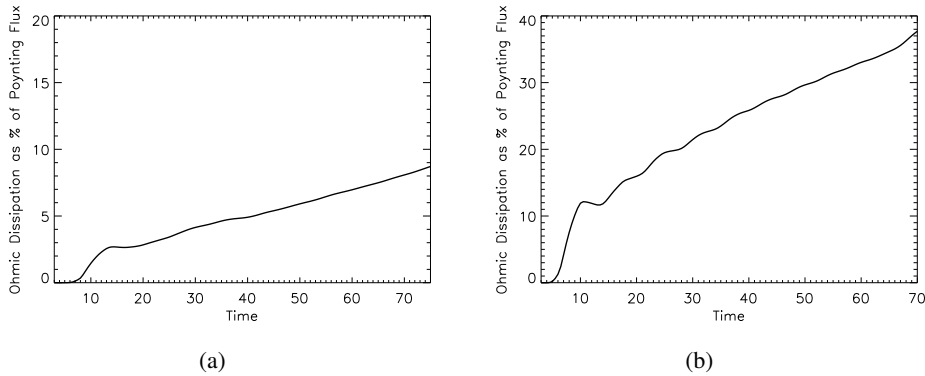


Figure A.6: The integrated Ohmic dissipation as a percentage of the integrated Poynting flux for cases (a) and (b).

the cases with magnetic sources (see Tables A.2 and A.3). This is likely due to the large region of current formation, allowing for a greater area of diffusion and associated heating, compared to the narrow current layer in the cases with flux sources. However, this finding is a result of the resistivity chosen in the experiments. The resistivity is localised in z in the domain but it acts uniformly across the plane. Similarly, it does not require a threshold current value in order to become effective. This implies that if the same experiments were considered with an anomalous resistivity, then the small current produced in the uniform case would produce little heating compared to the cases with flux sources.

The viscous heating is very small in these uniform field cases and produces significantly less heating compared to the flux source cases, shown in the comparison Tables A.2 and A.3. This is due the broad current region formed, unlike the typical narrow current layers and therefore the associated fast outflow of reconnection does not occur.

These cases are included here as an additional interesting comparison, but again show the value and application of numerical parameters, such as resistivity, can affect the results and their interpretation.

Table A.2: Comparison of uniform field case (a) with cases (i) and (ii) from Chapter 6

$\eta_0 = 10^{-4}$	(i) 2 Sources	(ii) 4 Sources	Uniform Field: case (a)
Time of experiment:	$0 < t < 75$ (≈ 43 minutes)	$0 < t < 75$ (≈ 43 minutes)	$0 < t < 75$ (≈ 43 minutes)
Total angle rotated (2θ) :	11.60 rad	11.60 rad	11.60 rad
Maximum current value: (in $0.4 < x, y, z < 0.6$)	23.5 at $t = 61.5$	12.0 at $t = 71$	2.35 at $t = 75$
Total viscous heating:	$\approx 2.8 \times 10^{-4}$	$\approx 8.3 \times 10^{-5}$	$\approx 2.5 \times 10^{-6}$
Total Ohmic heating:	$\approx 3.6 \times 10^{-4}$	$\approx 2.4 \times 10^{-4}$	$\approx 6.7 \times 10^{-5}$
Total Poynting flux: (energy into the domain)	$\approx 3.6 \times 10^{-3}$	$\approx 3.9 \times 10^{-3}$	$\approx 7.7 \times 10^{-4}$
% of total Poynting flux as Viscous heating:	$\approx 7.8\%$	$\approx 2.1\%$	$\approx 0.3\%$
% of total Poynting flux as Ohmic heating:	$\approx 10\%$	$\approx 6.2\%$	$\approx 8.7\%$

Table A.3: Comparison of uniform field case (b) with cases (iii) and (iv) from Chapter 7

$\eta_0 = 10^{-3}$	(iii) 2 Sources, $B_{bg} = 0.01$	(iv) 4 Sources, $B_{bg} = 0.01$	Uniform Field: case (b)
Time of experiment:	$0 < t < 67$ (≈ 38 minutes)	$0 < t < 70$ (≈ 43 minutes)	$0 < t < 70$ (≈ 40 minutes)
Total angle rotated (2θ) :	10.31 rad	10.78 rad	10.78 rad
Maximum current value: (in $0.4 < x, y, z < 0.6$)	6.1 at $t = 64.5$	3.7 at $t = 60.5$	2.3 at $t = 70^*$
Total viscous heating:	$\approx 2.7 \times 10^{-4}$	$\approx 2.7 \times 10^{-4}$	$\approx 1.5 \times 10^{-5}$
Total Ohmic heating:	$\approx 1.2 \times 10^{-3}$	$\approx 1.3 \times 10^{-3}$	$\approx 4.2 \times 10^{-4}$
Total Poynting flux: (energy into the domain)	$\approx 3.7 \times 10^{-3}$	$\approx 4.3 \times 10^{-3}$	$\approx 1.1 \times 10^{-3}$
% of total Poynting flux as Viscous heating:	$\approx 7.2\%$	$\approx 6.3\%$	$\approx 1.4\%$
% of total Poynting flux as Ohmic heating:	$\approx 32\%$	$\approx 30\%$	$\approx 38\%$

*This is the final current value after a sharp increase at the end of the experiment, but is not representative of the maximum current for the length of the simulation.

Bibliography

- T. D. Arber, A. W. Longbottom, C. L. Gerrard, and A. M. Milne. A Staggered Grid, Lagrangian-Eulerian Remap Code for 3-D MHD Simulations. *Journal of Computational Physics*, 171: 151–181, July 2001. doi: 10.1006/jcph.2001.6780.
- T. D. Arber, M. Haynes, and J. E. Leake. Emergence of a Flux Tube through a Partially Ionized Solar Atmosphere. *Astrophys. J.*, 666:541–546, September 2007. doi: 10.1086/520046.
- C. K. Armstrong and I. J. D. Craig. Visco-Resistive Dissipation in Strongly Driven Transient Reconnection. *Solar Phys.*, 289:869–877, March 2014. doi: 10.1007/s11207-013-0363-z.
- I. Arregui. Wave heating of the solar atmosphere. *Philosophical Transactions of the Royal Society of London Series A*, 373:20140261–20140261, April 2015. doi: 10.1098/rsta.2014.0261.
- G. Aulanier. Coronal heating and flaring in QSLs. In D. Prasad Choudhary and K. G. Strassmeier, editors, *IAU Symposium*, volume 273 of *IAU Symposium*, pages 233–241, August 2011. doi: 10.1017/S1743921311015304.
- G. Aulanier, E. Pariat, P. Démoulin, and C. R. DeVore. Slip-Running Reconnection in Quasi-Separatrix Layers. *Solar Phys.*, 238:347–376, November 2006. doi: 10.1007/s11207-006-0230-2.
- A. A. van Ballegoijen. Force free fields and coronal heating part I. The formation of current sheets. *Geophysical and Astrophysical Fluid Dynamics*, 41:181–211, 1988. doi: 10.1080/03091928808208850.
- M. R. Bareford, M. Gordovskyy, P. K. Browning, and A. W. Hood. Energy Release in Driven Twisted Coronal Loops. *Solar Phys.*, 291:187–209, January 2016. doi: 10.1007/s11207-015-0824-7.
- G. Baumann, K. Galsgaard, and Å. Nordlund. 3D Solar Null Point Reconnection MHD Simulations. *Solar Phys.*, 284:467–487, June 2013. doi: 10.1007/s11207-012-0168-5.
- J. Birn and E. R. Priest. *Reconnection of magnetic fields : magnetohydrodynamics and collisionless theory and observations*. 2007.
- J. Birn, L. Fletcher, M. Hesse, and T. Neukirch. Energy Release and Transfer in Solar Flares: Simulations of Three-Dimensional Reconnection. *Astrophys. J.*, 695:1151–1162, April 2009. doi: 10.1088/0004-637X/695/2/1151.
- J. A. Bonet, I. Márquez, J. Sánchez Almeida, I. Cabello, and V. Domingo. Convectively Driven

- Vortex Flows in the Sun. *Astrophys. J. Lett.*, 687:L131–L134, November 2008. doi: 10.1086/593329.
- G. J. J. Botha, T. D. Arber, and A. W. Hood. Thermal conduction effects on the kink instability in coronal loops. *Astron. Astrophys.*, 525:A96, January 2011. doi: 10.1051/0004-6361/201015534.
- R. Bowness, A. W. Hood, and C. E. Parnell. Coronal heating and nanoflares: current sheet formation and heating. *Astron. Astrophys.*, 560:A89, December 2013. doi: 10.1051/0004-6361/201116652.
- M. Carlsson, V. H. Hansteen, and B. V. Gudiksen. Chromospheric heating and structure as determined from high resolution 3D simulations. *Mem. Societa Astronomica Italiana*, 81:582, 2010.
- I. De Moortel and P. Browning. Recent advances in coronal heating. *Philosophical Transactions of the Royal Society of London Series A*, 373:20140269–20140269, April 2015. doi: 10.1098/rsta.2014.0269.
- I. De Moortel and K. Galsgaard. Numerical modelling of 3D reconnection due to rotational footpoint motions. *Astron. Astrophys.*, 451:1101–1115, June 2006a. doi: 10.1051/0004-6361:20054587.
- I. De Moortel and K. Galsgaard. Numerical modelling of 3D reconnection. II. Comparison between rotational and spinning footpoint motions. *Astron. Astrophys.*, 459:627–639, November 2006b. doi: 10.1051/0004-6361:20065716.
- I. De Moortel and V. M. Nakariakov. Magnetohydrodynamic waves and coronal seismology: an overview of recent results. *Philosophical Transactions of the Royal Society of London Series A*, 370:3193–3216, July 2012. doi: 10.1098/rsta.2011.0640.
- P. Démoulin. Where will efficient energy release occur in 3D magnetic configurations? In *36th COSPAR Scientific Assembly*, volume 36 of *COSPAR Meeting*, page 118, 2006a.
- P. Démoulin. Extending the concept of separatrices to QSLs for magnetic reconnection. *Advances in Space Research*, 37:1269–1282, 2006b. doi: 10.1016/j.asr.2005.03.085.
- P. Démoulin, J. C. Henoux, E. R. Priest, and C. H. Mandrini. Quasi-Separatrix layers in solar flares. I. Method. *Astron. Astrophys.*, 308:643–655, April 1996.
- C. R. Evans and J. F. Hawley. Simulation of magnetohydrodynamic flows - A constrained transport method. *Astrophys. J.*, 332:659–677, September 1988. doi: 10.1086/166684.
- A. H. Gabriel. A magnetic model of the solar transition region. *Philosophical Transactions of the Royal Society of London Series A*, 281:339–352, May 1976. doi: 10.1098/rsta.1976.0031.
- K. Galsgaard. Flux braiding in a stratified atmosphere. In H. Sawaya-Lacoste, editor, *SOLMAG 2002. Proceedings of the Magnetic Coupling of the Solar Atmosphere Euroconference*, volume 505 of *ESA Special Publication*, pages 269–272, October 2002.
- K. Galsgaard and Å. Nordlund. Heating and activity of the solar corona 1. Boundary shearing of an initially homogeneous magnetic field. *J. Geophys. Res.*, 101:13445–13460, June 1996. doi: 10.1029/96JA00428.

- K. Galsgaard and C. E. Parnell. Elementary heating events - magnetic interactions between two flux sources. III. Energy considerations. *Astron. Astrophys.*, 439:335–349, August 2005a. doi: 10.1051/0004-6361:20052775.
- K. Galsgaard and C. E. Parnell. Elementary heating events - magnetic interactions between two flux sources. III. Energy considerations. *Astron. Astrophys.*, 439:335–349, August 2005b. doi: 10.1051/0004-6361:20052775.
- K. Galsgaard and D. I. Pontin. Steady state reconnection at a single 3D magnetic null point. *Astron. Astrophys.*, 529:A20, May 2011. doi: 10.1051/0004-6361/201014359.
- K. Galsgaard, C. E. Parnell, and J. Blaizot. Elementary heating events - Magnetic interactions between two flux sources. *Astron. Astrophys.*, 362:395–405, October 2000.
- J. P. H. Goedbloed and S. Poedts. *Principles of Magnetohydrodynamics*. August 2004.
- B. V. Gudiksen and Å. Nordlund. Bulk Heating and Slender Magnetic Loops in the Solar Corona. *Astrophys. J. Lett.*, 572:L113–L116, June 2002. doi: 10.1086/341600.
- B. V. Gudiksen and Å. Nordlund. An Ab Initio Approach to the Solar Coronal Heating Problem. *Astrophys. J.*, 618:1020–1030, January 2005. doi: 10.1086/426063.
- J. Heerikhuisen and I. J. D. Craig. Magnetic Reconnection in Three Dimensions - Spine, Fan and Separator Solutions. *Solar Phys.*, 222:95–114, July 2004. doi: 10.1023/B:SOLA.0000036878.13759.68.
- M. Janvier, G. Aulanier, and P. Démoulin. From Coronal Observations to MHD Simulations, the Building Blocks for 3D Models of Solar Flares (Invited Review). *Solar Phys.*, 290:3425–3456, December 2015. doi: 10.1007/s11207-015-0710-3.
- J. A. Klimchuk. Key aspects of coronal heating. *Philosophical Transactions of the Royal Society of London Series A*, 373:20140256–20140256, April 2015. doi: 10.1098/rsta.2014.0256.
- J. A. Klimchuk. On Solving the Coronal Heating Problem. *Solar Phys.*, 234:41–77, March 2006. doi: 10.1007/s11207-006-0055-z.
- Y.-T. Lau and J. M. Finn. Three-dimensional kinematic reconnection in the presence of field nulls and closed field lines. *Astrophys. J.*, 350:672–691, February 1990. doi: 10.1086/168419.
- R. H. Levine. A New Theory of Coronal Heating. *Astrophys. J.*, 190:457–466, June 1974. doi: 10.1086/152898.
- R. P. Lin, R. A. Schwartz, S. R. Kane, R. M. Pelling, and K. C. Hurley. Solar hard X-ray microflares. *Astrophys. J.*, 283:421–425, August 1984. doi: 10.1086/162321.
- D. W. Longcope and R. N. Sudan. Evolution and statistics of current sheets in coronal magnetic loops. *Astrophys. J.*, 437:491–504, December 1994. doi: 10.1086/175013.
- D. Mackay and A. Yeates. The Sun's Global Photospheric and Coronal Magnetic Fields: Observations and Models. *Living Reviews in Solar Physics*, 9:6, November 2012. doi: 10.12942/lrsp-2012-6.
- C. Mellor, C. L. Gerrard, K. Galsgaard, A. W. Hood, and E. R. Priest. Numerical Simulations of the Flux Tube Tectonics Model for Coronal Heating. *Solar Phys.*, 227:39–60, March 2005. doi: 10.1007/s11207-005-1713-2.

- Z. Mikic, D. D. Schnack, and G. van Hoven. Creation of current filaments in the solar corona. *Astrophys. J.*, 338:1148–1157, March 1989. doi: 10.1086/167265.
- C. S. Ng, L. Lin, and A. Bhattacharjee. High-Lundquist Number Scaling in Three-dimensional Simulations of Parker’s Model of Coronal Heating. *Astrophys. J.*, 747:109, March 2012. doi: 10.1088/0004-637X/747/2/109.
- E. N. Parker. Topological Dissipation and the Small-Scale Fields in Turbulent Gases. *Astrophys. J.*, 174:499, June 1972. doi: 10.1086/151512.
- E. N. Parker. Nanoflares and the solar X-ray corona. *Astrophys. J.*, 330:474–479, July 1988. doi: 10.1086/166485.
- C. E. Parnell and I. De Moortel. A contemporary view of coronal heating. *Philosophical Transactions of the Royal Society of London Series A*, 370:3217–3240, July 2012. doi: 10.1098/rsta.2012.0113.
- C. E. Parnell and K. Galsgaard. Elementary heating events - magnetic interactions between two flux sources. II. Rates of flux reconnection. *Astron. Astrophys.*, 428:595–612, December 2004. doi: 10.1051/0004-6361:20034350.
- C. E. Parnell, A. L. Haynes, and K. Galsgaard. Structure of magnetic separators and separator reconnection. *Journal of Geophysical Research (Space Physics)*, 115:A02102, February 2010. doi: 10.1029/2009JA014557.
- C. E. Parnell, R. C. Maclean, A. L. Haynes, and K. Galsgaard. 3D Magnetic Reconnection. In N. H. Brummell, A. S. Brun, M. S. Miesch, and Y. Ponty, editors, *IAU Symposium*, volume 271 of *IAU Symposium*, pages 227–238, August 2011. doi: 10.1017/S1743921311017650.
- C. E. Parnell, J. E. H. Stevenson, J. Threlfall, and S. J. Edwards. Is magnetic topology important for heating the solar atmosphere? *Philosophical Transactions of the Royal Society of London Series A*, 373:20140264–20140264, April 2015. doi: 10.1098/rsta.2014.0264.
- H. Peter. What can large-scale magnetohydrodynamic numerical experiments tell us about coronal heating? *Philosophical Transactions of the Royal Society of London Series A*, 373:20150055–20150055, April 2015. doi: 10.1098/rsta.2015.0055.
- H. Peter, B. V. Gudiksen, and Å. Nordlund. Coronal Heating through Braiding of Magnetic Field Lines. *Astrophys. J. Lett.*, 617:L85–L88, December 2004. doi: 10.1086/427168.
- D. I. Pontin, K. Galsgaard, G. Hornig, and E. R. Priest. A fully magnetohydrodynamic simulation of three-dimensional non-null reconnection. *Physics of Plasmas*, 12(5):052307, May 2005. doi: 10.1063/1.1891005.
- E. Priest. *Magnetohydrodynamics of the Sun*. May 2014.
- E. Priest and T. Forbes, editors. *Magnetic reconnection : MHD theory and applications*, 2000.
- E. R. Priest. *Solar magneto-hydrodynamics*. 1982.
- E. R. Priest and V. S. Titov. Magnetic Reconnection at Three-Dimensional Null Points. *Philosophical Transactions of the Royal Society of London Series A*, 354:2951–2992, December 1996. doi: 10.1098/rsta.1996.0136.
- E. R. Priest, J. F. Heyvaerts, and A. M. Title. A Flux-Tube Tectonics Model for Solar Coronal

- Heating Driven by the Magnetic Carpet. *ApJ*, 576:533–551, September 2002. doi: 10.1086/341539.
- E. R. Priest, D. W. Longcope, and J. Heyvaerts. Coronal Heating at Separators and Separatrices. *Astrophys. J.*, 624:1057–1071, May 2005. doi: 10.1086/429312.
- A. F. Rappazzo, M. Velli, G. Einaudi, and R. B. Dahlburg. Coronal Heating, Weak MHD Turbulence, and Scaling Laws. *Astrophys. J. Lett.*, 657:L47–L51, March 2007. doi: 10.1086/512975.
- A. F. Rappazzo, M. Velli, G. Einaudi, and R. B. Dahlburg. Nonlinear Dynamics of the Parker Scenario for Coronal Heating. *Astrophys. J.*, 677:1348–1366, April 2008. doi: 10.1086/528786.
- F. Reale. Coronal Loops: Observations and Modeling of Confined Plasma. *Living Reviews in Solar Physics*, 7:5, November 2010. doi: 10.12942/lrsp-2010-5.
- K. Schindler, M. Hesse, and J. Birn. General magnetic reconnection, parallel electric fields, and helicity. *J. Geophys. Res.*, 93:5547–5557, June 1988. doi: 10.1029/JA093iA06p05547.
- C. J. Schrijver, A. M. Title, A. A. van Ballegooijen, H. J. Hagenaar, and R. A. Shine. Sustaining the Quiet Photospheric Network: The Balance of Flux Emergence, Fragmentation, Merging, and Cancellation. *Astrophys. J.*, 487:424–436, September 1997.
- C. J. Schrijver, A. M. Title, K. L. Harvey, N. R. Sheeley, Y.-M. Wang, G. H. J. van den Oord, R. A. Shine, T. D. Tarbell, and N. E. Hurlburt. Large-scale coronal heating by the small-scale magnetic field of the Sun. *Nature*, 394:152–154, July 1998. doi: 10.1038/28108.
- J. E. H. Stevenson, C. E. Parnell, E. R. Priest, and A. L. Haynes. The nature of separator current layers in MHS equilibria. I. Current parallel to the separator. *Astron. Astrophys.*, 573:A44, January 2015. doi: 10.1051/0004-6361/201424348.
- A. M. Title and C. J. Schrijver. The Sun’s Magnetic Carpet. In R. A. Donahue and J. A. Bookbinder, editors, *Cool Stars, Stellar Systems, and the Sun*, volume 154 of *Astronomical Society of the Pacific Conference Series*, page 345, 1998.
- V. S. Titov, G. Hornig, and P. Démoulin. Theory of magnetic connectivity in the solar corona. *Journal of Geophysical Research (Space Physics)*, 107:1164, August 2002. doi: 10.1029/2001JA000278.
- A. Vögler, S. Shelyag, M. Schüssler, F. Cattaneo, T. Emonet, and T. Linde. Simulations of magneto-convection in the solar photosphere. Equations, methods, and results of the MURaM code. *Astron. Astrophys.*, 429:335–351, January 2005. doi: 10.1051/0004-6361:20041507.
- R. W. Walsh and J. Ireland. The heating of the solar corona. *Astron. Astrophys. Rev.*, 12:1–41, 2003. doi: 10.1007/s00159-003-0021-9.
- A. L. Wilmot-Smith. An overview of flux braiding experiments. *Philosophical Transactions of the Royal Society of London Series A*, 373:20140265–20140265, April 2015. doi: 10.1098/rsta.2014.0265.
- A. L. Wilmot-Smith and I. De Moortel. Magnetic reconnection in flux-tubes undergoing spinning footpoint motions. *Astron. Astrophys.*, 473:615–623, October 2007. doi: 10.1051/0004-6361:20077455.